PROBING TRAPPED ION ENERGIES IN A QUADRUPOLE ION TRAP MASS SPECTROMETER

By

CECILIA BASIC

A DISSERTATION PRESENTED TO THE GRADUATE SCHOOL
OF THE UNIVERSITY OF FLORIDA IN PARTIAL FULFILLMENT
OF THE REQUIREMENTS FOR THE DEGREE OF
DOCTOR OF PHILOSOPHY

UNIVERSITY OF FLORIDA

1992

To my family who have provided love, understanding, and support throughout my studies.

ACKNOWLEDGEMENTS

I would like to extend my sincere thanks to Drs. Richard A. Yost and John R. Eyler for their support and guidance throughout this work. Their combined perspective on these studies has been most valuable. I would like to thank my committee members, Dr. Anna Brajter-Toth, Dr. Willard D. Harrison, and Dr. Stephen T. Gottesman, and acknowledge the NASA/Finnigan MAT AmTech project 88-01 for partial funding of this work.

I would like to acknowledge my fellow group members and extend a special thanks to Nathan A. Yates and Jodie V. Johnson for their friendship and conversations (scientific and otherwise) over the past few years and to Jody A. Freeman for her encouragement and companionship throughout my studies. I would also like to thank James E. Bruce for his many helpful discussions concerning the studies in chapters 2 and 3 of this work.

Finally, I would like to express my sincere thanks and gratitude to Nancy J. Mullins and Micheal S. Freund for their friendship, support, and fine, fine, home-cooking.

TABLE OF CONTENTS

Page

ACKNOWLEDGEMENTS iii

LIST OF TABLES vii

LIST OF FIGURES ix

ABSTRACT xvii

CHAPTERS

1 INTRODUCTION 1

Principles of the Quadrupole Ion Trap 2
Brief History 2
Principles of Operation 4
The Ion Trap Mass Spectrometer™ 10
Theoretical Models of Trapped Ion Energies 14
Calculations of Individual Ion Trajectories 14
Pseudo-potential Well Model 17
Phase-space Dynamics 20
Temporal Invariance 23
Models of Resonant Excitation 24
Experimental Determination of Trapped Ion Energies 25
Kinetic and Thermodynamic Thermometers 25
QET and *n*-Alkylbenzene Internal Energy Thermometers 26
Scope of the Dissertation 27

2 KINETIC THERMOMETER REACTIONS 28

Introduction 28
Physiochemical Basis of the Thermometers 30
Previous Ion Energy Determinations in a Rf Ion Trap 33
Experimental 35
Instrumental and Chemicals 35
Neutral Gas Pressure Determinations 38

Calibration Reaction 44
$K.E._{cm}$ Determinations 45
Calculation of Experimental Error 47
Results and Discussion 47
$CH_4^+ + CH_4 \rightarrow CH_5^+ + CH_3$ Calibration Reaction 47
$K.E._{cm}$ Dependent $Ar^+ + N_2 \rightarrow N_2^+ + Ar$ Reaction 52
$K.E._{cm}$ Dependent $O_2^+ + CH_4 \rightarrow CH_3O_2^+ + H$ Reaction 63
"Effective" Ion Temperatures 70
Conclusions 74
Utility of Kinetic Thermometer Reactions 75

3 THERMODYNAMIC THERMOMETER REACTIONS 77

Introduction 77
Mass Spectrometric Determinations of K_{eq} 77
Previous Determinations of K_{eq} on Rf Ion Traps 81
Physiochemical Basis of the Thermometers 82
Experimental 83
K_{eq} and Ion Temperature Determinations 84
Calculation of Experimental Error 89
Results 89
Proton Transfer Equilibrium between Toluene and Ethylbenzene 89
Proton Transfer Equilibrium between Diethylamine and di-*n*-Propylamine 95
Charge Transfer between Fluorobenzene and *m*-Dichlorobenzene 95
Discussion 99
Conclusions 104
Utility of Thermodynamic Thermometer Reactions 105

4 QET BREAKDOWN GRAPHS AS INTERNAL ENERGY THERMOMETERS 108

Introduction 108
Collision-induced Dissociation 108
Collision-induced Dissociation in the QITMS 111
Quasi-equilibrium Theory 113
CID versus QET Breakdown Graphs 116
Basis of the QET Thermometers 117
Experimental 118
Results 119
Acetone 119
2-Pentanone 122
Propane 129
Toluene 133
Benzene 133

Discussion 145
Conclusions 155
Utility of QET Breakdown Graphs as Internal Energy Thermometers 156

5 *n*-ALKYLBENZENE INTERNAL ENERGY THERMOMETERS 157

Introduction 157
Physiochemical Basis and Previous Applications of the *n*-Alkylbenzene Thermometers 157
Previous Internal Energy Determination in a QITMS 163
Experimental 167
Instrumental and Chemicals 167
Data Manipulation 168
Results and Discussion 176
Three-dimensional CID Breakdown Surfaces 176
Two-dimensional CID Breakdown Graphs 187
Variable He Buffer and *n*-Butylbenzene Pressure Studies 197
Conclusions 213
Utility of *n*-Alkylbenzene Internal Energy Thermometers 215

6 CONCLUSIONS AND FUTURE WORK 217
Conclusions 217
Overview of the Chemical "Thermometer" Results 220
Future Work 222
Practical Suggestions for Chemical Thermometer Studies 224
Experimental Considerations 224
Calculation Considerations 226

APPENDICES

A FORTH PROGRAM FOR VARYING REACTION TIME 228

B FORTH PROGRAM FOR OPTIMIZING RESONANT EXCITATION FREQUENCIES 230

C BASIC PROGRAM FOR TWO-DIMENSIONAL DATA SMOOTHING 232

REFERENCES 238

BIOGRAPHICAL SKETCH 258

LIST OF TABLES

Table Page

1-1 Scan function for performing MS/MS of mass-selected *m/z* 134 on an ITMS™ using axial modulation 15

2-1 ITMS™ ion gauge correction factors 43

2-2 Rate constants for the calibration reaction of CH_4^+ with CH_4 with no He buffer in the trap 51

2-3 Rate constants for calibration reaction of CH_4^+ with CH_4 with He buffer in the trap 53

2-4 Rate constants, *k*, and $K.E._{cm}$ for the reaction of Ar^+ with N_2 with no He buffer gas 57

2-5 Rate constants, *k*, and $K.E._{cm}$ for the reaction of Ar^+ with N_2 at a variety of He buffer gas pressures 59

2-6 Pseudo-potential well depth and kinetic energy calculations for Ar^+ ions in the ITMS™ 64

2-7 Langevin collision rates for a Ar^+, N_2^+, and CH_4^+ in various gases 72

3-1 K_{eq} and ion temperatures from the proton transfer equilibrium between toluene and ethylbenzene 94

3-2 K_{eq} and ion temperatures from the proton transfer equilibrium between diethylamine and di-*n*-propylamine 98

3-3 K_{eq} and ion temperatures from the charge transfer equilibrium between fluorobenzene and *m*-dichlorobenzene 102

4-1 Comparison of fluences calculated from crossovers in the time-resolved CID breakdown graphs of the M^+ ions of acetone and 2-pentanone with crossovers calculated from QET. 124

4-2 Fluences from selected points on the time-resolved CID breakdown graphs of the M^+ ion of propane 132

4-3 Fluences for the isomerization of the M^+ ion of toluene calculated at the midpoint of the first *m/z* 91 and 92 ion signal plateaus in the time-resolved CID breakdown graphs 138

4-4 Comparison of fluences calculated from crossovers in the time-resolved CID breakdown graphs of the M^+ ions of toluene and benzene with crossovers calculated from QET 140

4-5 Slopes of the resonant excitation voltage versus excitation time plots for the M^+ ions of acetone, 2-pentanone, propane, toluene, and benzene 154

5-1 Slopes of the resonant excitation voltage versus excitation time in the log-log CID topographical plots at selected $91^+/92^+$ ratios for the M^+ ions of the *n*-alkylbenzenes 186

5-2 Fluences and CID efficiencies for the M^+ ions of the *n*-alkylbenzenes calculated at the onset of the $91^+/92^+$ plateaus 192

5-3 Internal energies and percent energy conversions from the *n*-alkylbenzene thermometers 195

5-4 Internal energies and CID efficiencies for the M^+ ion of *n*-butylbenzene at various He buffer pressures 205

LIST OF FIGURES

Figure Page

1-1 Schematic of the quadrupole ion trap showing the arrangement of the three hyperbolic electrodes. The radius of the ring electrode, r_0, and the half distance between the two end-cap electrodes, z_0, are related by $r_0^2 = 2z_0^2$ (Adapted with permission, March and Hughes, 1989.) 5

1-2 a) Solutions to the Mathieu equation for an rf ion trap. Ions with a,q parameters within the regions of stability in both the r and the z-directions will follow stable trajectories. The first stability region is shaded here and enlarged in Figure 1-2b. Inset: the 2:1 Lissajous form of an ion's trajectory in the rz plane. (Adapted with permission, March and Hughes, 1989.) 8

1-2 (continued) b) An enlargement of the first stability region in Figure 1-2a. In rf-only operation (*i.e.* $a_z = 0$) ions with a m/z ratio greater than that of the low-mass cut-off at $q_z = 0.908$ will follow stable trajectories. The β_r and β_z lines define the fundamental secular frequencies of the ions in the r and z directions, respectively. (Adapted with permission, March and Hughes, 1989.). 9

1-3 A schematic of the Finnigan MAT ITMS™. The ring electrode has a radius r_0 = 1 cm and z_0 = 0.707 cm. A drive potential of 1.1 MHz is applied to the ring electrode. The supplemental rf potential is applied to the end-cap electrodes in the dipolar mode 11

1-4 An illustration of the pseudo-potential wells of depth $\overline{D}_z$ and $\overline{D}_r$ for an rf ion trap. According to this model, an ion is considered to oscillate in the wells with frequencies $\omega_{0,z}$ and $\omega_{0,r}$ in the r and z directions, respectively. (Adapted with permission, March and Hughes, 1989.) 19

1-5 Critical dimensions of a phase-space ellipse used in the phase-space dynamical model of ion motion. The maximum kinetic energy of an ion at a rf given phase angle, ξ, is related to the parameters Γ and B. (Adapted with permission, March and Hughes, 1989.) 21

2-1 Rate constant, k, versus $K.E._{cm}$ for the reaction $Ar^+ + N_2 \rightarrow N_2^+ + Ar$ reported by Dotan and Lindinger, 1982. FA = flowing afterglow. (Adapted with permission.) 29

2-2 Rate constant, *k*, versus $K.E._{cm}$ for the reaction $O_2^+ + CH_4 \rightarrow CH_3O_2^+ + H$ reported by Dotan *et al.*, 1978. (Adapted with permission.) 31

2-3 Schematic scan function (not to scale) for performing ion-molecule reactions rate studies on a QITMS 36

2-4 Ion gauge calibration curve for a) CH_4; b) residuals for the pressure calibration presented in a) 40

2-4 (continued) Ion gauge calibrations curves for c) N_2; and d) Ar 41

2-4 (continued) Ion gauge calibrations curves for e) He entered into the ion trap volume; and f) He entered into the ion trap chamber 42

2-5 Ion intensity versus reaction time for the calibration reaction, $CH_4^+ + CH_4 \rightarrow CH_5^+ + CH_3$. a) Methane at $1.0x10^{-6}$ torr; $q_z(CH_4^+) = 0.732$; *m/z* 16 ion signal shown with a first-order exponential fit; no He buffer gas 48

2-5 (continued) Ion intensity versus reaction time for the calibration reaction, $CH_4^+ + CH_4 \rightarrow CH_5^+ + CH_3$. b) Methane at $1.0x10^{-6}$ torr; $q_z(CH_4^+) = 0.732$; *m/z* 16 ion signal shown with a first-order exponential fit; He buffer gas added to $1.0x10^{-4}$ torr 49

2-6 Ion intensity versus reaction time for the reaction of Ar^+ with N_2 without N_2^+ ejection. a) 1:1 Ar:N_2 at $1.0x10^{-5}$ torr; $q_z(Ar^+)= 0.295$ with no He buffer 54

2-6 (continued) Ion intensity versus reaction time for the reaction of Ar^+ with N_2 without N_2^+ ejection. b) 1:1 Ar:N_2 at $1.0x10^{-5}$ torr; $q_z(Ar^+) = 0.295$ with He buffer gas added to $1.0x10^{-4}$ torr 55

2-7 $K.E._{cm}$ versus $q_z(Ar^+)$ as determined from k for the reaction $Ar^+ + N_2 \rightarrow N_2^+ + Ar$. a) All points for a 100 ms reaction time; (○) 1:1 Ar:N_2 at $1.0x10^{-5}$ torr; (☐) He buffer gas added to $1.0x10^{-4}$ torr 60

2-7 (continued) $K.E._{cm}$ versus $q_z(Ar^+)$ as determined from k for the reaction $Ar^+ + N_2 \rightarrow N_2^+ + Ar$. b) All points for a 100 ms reaction time; (○) 1:1 Ar:N_2 at $2.2x10^{-6}$ torr; (☐) He buffer gas added to $1.0x10^{-4}$ torr 61

2-8 Ion intensity versus reaction time for the reaction $O_2^+ + CH_4 \rightarrow CH_3O_2^+ + H$. a) 1:1 O_2:CH_4 at $1.0x10^{-5}$ torr; $q_z(O_2^+) = 0.369$; no He buffer gas 65

2-8 (continued) Ion intensity versus reaction time for the reaction $O_2^+ + CH_4 \rightarrow CH_3O_2^+ + H$. b) 1:1 O_2:CH_4 at $1.0x10^{-5}$ torr; $q_z(O_2^+) = 0.369$; He buffer gas added to $1.0x10^{-4}$ torr. (○) sum of m/z 32 and 33 intensities showing first-order fit used in the calculation of *k* 66

2-9 O_2^+ ion peak profiles at a variety of reaction times in the absence and presence of He buffer 68

3-1 Product ions for the reaction of protonated toluene (*m/z* 93) with ethylbenzene after a 10 s reaction time. a) 1:1 toluene:ethylbenzene at 2.2×10^{-6} torr; b) He buffer added to 1.0×10^{-4} torr 85

3-2 Product ions for the reaction of protonated diethylamine (*m/z* 74) with di-*n*-propylamine after a 3 s reaction time. a) 2.5:1 diethylamine:di-*n*-propylamine at 5.4×10^{-6} torr; b) He buffer gas added to 1.0×10^{-4} torr 87

3-3 Product ions for the reaction of fluorobenzene (*m/z* 96) with *m*-dichlorobenzene after a 5 s reaction time. a) 1:1 fluorobenzene:*m*-dichlorobenzene at 7.3×10^{-7} torr; b) He buffer gas added to 1.0×10^{-4} torr 88

3-4 Ion intensity versus reaction time for $[C_6H_5CH_3]H^+ + [C_6H_5C_2H_5] \rightarrow C_6H_5CH_3 + [C_6H_5C_2H_5]H^+$ a) with only the *m/z* 107 ions plotted. (■) 1:1 toluene:ethylbenzene at 2.2×10^{-6} torr; CH_4 present at $\approx 6.0 \times 10^{-6}$ torr; (□) He buffer gas added to 1.0×10^{-4} torr 90

3-4 (continued) Ion intensity versus reaction time for $[C_6H_5CH_3]H^+ + [C_6H_5C_2H_5] \rightarrow C_6H_5CH_3 + [C_6H_5C_2H_5]H^+$ b) with the sum of the *m/z* 105, 106, 107, and 108 ions plotted. (■) 1:1 toluene:ethylbenzene at 2.2×10^{-6} torr; CH_4 present at $\approx 6.0 \times 10^{-6}$ torr; (□) He buffer gas added to 1.0×10^{-4} torr 91

3-4 (continued) c) Ratio of the sum of the *m/z* 105, 106, 107, and 108 ions to the *m/z* 93 ions for $[C_6H_5CH_3]H^+ + [C_6H_5C_2H_5] \rightarrow C_6H_5CH_3 + [C_6H_5C_2H_5]H^+$. (■) 1:1 toluene:ethylbenzene at 2.2×10^{-6} torr; CH_4 present at $\approx 6.0 \times 10^{-6}$ torr; (□) He buffer gas added to 1.0×10^{-4} torr 92

3-5 Ion intensity versus reaction time for $[(n\text{-}C_2H_5)_2NH]H^+ + (n\text{-}C_3H_7)_2NH \rightarrow (n\text{-}C_2H_5)_2NH + [(n\text{-}C_3H_7)_2NH]H^+$. a) (▲) 2.5:1 diethylamine:di-*n*-propylamine at 5.4×10^{-6} torr; (△) He buffer gas added to 1.0×10^{-4} torr 96

3-5 (continued) Ion intensity versus reaction time for $[(n\text{-}C_2H_5)_2NH]H^+ + (n\text{-}C_3H_7)_2NH \rightarrow (n\text{-}C_2H_5)_2NH + [(n\text{-}C_3H_7)_2NH]H^+$. b) (▲) 4.15:1 diethylamine:di-*n*-propylamine at 2.7×10^{-6} torr; (△) He buffer gas added to 1.0×10^{-4} torr 97

3-6 Ion intensity versus reaction time for $C_6H_5F^+ + m\text{-}C_6H_4(Cl)_2 \rightarrow C_6H_5F + m\text{-}C_6H_4(Cl)_2^+$. a) (●) 1:1 fluorobenzene:*m*-dichlorobenzene at 7.3×10^{-7} torr; (○) He buffer gas added to 1.0×10^{-4} torr 100

3-6 (continued) Ion intensity versus reaction time for $C_6H_5F^+ + m\text{-}C_6H_4(Cl)_2 \rightarrow C_6H_5F + m\text{-}C_6H_4(Cl)_2^+$. b) (●) 1:1 fluorobenzene:*m*-dichlorobenzene at 2.8×10^{-6} torr; (○) He buffer gas added to 1.0×10^{-4} torr 101

4-1 Breakdown graph for the M^+ ion of propane (*m/z* 44) calculated from quasi-equilibrium theory (Vestal and Lerner, 1967) 115

4-2 Time-resolved collision-induced dissociation breakdown graphs for the M^+ ion of acetone (*m/z* 58) using a) 50 mV and b) 100 mV resonant excitation amplitudes.

Acetone at 1.1×10^{-6} torr; He added to 1.0×10^{-4} torr; every second data point plotted 120

4-3 Collision-induced dissociation spectra of the M^+ ion of acetone at the *m/z* 58 and 43 crossover points a) 50 mV resonant excitation, 2.6 ms and b) 100 mV excitation, 0.95 ms 121

4-4 Breakdown graph for the M^+ ion of acetone (*m/z* 58) calculated from quasi-equilibrium theory (Vestal and Lerner, 1967) 123

4-5 Time-resolved collision-induced dissociation breakdown graphs for the M^+ ion of 2-pentanone (*m/z* 86) using a) 100 mV and b) 200 mV resonant excitation amplitudes. 2-Pentanone at 1.3×10^{-6} torr; He added to 1.0×10^{-4} torr; every second data point plotted 126

4-6 Collision-induced dissociation spectra of the M^+ ion of 2-pentanone at the *m/z* 86 and 58 crossover points a) 100 mV resonant excitation, 2.0 ms and b) 200 mV excitation, 0.80 ms 127

4-7 Breakdown graph for the M^+ ion of 2-pentanone (*m/z* 86) calculated from quasi-equilibrium theory (Vestal and Lerner, 1967) 128

4-8 Time-resolved collision-induced dissociation breakdown graphs for the M^+ ion of propane (*m/z* 44) using a) 100 mV and b) 200 mV resonant excitation amplitudes. Propane at 1.3×10^{-6} torr; He added to 1.0×10^{-4} torr; every second data point plotted 130

4-9 Collision-induced dissociation spectra of the M^+ ion of propane at the *m/z* 44 and 28 crossover points a) 100 mV resonant excitation, 0.85 ms and b) 200 mV excitation, 0.40 ms 131

4-10 Time-resolved collision-induced dissociation breakdown graphs for the M^+ ion of toluene (*m/z* 92) using a) 75 mV and b) 125 mV resonant excitation amplitudes. Toluene at 1.2×10^{-6} torr; He added to 1.0×10^{-4} torr; every forth data point plotted 134

4-10 (continued) Time-resolved collision-induced dissociation breakdown graphs for the M^+ ion of toluene (*m/z* 92) using c) 150 mV and d) 300 mV resonant excitation amplitudes. Toluene at 1.2×10^{-6} torr; He added to 1.0×10^{-4} torr; every forth data point plotted 135

4-11 Collision-induced dissociation spectra of the M^+ ion of toluene at the *m/z* 92 and 91 crossover points a) 75 mV resonant excitation, 8.5 ms and b) 125 mV excitation, 4.0 ms 136

4-11 (continued) Collision-induced dissociation spectra of the M^+ ion of toluene at the *m/z* 92 and 91 crossover points c) 150 mV resonant excitation, 3.2 ms and d) 300 mV excitation, 1.7 ms 137

4-12 Breakdown graph for the M^+ ion of toluene (*m/z* 92) calculated from quasi-equilibrium theory (Vestal and Lerner, 1967) 139

4-13 Time-resolved collision-induced dissociation breakdown graphs for the M^+ ion of benzene (*m/z* 78) using a) 175 mV and b) 225 mV resonant excitation amplitudes. Benzene at 1.2×10^{-6} torr; He added to 1.0×10^{-4} torr; every forth data point plotted 142

4-14 Collision-induced dissociation spectra of the M^+ ion of benzene at the *m/z* 78 and 77 crossover points a) 175 mV resonant excitation, 69 ms and b) 225 mV excitation, 23 ms 143

4-15 Breakdown graph for the M^+ ion of benzene (*m/z* 78) calculated from quasi-equilibrium theory (Vestal and Lerner, 1967) 144

4-16 a) Scheme for the isomerization and H atom loss pathways involving (I) the $C_7H_8^+$ of toluene, (II) the $C_7H_8^+$ cycloheptatriene isomer, (III) the $C_7H_7^+$ benzyl cation, and (IV) the $C_7H_7^+$ tropylium ion (McLafferty and Bockhoff, 1979) 147

4-16 (continued) b) Potential energy surface for the scheme presented in Figure 4-16a (Ausloos, 1982) 148

4-17 Resonant excitation time versus excitation voltage for a) the M^+ ion of propane; (○) *m/z* 43 and 44 crossover points; (●) *m/z* 28 and 44 crossover points (shown with a power fit); and (□) *m/z* 43 plateau Propane at 1.3×10^{-6} torr; He added to 1.0×10^{-4} torr. Error bars are the sample standard deviation 151

4-17 (continued) Resonant excitation time versus excitation voltage for b) the *m/z* 43 and 58 crossover points of acetone, the *m/z* 58 and 86 crossover points of 2-pentanone, the *m/z* 28 and 44 crossover points of propane, the *m/z* 91 and 92 crossover points of toluene, and the *m/z* 77 and 78 crossover points of benzene. The corresponding internal energies calculated by quasi-equilibrium theory are shown in brackets. Error bars are the sample standard deviation 152

5-1 The $91^+/92^+$ ratio as a function of internal energy of the M^+ ion of *n*-butylbenzene (•) PEPICO technique at 298 K (Baer *et al.*, 1988) and (▵) charge exchange mass spectrometry at 373 K (Harrison and Lin, 1983) 161

5-2 The $91^+/92^+$ ratios as a function of the internal energy of the M^+ ions of the *n*-alkylbenzenes from charge exchange mass spectrometry (Nacson and Harrison, 1988) 164

5-3 Collision-induced dissociation spectra of the M^+ ion of *n*-butylbenzene (*m/z* 134) a) 300 mV excitation amplitude and 1.05 ms excitation time and b) 500 mV excitation amplitude and 0.55 ms excitation time 169

5-3 (continued) Collision-induced dissociation spectra of the M$^+$ ion of *n*-pentylbenzene (*m/z* 148) c) 300 mV excitation amplitude and 1.15 ms excitation time and d) 500 mV excitation amplitude and 0.65 ms excitation time . . . 170

5-3 (continued) Collision-induced dissociation spectra of the M$^+$ ion of *n*-hexylbenzene (*m/z* 162) e) 300 mV excitation amplitude and 1.05 ms excitation time and f) 500 mV excitation amplitude and 0.75 ms excitation time 171

5-3 (continued) Collision-induced dissociation spectra of the M$^+$ ion of *n*-octylbenzene (*m/z* 190) g) 300 mV excitation amplitude and 1.35 ms excitation time and h) 500 mV excitation amplitude and 0.90 ms excitation time 172

5-4 Collision-induced dissociation breakdown surface of the M$^+$ ion of *n*-butylbenzene showing the 91$^+$/92$^+$ ratio. a) No smoothing of the data was performed. *n*-Butylbenzene at ≈ 2.0x10^{-6} torr; He buffer gas added to 1.0x10^{-4} torr 174

5-4 (continued) Collision-induced dissociation breakdown surface of the M$^+$ ion of *n*-butylbenzene showing the 91$^+$/92$^+$ ratio. b) A spline smoothing of the data was performed. *n*-Butylbenzene at ≈ 2.0x10^{-6} torr; He buffer gas added to 1.0x10^{-4} torr 175

5-5 Collision-induced dissociation breakdown surface of a) the M$^+$ ion of *n*-butylbenzene showing the 91$^+$/92$^+$ ratio. Both two-dimensional 5-point and spline smoothing of the data were performed. *n*-Butylbenzene at ≈ 2.0x10^{-6} torr; He buffer gas added to 1.0x10^{-4} torr 177

5-5 (continued) Collision-induced dissociation breakdown surface of b) the M$^+$ ion of *n*-pentylbenzene showing the 91$^+$/92$^+$ ratio. Both two-dimensional 5-point and spline smoothing of the data were performed. *n*-Pentylbenzene at ≈ 2.0x10^{-6} torr; He buffer gas added to 1.0x10^{-4} torr 178

5-5 (continued) Collision-induced dissociation breakdown surface of c) the M$^+$ ion of *n*-hexylbenzene showing the 91$^+$/92$^+$ ratio. Both two-dimensional 5-point and spline smoothing of the data were performed. *n*-Hexylbenzene at ≈ 2.0x10^{-6} torr; He buffer gas added to 1.0x10^{-4} torr 179

5-5 (continued) Collision-induced dissociation breakdown surface of d) the M$^+$ ion of *n*-octylbenzene showing the 91$^+$/92$^+$ ratio. Both two-dimensional 5-point and spline smoothing of the data were performed. *n*-Octylbenzene at ≈ 2.0x10^{-6} torr; He buffer gas added to 1.0x10^{-4} torr 180

5-6 Topographical plot of a) the collision-induced dissociation breakdown surface of the M$^+$ ion of *n*-butylbenzene showing the 91$^+$/92$^+$ ratio presented in Figure 5-5a. b) The same data on a log-log scale. *n*-Butylbenzene at ≈ 2.0x10^{-6} torr; He buffer gas added to 1.0x10^{-4} torr 182

5-6 (continued) Topographical plot of c) the collision-induced dissociation breakdown surface of the M$^+$ ion of *n*-pentylbenzene showing the 91$^+$/92$^+$ ratio presented in

Figure 5-5b. d) The same data on a log-log scale. *n*-Pentylbenzene at ≈ 2.0x10^{-6} torr; He buffer gas added to 1.0x10^{-4} torr 183

5-6 (continued) Topographical plot of e) the collision-induced dissociation breakdown surface of the M$^+$ ion of *n*-hexylbenzene showing the 91$^+$/92$^+$ ratio presented in Figure 5-5c. f) The same data on a log-log scale. *n*-Hexylbenzene at ≈ 2.0x10^{-6} torr; He buffer gas added to 1.0x10^{-4} torr 184

5-6 (continued) Topographical plot of g) the collision-induced dissociation breakdown surface of the M$^+$ ion of *n*-octylbenzene showing the 91$^+$/92$^+$ ratio presented in Figure 5-5d. h) The same data on a log-log scale. *n*-Octylbenzene at ≈ 2.0x10^{-6} torr; He buffer gas added to 1.0x10^{-4} torr 185

5-7 a) Time-resolved collision-induced dissociation breakdown graph of the M$^+$ ion of *n*-butylbenzene using a 500 mV excitation amplitude. b) Voltage-resolved breakdown graph at a 1.5 ms excitation time. *n*-Butylbenzene at ≈ 2.0x10^{-6} torr; He buffer 1.0x10^{-4} torr 188

5-7 (continued) c) Time-resolved collision-induced dissociation breakdown graph of the M$^+$ ion of *n*-pentylbenzene using a 500 mV excitation amplitude. d) Voltage-resolved breakdown graph at a 1.5 ms excitation time. *n*-Pentylbenzene at ≈ 2.0x10^{-6} torr; He buffer gas 1.0x10^{-4} torr 189

5-7 (continued) e) Time-resolved collision-induced dissociation breakdown graph of the M$^+$ ion of *n*-hexylbenzene using a 500 mV excitation amplitude. f) Voltage-resolved breakdown graph at a 1.5 ms excitation time. *n*-Hexylbenzene at ≈ 2.0x10^{-6} torr; He buffer gas 1.0x10^{-4} torr 190

5-7 (continued) g) Time-resolved collision-induced dissociation breakdown graph of the M$^+$ ion of *n*-octylbenzene using a 500 mV excitation amplitude. h) Voltage-resolved breakdown graph at a 1.5 ms excitation time. *n*-Octylbenzene at ≈ 2.0x10^{-6} torr; He buffer gas 1.0x10^{-4} torr 191

5-8 The 91$^+$/92$^+$ ratios from a) time-resolved collision-induced dissociation of the M$^+$ ions of the *n*-alkylbenzenes, 500 mV excitation amplitude and b) voltage-resolved CID of the M$^+$ ions, 1.5 ms excitation time. *n*-Alkylbenzenes at ≈ 2.0x10^{-6} torr; He buffer gas 1.0x10^{-4} torr. 194

5-9 a) The time-resolved collision-induced dissociation breakdown graph of the M$^+$ ion of *n*-butylbenzene showing the relative intensities of the *m/z* 134 and *m/z* 92 ions at a variety of He buffer pressures. *n*-Butylbenzene at 2.6x10^{-6} torr; 500 mV resonant excitation amplitude 198

5-9 (continued) b) The *m/z* 91 ion intensities following collision-induced dissociation of the M$^+$ ion of *n*-butylbenzene at a variety of He buffer gas pressures. *n*-Butylbenzene at 2.6x10^{-6} torr; 500 mV resonant excitation amplitude 199

5-9 (continued) The $91^+/92^+$ ratios from the time-resolved collision-induced dissociation of the M^+ ions of *n*-butylbenzene at a variety of He buffer gas pressures using c) a 300 mV resonant excitation amplitude. *n*-Butylbenzene at ≈ 2.6×10^{-6} torr 200

5-9 (continued) The $91^+/92^+$ ratios from the time-resolved collision-induced dissociation of the M^+ ions of *n*-butylbenzene at a variety of He buffer gas pressures using d) a 500 mV resonant excitation amplitude. *n*-Butylbenzene at ≈ 2.6×10^{-6} torr 201

5-9 (continued) e) The *m/z* 92 and *m/z* 135 ion intensities from the time-resolved collision-induced dissociation breakdown graph of the M^+ ion of *n*-butylbenzene at He buffer pressures of 4.0×10^{-5} torr and 2.2×10^{-4} torr. *n*-Butylbenzene at 2.6×10^{-6} torr; 500 mV resonant excitation amplitude 202

5-10 a) The time-resolved collision-induced dissociation breakdown graph of the M^+ ion of *n*-butylbenzene showing the relative intensities of the *m/z* 134 and *m/z* 92 ions at a variety of *n*-butylbenzene pressures. He buffer at 1.0×10^{-4} torr; 500 mV resonant excitation amplitude 207

5-10 (continued) b) The *m/z* 91 ion intensities following collision-induced dissociation of the M^+ ion of *n*-butylbenzene at a variety of *n*-butylbenzene pressures. He buffer at 1.0×10^{-4} torr; 500 mV resonant excitation amplitude 208

5-10 (continued) c) The $91^+/92^+$ ratios from the time-resolved collision-induced dissociation of the M^+ ions of *n*-butylbenzene at a variety of *n*-butylbenzene pressures. He buffer at 1.0×10^{-4} torr; 500 mV excitation amplitude 209

5-10 (continued) d) The *m/z* 92 and *m/z* 135 ion intensities from the time-resolved collision-induced dissociation breakdown graph of the M^+ ion of *n*-butylbenzene at *n*-butylbenzene pressures of 9.8×10^{-7} torr and 5.6×10^{-6} torr. He buffer at 1.0×10^{-4} torr; 500 mV resonant excitation amplitude 210

Abstract of Dissertation Presented to the Graduate School
of the University of Florida in Partial Fulfillment of the
Requirements for the Degree of Doctor of Philosophy

PROBING TRAPPED ION ENERGIES IN A QUADRUPOLE ION TRAP MASS SPECTROMETER

By

Cecilia Basic

August 1992

Chairman: Dr. Richard A. Yost
Cochairman: Dr. John R. Eyler
Major Department: Chemistry

This dissertation presents a series of studies elucidating the energies of ions stored in a quadrupole ion trap mass spectrometer. Two kinetic and three thermodynamic "thermometer" reactions are used to assign ion energies when no supplemental resonant excitation potentials are employed. The collision-induced dissociation, CID, breakdown graphs for a series of small molecules are then used to determine average ion internal energies upon application of an excitation potential to effect CID.

Rate constants for the charge exchange reaction of Ar^+ with N_2 and for the reaction of O_2^+ with CH_4 are used to assign center-of-mass kinetic energies, $K.E._{cm}$, to ions as a function of the neutral pressures, the q_z value of the ion, and the pressure of the He buffer gas. The $K.E._{cm}$ values reflect anticipated trends in ion energy and range

from 0.1 to 0.3eV. These values correspond to "effective" ion temperatures for the He buffered Ar^+ ions of ≈1700K to 3300K.

The ion-molecule equilibrium constants, K_{eq}, for the proton transfer reactions of protonated toluene with ethylbenzene, and of protonated diethylamine with di-*n*-propylamine, and the charge exchange reaction of ionized fluorobenzene with *m*-dichlorobenzene are used to calculate temperatures of ions stored for 2 to 10s. The resulting average temperatures are 280 ± 170K with no He buffer and 220 ± 145K with He buffer.

The CID breakdown graphs for ionized acetone, 2-propanone, propane, toluene, and benzene are compared to the corresponding graphs calculated from quasi-equilibrium theory, QET. Correlations between the energies for selected crossover points on the QET graphs and the requisite experimental fluences indicate that there is a 1.4:1 relation between the resonance excitation time and excitation amplitude for fragmentation processes requiring less than 3eV of internal energy. This increases to 3:1 for processes requiring ≈6eV.

The CID breakdown surfaces for the molecular ions of *n*-butylbenzene, *n*-pentylbenzene, *n*-hexylbenzene, and *n*-octylbenzene are used to assign average ion internal energies upon resonance excitation on the $91^+/92^+$ fragment ion ratios. The internal energies range from 3 to 8eV based on the excitation amplitude and time and increase with increasing size of the *n*-alkyl group.

CHAPTER 1
INTRODUCTION

In recent years the quadrupole ion trap mass spectrometer, QITMS, has seen increased use in both fundamental and applied mass spectrometric studies. As a result, an understanding of the energies of the ions stored under a variety of experimental conditions has become increasingly important. This dissertation presents the results obtained from a number of chemical "thermometer" reactions used to probe the energies of the ions stored in a QITMS. A chemical thermometer reaction is defined here as an ion-molecule reaction possessing a physiochemical property which changes in a well-defined manner as a function of ion energy and which can be easily measured. Two "kinetic" and three "thermodynamic" thermometers are presented which succeed in probing the ion energies when no supplemental resonant excitation potential is applied to the trap electrodes (normal electron ionization, EI, and chemical ionization, CI, analyses). A series of small organic molecules for which the results of quasi-equilibrium theory, QET, calculations are available, and a homologous series of *n*-alkylbenzenes are then used to probe the ion energies following resonant excitation (tandem mass spectrometric, MS/MS, and MS^n analyses). The combined results of these thermometer reactions provide a detailed profile of the ion energies under a number of experimental conditions.

This introductory chapter begins with a brief history of the radiofrequency, rf, ion trap, or QITMS, followed by a presentation of the operational principles underlying the ion trap, and a description of the QITMS used in the present study. A summary of the principal models used in the theoretical calculation of trapped ion energies will also be presented. The chapter concludes with an introduction to the chemical thermometers of interest in the present study and an overview of the dissertation.

Principles of the Quadrupole Ion Trap

Brief History

The quadrupole ion trap mass spectrometer, QITMS, is the three-dimensional analogue of the more familiar quadrupole mass filter. Mass analysis in both mass spectrometers is based on the ability to selectively control the stability of an ion's trajectory in a quadrupolar electric field. Use of both two-dimensional (quadrupole mass filter) and three-dimensional (rf ion trap) quadrupolar fields to mass analyze ions was first presented in 1953 by Paul and his colleagues at the University of Bonn (Paul and Steinwedel, 1953), and by Post and Henrich (1953) and Good (1953) at the University of California, Berkeley. Paul and Steinwedel (1956) patented both the quadrupole mass filter and the rf ion trap. A detailed account of mass-selective ion detection *via* resonant absorption was presented by Fischer (1959). The quadrupole mass filter was the first of these two devices to see widespread use in both single stage MS (Dawson, 1976) and tandem mass spectrometric, MS/MS, analyses (Yost and Enke, 1978; Yost *et al.*, 1979).

Early applications of the rf ion trap involved its use as an ion containment device in rf spectroscopy studies (Wuerker *et al.*, 1959; Dehmelt, 1967, 1969; Major and Dehmelt, 1968; Walls and Dunn, 1974). While the mass spectrometric capabilities of the ion trap were further explored by Dawson *et al.* in the late 1960s (Dawson and Whetten, 1968a,b, 1969, 1971), it was not until the early 1970s and the pioneering work by Todd and colleagues at the University of Kent that experimental applications of the rf ion trap in mass spectrometric studies were reported (Bonner *et al.*, 1972, 1972/73, 1974; Lawson *et al.*, 1973). At this time, Todd and colleagues coined the term "quadrupole ion store" or QUISTOR for the rf ion trap. Studies with the QUISTOR were continued in conjunction with March and colleagues at Trent University throughout the 1970s. During this time, detailed studies of the ion containment mechanisms were reported (Bonner *et al.*, 1976; Bonner and March, 1977; Lawson and Todd, 1977; Todd *et al.*, 1978; Fulford and March, 1979a,b; Doran *et al.*, 1980) as were a number of theoretical models of ion motion and kinetic energies (Dawson and Lambert, 1975; Lawson *et al.*, 1976; Todd *et al.*, 1980a,c) and ion-ion repulsion or space-charge effects (Todd *et al.*, 1980d,e). Reaction kinetic studies of a number of ion-molecule systems were presented (Lawson *et al.*, 1976a; Fulford *et al.*, 1978) as were both resonant excitation and resonant ion ejection methods (Armitage *et al.*, 1979, 1980; Todd and Waldren, 1979; Waldren and Todd, 1979a,b,c; Fulford *et al.*, 1980a; Mather and Todd, 1979). The first MS/MS analyses using an rf ion trap were reported (Fulford and March, 1978) along with simultaneous positive/negative chemical ionization studies (Mather and Todd, 1980) and models for injecting ions formed in an external ion source (Kishore and Ghosh, 1979; Chattopadhyaya and Ghosh, 1980, 1981; Todd *et al.*, 1980b). In the early 1980s, multiphoton dissociation of a variety of trapped ion species was demonstrated using infrared radiation (Hughes *et al.*, 1982, 1983a,b,c; Young *et al.*, 1985).

Use of the rf ion trap as a gas chromatograph, GC, detector was first presented by March and Armitage (Armitage, 1979); however, it was not until the disclosure of the ion trap detector, ITD™, by Finnigan MAT Corporation (Kelley *et al.*, 1985a) that the rf ion trap became commercially available as a mass spectrometer and started seeing widespread application in routine GC analyses. The ITD™ is the predecessor of the ion trap mass spectrometer, ITMS™, which was introduced in 1985 (Kelley *et al.*, 1985b). Unlike the ITD™, the ITMS™ allows both routine MS and more advanced MS^n analyses due to the ability to mass-select a parent ion of interest and perform collision-induced dissociation, CID, by resonantly exciting the ion of interest. Renewed interest in the mass spectrometric capabilities of quadrupole ion traps has increased dramatically since the introduction of the ITMS™. Applications and the fundamental principles underlying the QITMS have been the subject of a recent book (March and Hughes, 1989) and a number of reviews (Todd, 1981; Cooks and Kaiser, 1990; Nourse and Cooks, 1990; Cooks *et al.*, 1991; March, 1991; Todd, 1991; Todd and Penman, 1991).

Principles of Operation

The quadrupole ion trap consists of three hyperbolic electrodes arranged as depicted in Figure 1-1. Because of the circular symmetry about the *z*-axis, the geometry of the ion trap is considered in terms of the points r and z, where $r = [x^2 + y^2]^{1/2}$. The ring electrode has a radius, r_0; the half distance, z_0, between the two end-cap electrodes is related to r_0 by $r_0^2 = 2z_0^2$ (Knight, 1983). A three-dimensional quadrupolar field is formed within the volume of the ion trap by applying a combined rf, $V\cos\Omega t$, and direct current (dc) U, potential to the ion trap electrodes. The applied potential, ϕ_0 is of the form,

$$\phi_0 = U - V\cos\Omega t \qquad (1\text{-}1)$$

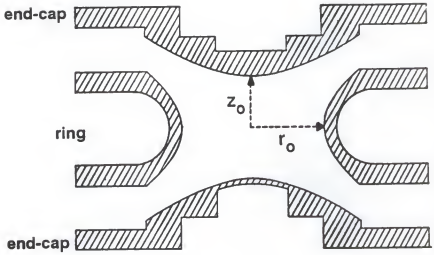

Figure 1-1: Schematic of the quadrupole ion trap showing the arrangement of the three hyperbolic electrodes. The radius of the ring electrode, r_0, and the half distance between the two end-cap electrodes, z_0, are related by $r_0^2 = 2z_0^2$ (Adapted with permission, March and Hughes, 1989.)

where Ω is the angular frequency of the rf potential (rad s^{-1}) and V is the zero-to-peak amplitude of the rf potential ($V_{0\text{-}p}$).

Ion traps can be operated in one of three modes (Bonner, 1977; March and Hughes, 1989). In mode I, ϕ_0 is applied to the ring electrode and $-\phi_0$ is applied to the end-cap electrodes; in mode II, ϕ_0 is applied to the ring electrode and the end-cap electrodes are held at ground; and in mode III, $V\cos\Omega t$ is applied to the ring, while $-U$ is applied to the end-cap electrodes. The ITMS™ used in this study is operated in mode II. In this mode, the field, ϕ, at any point, r,z, in the ion trap is given by

$$\phi(r,z) = \frac{\phi_0}{2r_0^2}(r^2 - 2z^2) + \frac{\phi_0}{2}. \tag{1-2}$$

The equations of r and z motion for the ions in this three-dimensional field are uncoupled and are given by

$$\frac{d^2r}{dt^2} + \frac{2e}{mr_0^2}(U - V\cos\Omega t)r = 0 \tag{1-3}$$

and

$$\frac{d^2z}{dt^2} - \frac{4e}{mr_0^2}(U - V\cos\Omega t)z = 0 \tag{1-4}$$

where m is the mass (kg) and e is the charge (C) of the ion, respectively. These equations are of the form of the second-order linear differential Mathieu equation (Mathieu, 1868; Zwillinger, 1989),

$$\frac{d^2u}{d\xi^2} + (a_u - 2q_u\cos 2\xi)u = 0 \tag{1-5}$$

where u represents one of the coordinate axes, r or z, ξ is equal to $\Omega t/2$ and the Mathieu stability parameters a_u and q_u are given by

$$a_u = a_z = -2a_r = \frac{-8eU}{mr_0^2\Omega^2} \tag{1-6}$$

and

$$q_u = q_z = -2q_r = \frac{-4eV}{mr_0^2\Omega^2}. \tag{1-7}$$

If an ion of a given mass-to-charge ratio, m/z, defines a_u and q_u parameters which give rise to stable solutions to the Mathieu equation 1-5 in both the r and z directions, then the ion will follow a stable trajectory and be confined within the volume of the ion trap. A stable solution is one in which u remains finite as ξ increases. The range of a_u and q_u values which give rise to stable solutions in both the r and z-directions can be plotted in the form of a stability diagram (Figure 1-2a). The ITMS™ uses first stability region presented in terms of a_z and q_z in Figure 1-2b.

The stable solutions to the Mathieu equation 1-5 presented in Figure 1-2a are of the form

$$u(\xi) = A\sum_{-n=\infty}^{\infty} C_{2n}\cos(2n + \beta)\xi + B\sum_{-n=\infty}^{\infty} C_{2n}\sin(2n + \beta)\xi. \tag{1-8}$$

Equation 1-8 effectively describes the frequency spectrum of the ion motion, $u(\xi)$. Each term corresponds to an oscillation with an amplitude given by the coefficient, C_{2n}. The coefficients A and B are real and imaginary constants of integration, respectively, related to the initial position and velocity of the ion. The frequencies of the ion motion are represented by the $(2n + \beta)$ terms, where, transforming into real time,

$$\cos(2n + \beta)\xi \equiv \cos\omega_n t \tag{1-9}$$

and recalling $\xi = \Omega t/2$,

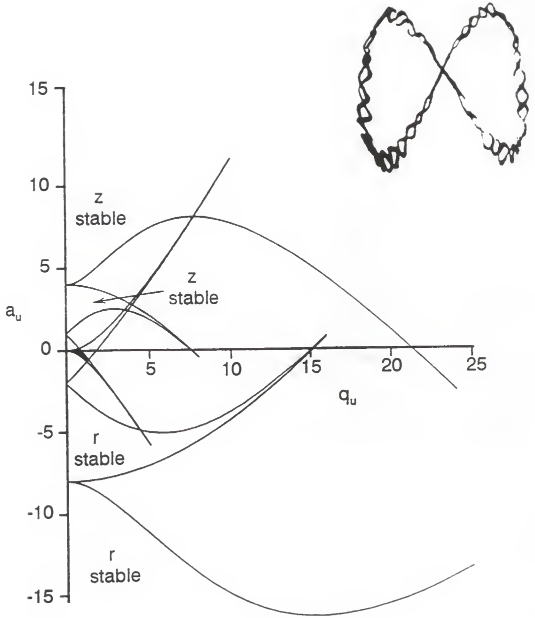

Figure 1-2: a) Solutions to the Mathieu equation for an rf ion trap. Ions with *a*,*q* parameters within the regions of stability in both the *r* and the *z*-directions will follow stable trajectories. The first stability region is shaded here and enlarged in Figure 1-2b. Inset: the 2:1 Lissajous form of an ion's trajectory in the *rz* plane. (Adapted with permission, March and Hughes, 1989.)

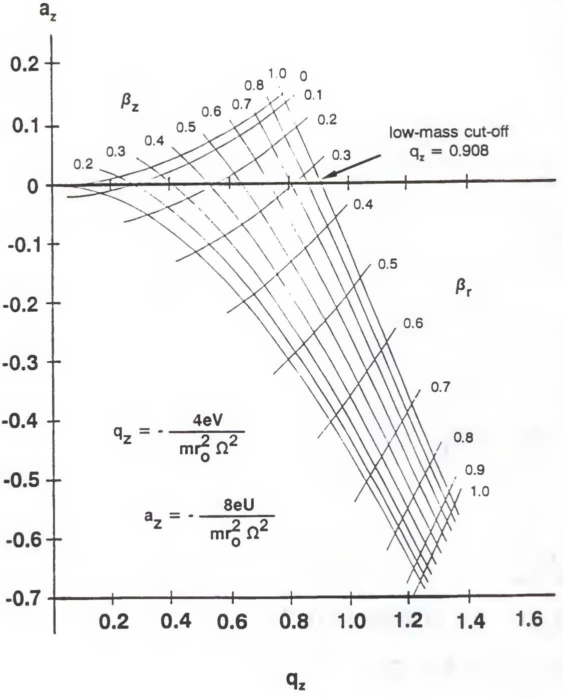

Figure 1-2: (continued) b) An enlargement of the first stability region in Figure 1-2a. In rf-only operation (*i.e.* $a_z = 0$) ions with a *m/z* ratio greater than that of the low-mass cut-off at $q_z = 0.908$ will follow stable trajectories. The β_r and β_z lines define the fundamental secular frequencies of the ions in the *r* and *z* directions, respectively. (Adapted with permission, March and Hughes, 1989.)

$$\omega_n = \frac{(2n + \beta)\Omega}{2} \qquad n = -\infty,\ldots -1,0,1\ldots,\infty. \tag{1-10}$$

Defining ω_n as the frequency of the *n*th term, the fundamental angular frequency, ω_0 in either the *r* or the *z* plane is given by $\beta\Omega/2$. Values for β for the stability region $q_z \leq 0.4$ ($q_r \leq 0.2$, Figure 1-2b), where $0 \leq \beta \leq 1$, can be approximated by (Wuerker *et al.*, 1959)

$$\beta = \left[a_z + \frac{q_z}{2}\right]^{1/2} \tag{1-11}$$

Thus, ions with the same β values will have trajectories of the same secular frequency; however, the amplitude of their trajectories will be governed by their a_u and q_u values and further modified by the *A* and *B* values defined by the initial position and velocity of the ions at the time they are formed in the field. The trajectory of an ion in the *rz* plane has the form of a 2:1 Lissajous figure (inset, Figure 1-2a) composed of the two secular frequency components ω_r and ω_z with a superimposed rf micromotion (or "ripple") of frequency Ω.

The Ion Trap Mass Spectrometer™

A schematic of the Finnigan MAT ITMS™ is presented in Figure 1-3. The stainless steel electrodes have a ring radius $r_0 = 1$ cm; thus $z_0 = 0.707$ cm. The drive potential, ϕ_0, is applied to the ring electrode and has a frequency $f = \Omega/2\pi = 1.1$ MHz. Ions are initially formed within the volume of the ion trap *via* electron ionization, EI. The ionizing electrons are formed from a heated filament located outside one of the end-cap electrodes. Electrons enter into the trap by gating an entrance lens ± 180 V for a variable time equal to the ionization time. Chemical ionization, CI, is effected by forming

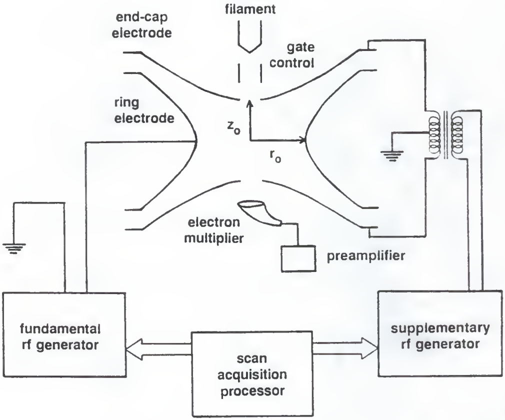

Figure 1-3: A schematic of the Finnigan MAT ITMS^{TM}. The ring electrode has a radius r_0 = 1 cm and z_0 = 0.707 cm. A drive potential of 1.1 MHz is applied to the ring electrode. The supplemental rf potential is applied to the end-cap electrodes in the dipolar mode.

an initial population of ions, then mass-selecting (see below) a reagent ion of interest and allowing it to undergo ion-molecule reactions with the background neutrals for a variable CI time.

An ion of a given *m/z* will be trapped and stored in the ITMS™ if its a_z,q_z parameters fall in the region of stability. In normal EI or CI analyses, a range of mass-to-charge ratios are stored at any given time based on the *m/z* of the ion which defines a q_z = 0.908 (see Figure 1-2b). Ions with *m/z* ratios *greater* than this "low-mass cut-off" and which define q_z values between $q_z \approx 0.2$ and $q_z = 0.908$ will be trapped and stored. The maximum *m/z* which can be detected in normal operating mode is determined from the maximum amplitude of the rf voltage which can be applied to the ring. For the ITMS™, V_{max} = 7500 $V_{0\text{-}p}$; thus, from equation 1-7, at $q_{z,max}$ = 0.908, m/z_{max} = 650 amu.

Ion detection is performed on the ITMS™ by ramping the amplitude of the ring rf voltage (scan rate = 0.18 ms amu^{-1}). This is referred to as the mass-selective instability mode of ion detection (Stafford *et al.*, 1984; Kelley *et al.*, 1985b). As the ring rf voltage is ramped, ions of increasing *m/z* are brought sequentially to a value of q_z = 0.908 at the β_z = 1 stability edge (Figure 1-2b). At β_z = 1 the fundamental frequency of the ion motion, $\omega_{0,z} = \beta_z \times f$ = 550 kHz (equation 1-10). As the ions cross this stability edge, their trajectories become unstable in the *z* or axial direction, and they are ejected from the trap and detected by a channeltron electron multiplier. Typically an additional "axial modulation" frequency of 530 kHz is applied to the end-cap electrodes during the data acquisition ramp. Application of an axial modulation frequency increases the amplitude of the ion's trajectory in the axial direction just before they come into instability at the low-mass cut-off, resulting in increased ion detection efficiency and mass resolution (Weber-Grabau *et al.*, 1988).

The ITMS™ is typically operated with $\approx 1\mathrm{x}10^{-3}$ torr of background He "buffer" gas. The buffer gas dampens the trajectory of the ions, resulting in an increased population of ions in the center of the trap and thus increased ion detection efficiency (Church and Dehmelt, 1969; Stafford *et al.*, 1984; Wu and Brodbelt, 1991).

Ions of a single *m/z* can be mass-selected for MS/MS and MS^n analyses by ramping the amplitude of the rf potential so that the ion of interest defines a q_z under the upper apex of the stability diagram (Figure 1-3). A negative dc offset, $U_{0\text{-}p}$, is then applied to the ring so that the ion defines a_z, q_z values located at the upper apex of the stability diagram ($a_z = 0.15$, $q_z = 0.78$). In so doing, all ions of differing *m/z* follow unstable trajectories and are ejected from the trap. This method of mass-selection is known as rf/dc apex isolation. Other methods of single ion isolation using a combination of stability edges have also been reported (Ardanaz *et al.*, 1991; Yates and Yost, 1991).

Multiple stages of mass spectrometry, MS^n, are performed in the ITMS™ by first rf/dc isolating the precursor ion of interest and then applying a supplemental rf potential to the end-cap electrodes. In standard MS/MS mode, this supplemental excitation potential is applied 180° out-of-phase to the two end-cap electrodes at the fundamental secular frequency of the ion in the *z*-direction ($\omega_{0,z} = \beta\Omega/2$). As the ion of interest comes into resonance with this resonant excitation potential (or "tickle" frequency), the amplitude of its trajectory in the *z*-direction increases, resulting in increasingly energetic collisions with the background gases. These collisions can result in CID of the precursor ion. The resulting fragment ions can then be detected, or a fragment ion of interest can be mass selected and induced to dissociate *via* a second resonant excitation step. Typical CID times range from 5 to 20 ms; excitation frequencies are on the order of hundreds of kilohertz with a maximum of 550 kHz at the $\beta_z = 1$ stability edge. Sequential stages of mass-selection and followed by CID lead to MS^n analyses (Louris *et al.*, 1990; Johnson *et al.*, 1990a,b; McLuckey *et al.*, 1991a,b; Gronowska *et al.*, 1991).

The sequence, frequencies, and amplitudes of the rf and dc potentials, as well as the various EI, CI, and CID times are controlled by constructing a scan function with the ITMS™ data system. A sample MS/MS scan function is presented in Table 1-1.

Theoretical Models of Trapped Ion Energies

Summaries of five approaches to modeling trapped ion trajectories will be presented below. These models include 1) calculations of individual ion trajectories; 2) the pseudo-potential well model; 3) the phase space dynamical model; 4) the temporal invariance model; and 5) the field interpolation model. Application of these models provides simulations of ion spatial and velocity components and thus leads to estimates of the ion kinetic energies. Of these models, only the pseudo-potential well model will be presented in detail.

Calculations of Individual Ion Trajectories

The position, u, and velocity, $\dot{u}$, of an ion in a three-dimensional quadrupolar field can be calculated by numerically integrating the Mathieu equation 1-5 using a fourth-order Runge-Kutta step-wise integration method (Dawson and Whetton, 1968a). Pedder and Yost have used this approach in the development of a computer simulation program, HYPERION, which allows calculation of the ion trajectory and kinetic energy under a variety of experimental conditions using a personal computer. The experimental

Table 1-1: Scan function for performing MS/MS of mass-selected *m/z* 134 on an ITMS™ using axial modulation.

	rf amplitude[*]			resonance excitation			
	start (amu)	**end** (amu)	**dc offset** (V_{0-p})	**mass** (amu)	**voltage** (mV)	**frequency** (kHz)	**time** (ms)
ionization							
trigger	10.0	10.0					0.50
pause	10.0	10.0					0.10
ionize	10.0	10.0					1.00
rf/dc isolation							
ramp to q_z = 0.78	10.0	100.0					1.00
rf isolation	100.0	117.0					1.00
pause	117.0	117.0					0.50
dc pulse	117.0	117.0	-134.0				0.30
pause	117.0	117.0					0.50
reaction							
ramp to q_z = 0.3	117.0	50.0					1.00
rf isolation	50.0	44.4					1.00
settle rf/cool	44.4	44.4					5.00
warm-up	44.4	44.4		10.0	500		1.00
CID time	44.4	44.4		134.0	500	120	5.00
acquisition							
multiplier on	44.4	44.4					1.00
acquire data[†]	44.4	200.0		44.5	6000	530	28.00
shut-down	0.0	0.0					0.00
						total time	46.90

---

[*] The rf amplitude is expressed in terms of the *m/z* with a q_z = 0.908 at the low-mass cut-off can be converted to V_{0-p} *via* equation 1-7.

The rf ramp times were calculated using the ramp rate of 0.18 ms amu^{-1}.

[†] Axial modulation is applied at a q_z = 0.906 using 530 kHz at 6000 mV_{0-p} (Weber-Grabau, 1987).

conditions include collisions with a He buffer gas and application of a resonant excitation potential (Pedder and Yost, 1988).

Estimates of u and $\dot{u}$ can be obtained from the first derivative of the generalized solutions to the Mathieu equation given in equation 1-8 for specific initial conditions u_0, $\dot{u}_0$ and ξ_0. If it is assumed that the initial velocity of the ion is zero, then the velocities for successive values of ξ can be calculated and averaged. This "complete general solution" requires lengthy calculations and can lead to large errors if the ξ increments are too large (Todd *et al.*, 1980c). Another approach to estimating ion energies based on the first derivative of equation 1-8 is that of the "smoothed general solution" (Lawson *et al.*, 1976b; Todd *et al.*, 1976). In this approach, it is assumed that for $0 < \beta < 0.4$, motion due to the higher harmonics given by equation 1-10 can be ignored; thus, only the secular ion motion is considered to contribute to the energy of the ion. The first derivative of equation 1-8 is thus simplified, and both the average and maximum velocities can be calculated for each of the three coordinate directions, x, y, z. Both these approaches result in single ion energies under collision-free conditions.

Monte-Carlo methods have been used to calculate the trajectories for up to 150 ions based on equation 1-8 (Bonner *et al.*, 1976). This approach incorporated changes in ion energy following ≈ 15 charge exchange collisions based on a simplified model of the collision process (Bonner and March, 1977; Doran *et al.*, 1980).

Reiser and coworkers have developed an ion trap simulation program, ITSIM, based on the simplified iterative approach to calculating the displacement of an ion based on the equations of motion in a three-dimensional rf field (equations 1-3 and 1-4) presented by Turner *et al.*, 1976. The program simulates ion trajectories and calculates mass spectra for the mass-selected instability mode of operation and includes both He buffer gas and space-charge effects (Reiser *et al.*, 1991a,b; Julian *et al.*, 1991).

Pseudo-potential Well Model

The pseudo-potential well model was first presented by Dehmelt (Dehmelt, 1967; Major and Dehmelt, 1968) and subsequently developed by Todd *et al.* (Todd *et al.*, 1976; Lawson *et al.*, 1976). The pseudo-potential well model also assumes that motion due to the higher harmonics can be ignored and as such provides a second means for estimating the mean kinetic energy of the ions due to their secular motion. In this approach, motion in the *z*-direction is due to both a displacement, δ, due to the rf micromotion, and a displacement, Z, due to the secular motion. It is assumed that δ is small compared to Z (which holds for $q_z < 0.4$ (Todd *et al.*, 1976)). With this, integration of the Mathieu equation 1-5 over one period of the rf potential leads to an expression for the average displacement of the ion

$$\frac{d^2Z}{dt^2} = -\left(a_z + \frac{q_z^2}{2}\right)\frac{\Omega^2}{4}Z. \tag{1-12}$$

From equations 1-10 and 1-11, with $\omega_{nz} = \omega_{0z}$

$$\frac{d^2Z}{dt^2} = -\omega_{0z}^2 Z \tag{1-13}$$

which corresponds to simple harmonic motion of the Z component of the secular motion, with a frequency equal to the fundamental secular frequency, ω_{0z}. For the case $a_z = 0$, and substituting q_z given by equation 1-7 into equation 1-13,

$$\frac{d^2Z}{dt^2} = -\left(\frac{e^2V^2}{2m^2z_0^4\Omega^2}\right)Z. \qquad (1\text{-}14)$$

The force F, on an ion of mass *m* and charge e in a potential well is given by

$$F = m\frac{d^2Z}{dt^2} = e\,\frac{d\overline{D}_z}{dZ} \quad \text{where} \quad \frac{d\overline{D}_z}{dZ} = -\frac{eV^2}{2mz_0^4\Omega^2}Z \qquad (1\text{-}15)$$

where $\overline{D}_z$ = the depth of the potential well in the *z*-direction. Integrating $d\overline{D}_z$/dZ over the limits $Z = 0$ to $Z = z_0$,

$$\overline{D}_z = -\frac{eV^2}{4mz_0^2\Omega^2} = \frac{q_zV}{8} \qquad (1\text{-}16)$$

The well depth in the *r*-direction is derived similarly and since $r_0^2 = 2z_0^2$, $D_z = 2D_r$. Thus, the ion's motion is considered to exhibit simple oscillatory motion at the secular frequencies ω_{0z} and ω_{0r} in pseudo-potential wells of depth $\overline{D}_z$ and $\overline{D}_r$ shown in Figure 1-4.

The average kinetic energy of an ion, $K.E._{ave,z}$, over one cycle of the secular motion, and the maximum kinetic energy $K.E._{max,z}$ in the *z*-directions are

$$K.E._{ave,z} = \frac{4}{\pi^2}e\overline{D}_z \quad ; \qquad K.E._{max,z} = e\overline{D}_z \qquad (1\text{-}17)$$

The average total kinetic energy, $K.E._{ave,\,total}$ and the maximum kinetic energy, $K.E._{max,total}$ due to motion in both *z* and *r* are given by

$$K.E._{ave,total} = \frac{8}{\pi^2}e\overline{D}_z \quad ; \qquad K.E._{max,total} = 2e\overline{D}_z \qquad (1\text{-}18)$$

Calculated $\overline{D}_z$ values at a variety of q_z values in the ITMS™ will be presented in chapters 2 and 5.

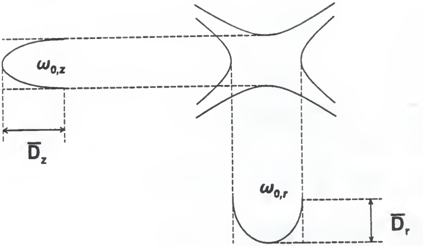

Figure 1-4: An illustration of the pseudo-potential wells of depth $\overline{D}_z$ and $\overline{D}_r$ for an rf ion trap. According to this model, an ion is considered to oscillate in the wells with frequencies $\omega_{0,z}$ and $\omega_{0,r}$ in the r and z directions, respectively. (Adapted with permission, March and Hughes, 1989.)

Phase-space Dynamics

In contrast to the models presented thus far, the phase-space dynamics model calculates changes in the position, u, and velocity, $\dot{u}$, distribution of an ion "cloud" as a function of time. The phase-space approach was initially developed in the 1970s to model ion transmission through quadrupole mass filters (Dawson, 1974, 1976; Dawson and Lambert, 1975), and has been extended to model ion-focussing in quadrupole ion traps (Lawson *et al.*, 1976b; Todd *et al.*, 1980 a,b,d; Todd, 1981; Baril, 1981).

The phase-space approach considers a group of noninteracting particles whose motions in the three orthogonal directions, x, y, z, are considered to be independent of each other. Changes in the ion cloud are mapped by considering variations in the initial position, u_0, and velocity, $\dot{u}_0$, with time. A plot of u and $\dot{u}$ in Cartesian coordinates forms a two-dimensional "phase-space." The properties of phase-space state that if a certain group of particles has a boundary, C_1, at time t_1, then at time t_2, C_1 will have transformed into C_2 which will bound the same group of particles. Thus, a large group of particles undergoing a transition in time can be accounted for, or mapped, by following the changes in the phase-space boundaries with time.

The u and $\dot{u}$ boundaries for groups of ions travelling in rf quadrupole fields were found to be perfect ellipses (Dawson, 1974), and in the notation of phase-space dynamics are of the form,

$$\Gamma u^2 + 2Au\dot{u} + B\dot{u}^2 = \epsilon \tag{1-19}$$

where A, B, and Γ are phase-dependent parameters describing the geometry of the ellipse and ϵ is the area of the ellipse divided by π (see Figure 1-5). At a fixed phase angle, ξ, all u, $\dot{u}$ pairs in each of the directions x, y, and z, lie on concentric ellipses, the

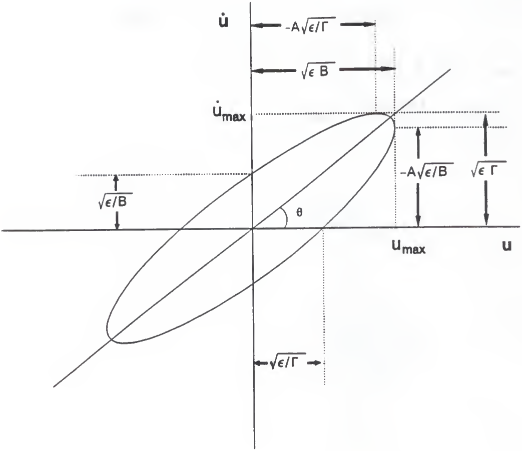

Figure 1-5: Critical dimensions of a phase-space ellipse used in the phase-space dynamical model of ion motion. The maximum kinetic energy of an ion at a rf given phase angle, ξ, is related to the parameters Γ and B. (Adapted with permission, March and Hughes, 1989.)

maximum extents of which are determined by the inter-electrode distance. Over a complete cycle of the rf, these ellipses vary their eccentricity and orientation, but maintain a constant area.

The maximum kinetic energy, $K.E._{max}$, at a given phase angle, ξ, is given by

$$K.E._{max} = \frac{V}{4q_z}\left[4\left[\frac{\Gamma(\xi)}{B_{max}}\right]_{x\ or\ y} + \left[\frac{\Gamma(\xi)}{B_{max}}\right]_{z}\right] \tag{1-20}$$

while the average kinetic energy, $K.E._{ave}$, is given by

$$K.E._{ave} = \frac{V}{9\pi^2 q_z}\left[4\left[\frac{\Gamma(\xi)}{B_{max}}\right]_{x\ or\ y} + \left[\frac{\Gamma(\xi)}{B_{max}}\right]_{z}\right] \tag{1-21}$$

Equations 1-20 and 1-21 give the energy of the ion cloud at a particular phase angle. Thus, to get at energies comparable to those obtained from the pseudo-potential well model (equations 1-17 and 1-18), equations 1-20 and 1-21 must be averaged over a complete cycle of the rf potential. Note, however, that the kinetic energies so obtained still differ from the pseudo-potential well energy values in that the previous values in equations 1-17 and 1-18 are averages over a cycle of the secular motion of the ion, as opposed to an average over a cycle of rf.

One of the advantages of the phase-space model over that of the pseudo-potential well is that it can give rise to energies over the entire range of q_z, as opposed to being limited to q_z values less than 0.4. Moreover, phase-space dynamical calculations reflect the interrelationship between the a,q pairs and β. A comparison of the average energies obtained from the "smoothed general solution," pseudo-potential well, and phase-space dynamics models for Ar^+ ions stored at a variety of q_z values has been presented (Todd *et al.*, 1980c).

Temporal Invariance

The temporal invariance model for ions stored in an rf ion trap was first presented by André and coworkers (André, 1976; André and Vedel, 1977). As in the phase-space dynamics model, the temporal invariance approach considers changes in the properties of the ion cloud. The model calculates the spatial and energy probability densities of the ion cloud based on the assumption that after a fixed reorganization time following ionization, collisions with residual gases and the buffer gas will lead to an equilibrium repartition of the ion spatial and velocity components. The probability densities of these components are then described by a Gaussian repartition function. This function is not stationary due to the periodicity of the rf field; it is, however, invariant to the temporal translation of the driving rf field. Since the model is based on a Gaussian distribution, the ion population is described in terms of an ion "temperature" as opposed to a kinetic energy. Because the ion temperature changes as a function of time, it is referred to as a "pseudo-temperature." An average ion pseudo-temperature in either the x, y, or z-directions, T (K), can be obtained by averaging the time-dependent temperature over one cycle of the rf potential.

The temporal invariance model has been used to calculate the spatial and energy probability densities of the stored ions as a function of the a_u, q_u parameters (Vedel *et al.*, 1983), the pressure and nature of buffer gas species (André and Vedel, 1977; Vedel *et al.*, 1983) and the number of stored ions, n, where n determines the extent of space-charge effects, on the ion energies (Vedel *et al.*, 1981a, b, 1983; Vedel and André, 1984, 1985). Calculated ion pseudo-temperatures in the *z*-direction for a population of Cs^+ ions cooled by He buffer range from 550 to 3000 K over the q_z range of 0 to 0.908. Shifts in the calculated fundamental secular frequencies, $\omega_{0,x}$ and $\omega_{0,z}$ with increasing n predicted with this model have been confirmed experimentally (Vedel *et al.*, 1990).

Models of Resonant Excitation

Detailed modelling of the resonant excitation process in rf ion traps has been limited. March *et al.* have recently reported a series of simulation studies comparing the effects of quadrupolar excitation (supplemental rf "tickle" potential applied in-phase to both end-cap electrodes), versus dipolar excitation (tickle applied out-of-phase to both end-caps), versus monopolar excitation (tickle applied to one end-cap electrode) on the motion of ions in the trap (March *et al.*, 1989, 1990, 1991). The simulations were initially based on numerical integration of the equations of motion arising from the field equation describing the field formed within the volume of the ion trap upon quadrupolar excitation (March *et al.*, 1989, 1990). The model has since been revised to that of a field interpolation method, FIM, wherein successive positions of the ion trajectory in time are determined by interpolating the field conditions at each point based on an initial array describing the oscillating rf field (March *et al.*, 1991). Temporal variations of the ion displacements in both the *r* and *z*-directions as well as the direction of ion ejection have been determined as a function of ion mass, a_u, q_u, initial ion position and velocity, drive and supplemental potential phase angles, supplemental potential amplitude and frequency, and the mass of the inert buffer gas. The ion kinetic energy is calculated as the mean kinetic energy over the final three phases of the rf prior to ejection. In these studies, the energy absorbed by the ions from the supplemental rf potential is calculated in terms of a fluence, where the fluence is equal to the amplitude of the supplemental rf potential times the time it takes to eject the ion from the trap. It was found that for changes in q_z, a constant fluence was required to eject ions of m/z 134 from the trap upon dipolar excitation (March, *et al*, 1991).

Experimental Determination of Trapped Ion Energies

Theoretical models of the ions trapped in an rf ion trap provide estimates of ion energies under ideal conditions. Models which incorporate any of the number of possible deviations from ideal conditions, e.g. field inhomogeneities or temporal variations of any space-charge effects, would be extremely complex and time-consuming to simulate. Thus, ion energies are best determined experimentally. To this end, a series of chemical "thermometer" reactions will be used to probe the energy of the ions under a variety of experimental conditions (Bartmess, 1987; Vedel, 1991). A chemical thermometer reaction is defined here as an ion-molecule reaction possessing a physiochemical property which changes in a well-defined manner as a function of ion energy and which can be easily measured. In the present study a number of chemical thermometer reactions are used to probe the ion energies under a variety of experimental conditions.

Kinetic and Thermodynamic Thermometers

"Kinetic" and "thermodynamic" thermometers are used to probe the ion energies when no supplemental rf potentials are applied to the trap to resonantly excite the ions; i.e., the thermometers probe the ion energies under standard EI or CI conditions. The thermometers measure the mean kinetic energies (eV) and equilibrium temperatures (K) of the ions, respectively. The kinetic thermometers include 1) the charge-exchange reaction between Ar^+ and N_2, and 2) the reaction of O_2^+ with CH_4. The rate constants, k, for these reactions are known to change in a well-defined manner as a function of the ion-molecule center-of-mass kinetic energy, $K.E._{cm}$ (eV). The thermodynamic thermometers include 1) the proton transfer reaction between toluene and ethylbenzene; 2) the proton-transfer reaction between *n*-diethylamine and di-*n*-propylamine; and 3) the charge exchange reaction between fluorobenzene and *m*-dichlorobenzene. The equilibrium constants, K_{eq} for these reactions change as a function of the thermodynamic temperature, T (K), of the ions. The ion energies are measured with these thermometers as a function of 1) the relative pressures of the reacting species; 2) the presence and pressure of He buffer gas; and, with the kinetic thermometers, 3) the q_z of the reactant ion.

QET and *n*-Alkylbenzene Internal Energy Thermometers

A series of small organic molecules for which the results of quasi-equilibrium theory, QET, calculations are available, and a homologous series of *n*-alkylbenzenes are used to probe the ion energies upon application of a supplemental resonant excitation potential. These thermometers probe the ion internal energies (eV) under the conditions used in the MS/MS analyses. The QET thermometer molecules include ionized acetone, 2-propanone, propane, toluene, and benzene. Correlations between the energies for selected crossover points on the QET graphs and the requisite experimental fluences of the corresponding points on the CID breakdown graphs provide insights into the relationship between the resonant excitation time and excitation amplitude. The *n*-alkylbenzene thermometer molecules include ionized *n*-butyl, *n*-pentyl, *n*-hexyl, and *n*-

octylbenzene. Previous CID studies have shown that the branching ratio of the *m/z* 91 and 92 fragment ions varies in a well-defined manner as a function of the internal energy of the precursor molecular ion. The ion trap parameters of interest include 1) the neutral pressure of the species undergoing CID; 2) the pressure of the He buffer gas; 3) the amplitude of the supplemental resonant excitation potential; and 4) the resonant excitation time.

Scope of the Dissertation

This dissertation presents the results obtained from a series of chemical thermometer reactions used to experimentally probe the energies of the ions stored in a QITMS. Chapter 1 has provided a summary of the operating principles behind the QITMS as well as specific details of the Finnigan MAT ITMS™ used in this study. It has also provided a summary of the principal theoretical models for calculating trapped ion energies. Chapters 2 and 3 will present the experimental methods and results obtained from the two kinetic thermometers and the three thermodynamic thermometer reactions, respectively. Chapters 4 and 5 will present the experimental methods and results obtained from the QET and *n*-alkylbenzene thermometers, respectively. The final chapter, Chapter 6, summarizes the overall ion energy results obtained from the four types of chemical thermometer reactions and provides a summary of practical considerations involved in performing ion-molecule reaction studies on the ITMS™, as well as suggestions for future studies.

CHAPTER 2
KINETIC THERMOMETER REACTIONS

Introduction

Two ion-molecule reactions will be examined in detail in this chapter in an effort to probe the kinetic energies of the ions stored in a quadrupole ion trap mass spectrometer, QITMS,

$$Ar^+ + N_2 \xrightarrow{k} N_2^+ + Ar \tag{2-1}$$

$$O_2^+ + CH_4 \xrightarrow{k} CH_3O_2^+ + H \tag{2-2}$$

The charge exchange reaction 2-1 is 0.18 eV exothermic and is one of the simplest and most well-studied ion-molecule reactions. Studies of the dynamical aspects of the reaction have included examinations of the effect of the Ar^+ spin state on the reactivity (Liao *et al.*, 1986a,b; Hamdan *et al.*, 1984) and reports on the rotational product distributions for the N_2^+ ion (Hüwel *et al.*, 1984; Sonnenfroh and Leone, 1986; Lin *et al.*, 1986). Quantum mechanical calculations of the cross sections for reaction 2-1 have also been reported (Clary and Sonnenfroh, 1989). Previous studies of the rate constant, k, for this reaction using the flow-drift technique have shown that k increases with increasing ion-molecule center-of-mass kinetic energy, $K.E._{cm}$, as shown in Figure 2-1 (Lindinger *et al.*, 1981; Smith and Adams, 1981; Dotan and Lindinger, 1982). Thus, the reaction of Ar^+ with N_2 can be used as a chemical "thermometer" to estimate the $K.E._{cm}$

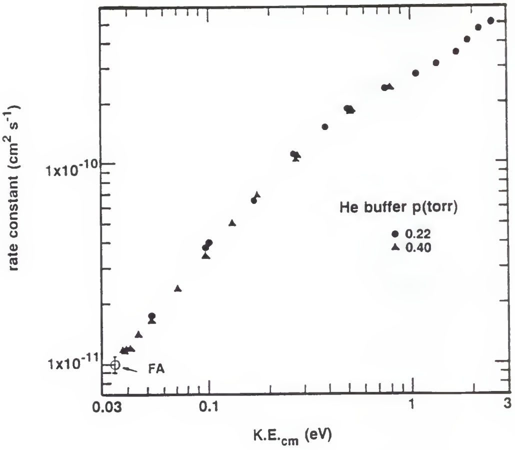

Figure 2-1: Rate constant, *k*, versus *K.E.*$_{cm}$ for the reaction $Ar^+ + N_2 \rightarrow N_2^+ + Ar$ reported by Dotan and Lindinger, 1982. FA = flowing afterglow. (Adapted with permission.)

for reaction 2-1 under a given set of experimental conditions (Bartmess, 1987) in the quadrupole ion trap mass spectrometer QITMS.

The reaction of O_2^+ with CH_4 has also been studied extensively and is perhaps the most well-studied ion-molecule reaction involving more than three atoms. The rate constant for this reaction has been studied as a function of both the temperature (Rowe *et al.*, 1984) and the rotational state of the neutral CH_4 (Viggiano *et al.*, 1992) and as a function of the electronic and vibrational states of the O_2^+ (Lindinger *et al.*, 1979; Durup-Ferguson *et al.*, 1984; Lindsay *et al.*, 1989). Detailed studies of the reaction mechanism giving rise to the $CH_3O_2^+$ ion have been performed (Adams *et al.*, 1985; Barlow *et al.*, 1986) as have studies into the structure of the $CH_3O_2^+$ product ion (Van Doren *et al.*, 1986; Kirshner *et al.*, 1989). As with the reaction of Ar^+ with N_2, flow-drift studies of reaction 2-2 have shown that the rate constant, *k*, changes in a well-defined manner as a function of $K.E._{cm}$ of the ion-molecule pair (Dotan *et al.*, 1978) as shown in Figure 2-2. Thus, the reaction of O_2^+ with CH_4 can also be used as a chemical thermometer reaction. In fact, Nourse and Kenttämaa (1990) have reported "effective" ion temperatures for the O_2^+ ions stored in a QITMS based on this reaction. A detailed comparison of the ion energies obtained by Nourse and Kenttämaa (1990) and those reported in this study will be presented in this chapter.

Physiochemical Basis of the Thermometers

The physiochemical basis of the "kinetic" thermometers presented in this chapter thus lies in the fact that the rate constants for these reactions change as a function of the $K.E._{cm}$ of the reacting ion-molecule pair, as determined in previous flow-drift studies. In a flow-drift experiment, the reagent ions are injected into the flow tube ($\approx$8cm i.d. and

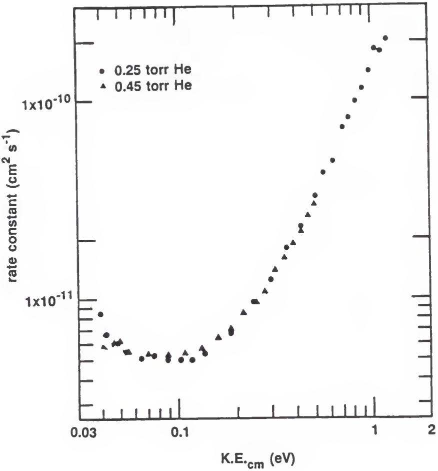

Figure 2-2: Rate constant, *k*, versus *K.E.*$_{cm}$ for the reaction $O_2^+ + CH_4 \rightarrow CH_3O_2^+ + H$ reported by Dotan *et al.*, 1978. (Adapted with permission.)

125 cm long) and transported down the first section by a flowing buffer gas, typically He or Ar (tube pressure 0.19 to 1.25 torr), where they are mass-analyzed and thermalized due to collisions with the buffer gas. The ions are then passed into the drift-reaction section of the flow tube at which point the ions drift and flow past a port where the neutral reactant gas is added at a measured rate. As the ions react with the neutral reagent, the ion signal is depleted and the rate constant is calculated from the decrease in the ion signal as a function of the reactant concentration. The $K.E._{cm}$ of the reaction is varied by changing the magnitude of the drift potential applied to the drift section of the tube; thus k can be measured as a function of ion kinetic energy (McFarland *et al.*, 1973a,b; Smith and Adams, 1979).

Rate constants in a QITMS can be determined by first mass-selecting the reagent ions of interest, and then allowing them to react with the neutral reagent for a variable reaction time, t. The rate constants are determined from the decay of the reactant ion signal with time *via* the pseudo-first-order rate equation, *i.e.*, for

$$A^+ + B \xrightarrow{k} B^+ + A \tag{2-3}$$

$$\text{rate} = \frac{-d[A^+]}{dt} = k\,[A^+][B] \tag{2-4}$$

and since [B] >> [A$^+$], integration of equation 2-4 gives

$$[A^+]_t = [A^+]_0 e^{-k[B]t} \tag{2-5}$$

where $[A^+]$ is the reactant ion intensity (counts), $[B]$ is the pressure of the neutral gas species (molecules cm^{-3}), t is the ion-molecule reaction time (s), and k is the rate constant (cm^3 s^{-1}). The $K.E._{cm}$ values for the ion-molecule pair under a variety of experimental conditions are then assigned from the flow-drift curves in Figure 2-1 and 2-2 based on the corresponding rate constants for the reaction.

Previous Ion Energy Determinations in a Rf Ion Trap

The energy of the ions stored in a rf ion trap is a function of both the heating effects induced by the rf field and the cooling effects due to collisions with background gases. A comparison of the theoretical estimations of the ion kinetic energies arising from the pseudo-potential well model, the "smoothed general solution" approach, and the phase-space dynamical model of the ion cloud has been presented (Todd *et al.*, 1980c). The models, which do not incorporate collisional processes, were used to calculate the energies of Ar^+ ions over the q_z range 0.0782 to 0.8595. The resulting average kinetic energies for the Ar^+ ions fell within the range 0.1 to 30 eV, with maximum ion kinetic energies as high as 50 eV, based on the q_z of the ion. These collision-free values can be compared to those resulting from Monte Carlo calculations incorporating the effects of charge exchange collisions on Ar^+ ions in pure Ar (Bonner, *et al*, 1976; Bonner and March, 1977). These calculations estimate that the Ar^+ ion kinetic energies are less than 0.1 eV following 15 collisions, with an upper average energy of 0.5 eV over the same q_z range. Similar energies were found for Ne^+ and CO_2^+ following 15 collisions (Doran *et al.*, 1980). As noted in chapter 1, the temporal invariance model gives rise to pseudo-temperatures between 500 and 5000 K for Cs^+ ions in 10^{-4} torr of He buffer at 300 K based on the a_u, q_u values of the ion (Vedel *et al.*, 1983).

A number of experimental determinations of the average energies of trapped monatomic species have also been reported. Bolometric methods (Church and Dehmelt, 1969; Church, 1988), optical measures (Iffländer and Werth, 1977; Knight and

Prior, 1979; Schaaf *et al.*, 1981; Cutler *et al.*, 1985, 1986; Münch *et al.*, 1987; Siemers *et al.*, 1988), and a time-of-flight method for profiling the extracted ion cloud (Lunney *et al.*, 1991) have been used to probe ion energies in the absence and presence of He buffer gas. In the absence of He buffer, the ion energies were found to be approximately 10% of the pseudo-potential well depth, $e\bar{D}$ (eV) (Church and Dehmelt, 1969; Iffländer and Werth, 1977; Knight and Prior, 1979; Schaaf *et al.*, 1981), although a lower average energy equal to 2% $e\bar{D}$ has also been reported (Siemers *et al.*, 1988). Ion energies measured in the presence of He buffer vary from 10% $e\bar{D}$ (Münch *et al.*, 1987) to energies between 0.2% and 5% $e\bar{D}$ (Schaaf *et al.*, 1981; Cutler *et al.*, 1985; Lunney *et al.*, 1991).

To date, the experimental determination of the energies of the stored ions using chemical thermometer reactions has been limited. Early reports by Lawson *et al.* (1976a) estimated the average ion energy to be on the order of 1 to 3 eV with no He buffer gas. These energies were based on the relative abundances and known appearance potentials of the *m/z* 15 (CH_3^+) and *m/z* 27 ($C_2H_3^+$) ions from ionized methane and on the appearance of the *m/z* 16 (NH_2^+) and *m/z* 18 (NH_4^+) ions from ionized ammonia. Effective ion temperatures of between 600-700 K for O_2^+ in He buffer gas prior to resonant excitation have been reported along with a temperature of approximately 1300K for O_2^+ following excitation (Nourse and Kenttämaa, 1990). These effective temperatures of the O_2^+ ions are based on the rate constant, *k*, and the branching ratio of the endothermic product ions arising from the reaction of O_2^+ with CH_4 (Adams *et al.*, 1985; Durup-Ferguson *et al.*, 1984). This will be discussed further in the Results and Discussion section below.

This chapter will present the rate constants, *k*, and assigned $K.E._{cm}$ values for the reaction of Ar^+ with N_2 at a variety of Ar and N_2 neutral gas pressures and pressure ratios, as a function of He buffer gas pressure, and $q_z(Ar^+)$. Moreover, the reaction of O_2^+ with CH_4 will be re-examined as a recent study by Viggiano *et al.* (1992) concludes that the original variable temperature data reported by Adams *et al.* (1985) and utilized by Nourse and Kenttämaa (1990) to assign effective ion temperatures to the ions in a QITMS is in error at low temperatures. This study further concludes that the relation $\Delta K.E._{cm}$ equals nkT_{eff} (where $\Delta K.E._{cm}$ = to the added kinetic energy of the drift tube, *n* is an empirical parameter, k = the Boltzmann constant, and T_{eff} is an effective ion temperature) developed by Adams *et al.* (1985) and utilized by Nourse and Kenttämaa is incorrect. Thus, the ion temperatures arising from the *k* versus T_{eff} curve reported Nourse and Kenttämaa have been called into question.

Experimental

Instrumental and Chemicals

All experiments were performed on the Finnigan MAT (San Jose, CA) ITMS™ quadrupole ion trap mass spectrometer described in chapter 1. Reagent and He buffer gases were introduced into the ion trap chamber *via* Granville-Phillips (Boulder, CO) variable leak valves. The He buffer gas line was cryocooled to remove excess water. The ion trap manifold temperature was 100 °C.

The reaction rate constants were determined by performing an rf/dc apex isolation of the reactant ion of interest and then allowing the ions to react for a variable reaction time, *t*. A schematic of the scan function employed is presented in Figure 2-3. The reagent ions were formed by electron ionization, EI, within the volume of the ion trap.

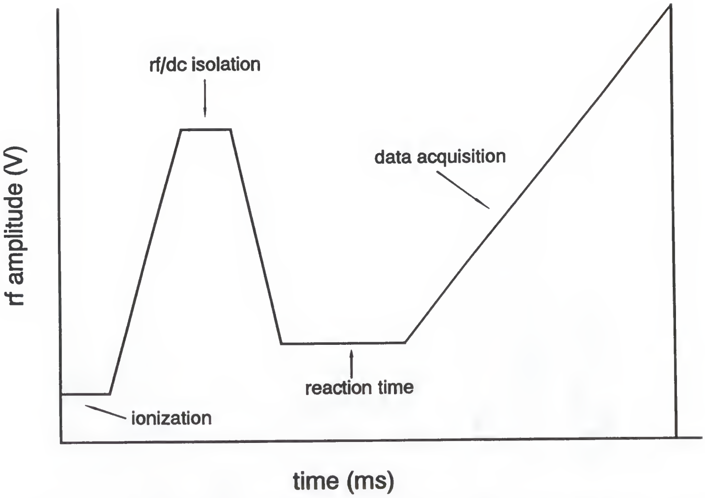

Figure 2-3: Schematic scan function (not to scale) for performing ion-molecule reactions rate studies on a QITMS.

In the ITMS™, the ionizing electron energy is a function of both the amplitude of the rf voltage applied to the ring during ionization and the phase of the rf as the electron enters the trap. As such, no single electron energy can be assigned. However, simulations of the electron energy have shown that for an rf amplitude of 112 $V_{0\text{-}p}$ (low-mass cut-off = 10 amu), the electron energy varies from 12.5 to 34.5 eV over one cycle of the rf (Pedder and Yost, 1988). The ionization time was varied to minimize space-charge as witnessed in distortions of the peak from a Gaussian profile in full-scan mode. Typical ionization times varied from 0.5 to 1 ms with no He buffer gas, and 0.05 to 0.5ms with He buffer gas.

The optimum dc voltage in the apex isolation was approximately equal to the mass of the reactant ion of interest, *i.e.*, -38 V for Ar^+ and -30 V for O_2^+ and was applied to the ring electrode for 0.30 ms. Following isolation, the ring rf amplitude was ramped to a chosen $V_{0\text{-}p}$ value so that the reactant ion defined the q_z of interest in the reaction rate determination. No ion "cooling" times were employed for the isolated Ar^+ ions prior to reaction with N_2. Rate constants for the reaction of O_2^+ with CH_4 were determined with a 200 ms cooling time to quench the excited states of the O_2^+ ions prior to apex isolation of the O_2^+ ions. Metastable $O_2^+(a^4\Pi_u)$ is effectively quenched to ground state $O_2^+(X^2\Pi_g)$ by collisions with O_2 and $O_2^+(v \geq 2)$ states are quenched by collisions with CH_4 (Durup-Ferguson *et al.* (1984). A similar cooling time was reported by Nourse and Kenttämaa (1990).

The reaction time was varied using a FORTH program written with the FORTH programming option available with the ITMS™ software (RXNTIME, Appendix A). A supplemental rf potential at the fundamental resonant frequency of N_2^+ (as calculated by the ITMS™ software) was applied to the end-cap electrodes during the reaction time.

In so doing, the N_2^+ product ions were ejected from the trap, thus preventing the reverse charge exchange reaction. This was necessary, as previous studies have shown that the reverse reaction decreases the observed rate constant (Lindinger *et al.*, 1981; Smith and Adams, 1981). At high supplemental rf amplitudes (3 $V_{0\text{-}p}$) and long reaction times (100ms) the Ar^+ ions could also be brought into resonance at the optimum frequency for N_2^+ ejection. Thus, to avoid possible excitation of the Ar^+ ions, a relatively low 1.5$V_{0\text{-}p}$ amplitude was chosen to eject the N_2^+ ions. Experiments in our laboratory have shown that upon application of the supplemental rf potential the N_2^+ ions are ejected in less than 100 microseconds; thus translational driving of the reverse reaction due to the ejection of the N_2^+ ions can be neglected. No supplemental rf voltages were employed in the study of O_2^+ with CH_4.

The reaction products were detected by performing a mass-selected instability scan (Stafford *et al.*, 1984) with no axial modulation applied during the acquisition ramp as poorer peak shape and resolution were found for ions in the mass range 10 to 50amu if axial modulation was used. The ion intensities were extracted using CHROLIST, a data reduction program developed in our laboratory, and plotted with a commercial graphing program (GRAPHER, Golden Software, Inc., Golden, CO).

The Ar, N_2, CH_4, and He gases were obtained from Alphagaz (LaPorte, TX) and were of greater than 99.9% purity. The O_2 gas was also obtained from Alphagaz had a purity of 99.5%.

Neutral Gas Pressure Determinations

The rate constants, *k*, were determined from the pseudo-first-order rate equation 2-5 and thus accurate neutral pressure readings ($[B] = CH_4$ and N_2) were required. As the ion gauge controller readout (Granville-Phillips series 280 digital controller) was originally calibrated to air by the manufacturer, calibration curves for CH_4, N_2, Ar, and He were obtained by plotting the ion gauge reading versus that of a capacitance manometer over the pressure range $1x10^{-6}$ to $1x10^{-3}$ torr (reading on the ion gauge). This was accomplished by fitting the sensing head of the capacitance manometer to the end of a hollow solids probe. The sensor was then introduced into the vacuum chamber through a solids probe inlet located at the same end of the chamber as the ion trap, allowing pressure measurements in the area adjacent to the trap (the ion gauge is located at the opposite end of the chamber). The gas of interest was metered into the ion trap chamber (with the exception of the He buffer gas - see below); the capacitance manometer readings were taken with the end of the probe ≈ 1" from the ion trap.

The ion gauge correction factors for each gas were calculated from the slope of the calibration curves. Each calibration was performed three times. Because the curves were not linear over the entire pressure range, the correction factors were determined over pressure ranges with a linear response. Sample calibration curves are presented in Figures 2-4a,c-f, with an example of the residuals obtained for a CH_4 calibration presented in Figure 2-4b. The resulting average correction factors for each gas are presented in Table 2-1.

It is interesting to note the correction factors obtained for the He buffer gas calibrations (Figures 2-4e and f). With the current gas inlet configuration, He buffer can be entered into the ITMS™ either through an unused GC transfer line inlet, effectively entering the gas into the volume of the ion trap (He_{in}), or through a second inlet which introduces the He buffer into the ion trap chamber (He_{out}). To obtain the readings for the He_{in} calibration, the probe with the capacitance manometer was docked flush against the

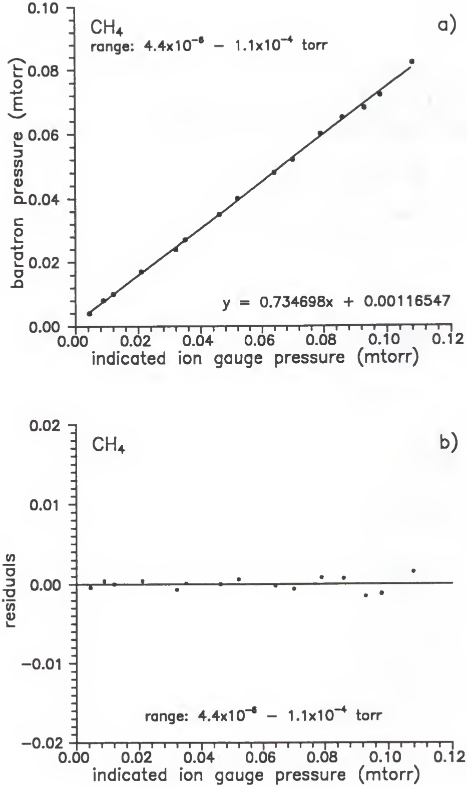

Figure 2-4: Ion gauge calibration curve for a) CH$_4$; b) residuals for the pressure calibration presented in a).

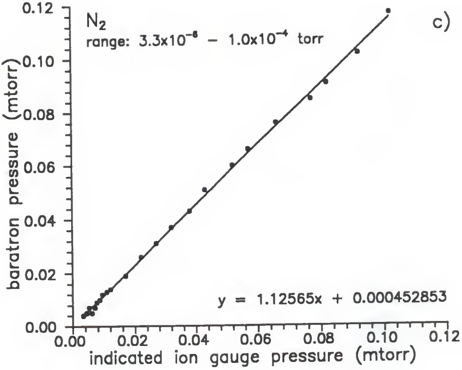

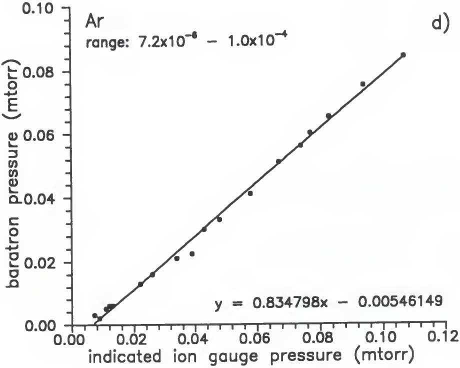

Figure 2-4: (continued) Ion gauge calibrations curves for c) N_2; and d) Ar.

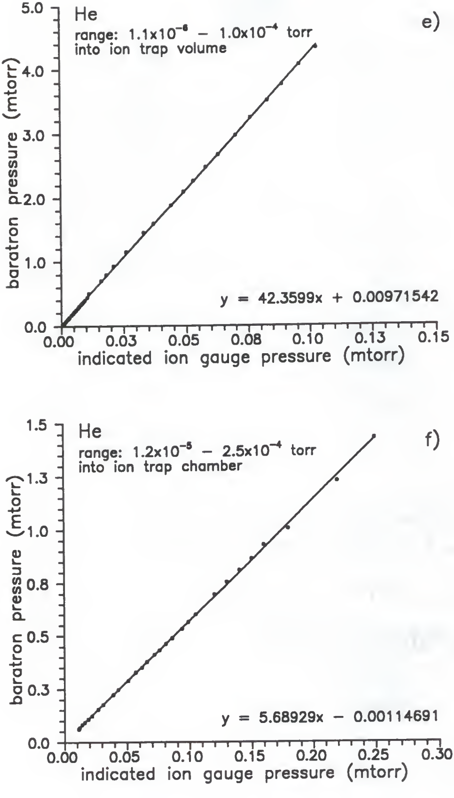

Figure 2-4: (continued) Ion gauge calibrations curves for e) He entered into the ion trap volume; and f) He entered into the ion trap chamber.

Table 2-1: ITMS™ ion gauge correction factors.

gas	pressure range (torr)	correction factor
CH_4	4.0×10^{-6} - 1.1×10^{-4}	0.80 ± 0.06
N_2	2.4×10^{-6} - 1.1×10^{-4}	1.14 ± 0.02
Ar	6.6×10^{-6} - 1.1×10^{-4}	0.81 ± 0.07
He_{in}	1.1×10^{-6} - 1.1×10^{-4}	41.4 ± 1.3
He_{out}	1.2×10^{-5} - 2.5×10^{-4}	5.1 ± 1.00

Errors calculated as the sample standard deviation of triplicate runs.

Rulon fitting on the side of the trap. The resulting calibrations show that the ion gauge correction factor obtained for the He_{in} study is a factor of ≈ ten higher than that obtained for the He_{out} study. This is in keeping with the rule of thumb that one should set the He pressure to ≈ $1\text{x}10^{-3}$ torr reading on the gauge when entering the He buffer through the GC transfer line and to ≈ $1\text{x}10^{-4}$ torr gauge reading when entering the into the trap chamber.

Note that, while ion gauge correction factors were obtained for CH_4, N_2, Ar, and He, only the CH_4 and N_2 factors are needed for calculations of the rate constants of the kinetic thermometer studies and that the He buffer was always introduced into the ion trap chamber (He_{out}). Moreover, while corrected ion gauge readings were used in the rate constant calculations, *uncorrected* ion gauge readings will be presented throughout this chapter.

Calibration Reaction

The reaction

$$CH_4^+ + CH_4 \xrightarrow{k} CH_5^+ + CH_3 \tag{2-6}$$

was used as a "calibration" reaction for the method of rate constant determinations employed in this study. The rate constant for reaction 2-6 is independent of ion energy (k_{lit} = $1.1\text{x}10^{-9}$ cm^3s^{-1}; Ikezoe *et al.*, 1987); thus, significant deviations of the experimentally determined k from k_{lit} would indicate an error in the neutral gas readings due to a pressure differential between the ion trap and the ion gauge. The rate constant for the calibration reaction was calculated from the first-order exponential decay of the normalized *m/z* 16 ion signal as a function of time. The *m/z* 16 ion signal was normalized with respect to the principal ions at *m/z* 15, 16, 17, 19, and 29 (no *m/z* 27 or

41 ions were seen). The decay of the *m/z* 16 was chosen as opposed to the growth of the *m/z* 17 ion as CH_5^+ ions react with background water at a greater rate (k=3.7x10^{-9} cm^{3}s^{-1}) than the CH_4^+ ions (k = 2.5x10^{-9} cm^{3}s^{-1}) (Ikezoe *et al.*, 1987).

$K.E._{cm}$ Determinations

Rate constants for the reaction of Ar^+ with N_2 were determined from the first-order exponential decay of the *m/z* 40 ion signal as a function of time. A normalized *m/z* 40 ion signal was not used in these determinations as the N_2^+ product ions were ejected during the reaction time. To correct the Ar^+ ion signal for trapping losses or losses due to side reactions, the decay of the *m/z* 40 ion signal was first determined when the mass-selected Ar^+ ions were allowed to react with the N_2 at a given total pressure of Ar and N_2, for a given reaction time. The decay of the *m/z* 40 ion signal was then determined at the same total pressure for the same reaction time with only Ar gas in the trap. This second decay was subtracted from the first for the calculation of k. This approach assumes that the loss of Ar^+ due to inefficient trapping or side reactions is more a function of the total pressure in the trap than the composition of the background gases.

The range of ionizing electron energies produced in the ITMS™ is sufficient to form both the $Ar^+(^2P_{3/2})$ and $Ar^+(^2P_{1/2})$ electronic states. Previous studies have shown that the thermal rate constant for the reaction of $Ar^+(^2P_{1/2})$ with N_2 is three times greater than for $Ar^+(^2P_{3/2})$ (Hamdan *et al.*, 1984). However, the collisional quenching of $Ar^+(^2P_{1/2})$ by Ar, N_2 and He competes with the charge exchange reaction 2-1. Since a range of background gas compositions was employed in this study, evidence of the excited $Ar^+(^2P_{1/2})$ state was sought in significant deviations of the *m/z* 40 ion signal from a first-order exponential fit at short reaction times (Bruce and Eyler, 1992). No evidence of excited $Ar^+(^2P_{1/2})$ was found in any of the studies involving He buffer gas. However, in some studies at low total pressures (1 to $2x10^{-6}$ torr) slight deviations of the *m/z* 40 signal from a first order fit were seen in the first 5 to 15 ms. Refitting of the data having excluded the points obtained within the first 5 to 15 ms resulted in no significant changes in the rate constant and assigned $K.E._{cm}$ values; *i.e.* the refitted results fell within the reported experimental error.

$K.E._{cm}$ values for the reaction of Ar^+ with N_2 were assigned using the *k* versus $K.E._{cm}$ curve obtained in the flow-drift studies reported by Dotan and Lindinger (1982) and presented in Figure 2-1. This curve had been obtained at 298 K with He buffer gas. In a recent variable temperature-selected ion flow-drift study, Viggiano *et al.* (1990) report that *k* for the reaction of Ar^+ with N_2 varies as a function of the neutral gas temperature for a given $K.E._{cm}$ over the range 0.05 to 0.20 eV. This increase in reactivity is attributed to an increase in the rotational temperature of the N_2 molecules. Therefore, they present changes in *k* as a function of average total energy (eV), where the average total energy is equal to the $K.E._{cm}$ plus the average rotational energy for N_2 at a given temperature (=kT, where k is the Boltzmann constant). In the present analysis of the ion energies in a QITMS, the $K.E._{cm}$ values were assigned based on flow-drift experiments performed at 298 K which corresponds to 0.026 eV of N_2 rotational energy. At the temperature of the ion trap in our experiments (373 K) N_2 has 0.032 eV of rotational energy. Thus, to correct for any possible rotational energy contribution from N_2, the difference between the rotational temperatures, 0.006 eV, was subtracted from the $K.E._{cm}$ values assigned from Dotan and Lindinger (1982).

The rate constant for the reaction of O_2^+ with CH_4 was calculated from the first-order exponential decay of the normalized *m/z* 32 ion signal as a function of time. The *m/z* 32 signal was normalized with respect to the ions at *m/z* 19, 29, 32, 33 and 47. $K.E._{cm}$ values were assigned based on the flow-drift studies in He buffer gas at 298 K reported by Dotan *et al.* (1978) and presented in Figure 2-2 consistent with the approach taken for the reaction of Ar^+ with N_2. No attempt was made to correlate the branching ratios of the endothermic product ions (*m/z* 15, 16, 17, and 29) with the $K.E._{cm}$ for this reaction as any endothermic product ions were of < 2% relative intensity over the reaction time studied.

Calculation of Experimental Error

Errors in the $K.E._{cm}$ values are expressed as the 95% confidence limits of the mean for at least three determinations, according to Shoemaker *et al.* (1981). Experimental values with no accompanying reported error are the results of a single k determination. The estimated precision of the assigned $K.E._{cm}$ values is ± 30%.

Results and Discussion

$CH_4^+ + CH_4 \rightarrow CH_5^+ + CH_3$ Calibration Reaction

Typical plots of ion intensity versus time for the reaction of CH_4^+ with CH_4 without and with He buffer gas are presented in Figures 2-5a and b. In addition to the calibration reaction of interest, possible reactions leading to the products observed following mass-selection of the *m/z* 16 ion include

$$CH_4^+ + H_2O \rightarrow H_3O^+ + CH_3 \tag{2-7}$$

$$CH_4^+ + M \rightarrow CH_3^+ + H + M \tag{2-8}$$

$$CH_5^+ + H_2O \rightarrow H_3O^+ + CH_4 \tag{2-9}$$

$$CH_5^+ + M \rightarrow CH_3^+ + H_2 + M \tag{2-10}$$

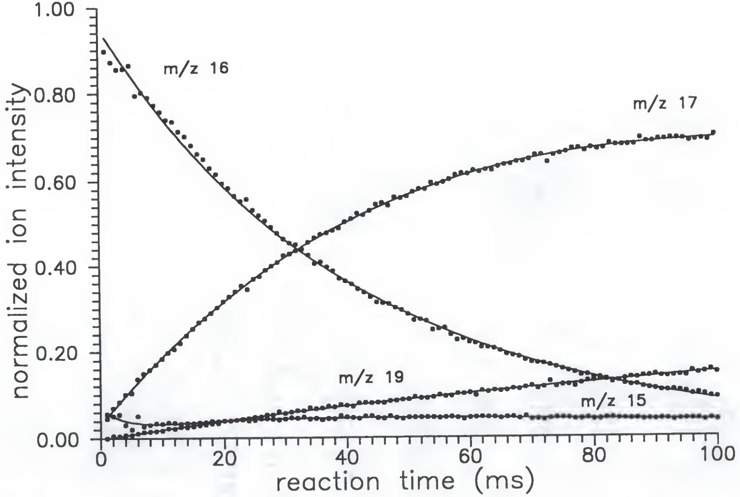

Figure 2-5: Ion intensity versus reaction time for the calibration reaction, $CH_4^+ + CH_4 \rightarrow CH_5^+ + CH_3$. a) Methane at 1.0×10^{-6} torr; $q_z(CH_4^+) = 0.732$; *m/z* 16 ion signal shown with a first-order exponential fit; no He buffer gas.

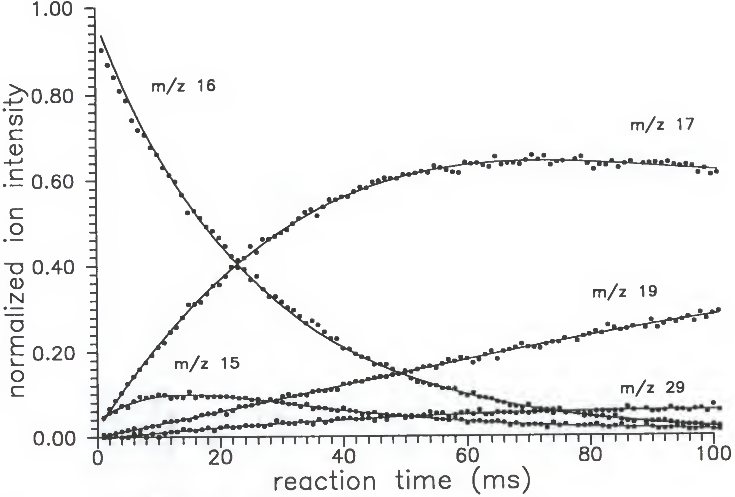

Figure 2-5: (continued) Ion intensity versus reaction time for the calibration reaction, $CH_4^+ + CH_4 \rightarrow CH_5^+ + CH_3$. b) Methane at 1.0×10^{-6} torr; $q_z(CH_4^+) = 0.732$; *m/z* 16 ion signal shown with a first-order exponential fit; He buffer gas added to 1.0×10^{-4} torr.

$$CH_3^+ + CH_4 \rightarrow C_2H_5^+ + H_2 \qquad (2\text{-}11)$$

where, M = CH_4 or He.

The decrease in *m/z* 16 in Figures 2-5a and b from reactions other than 2-6 can be attributed to proton transfer reaction 2-7 with background water and collision-induced dissociation, CID, with either CH_4 or He (reaction 2-8). Reaction 2-7 has a thermal rate constant of $k = 2.5\times10^{-9}$ cm^{3}s^{-1} (Ikezoe *et al.*, 1987); thus, it can be considered to be a significant side reaction at reaction times where the relative intensity of *m/z* 16 is greater than that of *m/z* 17. As *m/z* 17 increases, reaction 2-9 will begin to compete with reaction 2-7. Without He buffer gas (Figure 2-5a) the relative intensity of *m/z* 15 is seen to be slightly greater than 0.05 at reaction times < 10 ms. This may be due to CID of *m/z* 16 with CH_4 2-8. Upon addition of He buffer gas (Figure 2-5b), *m/z* 15 is seen to increase in intensity from 0 to 15 ms and then decrease with an accompanying increase in the *m/z* 29 ion intensity. This is likely due to an increase in the rate of the CID reactions with He buffer 2-8 and 2-10, followed by the formation of *m/z* 29 ions *via* reaction 2-11 at reaction times > 15 ms.

Rate constants for the calibration reaction 2-6 at a variety of methane pressures with no He buffer present in the trap are presented in Table 2-2. All *k* values were obtained at a $q_z(CH_4^+) = 0.732$ with no He buffer in the trap. The higher *k* values at lower methane pressures are due to an increase in CH_4^+ loss due to reaction 2-7, as the relative amount of background water (base pressure ≈ 4×10^{-8} torr) is greater at lower methane pressures. An average $k = 1.03\pm0.02\times10^{-9}$ cm^{3}s^{-1} is found at methane pressures above 2.2×10^{-6} torr. This value is in good agreement with the literature value, $k_{lit}=1.1\times10^{-9}$ cm^{3}s^{-1} (Ikezoe *et al.*, 1987), indicating that no pressure differentials are present between the gauge and the ion trap reaction volume (Bruce and Eyler, 1992).

Table 2-2: Rate constants for the calibration reaction of CH_4^+ with CH_4 with no He buffer in the trap.

CH_4 pressure (/10^{-7} torr)	total reaction time (ms)	*k* (/10^{-9} cm^3s^{-1})
1.8	240	1.32
2.6	240	1.30
3.6	240	1.30
4.3	240	1.32
4.9	240	1.25
5.8	250	1.185 ± 0.029
7.2	240	1.18
8.3	240	1.16
9.5	150	1.16
12	100	1.128 ± 0.042
22	100	1.04 ± 0.16
29	60	1.04
34	50	1.01 ± 0.13
40	40	1.04
50	25	1.01

All *k* values determined with $q_z(CH_4^+) = 0.732$ during the reaction time.

Thus, ion gauge readings corrected only for neutral species sensitivities can be used for the calculation of reaction rate constants. Further, the average value is in good agreement with previous determinations on a QITMS reported by Bonner *et al.* (1972/73) ($k = 1.1 \pm 0.4\times10^{-9}$ cm^{3}s^{-1}), Lawson *et al.* (1976) ($k = 1.1 \pm 0.1\times10^{-9}$ cm^{3}s^{-1}) and McLuckey *et al.* (1988) ($k = 1.5 \pm 0.5\times10^{-9}$ cm^{3}s^{-1}).

Rate constants for the calibration reaction 2-6 at a variety of He buffer gas pressures are presented in Table 2-3. A somewhat higher average $k = 1.40 \pm 0.09$ is found with He buffer present in the trap. This is attributed to an increased loss of the ions at *m/z* 16 *via* reaction 2-7 as an increase in background water is seen in full-scan mode upon addition of buffer even with cryocooling of the He line. The somewhat lower k values found at high He pressures are due to scattering losses of the CH_4^+ ions evident at these high pressures.

$K.E._{cm}$ Dependent $Ar^+ + N_2 \rightarrow N_2^+ + Ar$ Reaction

Typical plots of ion intensity versus time for the reaction of Ar^+ with N_2 without and with He buffer gas are presented in Figures 2-6a and b. The figures present the product ions formed when Ar^+ reacts with N_2 and were *not* used to determine k for this reaction as the N_2^+ product ions have not been ejected. Upon ejection of N_2^+ only ions of *m/z* 18 and *m/z* 40 are seen. In addition to the charge exchange thermometer reaction of interest 2-1, possible reactions leading to the principal ions observed in Figures 4a and b include

$$Ar^+ + H_2O \rightarrow H_2O^+ + Ar \qquad (2\text{-}12)$$

$$Ar^+ + Ar \rightarrow Ar^+ + Ar \qquad (2\text{-}13)$$

$$N_2^+ + Ar \rightarrow Ar^+ + N_2 \qquad (2\text{-}14)$$

Table 2-3: Rate constants for calibration reaction of CH_4^+ with CH_4 with He buffer in the trap.

CH_4 pressure (/10^{-7} torr)	total pressure with He (/10^{-5} torr)	total reaction time (ms)	k (/10^{-9} cm^3s^{-1})
12	2.6	100	1.32 ± 0.09
12	5.4	100	1.43 ± 0.19
12	10	100	1.41 ± 0.14
12	25	100	1.61 ± 0.25
12	51	100	1.56 ± 0.18
35	5.5	50	1.41
35	10	30	1.34
50	5.5	30	1.28
50	10	30	1.27
		average	1.40 ± 0.09

All k values determined with $q_z(CH_4^+)$ = 0.732 during the reaction time.

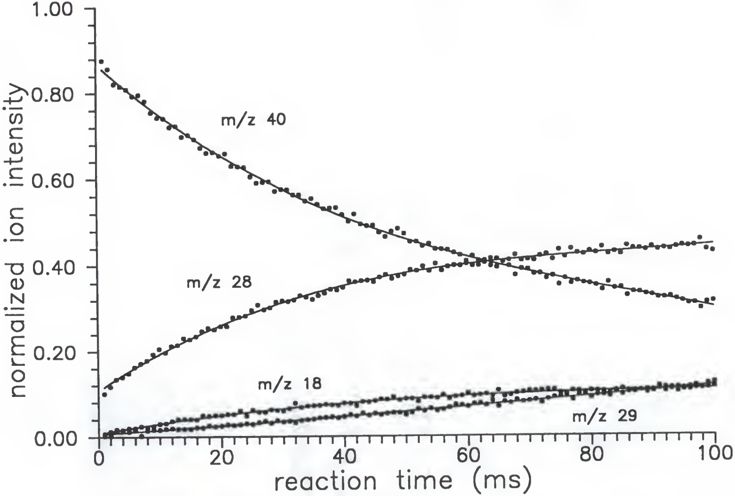

Figure 2-6: Ion intensity versus reaction time for the reaction of Ar^+ with N_2 without N_2^+ ejection. a) 1:1 $Ar:N_2$ at $1.0x10^{-5}$ torr; $q_z(Ar^+)$ = 0.295 with no He buffer gas.

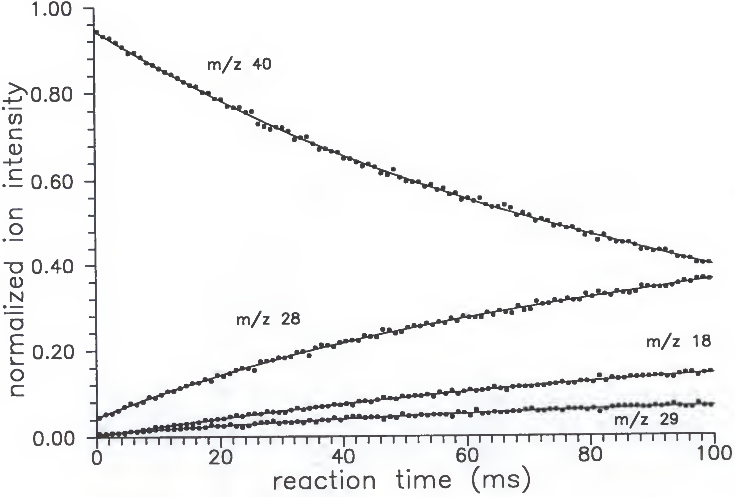

Figure 2-6: (continued) Ion intensity versus reaction time for the reaction of Ar^+ with N_2 without N_2^+ ejection. b) 1:1 $Ar:N_2$ at $1.0x10^{-5}$ torr; $q_z(Ar^+) = 0.295$ with He buffer gas added to $1.0x10^{-4}$ torr.

$$N_2^+ + H_2O \rightarrow H_2O^+ + N_2 \qquad (2\text{-}15)$$

$$\rightarrow HN_2^+ + OH \qquad (2\text{-}16)$$

The thermal rate constant for reaction 2-12 is 1.54×10^{-9} cm^3s^{-1} (Ikezoe *et al.*, 1987), and as such reaction 2-12 is a significant side reaction on the time scale of these experiments. However, the subtraction procedure used for the calculation of *k* should correct for any loss of Ar^+ due to reaction with background H_2O except for the H_2O coming in the N_2 line. The symmetric charge exchange reaction 2-13 simply serves to thermalize the Ar^+ ions while reactions 2-14, 2-15 and 2-16 need not be considered in the rate constant determinations upon ejection of N_2^+.

Rate constants and assigned kinetic energies, $K.E._{cm}$, for the reaction of Ar^+ and N_2 with no He buffer gas are presented in Table 2-4. The large errors associated with the $K.E._{cm}$ values at the lowest pressure (13.5×10^{-7} torr) are due to the fact that one of the triplicate determinations of the rate constant was a factor of two smaller than the other two for both $q_z(Ar^+)$ values. Performance of the statistical Q test did not allow rejection of these points due to the small number of determinations considered. The errors in these points are thus considered to be anomalously high.

Several trends in the data presented in Table 2-4 are noteworthy. Firstly, while the $K.E._{cm}$ for the two $q_z(Ar^+)$ values agree within experimental error, a lower average $K.E._{cm}$ is seen at the lower $q_z(Ar^+) = 0.295$ as anticipated at this lower rf amplitude. Secondly, the lower overall $K.E._{cm}$ values and higher precision found for *k* determinations performed with a higher relative pressures of N_2 likely reflect the higher buffering efficiency anticipated when a greater proportion of the lower molecular weight N_2 is present in the trap (Dehmelt, 1967). It may, however, also be due to a bias in the subtraction procedure used to determine the *m/z* 40 ion signal decay when N_2 is the

Table 2-4: Rate constants, *k*, and K.E.$_{cm}$ for the reaction of Ar^+ with N_2 with no He buffer gas.

total pressure ($/10^{-7}$ torr)*	$Ar:N_2$ pressure	total reaction time (ms)	$q_z(Ar^+) = 0.295$		$q_z(Ar^+) = 0.454$	
			k ($/10^{-11}$ cm^3s^{-1})	K.E.$_{cm}$ (eV)	*k* ($/10^{-11}$ cm^3s^{-1})	K.E.$_{cm}$ (eV)
13.5	10:4	200	11 ± 12	0.26 ± 0.28	12 ± 12	0.26 ± 0.27
14.7	3:10	100	5.6 ± 2.9	0.14 ± 0.07	9.5 ± 4.1	0.23 ± 0.10
17.4	10:7	200	7.5 ± 5.3	0.19 ± 0.12	11.3 ± 7.8	0.27 ± 0.19
16.7	4:10	100	5.6 ± 4.3	0.14 ± 0.10	9.5 ± 1.8	0.23 ± 0.04
22.3	8:10	200	7.2 ± 2.5	0.18 ± 0.06	9.8 ± 5.6	0.24 ± 0.13
22.0	9:10	200	5.6 ± 2.6	0.14 ± 0.06	8.41 ± 0.56	0.21 ± 0.01
63.0	10:2	200	5.3 ± 1.7	0.13 ± 0.04	6.8 ± 2.2	0.17 ± 0.05
61.7	2:10	100	5.0 ± 1.1	0.13 ± 0.03	6.6 ± 1.8	0.16 ± 0.04
110	10:1	200	5.8 ± 2.2	0.15 ± 0.10	6.6 ± 1.1	0.16 ± 0.03
123	1:10	80	4.2 ± 1.4	0.11 ± 0.03	5.3 ± 1.2	0.13 ± 0.03
		average	6.3 ± 1.6	0.16 ± 0.04	7.6 ± 1.5	0.21 ± 0.03

K.E.$_{cm}$ values assigned from Figure 2-1 (Dotan and Lindinger, 1982) and corrected for the rotational temperature of N_2.

principal component of the background gas as opposed to Ar. Finally, a greater decrease in $K.E._{cm}$ is seen with increasing pressure at a $q_z(Ar^+) = 0.454$, indicating that buffering of the ions by the background gases plays a greater role at higher $q_z(Ar^+)$ values.

Rate constants and assigned $K.E._{cm}$ values for the reaction of Ar^+ with N_2 at a variety of He buffer gas pressures are presented in Table 2-5. The He range studied spans the typical operating pressure of 1.0×10^{-4} torr (uncorrected ion gauge reading). It can be seen that at a $q_z(Ar^+) = 0.295$ and an Ar and N_2 pressure of 1.0×10^{-5} torr, no significant decrease in ion energy is seen when He buffer gas is added to the trap. A somewhat more marked decrease is seen at a $q_z(Ar^+) = 0.454$. These relatively small decreases in $K.E._{cm}$ indicate that the Ar and N_2 can provide a significant degree of buffering. The trend toward lower energies at higher He pressures is attributed to the increase in scattering losses of Ar^+ ions witnessed at these higher pressures. Thus, for the experimental conditions presented in Table 2-5, increasing the He buffer gas pressure above the standard operating pressure of 1.0×10^{-4} torr provides no additional cooling effect. A similar observation of the effect of increasing the He buffer gas pressure is reported by Schaaf *et al.* (1981). Further, the average $K.E._{cm}$ values over the He range studied for both $q_z(Ar^+) = 0.295$ and 0.454 are found to be approximately equal; this indicates that for an Ar and N_2 pressure of 1.0×10^{-5} torr, any effect of $q_z(Ar^+)$ on the $K.E._{cm}$ is masked by the collisional cooling of the Ar, N_2, and He.

A thorough examination of the effect of $q_z(Ar^+)$ on the $K.E._{cm}$ is presented in Figures 2-7a and b. In Figure 2-7a, the $q_z(Ar^+)$ for a 1:1 ratio of Ar:N_2 at a total pressure of 1.0×10^{-5} torr was varied both without and with He buffer gas present in the trap. The same study was repeated in Figure 2-7b with an Ar and N_2 pressure of 2.2×10^{-6} torr. In

Table 2-5: Rate constants, *k*, and $K.E._{cm}$ for the reaction of Ar^+ with N_2 at a variety of He buffer gas pressures.

total pressure with He	$q_z(Ar^+) = 0.295$		$q_z(Ar^+) = 0.454$	
($/10^{-5}$ torr)	*k* ($/10^{-11}$ cm^3s^{-1})	$K.E._{cm}$ (eV)	*k* ($/10^{-11}$ cm^3s^{-1})	$K.E._{cm}$ (eV)
no He	5.4 ± 1.5	0.14 ± 0.04	6.4 ± 2.4	0.16 ± 0.06
2.6	5.5 ± 0.89	0.14 ± 0.02	5.82 ± 0.20	0.15 ± 0.01
5.1	5.4 ± 1.4	0.14 ± 0.03	5.2 ± 1.7	0.13 ± 0.04
10.0	5.5 ± 2.6	0.14 ± 0.06	5.1 ± 2.3	0.13 ± 0.05
25.0	5.0 ± 0.7	0.13 ± 0.02	5.3 ± 1.5	0.13 ± 0.04
51.0	4.8 ± 1.0	0.12 ± 0.03	4.4 ± 1.3	0.11 ± 0.03
average with He	5.2 ± 0.4	0.13 ± 0.01	5.2 ± 0.7	0.13 ± 0.02

All $K.E._{cm}$ values assigned from Figure 2-1 (Dotan and Lindinger, 1982) and corrected for the rotational temperature of N_2. All values are for a 1:1 Ar:N_2 pressure ratio at a total pressure of 1.0×10^{-5} torr prior to addition of He buffer and a 100 ms reaction time.

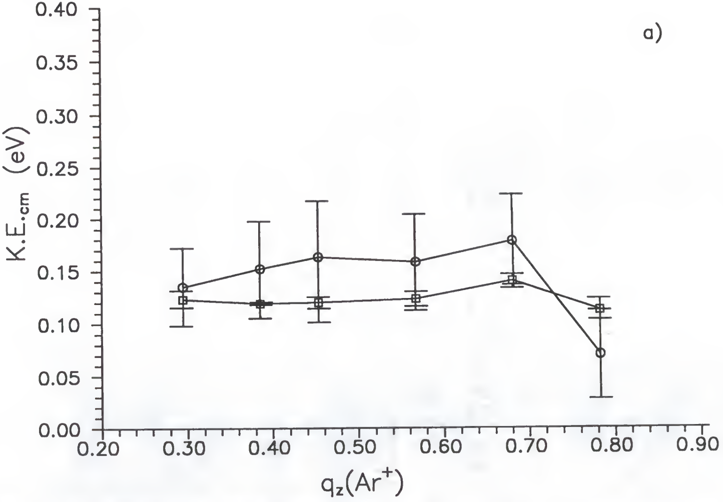

Figure 2-7: K.E.$_{cm}$ versus $q_z(Ar^+)$ determined from k for the reaction $Ar^+ + N_2 \rightarrow N_2^+ + Ar$. a) All points for a 100 ms reaction time; (○) 1:1 Ar:N_2 at 1.0x10^{-5} torr; (□) He buffer gas added to 1.0x10^{-4} torr.

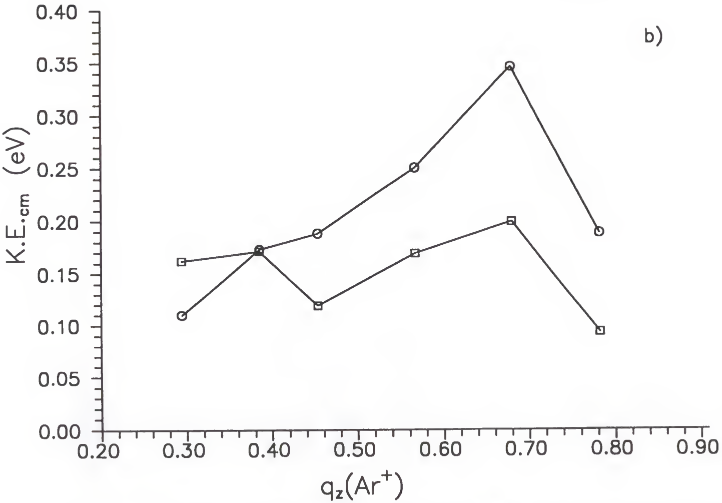

Figure 2-7: (continued) *K.E.$_{cm}$* versus $q_z(Ar^+)$ as determined from k for the reaction $Ar^+ + N_2 \rightarrow N_2^+ + Ar$. b) All points for a 100 ms reaction time; (○) 1:1 Ar:N_2 at 2.2×10^{-6} torr; (☐) He buffer gas added to 1.0×10^{-4} torr.

all cases, a decrease in the average $K.E._{cm}$ is seen upon addition of He buffer gas as is a trend towards higher $K.E._{cm}$ with increasing $q_z(Ar^+)$. These trends are much more marked for a lower total pressure of Ar and N_2 (Figure 2-7b). Thus, the amplitude of the rf applied to the ring during the reaction time has a greater effect on the $K.E._{cm}$ for lower partial pressures of Ar and N_2 where the buffering ability of these neutrals is less effective. The increase in precision of the rate constant determinations with He in Figure 2-7a is attributed to an increase in the ion extraction efficiency as ions are buffered toward the center of the trap (Stafford *et al.*, 1984). The crossover in $K.E._{cm}$ in the first two points in Figure 2-7b falls within the 30% accuracy associated with single *k* determinations. Further experiments are required to determine if this crossover is reproducible.

It is interesting to note the apparent decrease in $K.E._{cm}$ in Figures 2-7a and b at a $q_z(Ar^+) = 0.783$. This $q_z(Ar^+)$ corresponds to the position under the upper apex of the stability diagram. At this point, the trapping efficiency of the Ar^+ ions decreases, particularly with no He buffer gas (Wu and Brodbelt, 1991). Thus, the decay of the *m/z* 40 ion signal determined at high $q_z(Ar^+)$ reflect the loss of Ar^+ due to decreased trapping efficiencies to a greater extent than Ar^+ losses due to reaction with N_2. This leads to artificially low $K.E._{cm}$ values, and as such, the method of rate constant determinations employed in this study breaks down at high $q_z(Ar^+)$ values.

The 95% confidence limits presented in this study make it difficult to assign absolute $K.E._{cm}$ values under any set of experimental conditions, particularly when no He buffer is present in the trap. However, the average ion energies obtained with the Ar^+/N_2 chemical thermometer reaction reflect anticipated trends in ion energy and lead to $K.E._{cm}$ values in the range 0.11 to 0.34 eV. These values are a factor of 2 to 7 times above thermal (= 0.05 eV) and factor of 10 lower than those reported by Lawson *et al.* (1972/73).

Table 2-6 presents values for the pseudo-potential well depth, $e\overline{D}_z$, and corresponding average, $K.E._{ave,z}$, and maximum, $K.E._{max,z}$ kinetics energies of Ar^+ ions over the q_z range 0.200 to 0.454 (see equations 1-16 and 1-17 in chapter 1). Using the average $K.E._{cm}$ values from the Ar^+/N_2 thermometer over the range of q_z values studied and the average $e\overline{D}_z$ in Table 2-6, an average $\%e\overline{D}_z \approx 4\%$ is found with no He buffer and $\approx 2\%$ $e\overline{D}_z$ is found with He buffer present in the trap. These are in agreement with the range of $\%e\overline{D}_z$ values reported previously (Siemers *et al.*, 1988; Schaaf *et al.*, 1981; Cutler *et al.*, 1985; and Lunney *et al.*, 1991).

$K.E._{cm}$ Dependent $O_2^+ + CH_4 \rightarrow CH_3O_2^+ + H$ Reaction

Typical plots of ion intensity versus time for the reaction of O_2^+ with CH_4 (reaction 2-2) are presented in Figures 2-8a and b. All studies were performed at a $q_z(O_2^+)=0.369$ with 1.0×10^{-5} torr pressure of O_2 and CH_4 (1:1 ratio) and a 500 ms reaction time. The principal product ion is observed at *m/z* 47 both with and without He buffer; minor products at *m/z* 29 (≈ 2% relative intensity) and *m/z* 19 (<1% relative intensity) are also seen over the reaction time. The *m/z* 47 and 29 product ions can be attributed to the exothermic and endothermic reaction pathways, respectively (Durup-Ferguson *et al.*, 1984; Van Doren *et al.*, 1986),

$$O_2^+ + CH_4 \xrightarrow{k} CH_3O_2^+ + H \tag{2-2}$$

$$O_2^+ + CH_4 \rightarrow CH_3^+ + HO_2 \tag{2-17}$$

Table 2-6: Pseudo-potential well depth and kinetic energy calculations for Ar^+ ions in the ITMS^{TM}.

low-mass cut-off (amu)	q_z	rf amplitude ($V_{0\text{-}p}$)	$e\overline{D}_z$ (eV)	$K.E._{max,z}$ (eV)	$K.E._{ave,z}$ (eV)
8.8	0.200	99	2.48	2.48	1.00
13.0	0.295	146	5.39	5.39	2.19
17.0	0.386	191	9.22	9.22	3.74
20.0	0.454	225	12.7	12.7	5.17
		average	7.45	7.45	3.03

$a_z = 0$, $q_z = 0.908$ for the low-mass cut-off.

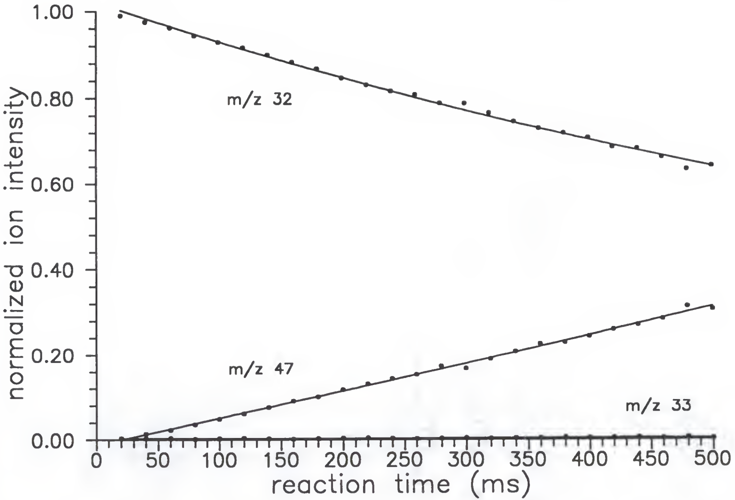

Figure 2-8: Ion intensity versus reaction time for the reaction $O_2^+ + CH_4 \rightarrow CH_3O_2^+ + H$. a) 1:1 O_2:CH_4 at 1.0×10^{-5} torr; $q_z(O_2^+) = 0.369$; no He buffer gas.

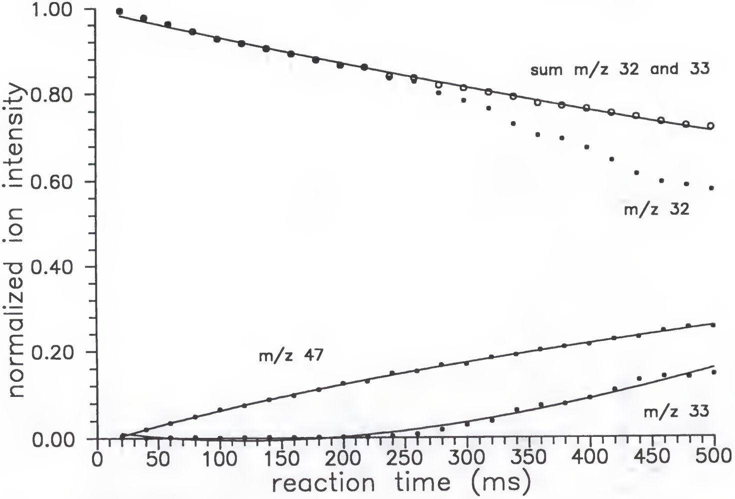

Figure 2-8: (continued) Ion intensity versus reaction time for the reaction $O_2^+ + CH_4 \rightarrow CH_3O_2^+ + H$. b) 1:1 O_2:CH_4 at 1.0×10^{-5} torr; $q_z(O_2^+) = 0.369$; He buffer gas added to 1.0×10^{-4} torr. (○) sum of m/z 32 and 33 intensities showing first-order fit used in the calculation of *k*.

where reaction 2-2 is exothermic by 1 eV, and where the *m/z* 15 products from the endothermic reaction 2-17 (-0.24 eV) react with excess methane to form the ion at *m/z* 29. No products arising from the second possible endothermic channel (-0.60 eV)

$$O_2^+ + CH_4 \rightarrow CH_4^+ + O_2 \qquad (2\text{-}18)$$

were seen in any of the kinetic studies presented. The *m/z* 19 ions may arise from either (Van Doren *et al.*, 1986)

$$O_2^+ + CH_4 \rightarrow H_3O^+ + HCO \qquad (2\text{-}19)$$

or,

$$CH_3O_2^+ + H_2O \rightarrow H_3O^+ + CH_2O_2 \qquad (2\text{-}20)$$

It is interesting to note that in the studies with He buffer, an anomalous ion at *m/z* 33 begins to appear at a 250 ms reaction time and increases to $\approx$15% by 500 ms. The appearance of this ion distorted the first-order exponential decay of the *m/z* 32 ion signal at reaction times greater than 250 ms, as seen in Figure 2-8b. This distortion, coupled with the fact that there is no accompanying decrease in the *m/z* 47 ion signal, indicates that the *m/z* 33 ion is arising directly from the O_2^+ ions and not from a possible consecutive reaction. Upon closer examination of the *m/z* 32 peak profile, it was found that the peak became skewed towards higher mass at reaction times greater than 250 ms *only* when He buffer was present in the trap as shown in Figure 2-9. Thus, the *m/z* 33 ion arises from an error in the centroiding of the *m/z* 32 peak by the ITMS™ data system. It is assumed that this distortion is due to the onset of space charge at these long reaction times as no distortion of the peak profile is seen in any of the studies with no He buffer. Thus, in calculating the rate constant for the reaction of O_2^+ with CH_4 in the studies with He buffer, the apparent intensity of the *m/z* 33 was added to that of the *m/z* 32 over the 500 ms reaction time (Figure 2-8b). This resulted in an anticipated first-order exponential decay with no distortions.

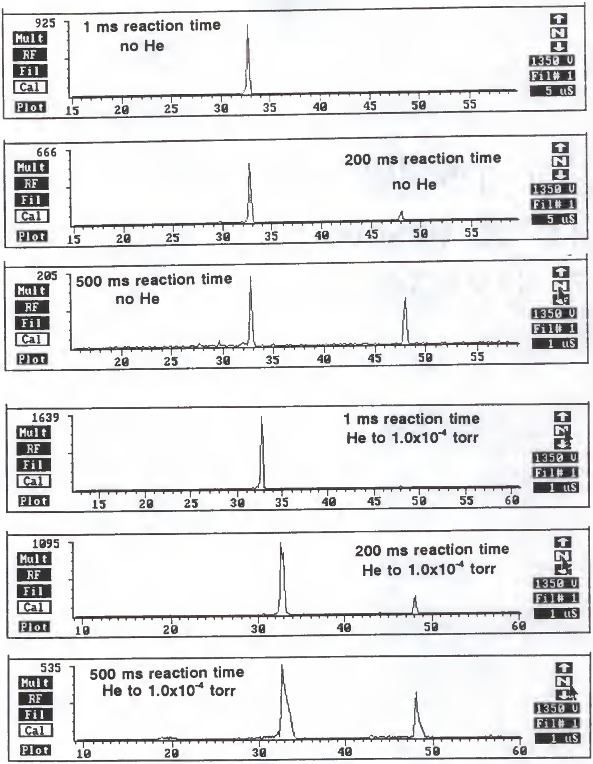

Figure 2-9: O_2^+ ion peak profiles at a variety of reaction times in the absence and presence of He buffer.

A rate constant, $k = 8.6 \pm 0.5 \times 10^{-12}$ cm^{3}s^{-1} was found for the reaction of O_2^+ with CH_4 with no He buffer gas present in the trap; $k = 6.26 \pm 0.09 \times 10^{-12}$ cm^{3}s^{-1} was found with 1.0×10^{-4} torr of He present in the trap. Based on these rate constants, $K.E._{cm}$ values of 0.23 ± 0.01 eV without He buffer and 0.17 ± 0.01 eV with He buffer are assigned from Dotan *et al.* (1978). These values are somewhat higher than those obtained from the Ar^+/N_2 thermometer reaction under similar conditions (second points, Figure 2-7a). However, they do fall within the range 0.11 to 0.34 eV.

The rate constants presented here are of the same order of magnitude as those obtained by Nourse and Kenttämaa (1990). However, Nourse and Kenttämaa report an increase in *k* for the reaction of O_2^+ with CH_4 in the presence of He buffer gas (6.6×10^{-12} cm^{3}s^{-1} ± 20% without He buffer gas versus 8.2×10^{-12} cm^{3}s^{-1} ±20% in the presence of 1 mtorr of He). Using the present method of ion energy assignment, these rate constants correspond to an increase in ion energy from $K.E._{cm} = 0.18$ eV to $K.E._{cm} = 0.22$ eV upon addition of He buffer. The decay of the *m/z* 32 signal over a 1.6 s reaction time in the presence of He buffer presented by Nourse and Kenttämaa (Figure 2 in Nourse and Kenttämaa, 1990) contains distortions from a first-order exponential fit at reaction times < 500 ms. These distortions are similar to those witnessed in the present analyses with He buffer when the growth of the signal at *m/z* 33 at reaction times greater than 250 ms had not been taken into account (Figure 2-8b). Moreover, a first-order analysis of the distorted *m/z* 32 signals with and without He buffer gas leads to the same effect on the rate constants as that reported by Nourse and Kenttämaa; *i.e.* a higher rate constant was obtained with He buffer. This suggests that the data reported by Nourse and Kenttämaa may have suffered from the same centroiding problems due to the onset of space charge at long reaction times, resulting in an apparent decrease in *k* with He buffer.

in k with He buffer. Given the increase in the rate constant reported by Nourse and Kenttämaa, upon addition of He buffer, and the recent reanalysis Viggiano *et al.*, 1992, we suggest that the present method of ion energy assignment for the reaction of O_2^+ with CH_4 is preferable to that presented by Nourse and Kenttämaa.

"Effective" Ion Temperatures

Use of the term "temperature" to describe the ions stored in a QITMS was first introduced by Dehmelt in 1967 (Dehmelt, 1967; Major and Dehmelt, 1968) and extended by Blatt *et al.* (1986). In this description, the ions possess Gaussian spatial distributions; an equilibrium temperature arises from a balancing of the rf heating effects with the those of the collisional cooling mechanisms active in the trap. Experimental measures of the ion density distribution were first presented by Knight and Prior (1979). In these measures, profiles of $^6Li^+$ ions trapped for 1 s at 10^{-9} torr with no He buffer were observed with a laser scanning method. The profiles were found to be consistent with a Gaussian distribution and observed values for the radius of the ion cloud led to ion temperatures of $\approx$ 5000 K. Implied Maxwell-Boltzmann distributions of stored ion energies have since been used in numerous ion "temperature" determinations (Nourse and Kenttämaa, 1990; Church and Dehmelt, 1969; Church, 1988; Cutler *et al.*, 1985; Siemers *et al.*, 1988; Lunney *et al.*, 1991).

The number of collisions an ion suffers can be calculated from the Langevin ion-induced dipole theory for nonpolar molecules (Gioumousis and Stevenson, 1958; Su and Bowers, 1979). In this model, both the ion and the molecule are considered to be point particles with no internal energy travelling at a given relative velocity, v_{rel} (ms^{-1}). The ion-molecule capture rate constant, k_L, is given by

$$k_L = \sigma v = e\sqrt{\frac{\pi\alpha}{\epsilon_0\mu}} \tag{2-21}$$

where σ is the capture cross section (m^2), e is the charge (C), α is the polarizability of the neutral (m^3), ϵ_0 is the vacuum permittivity ($8.854\times10^{-12}\ C^2N^{-1}m^{-2}$), and μ is the reduced mass of the ion-molecule pair. To obtain the number of collisions per millisecond an ion of a given *m/z* will experience with a given neutral, k_L is multiplied by the number density of the neutrals, *n/V*, obtained from the ideal gas law. Sample collision rates for Ar^+, N_2^+, and CH_4^+ in Ar, N_2, CH_4, and He are presented in Table 2-7.

In the present study, the Ar^+ ions suffer ≈ 7 collisions ms^{-1} when He buffer is present at 1.0×10^{-4} torr (uncorrected ion gauge reading). (This was calculated by first subtracting the average Ar and N_2 pressures from the total uncorrected ion gauge reading, multiplying by the ion gauge correction factor for He (He_{in} Table 2-1) and then calculating the total number of collisions ms^{-1} for Ar^+ in He from Table 2-7). These momentum-loss collisions should serve to balance any heating effects induced by the rf field. As such, ion temperatures can be determined assuming a Maxwell-Boltzmann distribution of ion energies.

A definition of "effective" temperature is proposed for He buffered Ar^+ ions based on the assigned $K.E._{cm}$ values arising from the charge exchange reaction 2-1 where (Kennard, 1938)

$$K.E._{cm} = 1/2\mu v_{rel}^2 \tag{2-22}$$

Assuming a Maxwell-Boltzmann distribution of energy for both the ion and the neutral species,

Table 2-7: Langevin collision rates for a Ar^+, N_2^+, and CH_4^+ in various gases.

	α (m^3)	k_L (m^3s^{-1})	pressure (torr)	collision rate (ms^{-1})
Ar^+ in He	2.0×10^{-31}	5.5×10^{-16}	1.0×10^{-4}	1.4
N_2^+ in He	2.0×10^{-31}	5.6×10^{-16}	1.0×10^{-4}	1.5
CH_4^+ in He	2.0×10^{-31}	5.9×10^{-16}	1.0×10^{-4}	1.5
Ar^+ in Ar	1.62×10^{-30}	6.7×10^{-16}	1.0×10^{-5}	0.17
Ar^+ in N_2	1.73×10^{-30}	7.6×10^{-16}	1.0×10^{-5}	0.20
CH_4^+ in CH_4	2.60×10^{-30}	1.3×10^{-15}	1.0×10^{-5}	0.35

α = polarizability of the neutral gas species (McClellan, 1963).
k_L = capture rate constant (m^3s^{-1}).

$$K.E._n = \frac{3}{2}kT_n = \frac{1}{2}m_n v_n^2 \quad \text{and} \quad K.E._I = \frac{3}{2}kT_I = \frac{1}{2}m_I v_I^2 \qquad (2\text{-}23)$$

Rearranging equation 2-23

$$v_n^2 = \frac{3kT_n}{m_n} \quad \text{and} \quad v_I^2 = \frac{3kT_I}{m_I} \qquad (2\text{-}24)$$

and substituting into equation 2-22 gives

$$K.E._{cm} = \frac{3k}{2}\left(\frac{m_I\, m_n}{m_I + m_n}\right)\left[\frac{T_I}{m_I} + \frac{T_n}{m_n}\right] \qquad (2\text{-}25)$$

Thus,

$$T_I = \left[\frac{2}{3k}\frac{(m_I + m_n)}{(m_I\, m_n)}K.E._{cm} - \frac{T_n}{m_n}\right] m_I \qquad (2\text{-}26)$$

where k is the Boltzmann constant (1.3807×10^{-23} JK^{-1}), m_I and m_n are the masses (kg), and v_I and v_n are the velocities (ms^{-1}) of the Ar^+ ion and N_2 neutral species, respectively, T_n is the neutral gas temperature (K), and T_I is the effective ion temperature (K). In the case of He buffered ground state Ar^+ ions for which the $K.E._{cm}$ values have been corrected for rotational contributions from N_2, T_I corresponds to an effective kinetic temperature of the trapped Ar^+ ions. Note that only the Ar^+ ions in He buffer can be considered to have suffered enough collisions to define a Maxwell-Boltzmann energy distribution and thus define a temperature. Moreover, this definition of ion temperature *cannot* be applied to the reaction of O_2^+ with CH_4, since the rotational and vibrational states of the reacting diatomic O_2^+ cannot be deduced and as such its energy cannot be reduced to pure kinetic energy.

Effective kinetic temperatures for the He buffered Ar^+ ions arising from the $K.E._{cm}$ values presented in Table 2-5 are 1930 ± 170 K for $q_z(Ar^+) = 0.295$ and 1890 ± 320 for $q_z(Ar^+) = 0.454$; those for the variable $q_z(Ar^+)$ studies (Figures 2-7a and b) range from

1700 ± 25 K (for Ar and N_2 at 1.0×10^{-5} torr, and a $q_z(Ar^+) = 0.386$) to 3300 K (for Ar and N_2 at 2.2×10^{-6} torr, and a $q_z(Ar^+) = 0.681$). Thus, the effective ion temperatures arising from the Ar^+/N_2 thermometer reaction are within the range ≈ 1700 to 3300 K. These are a factor of ≈ 50 higher than those reported by Nourse and Kenttämaa, (1990).

Conclusions

This chapter presents a detailed study of the kinetic energies of the ions stored in a QITMS. $K.E._{cm}$ values were assigned based on rate constants for the charge exchange reaction of Ar^+ with N_2 using previous flow-drift data. While the sometimes large experimental error arising from the use of this chemical "thermometer" reaction makes assignment of absolute $K.E._{cm}$ under any set of experimental conditions difficult, certain trends in the $K.E._{cm}$ values are noteworthy. 1) There is a consistent decrease in $K.E._{cm}$ upon addition of He buffer gas to the reaction system; however, increasing the He buffer pressure above 1.0×10^{-4} torr (uncorrected ion gauge reading) appears to have little additional cooling effect. 2) An increase in $K.E._{cm}$ is seen with increasing $q_z(Ar^+)$ both with and without He buffer gas. This increase in energy is more marked at lower pressures of Ar and N_2, presumably due to the decreased buffering abilities of these neutral gases at lower total pressures. The experimentally determined $K.E._{cm}$ values arising from the reaction of Ar^+ with N_2 under a variety of experimental conditions are found to all lie within the range 0.11 to 0.34 eV. These values indicate that the ions are a factor of 2 to 7 times above thermal energy (= 0.05 eV).

A definition of "effective" ion temperature for He buffered Ar^+ ions is presented based on the assigned $K.E._{cm}$ and the assumption that the ions are described by a

Maxwell-Boltzmann distribution of kinetic energies. The resulting ion temperatures lie within the range ≈1700 K to 3300 K.

The reaction of O_2^+ with CH_4 was also used as a chemical thermometer for probing ion energies in a QITMS. A method of assigning $K.E._{cm}$ values based on previous flow-drift studies was used consistent with the approach taken for the Ar^+/N_2 reaction. The $K.E._{cm}$ values arising from the O_2^+/CH_4 reaction are 0.23 ± 0.01 eV with no He buffer in the trap, and 0.17 ± 0.01 eV with He buffer. These are within the range of $K.E._{cm}$ values arising from the reaction of Ar^+ with N_2. It is suggested that the effective ion energies reported here for the O_2^+ ions are a more accurate indication of the ion temperatures than that of 600-700 K reported previously by Nourse and Kenttämaa, (1990).

Utility of Kinetic Thermometer Reactions

The kinetic thermometer reactions presented in this chapter probe the center-of-mass *kinetic* energies of the ion-molecule pairs, but provide no direct information as to the *internal* energy of the ions. In fact, it is assumed that the ions are in their ground electronic and vibrational states upon reaction. However, internal energy states formed upon electron ionization ($Ar^+(^2P_{1/2})$, $O_2^+(a^4\Pi_u)$, O_2^+ ($v \geq 2$, *etc.*) can contribute to the observed rate constant (Hamdan *et al.*, 1984; Durup-Ferguson *et al.*, 1984) and must be accounted for in any kinetic temperature determination. Moreover, rotational and vibrational contributions from the respective neutral must also be considered (Viggiano *et al.*, 1990, 1992) should the rate constants be determined at temperatures different from the original flow-drift experiments.

Due to the relatively long reaction times required to obtain an accurate rate constant (100 to 500 ms), these thermometers are limited to studies with no resonant excitation of the ion of interest. Application of a resonant excitation potential would result in substantial trapping losses in a time (10 to 20 ms) significantly less than that requires to obtain an accurate rate constant. In spite of these limitations, the kinetic thermometer reactions effectively probe $K.E._{cm}$ values under a number of experimental conditions; moreover, the values obtained reflect anticipated trends in ion energy.

CHAPTER 3
THERMODYNAMIC THERMOMETER REACTIONS

Introduction

Effective ion temperatures, T (K), for ions stored in q quadrupole ion trap mass spectrometer, QITMS, for times greater than 1 second will be presented in this chapter. The ion temperatures will be determined from the gas-phase ion-molecule equilibrium constants, K_{eq}, of the following proton transfer and charge exchange equilibria:

$$[C_6H_5CH_3]H^+ + C_6H_5C_2H_5 \rightleftharpoons C_6H_5CH_3 + [C_6H_5C_2H_5]H^+ \tag{3-1}$$

$$[(C_2H_5)_2NH]H^+ + (n\text{-}C_3H_7)_2NH \rightleftharpoons (C_2H_5)_2NH + [(n\text{-}C_3H_7)_2NH]H^+ \tag{3-2}$$

$$C_6H_5F^+ + m\text{-}C_6H_4Cl_2 \rightleftharpoons C_6H_5F + m\text{-}C_6H_4Cl_2^+ \tag{3-3}$$

Mass Spectrometric Determinations of K_{eq}

Proton transfer and charge exchange equilibria have been studied in detail since the late 1960s and early 1970s when mass spectrometric instrumentation capable of measuring gas-phase ion-molecule equilibrium constants was first introduced. Interest in gas-phase equilibria has been driven by the ability to obtain thermodynamic information for a series of acid-base pairs free of solvent effects. The principal mass spectrometric methods for determining K_{eq} include 1) pulsed high pressure mass spectrometry, HPMS; 2) pulsed ion cyclotron resonance mass spectrometry, ICRMS; and 3) flow-drift mass spectrometry.

Ion-molecule equilibria were first observed in a HPMS by Kebarle and Godbole (1963) and improved methods for obtaining K_{eq} with HPMS were subsequently developed by Kebarle and coworkers from 1964-1972 (Cunningham *et al.*, 1972). An HPMS consists of a field-free chamber in which several millitorr of reactant gases are combined with up to 4 to 10 torr of a bath gas, typically CH_4. In order to avoid the formation of cluster ions, the chamber is typically heated to 600 K. The reactant ions formed by high energy electron ionization, EI, are thermalized due to the collisions with the bath gas as they diffuse towards the walls of the chamber. Moreover, because the reagent neutrals are present in such high concentrations, the ions are able to reach equilibrium prior to being lost to the walls of the chamber. Ion intensities are measured as a function of time as some of the ions diffuse through a slit into a high vacuum chamber where they are mass-analyzed either by a magnetic sector or a quadrupole mass filter (Kebarle, 1977; Moylan and Brauman, 1983).

Bowers *et al.* (1971) reported the first ion-molecule equilibria observed with a pulsed electron beam ICRMS. ICRMS is performed at a lower pressure (10^{-6} to 10^{-7} torr) and temperature (300K) than HPMS and the ions are detected *in situ*. Ions are formed within the volume of a tetragonal cell by a pulse of electrons ($\approx$ 5 ms) and trapped for a variable reaction time by a combined external magnetic field, B_0, and static voltages ($\approx$ 1 V) applied to the trapping plates of the cell. In this static field, ions of a given mass-to-charge ratio, *m/z*, form circular trajectories in the *xy* plane with a characteristic cyclotron resonance frequency, v_c, given by

$$v_c = \frac{zB_0}{2\pi m}. \tag{3-4}$$

The ions are thermalized by allowing them to collide with background neutrals for ≈ 100 ms prior to monitoring the reaction of interest. Ion intensities are measured after a given reaction time by applying an oscillating voltage to the cell plates at the resonant frequency of a particular ion. The ions absorb power as they come into resonance, resulting in an image current on the detector plates. The amplitude of the current is a function of the number of ions. Ions of differing *m/z* can be brought into resonance by varying the applied frequency (Wolf *et al.*, 1977; Davidson *et al.*, 1977). Alternatively, in Fourier transform ICRMS, FT-ICRMS, the entire packet of trapped ions is excited by a single pulse. The resulting image current is then converted from the time domain into the frequency domain (and thus *m/z via* equation 3-4) by a Fourier transform (Marshall and Grosshans, 1991).

Equilibrium measurements with a flow-drift apparatus (described in detail in chapter 2) were first reported by Fehsenfeld and Ferguson (1973) and Bohme *et al.* (1973). As in the HPMS method, K_{eq} values are determined at relatively high pressures (≈ 1 torr). In contrast to both HPMS and ICR, K_{eq} values are calculated by determining the ratio of the forward and reverse rate constants.

The K_{eq} for toluene/ethylbenzene (3-1), diethylamine/di-*n*-propylamine (3-2), and fluorobenzene/*m*-dichlorobenzene (3-3) equilibria in the QITMS can be determined from the observed relative abundances of the equilibrated ions in a neutral mixture of known composition, *i.e.*, for

$$A^{+} + B \underset{k_f}{\overset{k_r}{\rightleftharpoons}} C^{+} + D \tag{3-5}$$

$$K_{eq} = \frac{k_f}{k_r} = \frac{[C^{+}][D]}{[A^{+}][B]}, \tag{3-6}$$

where k_f and k_r are the forward and reverse rate constants, respectively. Since the neutral reactants, B and D are present at concentrations much greater than the ionic reactants, the ratio [D]/[B] does not change as equilibrium is established and thus the attainment of equilibrium is reflected in the $[C^+]/[A^+]$ ratio.

For the hypothetical reaction

$$M + H^+ \rightarrow MH^+ \tag{3-7}$$

the gas-phase basicity is defined as the negative of the free energy change, ΔG, associated with the reaction, while the proton affinity, *PA*, is defined as the negative of the corresponding enthalpy change, ΔH (Lias *et al.*, 1984). Observed K_{eq} values for the proton transfer equilibrium

$$MH^+ + N \rightleftharpoons M + NH^+ \tag{3-8}$$

lead to relative gas-phase basicities values for the two compounds M and N from

$$-RT \ln K_{eq} = \Delta G = GB(\mathrm{N}) - GB(\mathrm{M}) = \Delta H - T\Delta S. \tag{3-9}$$

where T is the temperature and ΔS is the entropy change for the reaction. If a value for ΔS can be obtained or reliably estimated (Kebarle, 1977), ΔH for the reaction, or the relative proton affinities of the two species M and N can also be determined. Relative gas-phase basicities and *PA* values for a large number of compounds based on measured K_{eq} have been compiled (Taft, 1975; Walder and Field, 1980; Bartmess and McIver, 1979; Lias *et al.*, 1984). Absolute *PA* values are assigned based on a number of reference standards whose absolute *PA* values can be calculated from known heats of formation, ΔH_f, for both the neutral M and the MH^+ ion. Reference standards include ammonia (NH_3), ketene ($CH_2{=}C{=}O$), isobutene ($(CH_3)_2C{=}CH_2$), benzene (C_6H_6), *etc.* (Lias *et al.*, 1984). Because ΔH_f values for the reference standards may change from year to year, tabulated absolute *PA* also change from year to year and as such caution must be used in comparing *PA* values from two different sources (Lias *et al.*, 1984).

For the general charge exchange equilibrium

$$A^{+} + B \rightleftharpoons A + B^{+} \tag{3-10}$$

values for K_{eq} and ΔS can give rise to relative ionization energies, ΔH_{IP}. These ΔH_{IP} are approximately equal to the difference in the adiabatic ionization energies determined with photoelectron spectroscopy (Lias and Ausloos, 1978; Lias *et al.*, 1985).

Previous Determinations of K_{eq} on Rf Ion Traps

A limited number of K_{eq} determinations using an rf ion trap have been reported. Early studies in a QUISTOR-quadrupole combination resulted in relative proton affinities for ketene (Debrau *et al.*, 1978), methylketene (Armitage *et al.*, 1980), and 4-methyl-3-penten-2-one, 2-propyl ethanoate, and 4-hydroxy-4-methyl-2-pentanone (Kamar *et al.*, 1986) based on the observed K_{eq} for these compounds obtained with respect to an appropriate reference standard. All of these studies were performed without mass-selection of the reactant ion prior to establishing equilibrium. Brodbelt-Lustig and Cooks, (1989) have reported the first determination of the relative gas-phase basicities for a series of substituted pyridines in a QITMS based on the observed K_{eq} following mass-selected of the reagent ion. The relative gas-phase basicities were found to agree with those found with both HPMS and ICRMS methods to within ±0.8 kJ mol^{-1}.

Brodbelt-Lustig and Cooks (1989) also used the "kinetic method" (McLuckey *et al.*, 1981; McLuckey *et al.*, 1983) to determine the effective ion temperature for the proton-bound dimers of the same series of substituted pyridines. In the kinetic method, the proton-bound dimer of the two bases B_1 and B_2 is first formed and then collisionally dissociated. The relative intensities of the protonated bases B_1H^+ and B_2H^+ reflect the relative gas-phase basicities of the two compounds, and, in the absence of entropy effects, reflect the activation energy, ΔE_a, for each dissociation pathway. Using the relation

$$\ln\frac{[B_1H^+]}{[B_2H^+]} = \frac{\Delta G}{RT} = \frac{\Delta E_a}{RT} \tag{3-11}$$

an effective temperature of $T = 335$ K for the proton-bound dimers was calculated from the relative intensities of B_1H^+ and B_2H^+ and the ΔG determined from the K_{eq}.

The kinetic method has also been used to determine the relative *PA* for a series of alicyclic carboxylic acids, *o*-, *m*-, *p*-methylbenzoic acids, and to study the effect of deuterium labeling on the determination of relative *PA* in a QITMS (Nourse and Cooks, 1991).

Physiochemical Basis of the Thermometers

The physiochemical basis of the three "thermodynamic" thermometer reactions 3-1, 3-2, and 3-3 lies in the relation between ΔG and K_{eq} given in equation 3-9. "Effective" ion temperatures, T (K), for the ions stored in the QITMS for times long enough to reach equilibrium can be determined from the observed K_{eq} using tabulated values of the relative gas-phase basicities. This chapter presents the first reported ion temperatures for the ions stored in a QITMS using this method. The ion temperatures arising from these three thermometers will be presented for a variety of neutral pressures and neutral pressure ratios, both with and without He buffer gas present in the trap at the standard operating pressure of 1.0×10^{-4} torr. The three thermodynamic thermometer reactions have also been used by Bruce (1992) to determine the effective temperatures of the ions stored in a FT-ICRMS.

Experimental

All experiments were performed on a Finnigan MAT (San Jose, CA) ion trap mass spectrometer described in detail in chapter 1. The He buffer gas was cryocooled to remove excess water prior to being introduced to the ion trap chamber. The ion trap manifold was at 100°C. The toluene, ethylbenzene, fluorobenzene, and *m*-dichlorobenzene reagents were introduced into the ion trap chamber *via* Granville-Phillips (Boulder, CO) variable leak values following three freeze-pump-thaw cycles to remove dissolved gases. The diethylamine and di-*n*-propylamine reagents were introduced from a series of manometrically prepared glass bulbs of known concentration ratio. Three freeze-pump-thaw cycles were used prior to mixing the reagents.

Initial reagent ions were formed using electron ionization (EI). Typical ionization times were 0.5 to 2 ms with no He buffer present in the trap and 0.1 to 1 ms with He buffer. Protonated molecules for reactions 3-1 and 3-2 were formed in during a 30 to 50 ms reaction period following EI. Protonated toluene was formed *via* proton transfer with the mass-selected CH_5^+ ion of ionized methane (Berberich *et al.*, 1989). The methane was present in the trap at $\approx 5.5 \times 10^{-6}$ torr. Protonated diethylamine was formed *via* self-protonation (McLuckey *et al.*, 1988).

Protonated toluene (*m/z* 93) was mass-selected using a two-step isolation method (Yates and Yost, 1991). Protonated diethylamine (*m/z* 74) and the fluorobenzene molecular ions (*m/z* 96) were mass-selected using rf/dc apex isolation. The reaction time was varied from 1 to 10 s using a FORTH program (LRXNTIME in Appendix A). All equilibria were established at a q_z = 0.300 for the mass-selected ion.

The reaction products were detected by performing a mass-selected instability scan (Stafford *et al.*, 1984) with axial modulation employed during the acquisition. The ion intensities were extracted using CHROLIST, a data reduction program developed in our laboratory, normalized with a commercial spreadsheet program (QUATTRO, Borland International, Inc., Scotts Valley, CA) and plotted with a commercial graphing program (GRAPHER, Golden Software, Inc., Golden, CO).

The toluene (Eastman Kodak, Rochester, NY), *m*-dichlorobenzene (Eastman Kodak, Rochester, NY), ethylbenzene (Chem Service, West Chester, PA), diethylamine (Fischer Scientific, Fair Lawn, NJ), dipropylamine (Matheson, Coleman, and Bell, Norwood, OH), and fluorobenzene (Matheson, Coleman, and Bell, Norwood, OH) were of highest purity and used as received.

K_{eq} and Ion Temperature Determinations

K_{eq} for the proton transfer between toluene and ethylbenzene was calculated from the equilibrated ion intensities using the expression

$$K_{eq} = \frac{[C_6H_5C_2H_5+H]^+\ [C_6H_5CH_3]}{[C_6H_5CH_3+H]^+\ [C_6H_5C_2H_5]} \qquad (3\text{-}12)$$

The *m/z* 93 and 107 ions were normalized with respect to the sum of the *m/z* 91-93, 102, 105-108, 119, and 121 ions seen after a 10 s reaction time (Figure 3-1).

K_{eq} for the diethylamine/di-*n*-propylamine proton transfer reaction was determined from

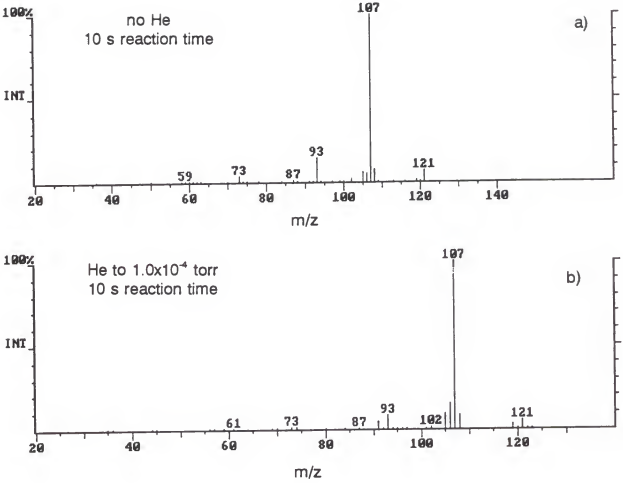

Figure 3-1: Product ions for the reaction of protonated toluene (*m/z* 93) with ethylbenzene after a 10 s reaction time. a) 1:1 toluene:ethylbenzene at 2.2×10^{-6} torr; b) He buffer added to 1.0×10^{-4} torr.

$$K_{eq} = \frac{[(C_3H_7)_2NH+H]^+ \ [(C_2H_5)_2NH]}{[(C_2H_5)_2NH+H]^+ \ [(C_3H_5)_2NH]} \qquad (3\text{-}13)$$

The *m/z* 74 ions were normalized with respect to the sum of the *m/z* 74 and 102 ions as these were the only ions seen after a 3 s reaction time (Figure 3-2). The relative concentrations of the neutral amines were determined during the preparation of the mixtures in the bulbs.

K_{eq} for the fluorobenzene/*m*-dichlorobenzene charge transfer was determined from

$$K_{eq} = \frac{[m\text{-}C_6H_4Cl_2]^+ \ [C_6H_5F]}{[C_6H_5F]^+ \ [m\text{-}C_6H_4Cl_2]} \qquad (3\text{-}14)$$

The *m/z* 96, 146, 147, and 148 ions were normalized with respect to the sum of the *m/z* 96, 97, 146-150, 170, 171, and 186 ions (Figure 3-3). An attempt had been made at mixing the fluorobenzene and *m*-dichlorobenzene reagents in glass bulbs. However, it was found that the reagents condensed on the sides of the bulbs during the course of the experiments.

The neutral concentrations for toluene, ethylbenzene, fluorobenzene, and *m*-dichlorobenzene were determined by multiplying the ion gauge readings by the appropriate correction factor. These factors were obtained by from the slope of the ion gauge calibration curves obtained with a capacitance manometer as outlined in chapter 2. The following correction factors were obtained: toluene, 0.205 ± 0.003, ethylbenzene, 0.18 ± 0.01, fluorobenzene, 0.230 ± 0.007, and *m*-dichlorobenzene, 0.175 ± 0.002. No ion gauge calibrations were needed for the diethylamine/di-*n*-propylamine equilibria. While

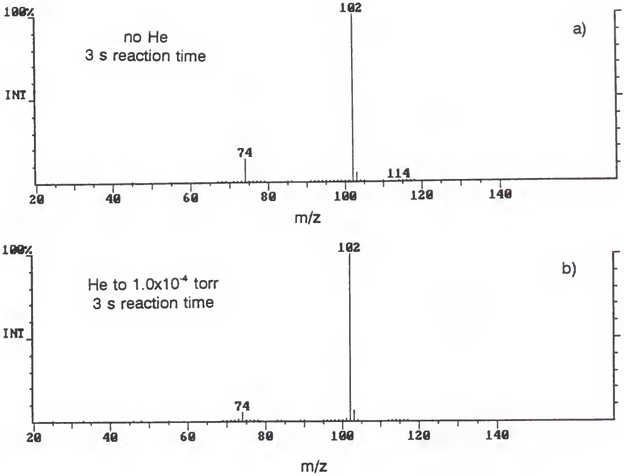

Figure 3-2: Product ions for the reaction of protonated diethylamine (*m/z* 74) with di-*n*-propylamine after a 3 s reaction time. a) 2.5:1 diethylamine:di-*n*-propylamine at 5.4x10^{-6} torr; b) He buffer gas added to 1.0x10^{-4} torr.

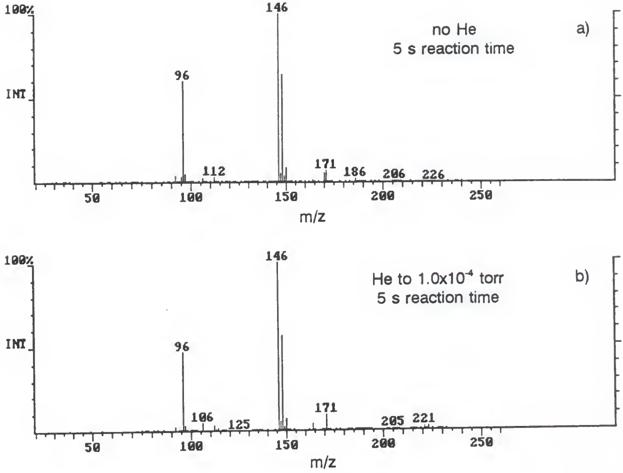

Figure 3-3: Product ions for the reaction of fluorobenzene (*m/z* 96) with *m*-dichlorobenzene after a 5 s reaction time. a) 1:1 fluorobenzene:*m*-dichlorobenzene at 7.3×10^{-7} torr; b) He buffer gas added to 1.0×10^{-4} torr.

corrected ion gauge readings were used in all the K_{eq} calculations, all pressures in this chapter are expressed as *uncorrected* ion gauge readings.

Effective ion temperatures were calculated from equation 3-9 using previously reported gas-phase basicity values. For reaction 3-1, $\Delta G = -0.9 \pm 0.5$ kcal mol^{-1} (average of the HPMS values reported by Lau and Kebarle, 1976 and the ICRMS values reported by Hehre *et al.*, 1974); reaction 3-2, $\Delta G = -1.9 \pm 0.4$ kcal mol^{-1} (average of the ICRMS values from Aue *et al.*, 1972 and Taft, 1975); and reaction 3-3, $\Delta G = -0.66 \pm 0.2$ kcal mol^{-1} (from the ICRMS values of Lias and Ausloos, 1978).

Calculation of Experimental Error

Errors in the ion temperatures are expressed as the 95% confidence limits, $\lambda_{95,T}$ using (Williams, 1990)

$$\lambda_{T,95} = \sqrt{\left[\frac{-1}{R \ln K_{eq}}\right]^2 \lambda_{\Delta G}^2 + \left[\frac{\Delta G}{R (\ln K_{eq})^2 K_{eq}}\right]^2 \lambda_{K_{eq}}^2} \qquad (3\text{-}15)$$

where $\lambda_{K_{eq}}$ are the 95% confidence limits of K_{eq} calculated from replicate determinations (Shoemaker *et al.*, 1981) and $\lambda_{\Delta G}$ are the uncertainties in these values reported by the respective authors.

Results

Proton Transfer Equilibrium between Toluene and Ethylbenzene

Ion intensity versus reaction time plots for the toluene/ethylbenzene proton transfer equilibrium are presented in Figures 3-4a and b. In Figure 3-4a, the protonated

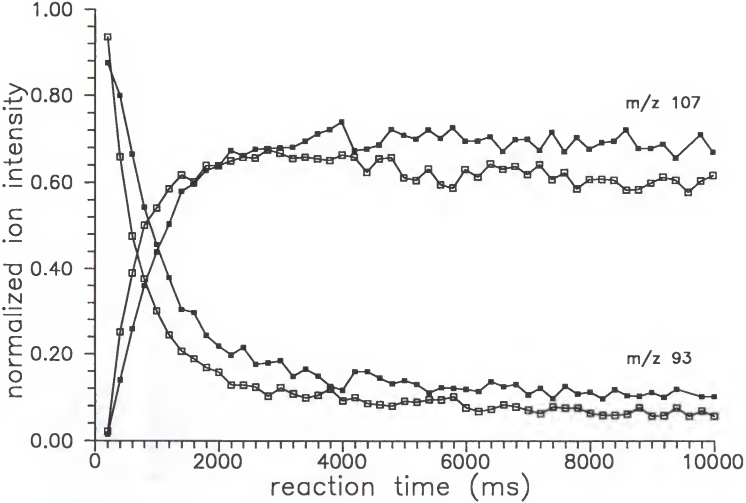

Figure 3-4: Ion intensity versus reaction time for $[C_6H_5CH_3]H^+ + [C_6H_5C_2H_5] \rightarrow C_6H_5CH_3 + [C_6H_5C_2H_5]H^+$ a) with only the *m/z* 107 ions plotted. (■) 1:1 toluene:ethylbenzene at 2.2×10^{-6} torr; CH_4 present at $\approx 6.0 \times 10^{-6}$ torr; (□) He buffer gas added to 1.0×10^{-4} torr.

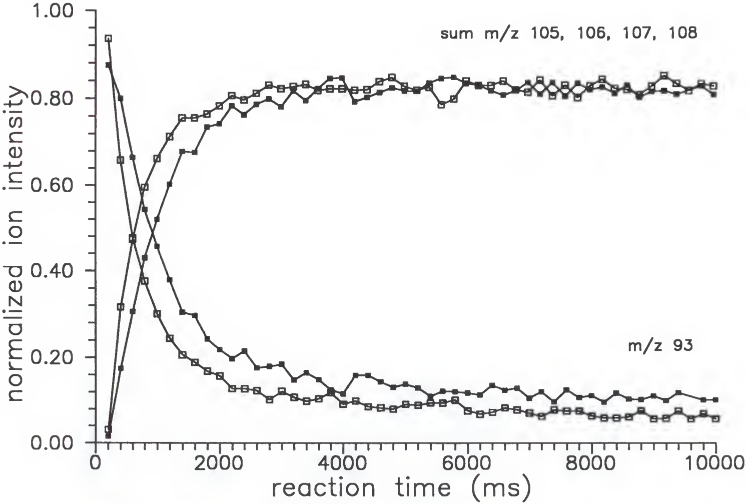

Figure 3-4: (continued) Ion intensity versus reaction time for $[C_6H_5CH_3]H^+ + [C_6H_5C_2H_5] \rightleftharpoons C_6H_5CH_3 + [C_6H_5C_2H_5]H^+$ b) with the sum of the *m/z* 105, 106, 107, and 108 ions plotted. (■) 1:1 toluene:ethylbenzene at 2.2×10^{-6} torr; CH_4 present at ≈ 6.0×10^{-6} torr; (□) He buffer gas added to 1.0×10^{-4} torr.

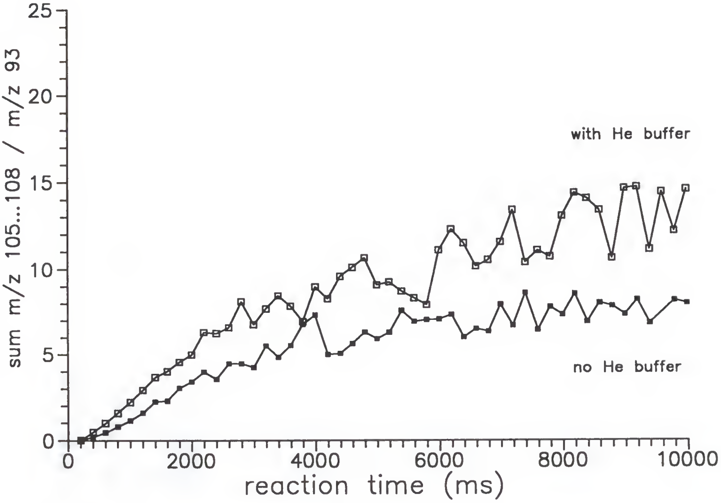

Figure 3-4: (continued) c) Ratio of the sum of the *m/z* 105, 106, 107, and 108 ions to the *m/z* 93 ions for $[C_6H_5CH_3]H^+$ + $[C_6H_5C_2H_5]$ $\rightleftharpoons$ $C_6H_5CH_3$ + $[C_6H_5C_2H_5]H^+$. (■) 1:1 toluene:ethylbenzene at 2.2×10^{-6} torr; CH_4 present at ≈ 6.0×10^{-8} torr; (□) He buffer gas added to 1.0×10^{-4} torr.

molecular ion of ethylbenzene (*m/z* 107) is seen to decrease in intensity at reaction times greater than 4 s when He buffer is present in the trap. Figure 3-4b presents the same data with the sum of the *m/z* 105 to 108 ion intensities plotted as opposed to just the *m/z* 107 ion. It is assumed that the *m/z* 105, 106, and 108 ions (Figure 3-1) arise either from secondary reactions of the *m/z* 107 ion or from space charge over these long reaction times leading to an error in centroiding similar to that seen with the O_2^+ ions in He in chapter 2 (Figure 2-8b). Therefore, all ion temperatures measured from equilibrium 3-1 were calculated using the sum of the *m/z* 105 to 108 ions both with and without He buffer.

The ratios of the sum of the *m/z* 105 to 108 ions to the *m/z* 93 ions both with and without He buffer were plotted (Figure 3-4c) to ensure that the system had reached equilibrium. It can be seen that by ≈ 8 s the equilibria have reached a steady state.

The He buffered *m/z* 93 and 107 ions reach a 1:1 ratio in 0.6 s versus the 1 s required by the unbuffered ions. This indicates that equilibrium is established at a faster rate with the He buffer present in the trap. Both the unbuffered and buffered *m/z* 105 to 108 ions attributed to protonated ethylbenzene ions are found to reach a relative intensity of ≈ 0.85 at equilibrium. At equilibrium, the He buffered *m/z* 93 ions are of lower relative intensity (≈ 0.06) than the unbuffered ions (≈ 0.12).

The K_{eq} and effective ion temperatures arising from equilibrium 3-1 are presented in Table 3-1. While the ion temperatures are found to be below thermal both with (160±90) and without He buffer (190±110), a quantitative cooling, $\Delta T = 33 \pm 3$ K is measured when He is present in the trap at the standard operating pressure of 1.0×10^{-4} torr.

Table 3-1: K_{eq} and ion temperatures from the proton transfer equilibrium between toluene and ethylbenzene.

toluene (/10^{-6} torr)	ethylbenzene (/10^{-6} torr)	total pressure (/10^{-6} torr)	He (/10^{-4} torr)	K_{eq}	T (K)	ΔT (K)
1.2	1.0	2.2	none	9	211	35
				12	186	32
				11	186	32
				11	186	32
			average	11 ± 2	190 ± 110	33 ± 2
1.2	1.0	2.2	1.0	13	176	
				19	154	
				19	154	
				19	154	
			average	18 ± 5	160 ± 90	

All K_{eq} obtained with a 10 s reaction time; CH_4 present at ≈ 6.0×10^{-6} torr (uncorrected ion gauge reading).
Errors in average K_{eq} and ΔT calculated as 95% confidence limits of replicate determinations (Shoemaker *et al.*, 1981); error in average T calculated using average K_{eq} and $\Delta GB = -0.9 \pm 0.5$ kcal mol^{-1} (average from Lau and Kebarle, 1976 and Hehre *et al.*, 1974) in equation 3-15 (Williams, 1990).

Proton Transfer Equilibrium between Diethylamine and di-*n*-Propylamine

Typical ion intensity versus reaction time plots for the diethylamine/di-*n*-propylamine proton transfer equilibrium are presented in Figures 3-5a and b. The plots illustrate changes in the equilibrium ion intensities with changes in the relative concentrations and total pressures of diethylamine and di-*n*-propylamine. In both cases, the *m/z* 102 and 74 ions reach a 1:1 ratio in less time when He buffer is present in trap. A more pronounced change in relative intensities of the equilibrated ions resulting in a larger K_{eq} is seen upon addition of He buffer gas.

The K_{eq} and effective ion temperatures arising from reaction 3-2 are presented in Table 3-2. With this thermometer, the ions are found to be approximately thermal with no He buffer (390 ± 100) and below thermal with He buffer (285 ± 75). A quantitative cooling, $\Delta T = 100 \pm 10$ K, is again seen with He buffer; however, it is a factor of ≈ 3 greater than that found with the toluene/ethylbenzene proton transfer thermometer.

Charge Transfer between Fluorobenzene and *m*-Dichlorobenzene

Typical ion intensity versus reaction time plots for the fluorobenzene/*m*-dichlorobenzene charge transfer equilibrium are presented in Figures 3-6a and b. The plots illustrate the changes in the equilibrium ion intensities with changes in the total pressure of fluorobenzene and *m*-dichlorobenzene. The K_{eq} were determined from the sum of the isotopic *m/z* 146, 147, and 148 peaks arising from *m*-dichlorobenzene. Once again, the fluorobenzene and *m*-dichlorobenzene molecular ions reach a 1:1 ratio in less time with He buffer; a shift towards a larger K_{eq} is seen when He buffer is present in the trap.

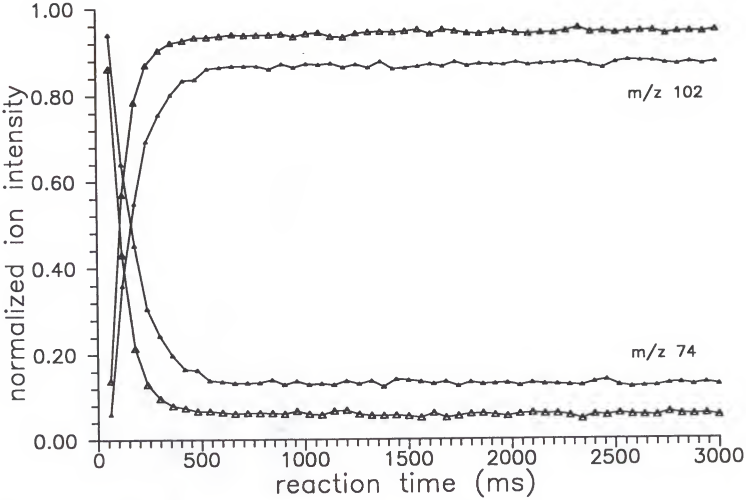

Figure 3-5: Ion intensity versus reaction time for $[(n\text{-}C_2H_5)_2NH]H^+ + (n\text{-}C_3H_7)_2NH \rightleftharpoons (n\text{-}C_2H_5)_2NH + [(n\text{-}C_3H_7)_2NH]H^+$. a) (▲) 2.5:1 diethylamine:di-*n*-propylamine at $5.4\text{x}10^{-6}$ torr; (△) He buffer gas added to $1.0\text{x}10^{-4}$ torr.

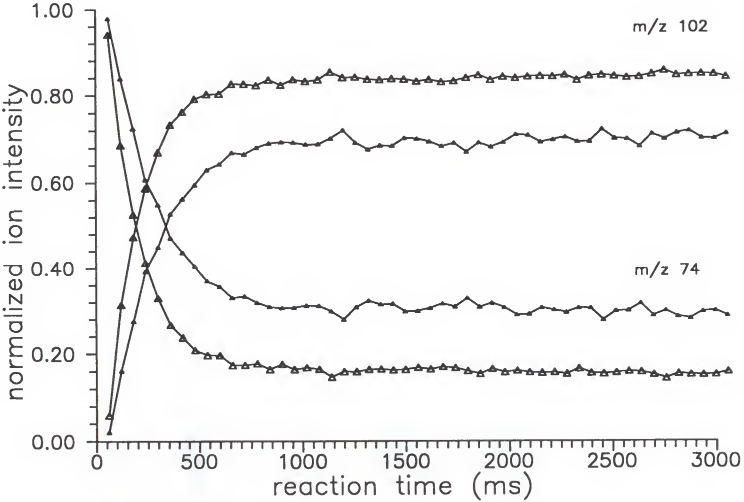

Figure 3-5: (continued) Ion intensity versus reaction time for $[(n\text{-}C_2H_5)_2NH]H^+ + (n\text{-}C_3H_7)_2NH \rightleftharpoons (n\text{-}C_2H_5)_2NH + [(n\text{-}C_3H_7)_2NH]H^+$. b) (▲) 4.15:1 diethylamine:di-*n*-propylamine at 2.7×10^{-6} torr; (△) He buffer gas added to 1.0×10^{-4} torr.

Table 3-2: K_{eq} and ion temperatures from the proton transfer equilibrium between diethylamine and di-*n*-propylamine.

	pressure	no He buffer		He buffer		
diethyl:di-*n*-propyl	(/10^{-6} torr)	K_{eq}	T (K)	K_{eq}	T (K)	ΔT (K)
2.51:1	2.5	13	368	29	284	84
2.51:1	5.4	17	336	39	260	76
3.08:1	2.7	15	357	33	274	83
3.08:1	5.0	13	368	31	279	89
4.15:1	2.65	10	412	22	310	102
		11	395	26	292	103
		11	404	--	--	--
4.15:1	4.9	10	422	24	300	122
5.07:1	2.85	13	373	30	282	91
		13	372	29	284	88
5.07:1	4.5	12	387	27	289	98
5.07:1	5.1	10	424	27	291	133
		10	410	--	--	--
		12	388	--	--	--
	average	12 ± 1	390 ± 100	29 ± 3	285 ± 75	100 ± 10

All K_{eq} calculated with a 3 s reaction time; He buffer added to 1.0×10^{-4} torr (uncorrected ion gauge reading).
Errors in average K_{eq} and ΔT calculated as 95% confidence limits over all determinations (Shoemaker *et al.*, 1981); error in average T calculated using average K_{eq} and $\Delta GB = -1.9 \pm 0.4$ kcal mol^{-1} (average from Aue *et al.*, 1972 and Taft, 1975) in equation 3-15 (Williams, 1990).

The K_{eq} and effective ion temperatures arising from equilibrium 3-3 are presented in Table 3-3. With this thermometer, the ions are below thermal (265 ± 80 K) without He and have a temperature of 210 ± 65 K with He buffer. A quantitative cooling effect, $\Delta T = 52 \pm 5$ K, is measured with this thermometer.

Discussion

The diethylamine/di-*n*-propylamine thermometer gives rise to ion temperatures which are approximately thermal without He buffer and which are ≈ 90 K below thermal with He buffer. The toluene/ethylbenzene and fluorobenzene/*m*-dichlorobenzene thermometers result in subthermal temperatures within the 95% confidence limits both with and without He buffer. Each of the three thermodynamic thermometers shows a shift in the position of the equilibrium towards higher K_{eq} values when He buffer is present in the trap; i.e an average cooling, $\Delta T = 60 \pm 10$ K, is found due to the He buffer. Moreover, each of the three reactions comes to equilibrium at a faster rate with He buffer in the trap perhaps due to collisional focussing of the ions towards the center of the trap. These observations are in contrast to the results of Brodbelt-Lustig and Cooks (1989) who report that regardless of the He pressure (the pressure range was not specified) the equilibrium attained and the rate of attainment remained constant within experimental limits.

The subthermal temperatures may be arising from 1) irreversible secondary reactions which deplete the ion populations thus leading to error in K_{eq}; and 2) errors in T due to uncertainties in the literature values for the relative gas-phase basicities for the amines and toluene/ethylbenzene and the relative free energy for the fluorobenzene/*m*-dichlorobenzene charge exchange.

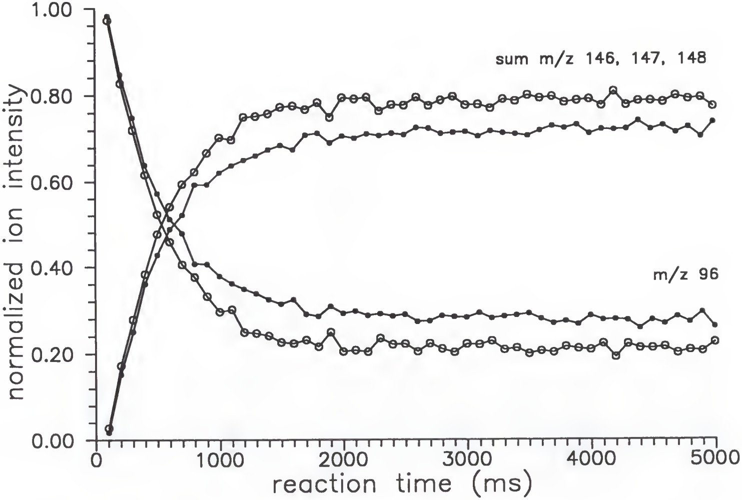

Figure 3-6: Ion intensity versus reaction time for $C_6H_5F^+$ + m-$C_6H_4(Cl)_2$ $\rightleftharpoons$ C_6H_5F + m-$C_6H_4(Cl)_2^+$. a) (●) 1:1 fluorobenzene:*m*-dichlorobenzene at 7.3×10^{-7} torr; (o) He buffer gas added to 1.0×10^{-4} torr.

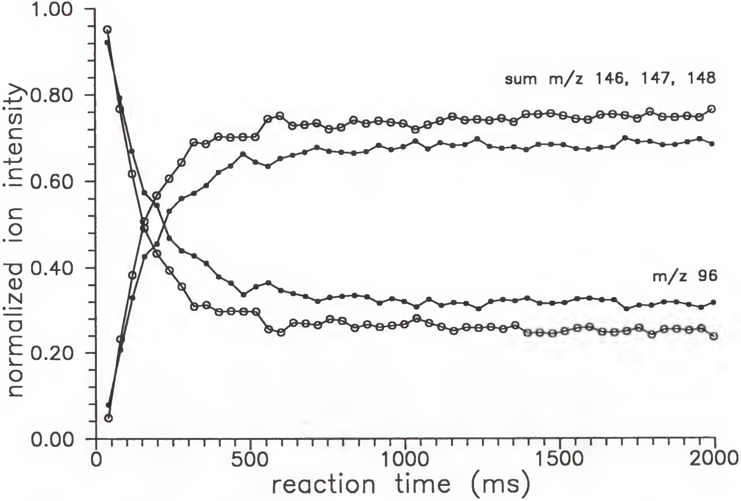

Figure 3-6: (continued) Ion intensity versus reaction time for $C_6H_5F^+ + m\text{-}C_6H_4(Cl)_2 \rightarrow C_6H_5F + m\text{-}C_6H_4(Cl)_2^+$. b) (●) 1:1 fluorobenzene:*m*-dichlorobenzene at 2.8×10^{-6} torr; (○) He buffer gas added to 1.0×10^{-4} torr.

Table 3-3: K_{eq} and ion temperatures from the charge transfer equilibrium between fluorobenzene and *m*-dichlorobenzene.

fluorobenzene	*m*-dichlorobenzene	total pressure	no He buffer		He buffer		
($/10^{-7}$ torr)	($/10^{-7}$ torr)	($/10^{-7}$ torr)	K_{eq}	T (K)	K_{eq}	T (K)	ΔT (K)
3.2	3.25	5.9	3.3	278	4.3	228	50
3.7	3.7	7.1	3.3	276	4.6	219	57
			3.5	267	4.7	216	51
			3.5	267	5.2	201	66
15	13	28	3.3	277	4.5	220	57
			3.6	257	5.1	203	54
			3.5	266	5.1	204	62
			3.3	277	--	--	--
28	20	50	3.7	252	5.1	204	48
30	29	60	3.6	258	4.5	221	37
			3.8	249	5.0	207	42
			3.9	245	--	--	--
		average	3.5 ± 0.1	265 ± 80	4.8 ± 0.2	210 ± 65	52 ± 5

Average reaction time = 2.8 s. He buffer added to 1.0×10^{-4} torr (uncorrected ion gauge reading).
Errors in average K_{eq} and ΔT calculated as 95% confidence limits over all determinations (Shoemaker *et al.*, 1981); error in average T calculated using average K_{eq} and $\Delta G = -0.7 \pm 0.2$ kcal mol^{-1} (Lias and Ausloos, 1978) in equation 3-15 (Williams, 1990).

The *m/z* 121 ions in Figures 3-1a and b indicate that side reactions did occur during the 10 s required to establish the toluene/ethylbenzene equilibrium. Since no ions of *m/z* greater than 140 were seen, the *m/z* 121 ion likely arises from either the addition of a C_2H_4 moiety to *m/z* 93 or the addition of a CH_2 moiety to *m/z* 107. Significant loss of the *m/z* 93 or 107 ions due to proton transfer to CH_4 can be neglected since $PA(CH_4) = 130.5$ kcal mol^{-1} $< PA\ (C_6H_5CH_3) = 191.2$ kcal mol^{-1} $< PA\ (C_6H_5C_2H_5) = 192.2$ kcal mol^{-1} (Harrison, 1983). Secondary reactions were also witnessed in the 3 to 5 s required for the fluorobenzene/*m*-dichlorobenzene thermometer to reach equilibrium (Figure 3-3a and b). The *m/z* 171 ions may be arising from a short-lived fluorobenzene-*m*-dichlorobenzene dimer which decomposes by loss of HCl to form *m/z* 206 and a subsequent loss of Cl to form *m/z* 171. The *m/z* 106 ion in Figure 3-3b is likely due to charge transfer to trace contaminations of ethylbenzene. However, because the *m/z* 106, 121, 170, and 171 ions are < 5% relative intensity, these reactions are not considered to have depleted the ion populations to an appreciable extent. The diethylamine/di-*n*-propylamine thermometer did not suffer from any secondary reactions over the 3 s required to reach equilibrium (Figure 3-2a and b).

The greatest source of error in the ion temperatures can be attributed to the range of literature values for the relative gas-phase basicities. Reported differences in the gas-phase basicities for toluene and ethylbenzene range from 0.4 ± 1 kcal mol^{-1} (Bartmess and McIver, 1979) resulting in ion temperatures of 85 ± 8 K without He buffer and 70 ± 8 K with He buffer, to 1.8 ± 0.3 kcal mol^{-1} (Lias *et al.*, 1984), resulting in temperatures of 385 ± 40 K with no He and 320 ± 35 K with He. $\Delta G = -0.9 \pm 0.5$ kcalmol^{-1} was used in the present study. This is the average of the ΔG obtained from the HPMS studies of Lau and Kebarle (1976) and the ICRMS study of Hehre *et al.* (1974). This value was chosen as in both the HPMS and ICRMS reports, the gas-phase basicity of both toluene and ethylbenzene were determined under the same experimental conditions relative to the same reference standards. The gas-phase basicities values reported by Bartmess and McIver (1979) and Lias *et al.*, (1984) are averages obtained over a range of experimental methods and reference standards. There is less variation in the range of reported values for the relative gas-phase basicities of diethylamine and di-*n*-propylamine. The relative gas-phase basicities range from 1.8 ± 0.2 kcal mol^{-1} (Aue *et al.*, 1972) to 2.0 kcal mol^{-1} (Taft, 1975). An average of 1.9 ± 0.4 Kcal mol^{-1} was thus used in the present study. Relative free energy changes for the fluorobenzene/*m*-dichlorobenzene reaction determined under the same experimental conditions (ICRMS) have been reported by Lias and Ausloos (1978); no alternative ΔG values are available. However, differences in the spectroscopically determined ionization potentials, $\Delta IP = \Delta H$, of fluorobenzene ($IP = 9.200 \pm 0.005$) and *m*-dichlorobenzene ($IP = 9.11 \pm 0.01$ eV) can be used to calculate an effective ion temperature if it is assumed that $\Delta S = 0$. Effective temperatures from this approach are ≈ 825 K without He buffer and ≈ 670 K with He buffer. These temperatures are a factor of three higher than those obtained with the other two thermometers and with the ΔG values of Lias and Ausloos (1978) indicating that the entropy factor may not be negligible.

Conclusions

The thermodynamic thermometer reactions give average ion temperatures of 280 ± 170 K with no He buffer and 220 ± 145 K with He buffer present in the trap at the standard operating pressure of 1.0x10^{-4} torr. The magnitude of the uncertainties and the resulting subthermal temperatures are attributed principally to the uncertainties in the literature values for the relative gas-phase basicities and relative free energy values. The 220 ± 145 K temperature in the presence of He agrees within experimental error with the effective temperature of 335 K reported by Brodbelt-Lustig and Cooks (1989). Since the temperature of Brodbelt-Lustig and Cooks (1989) is also subthermal (the experiments were preformed at 373 K), this suggests that ion temperature measures based on known thermodynamic quantities may consistently lead to lower overall values.

The temperature obtained with He is a factor of $\approx$ 10 lower than the 2500 K obtained for He buffered Ar^+ ions at a $q_z(Ar^+) = 0.295$ presented in chapter 2. These lower effective temperatures are not surprising given the larger number of internal degrees of freedom of the amines and substituted benzenes and the longer storage times employed in the thermodynamic thermometer studies (seconds versus hundreds of milliseconds). The thermodynamic thermometers do, however, show a shift in the position of the equilibrium upon addition of He buffer and as such "measure" an effective cooling $\Delta T = 60 \pm 10$ K when He buffer is present in the trap. This indicates that even at long storage times, the rf field is effectively heating the ions. One would thus expect to obtain ion temperatures which are somewhat above thermal without He and which are near thermal with He buffer, *i.e.* the thermodynamic thermometers are reading consistently lower temperatures.

Utility of Thermodynamic Thermometer Reactions

The thermodynamic thermometers presented in this chapter provide effective ion temperatures for ions trapped for 1 to 10 s storage time. The measured temperatures reflect the overall combined internal and kinetic components of the ion energy. The accuracy of the thermometers are a function of the accuracy of the K_{eq} values which can be evaluated in terms of the three criteria necessary for measuring gas-phase ion-molecule equilibria presented by Kebarle (1977). 1) *The reactants and products must be in thermal equilibrium with the buffer gas or walls of the reaction volume*. This condition is easily met by the reactant neutrals given their large excess concentrations. However, in the QITMS, as in the ICRMS (Bruce and Eyler, 1992), the ions may be nonthermal due to energy imparted to them by the trapping field. The ions must therefore be allowed to undergo a sufficient number of collisions so that the heating effects of the rf field are balanced by collisional cooling with the neutrals. In the present analysis, equilibrium was established within 2 to 10 s. The cooling effect measured by the thermodynamic thermometers upon addition of He buffer indicates that the total number of collisions does play an important role in establishing equilibrium. The ions may also gain excess energy due to the exothermicity of the reaction by which the ions are produced. For this reason, reactions with relatively small changes in free energy were chosen as the thermometer reactions. 2) *Equilibrium of the ion-molecule pairs must be appreciably faster than other processes affecting the concentrations of the ions*. Secondary reactions were noted for both the toluene/ethylbenzene and the fluorobenzene/*m*-dichlorobenzene thermometers, although the relative intensities of the product ions indicate that they likely do not result in any significant change in the equilibria. And finally, 3) *sufficient time must be given to reach equilibrium*. The ITMS™ software allows the storage of ions for tens of seconds in order to reach equilibrium. However, as noted with the toluene/ethylbenzene thermometer, changes in the relative neutral pressures can be of concern over the time periods necessary to acquire the data. While the equilibrium studies presented here were acquired at equal time intervals over the time required to reach equilibrium, it is possible to construct scan functions which acquire data at smaller initial time intervals and then at larger intervals once equilibrium is established. This would substantially reduce the time required to acquire the data and thus reduce the probability of pressure fluctuations. However, the largest source of errors in calculating ion temperatures from K_{eq} determinations, lies in the range of possible literature values for the relative gas-phase basicities and relative free energies.

CHAPTER 4
QET BREAKDOWN GRAPHS AS INTERNAL ENERGY THERMOMETERS

Introduction

This chapter will present the time-resolved collision-induced dissociation (CID) breakdown graphs for a series of small organic molecules obtained on a quadrupole ion trap mass spectrometer, QITMS. These breakdown graphs will be compared with those predicted from the quasi-equilibrium theory, QET, of mass spectra, a statistical theory which allows calculation of breakdown graphs following electron ionization (Rosenstock *et al.*, 1952). The molecules of interest include acetone (CH_3COCH_3), 2-pentanone ($CH_3COC_3H_7$), propane (C_3H_8), toluene ($C_6H_5CH_3$), and benzene (C_6H_6).

Collision-induced Dissociation

Collision-induced dissociation of polyatomic species was first described by Jennings (1968) and by Haddon and McLafferty (1968). In this method, ions of a given mass-to-charge ratio, *m/z*, which would otherwise be detected intact are mass-selected and induced to fragment by collision with an inert target gas. Analysis of the fragment ions of a specific precursor ion (also referred to as the parent ion) results in the collision-induced dissociation (CID) spectrum of the ion, also known as the collisionally activated dissociation (CAD) spectrum. The sequential selection and activation of a precursor ion followed by mass-analysis of the product ions is referred to as tandem mass spectrometry or MS/MS.

Two regimes of CID can be identified based on the kinetic energy of the precursor ion just prior to collision. High-energy CID involves ion-target collisions with ion kinetic energies greater than 1 keV and is usually performed on double and multiple sector mass spectrometers. Details of the instrumentation, mechanisms, efficiencies, and applications of high-energy CID have been presented in detail elsewhere (McLafferty *et al.*, 1973; Kim and McLafferty, 1978; Cooks, 1978; Laramée *et al.*, 1980; Levsen and Schwarz, 1983; McLafferty, 1983). The present discussion will focus on low-energy CID involving ion kinetic energies on the order of 5-100 eV. Low-energy CID can be performed on triple quadrupole mass spectrometers, TQMS (Yost and Enke, 1978 and 1979; Yost *et al.*, 1979), Fourier transform ion cyclotron resonance mass spectrometers, FT-ICRMS (Cody *et al.*, 1982; Cody and Freiser, 1982) and, more recently, on QITMS instruments (Weber-Grabau *et al.*, 1987; Louris *et al.*, 1987, 1990; McLuckey *et al.*, 1991a). Hybrid sector-quadrupole mass spectrometers are capable of accessing both high and low-energy CID (Harrison *et al.*, 1986).

Selected-ion fragmentation *via* low-energy CID on a TQMS was first demonstrated by Yost and Enke (1978). In a TQMS, the ion of interest is mass-selected by the first quadrupole, Q_1, and then undergoes CID in a second rf-only quadrupole, Q_2. The resulting fragment ions are then mass-analyzed with the third quadrupole mass filter, Q_3. The fragment ion yields are a function of the internal energy distribution of the activated ion, which in turn is a function of the initial ion kinetic energy and both the nature (He, N_2, Ar, *etc.*) and pressure of the target gas (Dawson *et al.*, 1982a,b). CID efficiencies obtained on a TQMS range from 15% to 65% due to the multiple-collision conditions (*e.g.* 10 collisions occur with Ar at 1.2×10^{-3} torr) and the high focussing and thus high collection efficiencies of the quadrupoles (Yost and Enke, 1978, 1979; Yost *et al.*, 1979).

These can be compared to the < 10% efficiencies typically achieved under the single-collision conditions used in high-energy CID analyses on sector instruments (Kondrat and Cooks, 1978).

CID in an FT-ICRMS is performed by applying a short (≈ 100 μs) rf pulse to the excite plates at the cyclotron frequency of the precursor ion of interest. (See chapter 3 for a more detailed description of FT-ICRMS). The kinetic energy of an ion in resonance with the rf frequency is increased, leading to increasingly energetic collisions with the target gas. The resulting fragment ions are then detected using the standard Fourier transform procedure (Cody *et al.*, 1982; Cody and Freiser, 1982). The collision energy can be varied by changing the amplitude or duration of the rf pulse. CID in an FT-ICRMS differs from that in a TQMS in that tandem instrumentation is not required *i.e.* the MS/MS experiment is tandem-in-time as opposed to tandem-in-space.

Data obtained from both high and low-energy CID are most conveniently expressed in terms of a breakdown graph. A breakdown graph is a plot of the relative intensities of the precursor and fragment ions as a function of the internal energy of the molecular ion undergoing fragmentation. Such breakdown graphs provide detailed information about the fragmentation reactions occurring and the relative rate of these reactions as a function of internal energy. In a TQMS, ion intensity is plotted against the kinetic energy of the precursor ion, E_{lab}, determined by the dc offset applied to Q_2. Alternatively, E_{lab} can be converted to the center-of-mass frame, E_{cm}, *via*

$$E_{cm} = E_{lab}\frac{m_g}{m_p + m_g} \tag{4-1}$$

where m_p and m_g are masses (amu) of the precursor ion and the target gas, respectively. In FT-ICRMS, CID breakdown graphs are constructed by plotting ion intensity versus the amplitude of the resonant rf pulse.

Collision-induced Dissociation in the QITMS

Details of the CID experiment on the QITMS are presented in chapter 1. Briefly, the precursor ion is first rf/dc isolated; a supplemental rf potential is then applied to the end-cap electrodes at the fundamental frequency of the ion in the z-direction, ω_z. Once in resonance, the kinetic energy of the ion increases, resulting in more energetic collisions with the He buffer and any other neutral gas species present in the trap. If the resulting product ions have q_z values within the stability region (Figure 1-3), they will be trapped and subsequently detected. The energy of the CID process can be varied by changing either the amplitude or the duration of the resonant excitation potential, the q_z of the precursor ion, or the pressure or nature of the buffer gas (Gronowska *et al.*, 1990; Johnson *et al.*, 1991a). A buffer gas is essential to the CID experiment as it not only acts as the principal target gas (He is usually present in a 100-fold excess of the sample) but it also dampens the trajectories of the accelerated ions thus preventing excessive trapping losses (Wu and Brodbelt, 1991). Multiple stages of mass spectrometry, MS^n, can be performed by repeating the ion isolation/activation sequence (Brodbelt-Lustig and Cooks, 1988; McLuckey *et al.*, 1991a; Nourse *et al.*, 1992).

In any given CID analysis on the QITMS, the resonant excitation potential is typically applied for 2 to 20 ms, although excitation times as long as 100 ms have been employed (Brodbelt-Lustig *et al.*, 1988; Nourse *et al.*, 1992). This can be compared to the 10 to 50 μs residence times of the ions in the center quadrupole of a TQMS and the

100 μs excitation time employed in conventional ICRMS. Because the precursor ion is resonantly excited *between* collisions, CID in the QITMS involves step-wise collisional activation coupled with collisional damping with the He buffer gas. This differs from CID on either a sector or a TQMS in which the ions are accelerated up to a certain collision energy, E. If the first collision does not lead to dissociation then, at high enough pressures, subsequent collisions may occur. However, these secondary collisions will have less than the initial kinetic energy and as such are less likely to lead to dissociation. Even in conventional CID in an ICRMS, given the lower pressures and the subsequently longer times between collisions, the precursor ions are typically accelerated to their final kinetic energy before the first collision. A further difference between CID in the ITMS™ and those in sector and TQMS methods is that the fragment ions are not in resonance with the applied excitation potential and as such do not undergo subsequent CID. This is in contrast to CID in a sector or TQMS where the fragment ions can experience activating collisions with the target gas and can thus undergo further fragmentation.

Two types of CID breakdown graphs can be constructed on the QITMS, 1) time-resolved breakdown graphs, plots of the ion intensities versus the duration of the resonant excitation potential; and 2) voltage-resolved breakdown graphs, plots of the ion intensities versus the amplitude of the resonant excitation potential. The amount of energy available to the resonant ion at any point on either a time-resolved or voltage-resolved breakdown graph is measured by the fluence *i.e.* the product of the excitation amplitude (V) and the excitation time (ms) (March *et al.*, 1989). This chapter will present the time-resolved breakdown graphs of the molecular ions, M^+, of acetone, 2-pentanone, propane, toluene, and benzene. Both the time-resolved and voltage-resolved breakdown graphs of the molecular ions of the *n*-alkylbenzenes will be presented in chapter 5.

Quasi-equilibrium Theory

The quasi-equilibrium theory (QET) of mass spectra is a statistical approach to depicting the unimolecular gas-phase processes which give rise to an observed electron ionization, EI, mass spectrum. QET was first developed by Rosenstock *et al.* in 1952. Improvements to the original approach and calculated mass spectra for a number of small molecules have been presented by Vestal and coworkers (Vestal *et al.*, 1962; Vestal, 1965; Vestal and Lerner, 1967). Several reviews of the QET of mass spectra have also been presented (Rosenstock and Krauss, 1963; Wahrhaftig, 1965; Vestal, 1968; Harrison and Tsang, 1972).

The QET of mass spectra is based on the following fundamental postulates: 1) The ionization of a polyatomic molecule by electron impact is considered to occur by a vertical Franck-Condon process. 2) Following ionization the excess energy is randomly distributed among the vibrational states of the ground electronic state *via* radiationless internal conversions. 3) The time for ionization and energy redistribution is small compared to that for dissociation. 4) The molecular ion fragments when sufficient energy has accumulated in one of the vibrational modes. 5) Rearrangement of the molecular ion or any fragment ion can occur at any time following ionization. Thus, the reactions which give rise to the observed peaks in the EI mass spectrum are considered to be a series of competing and consecutive unimolecular fragmentation reactions. 6) The rate constant for each of the fragmentation reactions can be calculated by statistical means using absolute rate theory (Glasstone *et al.*, 1941). According to absolute rate theory, the molecular ion is treated as an isolated system with internal energy *E*. The internal energy is partitioned among the internal degrees of freedom of the molecular ion. Some of these partitions lead to activated complexes for a given fragmentation reaction. The rate of this fragmentation reaction is then considered to be a function of the concentration of activated complexes and the rate at which these complexes pass over the barrier to products. The concentrations of the activated complexes are calculated assuming an equilibrium is established between the activated complexes and the reactants (the so-called quasi-equilibrium assumption).

A general expression for the rate of a unimolecular fragmentation as a function of internal energy, $k(E)$, is given by (Vestal, 1965)

$$k(E) = \frac{S}{h} \int_{0}^{E-\epsilon_0} \frac{\rho^{\ddagger}(E, \epsilon_0, \epsilon_t) d\epsilon_t}{\rho(E)} \tag{4-2}$$

where S is the number of equivalent reaction paths leading to the same product; h is Planck's constant; $\rho(E)dE$ is the number of states of the ion with energies between E and $E+dE$, $\rho^{\ddagger}(E, \epsilon_0, \epsilon_t)d\epsilon_t$ is the number of states of the ion of the activated complex configuration with activation energy ϵ_0 and translational energy between ϵ_t and $\epsilon_t+d\epsilon_t$. Calculation of $K(E)$ relies on a knowledge of the activation energy, ϵ_0, for each of the pathways as well as values for the vibrational frequencies of both the ion and the activated complex. Once the $K(E)$ has been determined for each possible fragmentation pathway, a breakdown graph can be constructed by calculating the relative abundances of the ions as a function of E using integrated rate equations for competing and consecutive unimolecular reactions. A breakdown graph for the molecular ion of propane calculated by Vestal and Lerner (1967) is presented in Figure 4-1. The mass spectrum of a molecule can then be obtained by summing the calculated ion abundances over an assumed internal energy distribution, $P(E)$.

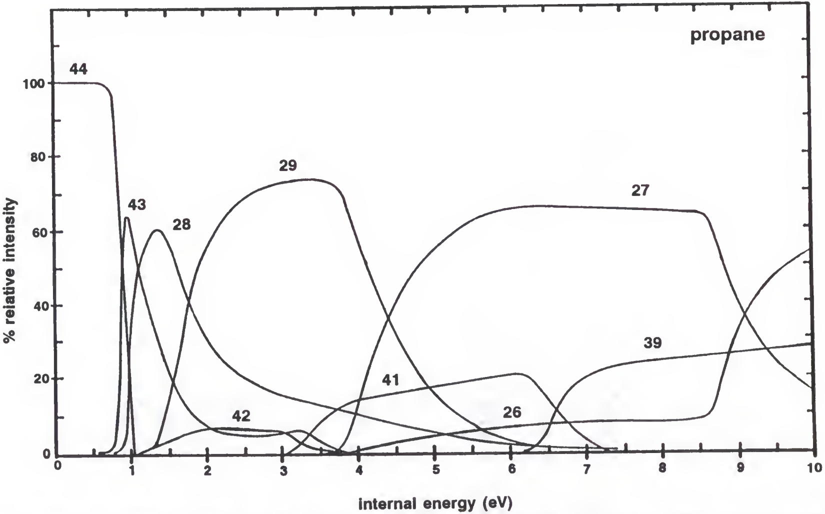

Figure 4-1: Breakdown graph for the M^+ ion of propane (*m/z* 44) calculated from quasi-equilibrium theory; time after ionization = 1×10^{-6} s (Vestal and Lerner, 1967).

Calculation of breakdown graphs and mass spectra using QET requires knowledge of 1) all the possible unimolecular fragmentation pathways; 2) the activation energies for each possible pathway; 3) the vibrational frequencies of both the ion and the activated complex; and 4) the internal energy distribution of the ions following EI. While many of these variables are available from experimental data, some of the parameters (notably the vibrational frequencies of the activated complexes) are a matter of intelligent guesswork (Harrison and Tsang, 1972). Despite the number of assumptions that must often be made, generally good agreement has been found between theoretical and experimental mass spectra for a number of small organic molecules (Vestal, 1965; Harrison and Tsang, 1972).

CID versus QET Breakdown Graphs

Detailed studies into the dynamics of the low-energy CID process reveal that fragmentation proceeds *via* a two-step mechanism involving an initial activation step to form an ion-target complex followed by a separate unimolecular reaction (Douglas, 1982; Dawson, 1982, 1983; Dawson and Douglas, 1983), *i.e.*,

$$AB^{+} \xrightarrow{N} [AB^{+}]^{\bullet} \rightarrow A^{+} + B \qquad (4\text{-}3)$$

In this mechanism it is assumed that the energy initially deposited upon collision is randomized to an appreciable extent amongst all the internal modes of the ion prior to dissociation. Thus, the CID process is generally taken to follow the assumptions of the statistical theory of mass spectra. Therefore, low-energy CID spectra have been interpreted on the basis of the unimolecular decay of gas-phase ions.

Comparisons between the QET and CID breakdown graphs for *n*-propanol and propane obtained on a TQMS have been presented by Fetterolf and Yost (1982). Similarities in the experimental E_{cm} and the internal energies predicted by QET were found for the maxima of the *m/z* 42 and 59 curves and the appearance energy for the *m/z* 29 ion. Agreement between the maxima and appearance thresholds of the CID curves for propane were also found. McLuckey *et al.* (1982) compared the QET breakdown graph of 2-pentanone to those obtained on both a FT-ICRMS and a hybrid BQQ (where B = magnetic sector). The CID breakdown graphs were in agreement with the QET predictions that the *m/z* 58 ion arising from the McLafferty rearrangement dominates at low internal energies, while the α-cleavage reaction leading to loss of a propyl group dominates at higher internal energies. These comparisons provide qualitative correlations between the precursor-ion kinetic energy and the internal energy imparted to the ion upon collision.

Basis of the QET Thermometers

The breakdown graphs predicted by QET for the M^+ ions of acetone, 2-pentanone, propane, toluene, and benzene will be compared to the time-resolved breakdown CID graphs obtained on the QITMS. The fluences calculated at a given parent/fragment ion crossover point will be compared to the internal energies of the corresponding crossover points on the QET breakdown graphs. This approach results in a qualitative characterization of the internal energies transferred upon CID in a QITMS similar to those presented by Fetterolf and Yost (1982) and McLuckey *et al.* (1982). More quantitative determinations of the amount of internal energy transferred during CID will be presented in chapter 5.

Experimental

All experiments were performed on a Finnigan MAT (San Jose, CA) ion trap mass spectrometer, ITMS™ described in detail in chapter 1. Samples were introduced into the ion trap chamber at a pressure of ≈ $1.2\text{x}10^{-6}$ torr (uncorrected ion gauge reading) *via* Granville-Phillips (Boulder, CO) variable leak values following three freeze-pump-thaw cycles to remove dissolved gases. The He buffer gas was cryocooled with liquid N_2 to remove excess water then added to the chamber to a total pressure of $1.0\text{x}10^{-4}$ torr (uncorrected ion gauge reading). The ion trap manifold was maintained at 100°C.

The acetone, 2-pentanone, propane, toluene, and benzene molecular ions were formed during a 1 ms electron ionization period. The M^+ ions were then rf/dc isolated at the upper apex of the stability diagram ($a_z = 0.15$, $q_z = 0.78$; see chapter 1 for details). The CID experiments were performed at a $q_z(M^+) = 0.300$.

The resonant excitation frequencies were optimized for each resonant excitation amplitude using the FORTH program JQFRCEC presented in Appendix B. The optimum frequencies were found to be within ±1200 Hz of those calculated by the ITMS™ software and are as follows: acetone, 117,477 Hz, 2-pentanone, 117,678 Hz, propane, 116,870 Hz, toluene, 118,259 Hz, and benzene, 118,178 Hz. A 1 ms "warm-up" period was added prior to varying the resonant excitation time to compensate for the finite rise time of the excitation potential (Johnson *et al.*, 1992). During this warm-up time the amplitude of interest was requested off-resonance (low-mass cut-off = 10 amu) to avoid resonantly excited the mass-selected ion. All resonant excitation potentials employed in this study are in $V_{0\text{-}p}$. The resonant excitation time was varied using the FORTH program RXNTIME presented in Appendix A. The CID product ions were detected using a mass-selected instability scan with axial modulation employed during the acquisition ramp (described in detail in chapters 1 and 2).

The ion intensities were extracted using CHROLIST, and normalized with a commercial spreadsheet program (QUATTRO, Borland International, Inc., Scotts Valley, CA). CID time-resolved breakdown graphs were plotted with a commercial graphing program (GRAPHER, Golden Software, Inc., Golden, CO).

All errors were calculated as the sample standard deviation of at least three determinations. All samples were checked for impurities using mass spectrometry.

Results

The experimental results for the five molecules of interest will be presented in this section, including the time-resolved breakdown graphs and fluences for the various crossover points of interest. The general trends observed will be discussed and interpreted in the Discussion section.

Acetone

Typical CID breakdown graphs of the M^+ ion of acetone (*m/z* 58) at resonant excitation amplitudes of 50 mV and 100 mV are presented in Figures 4-2a and b, respectively. The ion intensities were normalized with respect to the *m/z* 42, 43, 57, 58, 59, and 101 ions shown in Figures 4-3a and b. These spectra were taken at the *m/z* 43 and 58 crossover points in Figures 4-2a and b. The principal fragmentation to form *m/z* 43 corresponds to the loss of a CH_3 group from the M^+ ion (Murad and Inghram, 1964)

$$CH_3COCH_3^{\cdot+} \rightarrow CH_3CO^{+} + CH_3 \qquad (4\text{-}4)$$

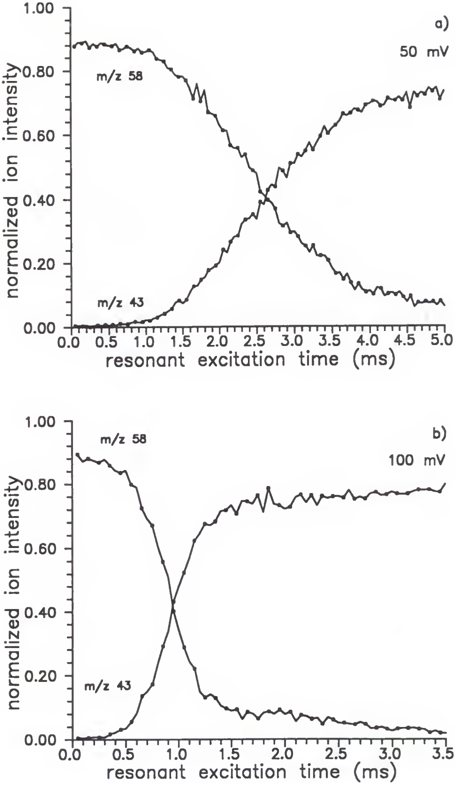

Figure 4-2: Time-resolved collision-induced dissociation breakdown graphs for the M^+ ion of acetone (*m/z* 58) using a) 50 mV and b) 100 mV resonant excitation amplitudes. Acetone at 1.1×10^{-6} torr; He added to 1.0×10^{-4} torr; every second data point plotted.

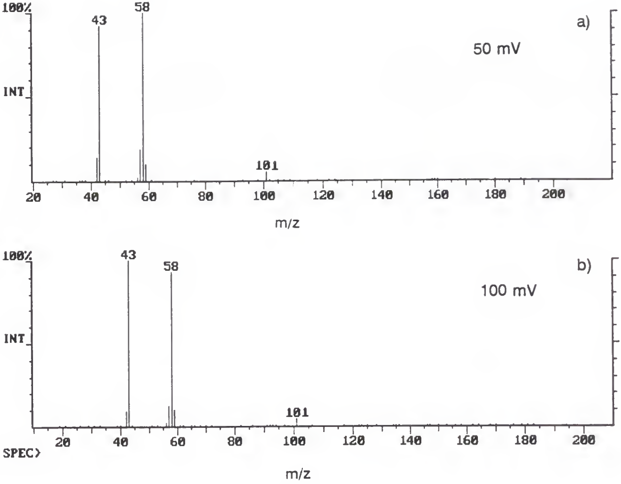

Figure 4-3: Collision-induced dissociation spectra of the M^+ ion of acetone at the *m/z* 58 and 43 crossover points a) 50 mV resonant excitation, 2.6 ms and b) 100 mV excitation, 0.95 ms.

The *m/z* 101 adduct ion likely arises from a reaction of the *m/z* 43 product ion with neutral acetone

$$CH_3COCH_3^{\cdot +} + CH_3COCH_3 \rightarrow (CH_3)_2COCH_3CO^{+} + CH_3 \qquad (4\text{-}5)$$

This reaction may occur during resonant excitation; however, it may also occur during the ≈ 7 ms period between resonant excitation and product ion detection. (The time between excitation and detection is calculated from the difference between the low-mass cut-off of the data acquisition table and the *m/z* of the product ion of interest times the rf scan rate of 0.180 ms amu^{-1}).

The CID breakdown graphs for the M$^+$ ion of acetone (Figures 4-2a and b) are characterized by sharp onsets of dissociation similar to those calculated from QET (Figure 4-4, Vestal and Lerner, 1967). Moreover, the onset of dissociation of the *m/z* 58 ion becomes increasingly sharper as the amplitude of the resonant excitation voltage is increased from 50 mV to 100 mV.

Fluences calculated at the *m/z* 43 and 58 crossover points for a variety of resonant excitation voltages and the corresponding internal energy from the QET breakdown graph are presented in Table 4-1. The fluence at the crossover point is found to decrease from 0.13 Vms to 0.060 Vms as the resonant excitation amplitude is increased from 50 mV to 300 mV.

2-Pentanone

Typical CID breakdown graphs for the M$^+$ ion of 2-pentanone (*m/z* 86) at 100 mV and 200 mV resonant excitation amplitudes are presented in Figures 4-5a and b, respectively. The ion intensities were normalized with respect to the *m/z* 43, 58, 71, and 85 to 87 ions shown in Figures 4-6a and b. These spectra were taken at the *m/z* 86 and

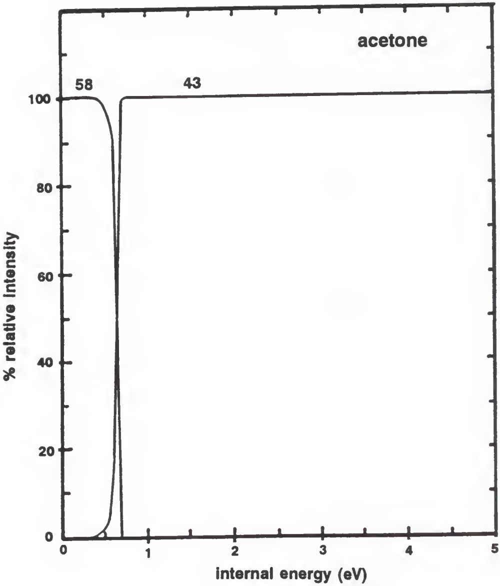

Figure 4-4: Breakdown graph for the M^+ ion of acetone (*m/z* 58) calculated from quasi-equilibrium theory (Vestal and Lerner, 1967).

Table 4-1: Comparison of fluences calculated from crossovers in the time-resolved CID breakdown graphs of the M^+ ions of acetone and 2-pentanone with crossovers calculated from QET.

		QET*	resonant excitation		crossover
	crossover	crossover	voltage	time	fluence
M^+	*m/z*	energy (eV)	(V)	(ms)	(Vms)
acetone	43 and 58	0.6	0.050	2.6	0.13
			0.075	1.4	0.10
			0.100	0.95	0.095
			0.125	0.70	0.088
			0.150	0.53	0.080
			0.300	0.20	0.060
2-pentanone	58 and 86	0.9	0.050	6.6	0.33
			0.075	3.2	0.24
			0.100	2.0	0.20
			0.125	1.4	0.18
			0.150	1.1	0.17
			0.175	0.93	0.16
			0.200	0.80	0.16
			0.250	0.60	0.15
			0.300	0.48	0.14

* From Figures 4-4 and 4-7 (Vestal and Lerner, 1967).

58 crossover points in Figures 4-5a and b. The *m/z* 58, 71 and 43 ions likely arise from the following fragmentation reactions (Murad and Inghram, 1964):

$$CH_3COCH_2CH_2CH_3^{+\cdot} \rightarrow CH_3COHCH_2^{+\cdot} + CH_2CH_2 \tag{4-6}$$

$$\rightarrow CH_3COCH_2CH_2 + CH_3 \tag{4-7}$$

$$\rightarrow CH_3CO^{+} + CH_2CH_2CH_3 \tag{4-8}$$

where reaction 4-6 is the lower energy McLafferty rearrangement of the M^{+} ion followed by loss of the CH_2CH_2 and reaction 4-8 is a higher energy α-cleavage reaction leading to loss of a C_3H_7 group.

The relative onsets of the *m/z* 58, 71, and 43 fragment ions agree with those predicted from QET (Figure 4-7, Vestal and Lerner, 1967) and with those reported by McLuckey *et al.* (1982) using FT-ICRMS and BQQ mass spectrometers. However, the *m/z* 58 fragment ion reaches a plateau in the CID curves (Figures 4-5a and b) as opposed to the maximum shown in the QET graph (Figure 4-7). The *m/z* 43 ion also appears to be reaching a plateau value. These plateaus are a characteristic feature of the CID breakdown graphs obtained on a QITMS (Evans *et al.*, 1990; Johnson *et al.*, 1990b).

Fluences calculated at the *m/z* 86 and 58 crossover points for a variety of resonant excitation voltages and the corresponding internal energy predicted from QET are presented in Table 4-1. Again, the fluences at the *m/z* 86 and 58 crossover point decrease by ≈ 50% as the resonant excitation voltage is increased from 50 to 300 mV.

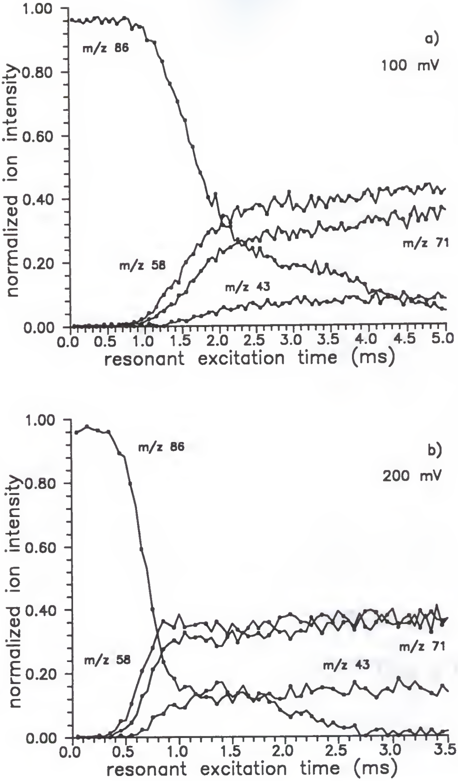

Figure 4-5: Time-resolved collision-induced dissociation breakdown graphs for the M^+ ion of 2-pentanone (*m/z* 86) using a) 100 mV and b) 200 mV resonant excitation amplitudes. 2-Pentanone at 1.3×10^{-6} torr; He added to 1.0×10^{-4} torr; every second data point plotted.

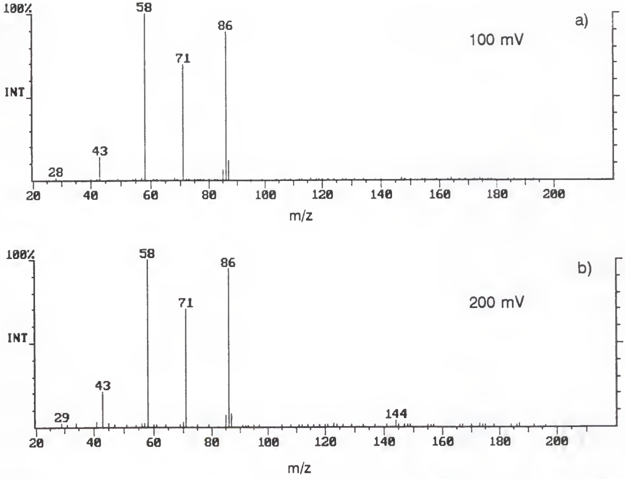

Figure 4-6: Collision-induced dissociation spectra of the M^+ ion of 2-pentanone at the *m/z* 86 and 58 crossover points a) 100 mV resonant excitation, 2.0 ms and b) 200 mV excitation, 0.80 ms.

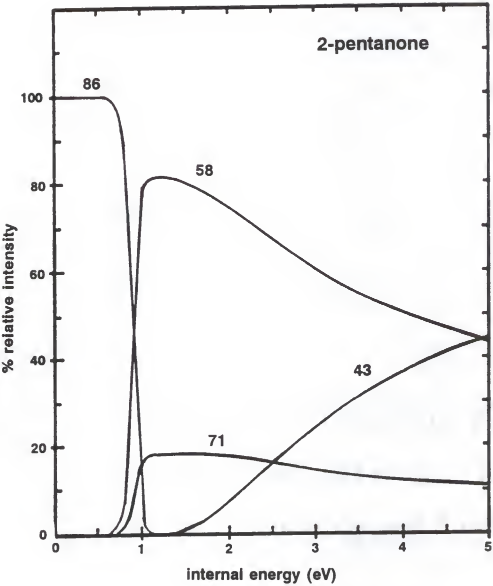

Figure 4-7: Breakdown graph for the M^+ ion of 2-pentanone (*m/z* 86) calculated from quasi-equilibrium theory (Vestal and Lerner, 1967).

Propane

Typical CID breakdown graphs for the M$^+$ ion of propane (*m/z* 44) at resonant excitation amplitudes of 100 and 200 mV are presented in Figures 4-8a and b, respectively. The ion intensities were normalized with respect to the *m/z* 28, 29, 42, 43, 44, and 45 ions shown in Figures 4-9a and b. These spectra were taken at the *m/z* 28 and 44 crossover points in Figures 4-8a and b. The *m/z* 43, 28, and 29 fragment ions likely arise from the following fragmentation reactions (Futrell and Tiernan, 1963):

$$CH_3CH_2CH_3^{+\cdot} \rightarrow CH_3CHCH_3^{+\cdot} + H \tag{4-9}$$

$$\begin{aligned} &\rightarrow CH_2CH_2^{+\cdot} + CH_4 \\ &\rightarrow CH_3CH^{\cdot +} + CH_4 \end{aligned} \tag{4-10}$$

$$\rightarrow CH_3CH_2^{+\cdot} + CH_3 \tag{4-11}$$

The QET breakdown graph for the M$^+$ ion of propane (Figure 4-1, Vestal and Lerner, 1967) contains a significantly greater number of fragment ions than that seen in the CID breakdown graphs (Figures 4-8a and b). The experimental fragment ions are limited to those found at internal energies < 2 eV, indicating that the internal energy of the activated M$^+$ ions is generally less that 2 eV. Within this lower energy range, the order of the *m/z* 43 and 44, *m/z* 28 and 44 crossover points, as well as the relative position of the *m/z* 43 plateau found in the CID curves correspond to the order predicted by QET (0.9 eV, 1.0 eV, and 1.0 eV, respectively).

Fluences calculated at the *m/z* 43 and 44, *m/z* 28 and 44 crossover points and the *m/z* 43 plateau are presented in Table 4-2 along with the corresponding QET internal energies. In all cases, a decrease in the fluence is found as the resonant excitation amplitude is increased from 60 mV to 300 mV.

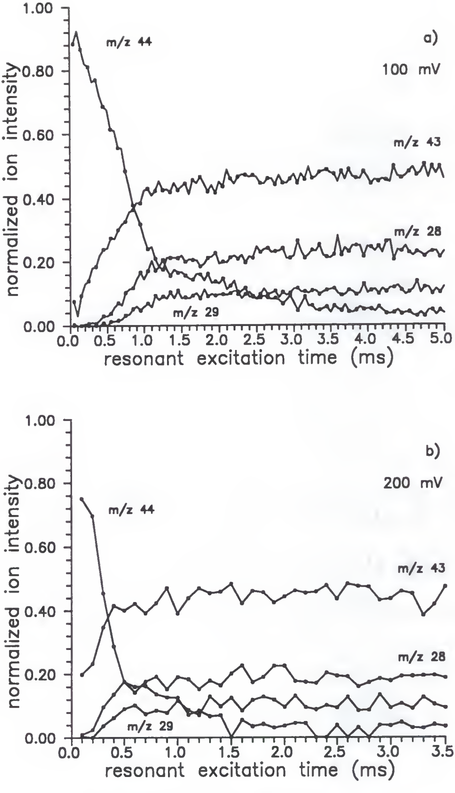

Figure 4-8: Time-resolved collision-induced dissociation breakdown graphs for the M^+ ion of propane (*m/z* 44) using a) 100 mV and b) 200 mV resonant excitation amplitudes. Propane at 1.3×10^{-6} torr; He added to 1.0×10^{-4} torr; every second data point plotted.

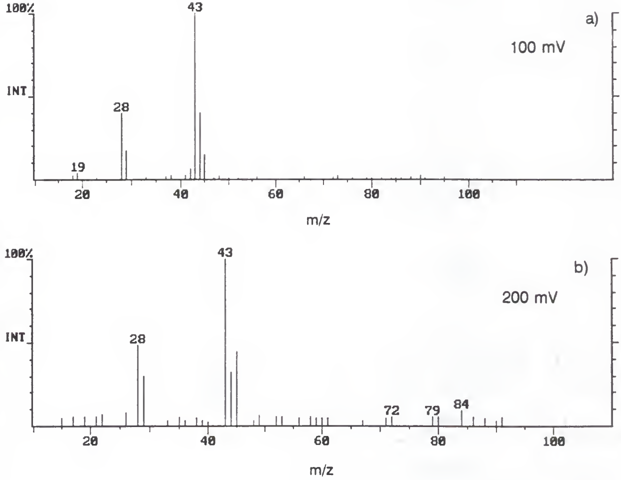

Figure 4-9: Collision-induced dissociation spectra of the M^+ ion of propane at the *m/z* 44 and 28 crossover points a) 100 mV resonant excitation, 0.85 ms and b) 200 mV excitation, 0.40 ms.

Table 4-2: Fluences from selected points on the time-resolved CID breakdown graphs of the M^+ ion of propane.

CID voltage (V)	*m/z* 43 and 44 crossover fluence (Vms)	*m/z* 43 plateau fluence (Vms)	*m/z* 28 and 44 crossover fluence (Vms)
0.060	0.17	0.25	0.28
0.075	0.11	0.17	0.14
0.080	0.10	0.16	0.14
0.090	0.095	0.15	0.13
0.100	0.085	0.12	0.11
0.115	0.078	0.12	0.11
0.125	0.075	0.10	0.11
0.135	0.068	0.095	0.11
0.150	0.069	0.11	0.11
0.165	0.066	0.099	0.10
0.175	0.067	0.084	0.11
0.200	0.065 ± 0.006*	0.10 ± 0.02*	0.10 ± 0.2*
0.225	0.068	0.090	0.10
0.250	0.065	0.090	0.096
0.300	0.066	0.12	0.10

QET internal energies: *m/z* 43 and 44 crossover point = 0.9 eV; *m/z* 43 plateau = 1.0 eV; *m/z* 28 and 44 crossover = 1.0 eV (Figure 4-1, Vestal and Lerner, 1967).

* Average of four determinations. Error expressed as the sample standard deviation.

Toluene

Typical CID breakdown graphs for the M^+ ion of toluene (*m/z* 92) at 75 mV, 125 mV, 150 mV, and 300 mV are presented in Figures 4-10a through d. The ions were normalized with respect to the *m/z* 91, 92, and 93 ions shown in Figures 4-11a through d. These spectra were taken at the *m/z* 91 and 92 crossover points in Figures 4-10a through d.

The CID breakdown graphs of the toluene M^+ ion have two features not present in the acetone, 2-pentanone, propane, or benzene (see below) CID graphs. Firstly, deviations from the initial decay of the *m/z* 92 and corresponding growth of the *m/z* 91 ions are seen as the amplitude of the resonant excitation is increased from 75 mV to 300 mV. The midpoint of this deviation is found to occur at a constant fluence = 0.38 Vms over the range of excitation voltages employed (Table 4-3). Secondly, at higher excitation voltages (Figure 4-10d) formation of an $(M+1)^+$ ion (*m/z* 93) competes with the *m/z* 92 to *m/z* 91 fragmentation reaction. These features will be discussed in the Discussion section below.

The QET breakdown graph for the M^+ ion of toluene (Figure 4-12, Vestal and Lerner, 1967) differs from the experimentally determined CID breakdown graphs due to the anomalies in the *m/z* 91 and 92 ion intensities. However, fluences calculated at the *m/z* 92 and 91 CID crossover points (Table 4-4) are again found to decrease over the range of excitation amplitudes employed.

Benzene

Typical CID breakdown graphs for the M^+ ion of benzene (*m/z* 78) are presented in Figures 4-13a and b. Note that the resonant excitation times are a factor of 2 to 10

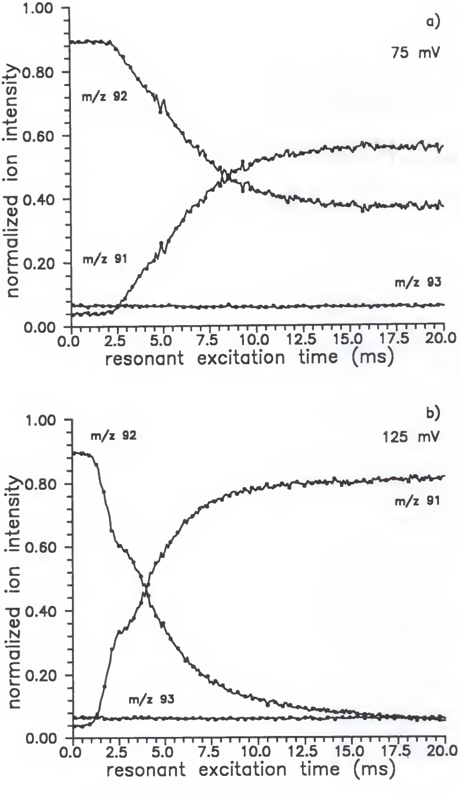

Figure 4-10: Time-resolved collision-induced dissociation breakdown graphs for the M^+ ion of toluene (*m/z* 92) using a) 75 mV and b) 125 mV resonant excitation amplitudes. Toluene at 1.2×10^{-6} torr; He added to 1.0×10^{-4} torr; every forth data point plotted.

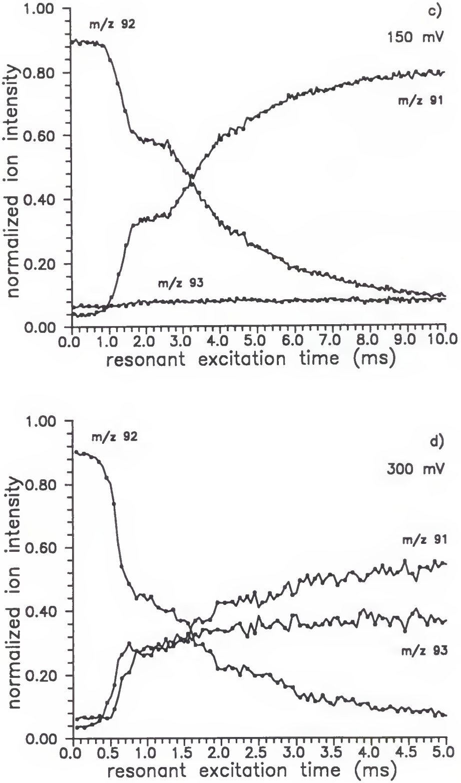

Figure 4-10: (continued) Time-resolved collision-induced dissociation breakdown graphs for the M$^+$ ion of toluene (*m/z* 92) using c) 150 mV and d) 300 mV resonant excitation amplitudes. Toluene at 1.2x10^{-6} torr; He added to 1.0x10^{-4} torr; every forth data point plotted.

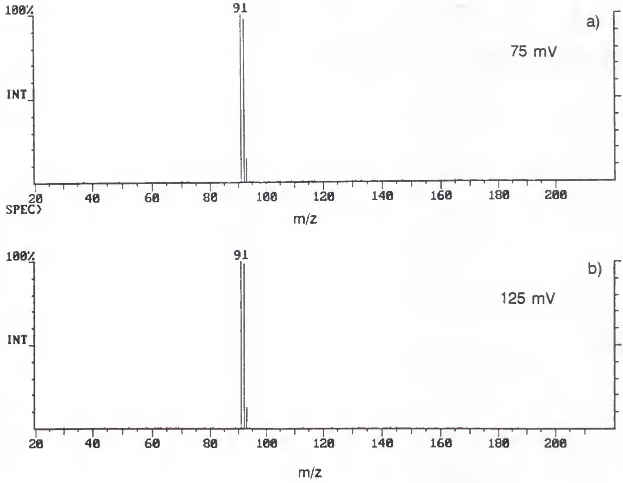

Figure 4-11: Collision-induced dissociation spectra of the M^+ ion of toluene at the *m/z* 92 and 91 crossover points a) 75 mV resonant excitation, 8.5 ms and b) 125 mV excitation, 4.0 ms.

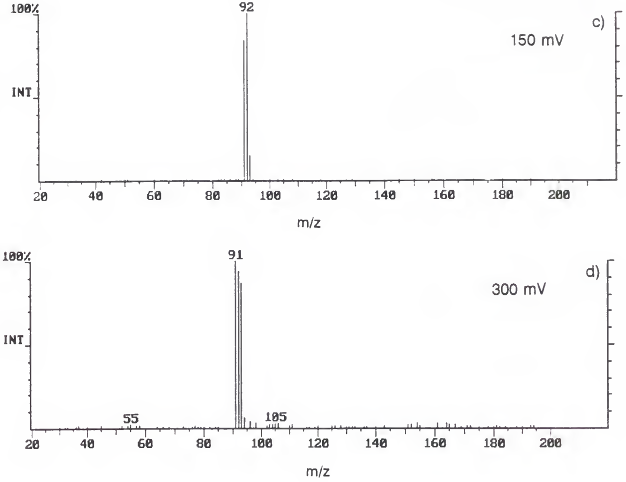

Figure 4-11: (continued) Collision-induced dissociation spectra of the M^+ ion of toluene at the *m/z* 92 and 91 crossover points c) 150 mV resonant excitation, 3.2 ms and d) 300 mV excitation, 1.7 ms.

Table 4-3: Fluences for the isomerization of the M^+ ion of toluene calculated at the midpoint of the first *m/z* 91 and 92 ion signal plateaus in the time-resolved CID breakdown graphs.

CID voltage (V)	time (ms)	fluence (Vms)
0.060	not seen	-
0.075	not seen	-
0.080	not seen	-
0.090	not seen	-
0.100	4.3	0.43
0.115	3.5	0.40
0.125	3.0	0.38
0.135	2.9	0.39
0.150	2.3	0.35
0.175	2.0	0.35
0.200	1.8	0.36
0.225	1.5	0.34
0.250	1.4	0.35
0.300	1.3	0.39
0.400	not seen*	-
0.500	not seen*	-

* Not seen due to extensive ion losses.

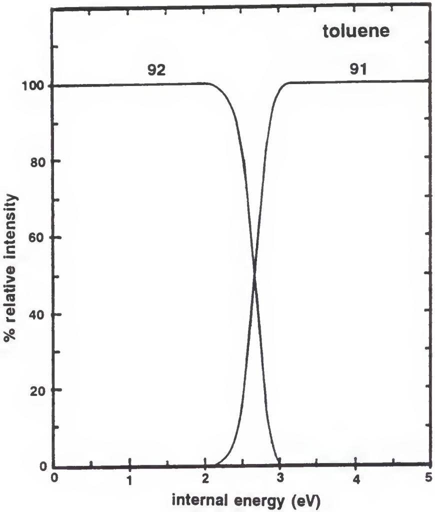

Figure 4-12: Breakdown graph for the M^+ ion of toluene (*m/z* 92) calculated from quasi-equilibrium theory (Vestal and Lerner, 1967).

Table 4-4: Comparison of fluences calculated from crossovers in the time-resolved CID breakdown graphs of the M^+ ions of toluene and benzene with crossovers calculated from QET.

M^+	crossover *m/z*	QET* crossover energy (eV)	CID voltage (V)	crossover time (ms)	crossover fluence (Vms)
toluene	91 and 92	2.7	0.075	8.5	0.64
			0.080	7.3	0.58
			0.090	6.0	0.54
			0.100	5.8	0.6 ± 0.1†
			0.115	4.4	0.50
			0.125	4.0	0.50
			0.135	3.6	0.49
			0.150	3.2	0.48
			0.175	2.8	0.49
			0.200	2.4	0.48
			0.225	2.2	0.50
			0.250	2.0	0.50
			0.300	1.7	0.50
			0.400	1.0	0.42
			0.500	0.75	0.38
benzene	77 and 78	5.6	0.175	69.0	12
			0.200	25.0	5.0
			0.225	23.0	5.1
			0.300	13.0	3.9

* From Figures 4-12 and 4-15 (Vestal and Lemer, 1967).

† Average of three determinations. Error expressed as the sample standard deviation.

times longer than those employed in the previous breakdown graphs. The ion intensities were normalized with respect to the *m/z* 39, 52, 76 to 79, and 155 ions presented in Figures 4-14a and b. These spectra were taken at the *m/z* 77 and 78 crossover points in Figures 4-13a and b. The *m/z* 77, 76, 52, and 39 fragment ions arise from a loss of H, H_2, C_2H_2, and C_3H_3 from the *m/z* 78 ion, respectively. The *m/z* 155 ion is likely an $(M_2\text{-}H)^+$ dimer of benzene formed either during excitation or during the ≈ 9.5 ms between excitation and detection. The signal-to-noise ratios, S/N, for the ions in the CID breakdown graphs for the M^+ ion of benzene are much lower than those for the M^+ ions of the other molecules of interest due to the higher excitation amplitudes employed and corresponding decrease in the trapping losses of the M^+ ion of benzene. (The *m/z* 39, 76, and 155 ions were not plotted in Figures 4-13a and b due to the low S/N of these ions at 225 mV).

All fragment ions in the QET breakdown graph (Figure 4-15) except the ion at *m/z* 63 are found in the experimental CID breakdown graphs. However, the experimental *m/z* 78 curve does not exhibit a sharp dissociation onset at 175 mV, nor does the *m/z* 77 ion reach a maximum. Moreover, the *m/z* 52 and 77 ions exhibit the same experimental onsets whereas the QET breakdown graph predicts a < 1 eV difference.

The QET breakdown graph indicates that ≈ 5.5 eV of internal energy is being deposited in the *m/z* 78 parent ion under the resonant excitation conditions employed in Figures 4-13a and b. While the fluences calculated at the *m/z* 77 and 78 crossover points (Table 4-4) are found to decrease with increasing excitation amplitudes, they are a factor of 10 to 100 times higher than those presented in Tables 4-1, 4-2, and 4-3, corresponding to 2 to 10 times higher QET crossover energies.

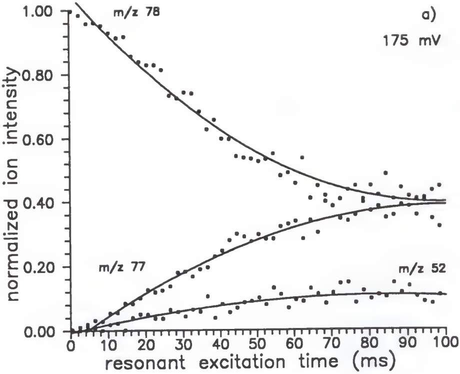

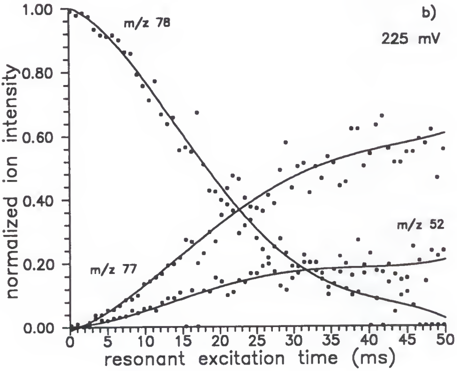

Figure 4-13: Time-resolved collision-induced dissociation breakdown graphs for the M^+ ion of benzene (*m/z* 78) using a) 175 mV and b) 225 mV resonant excitation amplitudes. Benzene at 1.2×10^{-6} torr; He added to 1.0×10^{-4} torr; every forth data point plotted.

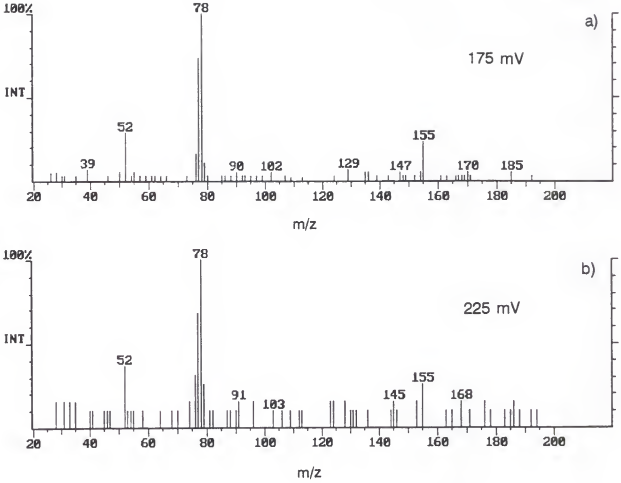

Figure 4-14: Collision-induced dissociation spectra of the M^+ ion of benzene at the *m/z* 78 and 77 crossover points a) 175 mV resonant excitation, 69 ms and b) 225 mV excitation, 23 ms.

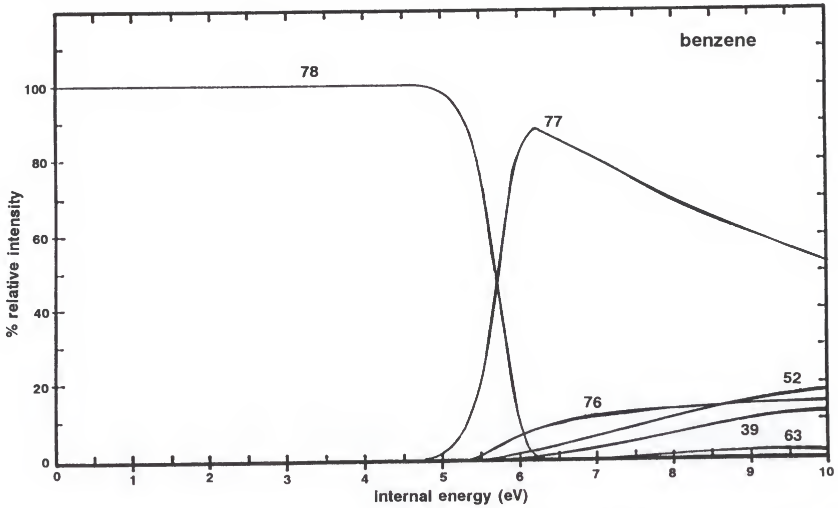

Figure 4-15: Breakdown graph for the M$^+$ ion of benzene (*m/z* 78) calculated from quasi-equilibrium theory (Vestal and Lerner, 1967).

Discussion

Generally good agreement is found between the nature, relative onsets, and relative crossover points of the fragment ions in the QET breakdown graphs and those found in the CID breakdown graphs for the M^+ ions of acetone, 2-pentanone, propane, and benzene. This indicates that there is a correlation between the amount of internal energy deposited and the duration of the resonant excitation potential. However, unlike the QET breakdown graphs, the product ion intensities in the CID curves reach plateau values as opposed to the maxima as the excitation time is increased. These plateaus are characteristic of time-resolved and voltage-resolved breakdown graphs obtained on an QITMS (Johnson *et al.*, 1990b; Evans *et al.*, 1991) and indicate that there is a limit to the amount of internal energy which can be deposited into the parent ion at a given resonant excitation voltage. This may be attributed to more effective competition of the collisional cooling of the M^+ ions with the He buffer at longer excitation times. Thus, while there is a correlation between the duration of the excitation potential in the time before the product ion plateaus, increasing the excitation time beyond the plateau value does not result in an increase in internal energy deposition.

The CID breakdown graphs of the M^+ ions of acetone, 2-pentanone, and toluene exhibit sharp dissociation onsets, notably at higher CID amplitudes. These can be compared with the often broad resolution of the CID breakdown graphs obtained on TQMS or FT-ICRMS instruments (Fetterolf and Yost, 1982; McLuckey *et al.*, 1982). The sharp onsets indicate that the M^+ ions have relatively narrow internal energy distributions. At lower excitation amplitudes (e.g. the CID of the M^+ ion of acetone in Figure 4-2a) or significantly longer excitation times (e.g. the CID of the M^+ ion of benzene in Figure 4-13a) the onset of dissociation is much broader, indicating a relatively wider range of internal energies, likely due to the less energetic, or greater number of collisions with the He buffer, respectively.

The CID breakdown graphs for the M^+ ion of toluene are complicated by the anomalous levelling of the *m/z* 91 and 92 ion signals as the resonant excitation amplitude is increased (Figures 4-10a through c). Since only the *m/z* 91, 92, and 93 ions are found over the range of excitation voltages and times employed, the change in the rate of dissociation of the *m/z* 92 to *m/z* 91 can be attributed to a change in the rate of an intermediate isomerization reaction of the *m/z* 92 M^+ ions. Detailed experimental (Winkler and McLafferty, 1973; McLafferty and Winkler, 1974; Dunbar, 1973, 1975; Jackson *et al.*, 1977; McLafferty and Bockhoff, 1979; Ausloos, 1980) and theoretical (Dewar and Landman, 1977; Cone *et al.*, 1977; Bartmess, 1982) studies into the decomposition of gaseous toluene ($C_6H_5CH_3^+$) and cycloheptatriene ($C_7H_8^+$) ions have resulted in the reaction scheme and corresponding potential energy surface presented in Figure 4-16a and b, respectively. According to this scheme (McLafferty and Bockhoff, 1979), upon electron ionization of toluene, an equilibrium is established between the two isomeric *m/z* 92 ions, the toluene ion (I) and the cycloheptatriene ion (II). This equilibrium proceeds *via* a 5-methylene-1,3-cyclohexadiene ion intermediate (V) shown on the potential energy surface in Figure 4-16b. This isomerization requires ≈ 1.5 eV less energy than H atom loss and favors the I isomer. At the threshold for H atom loss, a larger percent of the more stable tropylium ion (IV) is formed (Figure 4-16b). At slightly higher energies, formation of the benzyl isomer (III) *via* direct cleavage of the toluene ion (I) can occur. If III and IV are formed with high enough internal energy, then an equilibrium between the two isomeric *m/z* 91 ions is possible in which the more stable

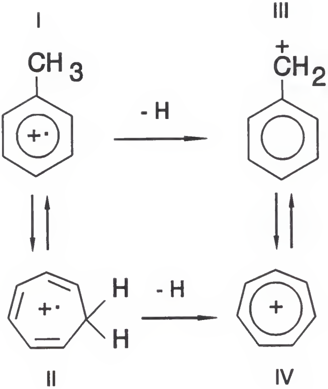

Figure 4-16: a) Scheme for the isomerization and H atom loss pathways involving (I) the $C_7H_8^+$ of toluene, (II) the $C_7H_8^+$ cycloheptatriene isomer, (III) the $C_7H_7^+$ benzyl cation, and (IV) the $C_7H_7^+$ tropylium ion (McLafferty and Bockhoff, 1979).

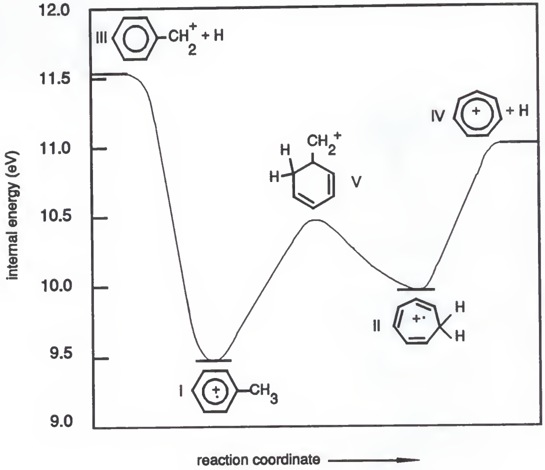

Figure 4-16: (continued) b) Potential energy surface for the scheme presented in Figure 4-16a (Ausloos, 1982).

tropylium ion (IV) is favored. (Further decomposition of the $C_7H_7^+$ isomers to $C_5H_5^+$ ions requires ≈ 3.9 eV of internal energy).

Trends in the CID breakdown graphs of the M^+ ion of toluene can be explained based on the reaction scheme presented in Figure 4-16a. Using Figure 4-10c as an example, the *m/z* 91 product ions formed between 0 and 1.6 ms likely arise from the isomerization I → II, followed by dissociation to IV. During this time, the II → IV dissociation is the rate determining step. At ≈ 1.6 ms (fluence = 0.24 Vms), the population of II becomes sufficiently decreased since the *m/z* 92 equilibrium favors isomer I. Thus, the isomerization of I → II becomes the rate determining step and a levelling in the *m/z* 92 signal is seen with an accompanying decrease in the amount of *m/z* 91 fragment ion. At resonant excitation times greater than ≈ 3.2 ms (fluence = 0.48 Vms), sufficient internal energy is available to drive the dissociation *via* I → II → IV; moreover, the direct cleavage of I → III may also be occurring following longer excitation times. At lower resonant excitation voltages (e.g. 75 mV in Figure 4-10a), the *m/z* 92 parent ions have lower kinetic energies; thus, the rate at which the II population is depleted due to dissociation to IV will decrease. As a result, the rate of formation of II is able to compete with the rate of dissociation of II to IV. It is particularly interesting to note that the proposed isomerization occurs at a constant fluence ≈ 0.38 Vms (Table 4-3). This indicates that proposed isomerization is taking place following the same amount of internal energy deposition over the range of excitation times and amplitudes employed.

The growth of the *m/z* 93 ion at higher resonant excitation voltages (300 mV In Figure 4-10d) may be attributed to translational driving of the self-protonation reaction. Note that despite the ≈ 13 ms period between excitation and detection the relative intensity of the *m/z* 93 ion does not increase significantly until the resonant excitation voltage approaches 300 mV and as such this reaction channel does not open until higher excitation voltages. The growth of the *m/z* 93 ion may, however, also be due to the loss of resolution of the *m/z* 92 ion at higher excitation amplitudes, resulting in an apparent *m/z* 93 ion due to the centroiding algorithm of the ITMS™ software. Detailed ion profiles studies would have to be performed to verify which process is giving rise to the *m/z* 93 ion.

At the chosen CID crossover points for each of the five molecules studied, the fluence decreases as the excitation voltage is increased (Tables 4-1, 4-2, and 4-4). This indicates that at higher excitation amplitudes, less time is needed to achieve the same internal energy deposition. The relationship between resonant excitation time and excitation voltage is examined in more detail in Figures 4-17a and 4-17b. Figure 4-17a presents plots of the resonant excitation voltage versus the excitation time for the *m/z* 43 and 44, and the *m/z* 28 and 44 crossover points, as well as the *m/z* 43 plateau for the M^+ ion of propane. The excitation times and voltages of the three internal energy reference points results in curves of similar hyperbolic shape. Similar shapes were found for the time/voltage curves of the for the M^+ ions of the four other molecules of interest. These plots are presented on a logarithmic scale in Figure 4-17b. In general, as the internal energy of the respective QET crossover points increases, the relative excitation times and voltages required to reach the corresponding CID crossover points also increase. However, the 2-pentanone and propane curves are in the reverse order than predicted from the relative QET internal energies. The reverse order of these curves can be attributed to the specific QET breakdown graphs for 2-pentanone and propane chosen for this study *i.e.* the QET graphs for propane have been calculated using a number of delay times after electron ionization (Vestal and Lerner, 1967). As the delay

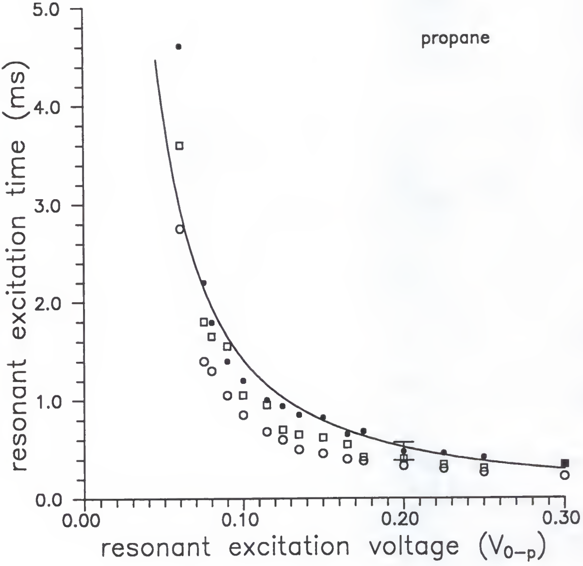

Figure 4-17: Resonant excitation time versus excitation voltage for a) the M^+ ion of propane; (○) *m/z* 43 and 44 crossover points; (●) *m/z* 28 and 44 crossover points (shown with a power fit); and (□) *m/z* 43 plateau. Propane at 1.3×10^{-6} torr; He added to 1.0×10^{-4} torr. Error bars are the sample standard deviation.

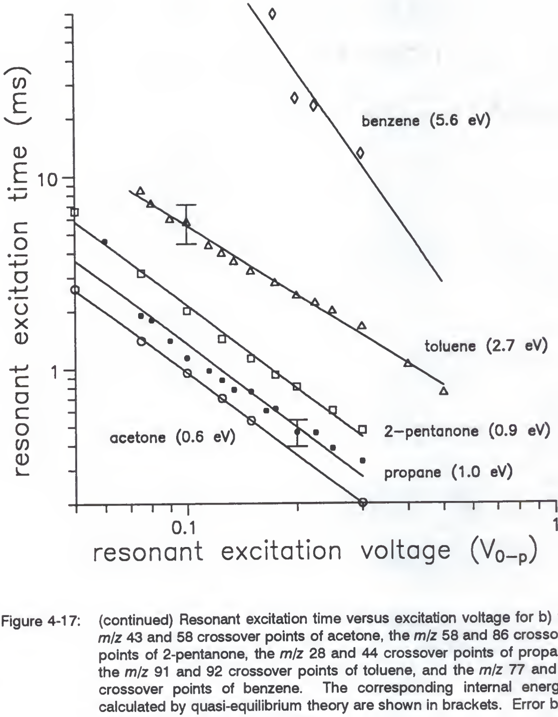

Figure 4-17: (continued) Resonant excitation time versus excitation voltage for b) the *m/z* 43 and 58 crossover points of acetone, the *m/z* 58 and 86 crossover points of 2-pentanone, the *m/z* 28 and 44 crossover points of propane, the *m/z* 91 and 92 crossover points of toluene, and the *m/z* 77 and 78 crossover points of benzene. The corresponding internal energies calculated by quasi-equilibrium theory are shown in brackets. Error bars are the sample standard deviation.

time is decreased from 1x10^{-6} s to 3x10^{-10} s, the *m/z* 28 and 44 crossover point is found to increase from 1.0 eV to 1.8 eV. (a delay time of 1x10^{-6} s was used in the QET graph in Figure 4-1). Since QET breakdown graphs for 2-pentanone at a variety of delay times are not available, and since the delay time used to calculate the 2-pentanone graph used in this study was not specified, the change in relative order of the 2-pentanone and propane curves in Figure 4-17b is not surprising. This highlights the qualitative nature of comparisons made between the QET and CID breakdown graphs.

The slopes of the resonant excitation voltage versus excitation time plots along with the corresponding fluences using 300 mV excitation and the QET internal energies at the crossover points of interest are presented in Table 4-5. For an estimated 10-fold increase in internal energy a 65-fold increase in the fluence is required at a resonant excitation amplitude of 300 mV. Thus, significantly higher fluences are required to increase the internal energy deposition from 0.06 eV to 3.9 eV than might be expected from a linear fluence/internal energy deposition relationship.

For estimated internal energies between 0.6 and 1.0 eV, the slopes of the log excitation time versus excitation voltage curves are ≈ -1.4 indicating that the excitation time and voltage have a ≈ 1.4:1; this ratio increases to ≈ 3:1 for estimated internal energies of 5.6 eV. (The -1.19 slope arising from the toluene study is due to the change in the initial decay and growth rates of the *m/z* 91 and 92 ions discussed above. If the *m/z* 91 and 92 curves at resonant excitation voltages above 100 mV (Table 4-3) are extrapolated using the initial growths and decays, then at higher excitation voltages, the *m/z* 91 and 92 crossover points occur at shorter excitation times than those plotted in Figure 4-17b. This would result in an increase in the slope of the resonant excitation versus amplitude plot for the M^+ ion of toluene in keeping with the trend in Table 4-5.)

Table 4-5: Slopes of the resonant excitation voltage versus excitation time plots for the M^+ ions of acetone, 2-pentanone, propane, toluene, and benzene.

M^+	crossover *m/z*	QET crossover internal energy (eV)	crossover fluence (Vms)	slope
acetone	43 and 58	0.6	0.060	-1.42
2-pentanone	58 and 86	0.9	0.14	-1.44
propane	28 and 44	1.0	0.10	-1.42
toluene	91 and 92	2.7	0.50	-1.19
benzene	77 and 78	5.6	3.9	-2.78

QET internal energies from Figures 4-4, 4-7, 4-1, 4-12, and 4-15, respectively (Vestal and Lerner, 1967).
Crossover fluences from Tables 4-1, 4-2, and 4-4.

These slopes reveal that longer excitation times are required to achieve a given internal energy deposition with a given excitation amplitude than would be predicted from a simple 1:1 relationship. These slopes thus provide a semi-quantitative measure of the competition between cooling and activation of the ions *via* collision with the He buffer.

Conclusions

This chapter presents a comparison between the time-resolved the CID breakdown graphs for the M^+ ions of acetone, 2-pentanone, propane, toluene, and benzene obtained on a QITMS with those predicted from QET. The experimentally determined CID curves are generally characterized by sharp dissociation onsets, similar to those seen in the QET breakdown graphs. These dissociation onsets become sharper as the resonant excitation voltage is increased, indicating that there is a narrower range of ion internal energies at higher resonant excitation amplitudes. The CID breakdown graphs differ from those predicted by QET since that fragment ion intensities reach plateau values as opposed to maxima as the resonant excitation time is increased. These plateaus indicate that there is a limit to the amount of internal energy deposited in the CID process, likely due to the successful competition of cooling versus activating collisions with the He buffer at longer excitation times.

Correlations between the fluences at selected crossover points on the CID breakdown graphs with the internal energy of the corresponding point on the QET breakdown graphs reveal that for an estimated 10-fold increase in internal energy a 65-fold increase in the fluence is required (using a resonant excitation amplitude of 300 mV). Thus, the fluence/internal energy relationship is not linear. Slopes of the resonant excitation time versus excitation voltage the M^+ ions of the five molecules of interest reveal that the excitation time/voltage relation is ≈ 1.4:1 at low internal energies (estimated from the QET breakdown graphs to range between ≈ 0.5 eV and 1.0 eV) and ≈ 3:1 at higher internal energies (≈ 6 eV).

An interesting anomaly is seen in the CID breakdown graphs for the M^+ ion of toluene. These are attributed to the opening of a proposed isomerization channel for the *m/z* 92 ion at high resonant excitation amplitudes.

Utility of QET Breakdown Graphs as Internal Energy Thermometers

The QET breakdown graphs of small organic molecules can be used to draw correlations between the fluence requirement for given points on experimentally determined CID breakdown graphs and the relative amount of internal energy required to bring about that process. However, absolute internal energy assignments based on the calculated QET energies should be avoided not only due to the numerous assumptions which underlie the construction of the QET breakdown graphs, but also due to fundamental difference between the energy deposition processes modelled by QET and those occurring experimentally. This latter point is highlighted by the CID breakdown graphs obtained for the M^+ ion of toluene, which revealed that ion-molecule processes other than just CID can be accessed upon resonant excitation in the QITMS.

CHAPTER 5
n-ALKYLBENZENE INTERNAL ENERGY THERMOMETERS

Introduction

This chapter will present the time-resolved and voltage-resolved collision-induced dissociation, CID, breakdown surfaces for the molecular ions, M^+, of a series of *n*-alkylbenzene molecules obtained on a quadrupole ion trap mass spectrometer, QITMS. The breakdown graphs will be used to quantitate the average internal energy deposited upon resonant excitation of the molecular ions. The *n*-alkylbenzenes of interest are *n*-butylbenzene, *n*-pentylbenzene, *n*-hexylbenzene, and *n*-octylbenzene. The time-resolved CID breakdown graphs of the M^+ ion of *n*-butylbenzene arising from a series of variable He buffer and *n*-butylbenzene pressure studies will be presented to determine the effect of these experimental parameters on the average internal energy transferred upon collision and to gain insight into the details of the CID mechanism.

Details of the CID experiment in a QITMS were presented in chapter 1 and briefly reviewed in chapter 4. A description of the CID process in a QITMS was also presented in chapter 4.

Physiochemical Basis and Previous Applications of the *n*-Alkylbenzene Thermometers

Of the four *n*-alkylbenzenes of interest, fragmentation of the M^+ ion of *n*-butylbenzene (*m/z* 134) has been the most extensively studied. Upon excitation, the M^+ ion of *n*-butylbenzene fragments *via* two principal pathways:

$$\begin{aligned} C_6H_5(CH_2)_3CH_3^{+\cdot} &\rightarrow C_6H_5CH_3^{+\cdot} + C_3H_6 \\ &\rightarrow C_6H_5CH_2^{+\cdot} + C_3H_7 \end{aligned} \qquad (5\text{-}1)$$

Detailed studies into the structure and energetics of the two fragment ions have been presented (Brown, 1970; Griffiths *et al.*, 1981a; Chen *et al.*, 1984; Baer *et al.*, 1988). The relative rates of formation of the $C_7H_7^+$ and $C_7H_6^+$ ions (Chen *et al.*, 1984) as well as modelling of the absolute dissociation rates of the *m/z* 134 ion using quasi-equilibrium theory, QET (Baer *et al.*, 1988) reveal that the $C_7H_7^+$ ion forms *via* direct cleavage of C_3H_7 with a high activation energy, ϵ_0, and a high frequency factor to form the benzyl cation (structure III in Figure 4-12a). The $C_7H_8^+$ ion forms *via* a rearrangement and loss of C_3H_6 with a low ϵ_0 and low frequency factor to form the methylene-1,3-cyclohexadiene cation. The activation energies, ϵ_0 for the direct cleavage and rearrangement reactions are $\approx$ 1.7 and 1 eV, respectively (Baer *et al.*, 1988).

The branching ratio of the *m/z* 91 and 92 ions, $91^+/92^+$, has been used as a thermometer for determining the average internal energy of the M^+ ion of *n*-butylbenzene since the first photodissociation, PD, studies of Mukhtar *et al.* (1981) revealed that the $91^+/92^+$ ratio increased with increasing photon energy and thus internal energy of the M^+ ion. The photodissociated $91^+/92^+$ ratio was also found to increase with increasing ion source temperature (Griffiths *et al.*, 1982). The PD breakdown graph was then used to calibrate the effects of the nature and pressure of the target gas species on the average internal energy deposited into the M^+ ions of *n*-butylbenzene upon high-energy CID (Griffiths *et al.*, 1981b).

Subsequent studies of the energy dependence of the $91^+/92^+$ ratio of the M^+ ion of *n*-butylbenzene using charge exchange mass spectrometry, CEMS, have been presented by Harrison and Lin (1983). In CEMS, the internal energy of the M^+ ion, $E(M^+)$, arising from the reaction

$$R^+ + M \rightarrow M^+ + R \tag{5-2}$$

is given by

$$E(M^+) = R.E.(R^+) - I.E.(M) + E_{therm} \tag{5-3}$$

where $R.E.(R^+)$ is the recombination energy (eV) of the reactant ion R^+ given by the exothermicity, $-\Delta H$, of the reaction

$$R^+ + e^- \rightarrow R \tag{5-4}$$

and where $I.E.(M)$ is the adiabatic ionization energy (eV) of the molecule, and E_{therm} is the thermal energy of the molecule prior to ionization (eV). The internal energy of the M^+ ion can be varied by choosing reactant ions of different recombination energies (e.g. $C_6F_6^+$, $R.E. = 10.0$ eV; COS^+, $R.E. = 11.2$ eV; N_2O^+, $R.E. = 12.9$ eV; N_2^+, $R.E. = 15.3$ eV; *etc.*). A breakdown graph can be constructed from the normalized charge exchange mass spectra of the M^+ ion by plotting the fragment ion intensity versus $E(M^+)$ (Li *et al.*, 1981; Herman *et al.*, 1982; Harrison, 1984). The CEMS breakdown graph of the M^+ ion of *n*-butylbenzene shows an increase in the $91^+/92^+$ ratio with increasing $E(M^+)$ over the range 2 to 6 eV (Harrison and Lin, 1983) similar to that of the PD breakdown graph (Mukhtar *et al.*, 1981). However, the PD breakdown graph shows a much stronger dependence of the $91^+/92^+$ ratio on internal energy than the CEMS graph.

The PD breakdown graph of the M^+ ion of *n*-butylbenzene has been reexamined by Chen *et al.* (1984) in a Fourier-transform ion cyclotron resonance mass spectrometer, FT-ICRMS. The FT-ICRMS results were found to agree with the CEMS results of Harrison and Lin (1983). The overall higher dependence of the $91^+/92^+$ ratio on photon energy first reported by Mukhtar *et al.* (1981) was attributed to the sampling of an ion population with a higher average internal energy given the short ($\approx 10^{-6}\ \mu$s) between electron ionization, EI, and PD (Boyd *et al.*, 1985). Both the FT-ICRMS and CEMS experiments sampled thermalized M^+ ions due to the long storage times and high source pressures, respectively.

Baer *et al.* (1988) have presented a breakdown graph of the $91^+/92^+$ ratio versus the internal energy of the M^+ ion of *n*-butylbenzene using the photoelectron-photoion coincidence, PEPICO, technique (Brehm and Puttkamar, 1967). In this approach, the kinetic energy of the electron, KE(e^-), ejected during the photoionization process

$$h\nu + M \rightarrow M^+ + e^- \tag{5-5}$$

is measured, allowing the internal energy of the fragmenting M^+ ion to be determined from

$$E(M^+) = h\nu - IE(M) - KE(e^-) + E_{therm} \tag{5-6}$$

A breakdown graph is constructed by measuring the masses and relative abundances of the ions in coincidence with the energy-analyzed electrons. The coincidence experiments result in extremely accurate determinations of the $91^+/92^+$ ratios as a function of internal energy of the M^+ ion. The PEPICO (Baer *et al.*, 1988) and CEMS (Harrision and Lin, 1983) breakdown graphs for the M^+ ion of *n*-butylbenzene are presented in Figure 5-1. The breakdown graphs should differ by ≈ 0.12 eV which is the difference in the thermal energies of the M^+ ions (0.21 eV in the PEPICO experiment versus 0.33 eV in the CEMS experiment). A detailed comparision of the photodissociation and CEMS breakdown and the variety of internal energy effects encountered in studies of the $91^+/92^+$ ratio of the M^+ ion of *n*-butylbenzene has been presented by Boyd *et al.* (1985).

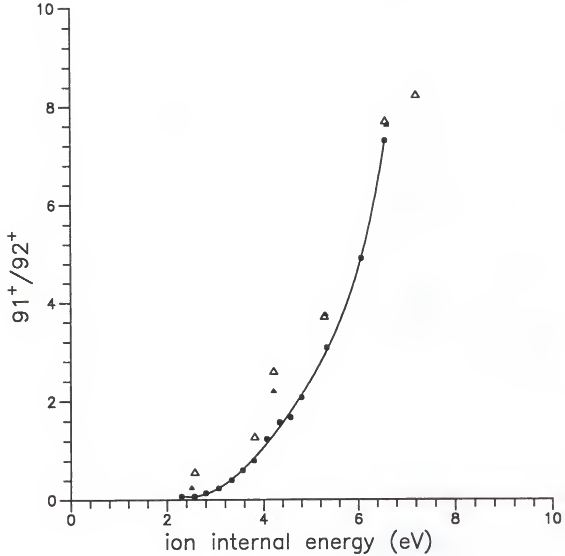

Figure 5-1: The $91^+/92^+$ ratio as a function of internal energy of the M^+ ion of *n*-butylbenzene (•) PEPICO technique at 298 K (Baer *et al.*, 1988) and (▵) charge exchange mass spectrometry at 373 K (Harrison and Lin, 1983).

McLuckey *et al.* (1984) have presented the CID breakdown graph of the M^+ ion of *n*-butylbenzene using N_2 target gas over laboratory collision energies, E_{lab}, of 10 to 6000eV (≈ 2eV to ≈ 1000 eV in the center-of-mass collision energy frame, E_{cm}) using a double magnetic sector mass spectrometer. The graph shows an initial increase in the $91^+/92^+$ ratio with a broad maximum of ≈ 2.5 between 50 and 250 E_{lab} (E_{cm} ≈ 9 eV to 44 eV) with the ratio dropping off at higher collision energies. Consistently higher $91^+/92^+$ ratios for the collected ions were found at lower (85 eV) versus higher (6000 eV) collision energies over a range of N_2 pressures. This was attributed to a greater average energy deposition is obtained at lower collision energies, and thus an overall higher efficiency of the translation to vibration energy conversion at low collision energies (McLuckey *et al.*, 1984).

The $91^+/92^+$ ratios arising from the charge exchange mass spectra of the M^+ ion *n*-butylbenzene using mass-selected reagent ion chemical ionization on a QITMS have been reported by Berberich *et al.* (1989). The resulting $91^+/92^+$ ratios are generally higher than those reported by Harrison and Lin (1983). These differences were attributed to differences in the internal energy transferred to the M^+ ion using mass-selected as opposed to non-mass-selected chemical ionzation (Berberich *et al.*, 1989).

The CEMS breakdown graph reported by Harrision and Lin (1983) and the PD breakdown graph reported by Griffiths *et al.* (1982) of the $91^+/92^+$ ratio of the M^+ ion of *n*-butylbenzene have been used to assign ion internal energies upon low-energy CID in a triple quadrupole mass spectrometer (Dawson and Sun, 1982) and on both FT-ICRMS and hybrid magnetic sector/quadrupole, BQQ, mass spectrometers (McLuckey *et al.*, 1982). A maximum $91^+/92^+$ ratio ≈ 4 with N_2 target gas at a center-of-mass collision energy ≈ 10 eV was obtained using the TQMS, whereas the $91^+/92^+$ plateau value was lower (≈ 2.5) using collision energies between 40 and 80 eV in the FT-ICRMS and BQQ instruments. According to the CEMS results of Harrison and Lin (1983), these ratios correspond to average energy transfers of 5.4 eV and 4.5 eV, respectively. These differences have been attributed by McLuckey *et al.* (1984) to differing relative contributions of metastable *m/z* 92 ions in the CID spectra arising from the two ionization methods employed (atmospheric pressure chemical ionization and 70 eV electron ionization, respectively).

The CEMS breakdown graphs for a homologous series of *n*-alkylbenzenes have been reported by Nacson and Harrison (1985) and are presented in Figure 5-2. The breakdown graphs were used to assign average internal energies and to calculate the percent energy converted upon low-energy CID of the M^+ ions in a TQMS. The average internal energy transferred was found to increase from 4.6 to 6.7 eV, with a corresponding increase in the energy conversion from 45% to 87%, as the size of the *n*-alkyl group was increased.

Previous Internal Energy Determination in a QITMS

Quantitative determinations of the average internal energy deposited into the ions in a QITMS upon resonant excitation have been limited. Louris *et al.* (1987) have presented a study of the $91^+/92^+$ ratio of the M^+ ion of *n*-butylbenzene as a function of the $q_z(M^+)$ value and the amplitude of the resonant excitation potential. The internal energies of the M^+ ions were assigned from the CEMS breakdown graph of Harrison and Lin (1983) and found to range from ≈ 1 eV to 5 eV, over the $q_z(M^+)$ values (0.36 and 0.60) and amplitudes (2.7 to 14.4 $V_{p\text{-}p}$) employed. In general, the ion internal energies were found to increase as the $q_z(M^+)$ was increased. It was also noted that at higher

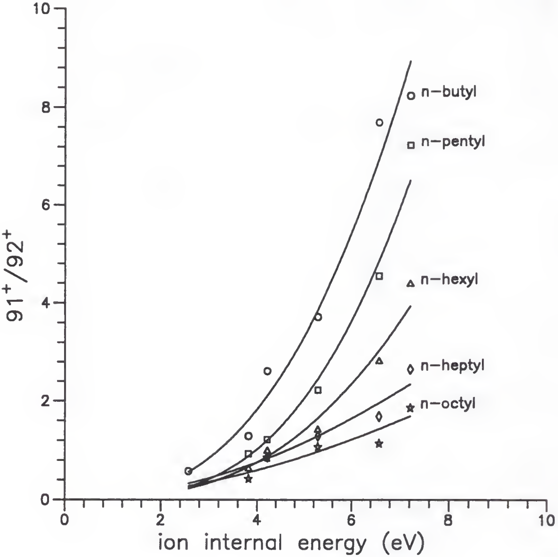

Figure 5-2: The $91^+/92^+$ ratios as a function of the internal energy of the M^+ ions of the *n*-alkylbenzenes from charge exchange mass spectrometry (Nacson and Harrison, 1988).

resonant excitation amplitudes loss of the M^+ ions competes with dissociation; thus, while the fragmentation efficiency increased, the overall CID efficiency decreased. The distribution of ion internal energies was also estimated by measuring the fragment ion intensities arising from CID of the M^+ ion of tetraethylsilane which fragments *via* the sequential loss of ethyl groups. Since the activation energy, ϵ_0, for each step is known, the internal energy distribution was estimated from the relative intensities of the fragment ions. The fragmentation patterns indicate that as the amplitude of the resonant excitation voltage is increased, the distribution of internal energies broadens thus allowing access to higher energy the pathways, *i.e.* the loss of three C_2H_5 groups with an ϵ_0 = 3.5 eV.

Johnson *et al.* (1990a) have presented a more detailed study of the average internal energy transferred upon resonant excitation of the ions in a QITMS based on the $91^+/92^+$ ratio of the M^+ ion of *n*-butylbenzene. The effects of the resonant excitation frequency, amplitude, and time, as well as the $q_z(M^+)$, and the nature and pressure of the He buffer gas on the $91^+/92^+$ ratio were examined. These studies indicate that the $91^+/92^+$ ratio changes over the range of excitation amplitudes, $q_z(M^+)$, and buffer pressures employed. In general, the internal energy of the M^+ ion was found to increase as the $q_z(M^+)$ was increased, and to decrease as the He buffer pressure was increased. This latter observation is attributed to the increase in the number of collisional cooling as opposed to collisional activating collisions at the higher He pressure. The maximum $91^+/92^+$ ratio obtained over the range of experimental conditions employed was $\approx$ 1.4, corresponding to an average internal energy of $\approx$ 3.4 eV (Harrison and Lin, 1983), in keeping with the energy range reported by Louris *et al.* (1987).

Brodbelt *et al.* (1988a) have presented estimated ion internal energies upon resonant excitation based on the CID spectra of the M^+ ions of dimethyl phosphonate and dimethyl phosphite. The CID spectra reflect the isomerization of the phosphate ion to the phosphite tautomer which is strongly dependent on the collision conditions employed (Kenttämaa and Cooks, 1985). The activation energies for the various fragmentation pathways of the two isomers are also well known (Rosenstock *et al.*, 1977). The authors suggest that the absence of the *m/z* 47 fragment ion (ϵ_0 = 5.8 eV) in the CID spectrum of the M^+ ion (*m/z* 110) of dimethyl phosphonate indicates that the average internal energy of the activated ions is less than 5.8 eV; however, the authors also note that the experiments were performed at a low-mass cut-off such that if ions of *m/z* 47 were formed it would not have been trapped and stored. As such, these results remain inconclusive.

A more recent study by Nourse *et al.* (1992) reports that a total of 29 eV of internal energy can be deposited into the M^+ ion of pyrene using six sequential stages of resonant excitation and mass-analysis (*i.e.* MS^6) each of which can deposit ≈ 5 eV of energy. They also report that under "extreme" activation conditions (6 $V_{0\text{-}p}$ resonant excitation voltage applied for 100 ms) fragment ions with estimated activation energies of 17 eV are formed from the M^+ ion of pyrene. Thus, while the majority of studies of the ion internal energies deposited upon resonant excitation in the QITMS indicate that the energies are in the low 2 eV to 4 eV range, substantially higher energies have also been reported.

This present chapter will present the time-resolved and voltage-resolved CID surfaces for the M^+ ions of *n*-butylbenzene, *n*-pentylbenzene, *n*-hexylbenzene, and *n*-octylbenzene under the standard operating conditions for MS/MS analyses, *i.e.*, $q_z(M^+)$ = 0.300 with a He buffer pressure = 1.0×10^{-4} torr (uncorrected ion gauge reading). The average ion internal energies transferred as a function of the mass of the M^+ ions will be assigned based on the CEMS breakdown graphs of Nacson and Harrison (1985). The percent energy transferred will be calculated based on the maximum available kinetic energy of the ions as calculated from the Dehmelt pseudo-potential well model (see chapter 1 for a detailed discussion of this model). The time-resolved breakdown graphs of the M^+ ion of *n*-butylbenzene as a function of He buffer and *n*-butylbenzene pressure will be presented to determine the effects of these parameters on the average internal energy of the M^+ ion and in so doing provide insight into the details of the CID mechanism.

Experimental

Instrumental and Chemicals

All experiments were performed on a Finnigan MAT (San Jose, CA) ion trap mass spectrometer, ITMS™ described in detail in chapter 1. Samples were introduced into the ion trap manifold *via* Granville-Phillips (Boulder, CO) variable leak values following three freeze-pump-thaw cycles to remove dissolved gases. The He was cryocooled to remove excess water prior to being introduced to the ion trap chamber. The ion trap manifold was at 100°C.

The M^+ ions of the *n*-alkylbenzenes were formed during a 1 ms electron ionization period. For the variable He buffer and *n*-butylbenzene pressure studies, the ionization time was varied between 0.2 and 1 ms, based on the He and *n*-butylbenzene pressures. The M^+ ions were then rf/dc isolated at the upper apex of the stability diagram (a_z = 0.15, q_z = 0.78) and resonantly excited at a $q_z(M^+)$ = 0.300. The resonant excitation frequencies were optimized for each amplitude employed using the FORTH program JQFRCEC presented in Appendix B. The optimum frequencies were 118,892 Hz for the

M^+ ion of *n*-butylbenzene (*m/z* 134), 118,095 Hz for the M^+ ion of *n*-pentylbenzene (*m/z* 148), 118,014 Hz for the M^+ ion of *n*-hexylbenzene (*m/z* 160), and 118,484 Hz for the M^+ ion of *n*-octylbenzene (*m/z* 190). The resonant excitation time was varied using the FORTH program RXNTIME presented in Appendix A. A 1 ms "warm-up" period was added prior to varying the resonant excitation time to compensate for the finite rise time of the excitation potential (Johnson *et al.*, 1992). The resonant excitation voltage was varied manually in the respective scan functions. All resonant excitation voltages were in $V_{0\text{-}p}$. The CID product ions were detected using the mass-selected instability scan with axial modulation employed during the acquisition.

The *n*-alkylbenzenes were commercial samples (Fluka Chemie AG, CH-9470 Buchs, Switzerland) of highest purity and checked for impurities using mass spectrometry.

Data Manipulation

The ion intensities were extracted using CHROLIST, a data reduction program developed in our laboratory, and normalized with a commercial spreadsheet program (QUATTRO, Borland International, Inc., Scotts Valley, CA). The ion intensities were normalized with respect to the sum of all the ions of > 5% relative intensity presented in Figures 5-3a through h. The two-dimensional CID breakdown graphs were plotted with a commercial graphing program (GRAPHER, Golden Software, Inc., Golden, CO).

The CID surfaces of the $91^+/92^+$ ratios were constructed by first performing a 5-point smoothing on the normalized data in both the *x* and the *y* directions using the BASIC program presented in Appendix C. The smoothed data were then imported into a commercial three-dimensional graphing program (SURFER, Golden Software, Inc.,

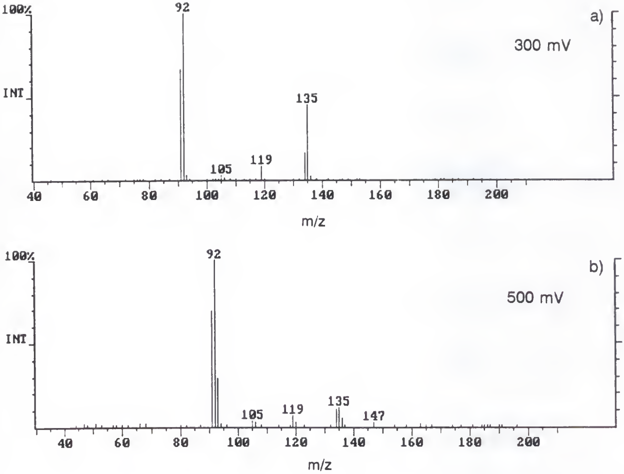

Figure 5-3: Collision-induced dissociation spectra of the M^+ ion of *n*-butylbenzene (*m/z* 134) a) 300 mV excitation amplitude and 1.05 ms excitation time and b) 500 mV excitation amplitude and 0.55 ms excitation time.

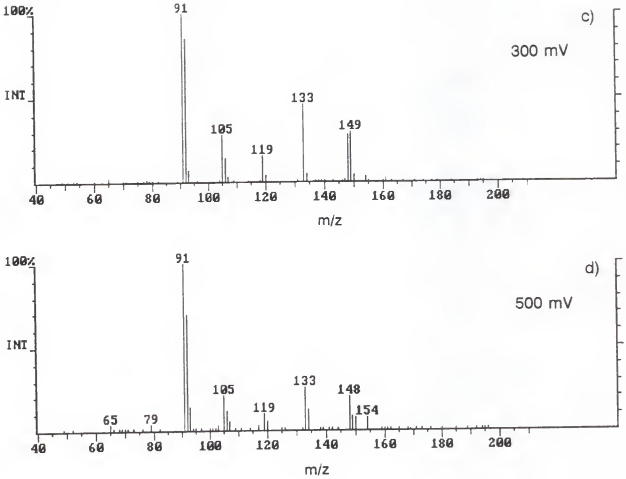

Figure 5-3: (continued) Collision-induced dissociation spectra of the M^+ ion of *n*-pentylbenzene (*m/z* 148) c) 300 mV excitation amplitude and 1.15 ms excitation time and d) 500 mV excitation amplitude and 0.65 ms excitation time.

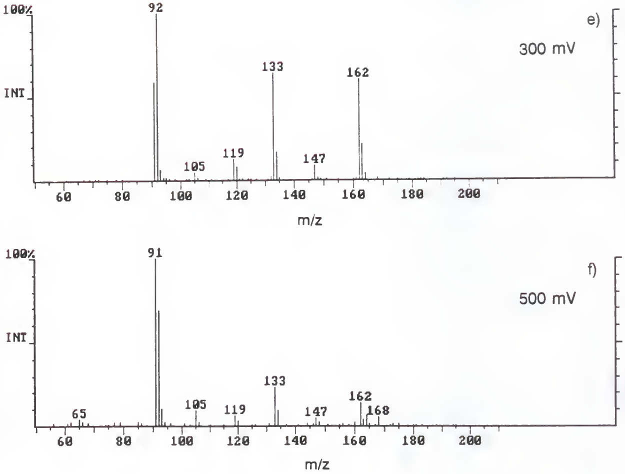

Figure 5-3: (continued) Collision-induced dissociation spectra of the M$^+$ ion of *n*-hexylbenzene (*m/z* 162) e) 300 mV excitation amplitude and 1.05 ms excitation time and f) 500 mV excitation amplitude and 0.75 ms excitation time.

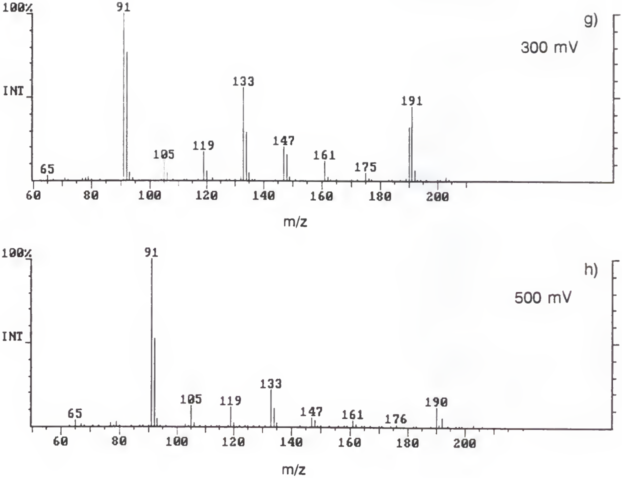

Figure 5-3: (continued) Collision-induced dissociation spectra of the M$^+$ ion of *n*-octylbenzene (*m/z* 190) g) 300 mV excitation amplitude and 1.35 ms excitation time and h) 500 mV excitation amplitude and 0.90 ms excitation time.

Golden, CO). A 25x25 data grid was constructed using the inverse distance gridding method (weighting power = 2) and smoothed with a spline (X = Y expansion factor = 2). Sample CID surfaces for the $91^+/92^+$ ratios arising from the M^+ ion of *n*-butylbenzene with no data smoothing, with spline smoothing, and with both 5-point smoothing in *x* and *y*-directions and spline smoothing are presented in Figures 5-4a and b, and Figure 5-5a, respectively.

The CID efficiencies were calculated as follows (Yost and Enke, 1978):

$$\text{fragmentation efficiency} = E_f = \frac{\sum F_i}{(P + \sum F_i)} \tag{5-7}$$

$$\text{collection efficiency} = E_c = \frac{(P + \sum F_i)}{P_0} \tag{5-8}$$

$$\text{overall efficiency} = E_{CID} = E_f E_c = \frac{\sum F_i}{P_0} \tag{5-9}$$

where P_0 is the initial parent ion intensity, and P and F_i are the parent and fragment ion intensities following CID.

The Dehmelt pseudo-potential well depths, $\overline{D}_z$, and the maximum kinetic energy, $K.E._{max,total}$, were calculated using equations 1-16 and 1-18, respectively. The center-of-mass collision energies, E_{cm}, were calculated using equation 4-1 where $E_{lab} = K.E._{max,total}$. The percent energy conversion was then calculated using the assigned average internal energies and the calculated E_{cm} at the $91^+/92^+$ plateaus of interest. The average internal energies of the *n*-alkylbenzene thermometers were assigned from the CEMS breakdown graphs of Nacson and Harrison (1985) presented in Figure 5-2. The average internal energies of the M^+ ion of *n*-butylbenzene in the variable He buffer and *n*-butylbenzene pressure studies were assigned using the PEPICO breakdown graphs (Baer *et al.*, 1988)

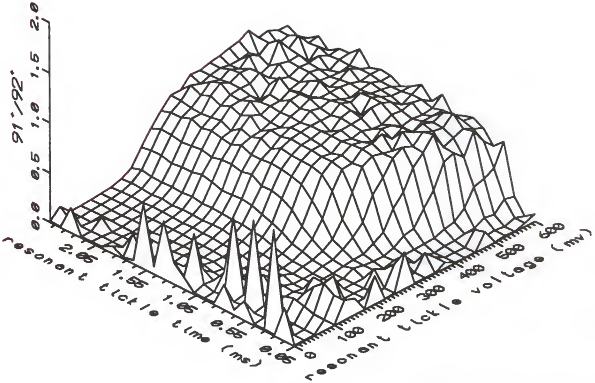

Figure 5-4: Collision-induced dissociation breakdown surface of the M^+ ion of *n*-butylbenzene showing the $91^+/92^+$ ratio. a) No smoothing of the data was performed. *n*-Butylbenzene at ≈ 2.0×10^{-6} torr; He buffer gas added to 1.0×10^{-4} torr.

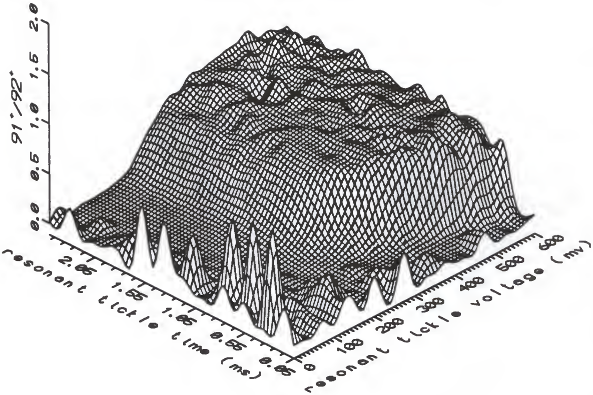

Figure 5-4: (continued) Collision-induced dissociation breakdown surface of the M^+ ion of *n*-butylbenzene showing the $91^+/92^+$ ratio. b) A spline smoothing of the data was performed. *n*-Butylbenzene at ≈ 2.0×10^{-6} torr; He buffer gas added to 1.0×10^{-4} torr.

presented in Figure 5-1 and corrected for the internal energy differences of the M^+ ion of the *n*-butylbenzene at 298 (0.21 eV) versus 373 K (0.33 eV) *i.e.* 0.12 eV was added to the internal energies assigned from the PEPICO breakdown graph to account for the additional internal energy of the M^+ ions at 373 K in the QITMS versus 298 K in the PEPICO experiments.

Results and Discussion

Three-dimensional CID Breakdown Surfaces

CID breakdown surfaces of the $91^+/92^+$ ratios for the four *n*-alkylbenzene thermometers of interest are presented in Figures 5-5a through d. The *n*-butylbenzene and *n*-pentylbenzene $91^+/92^+$ ratios clearly reach plateau values in both the *x* (resonant excitation voltage) and *y* (excitation time) directions. The $91^+/92^+$ ratios of the *n*-hexylbenzene and *n*-octylbenzene M^+ ion reach plateau values over the range of excitation times but not over the range of excitation voltages employed. Plateau values would presumably be reached should higher excitation amplitudes be employed for these molecules. The surface plateaus of the *n*-alkylbenzene thermometers indicate that there is an upper limit to the average internal energy transferred upon collision, similar to the conclusion drawn from the time-resolved CID breakdown graphs of the QET molecules studied in chapter 4. The variable voltage studies presented here for the M^+ ions of the *n*-alkylbenzenes further reveal that the heights of the time-resolved plateaus vary as a function of the amplitude of the excitation potential. Thus, for a q_z (M^+) = 0.300 the average internal energy of the M^+ ions can be varied based on the chosen excitation amplitude.

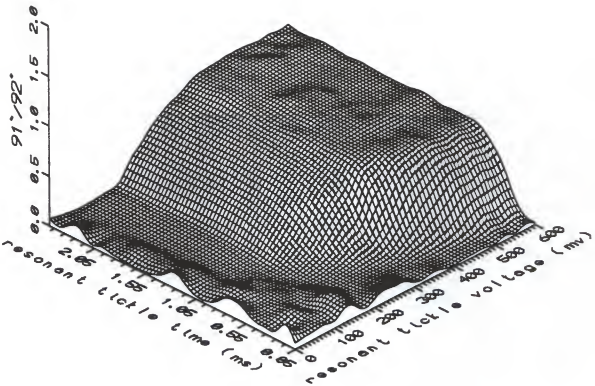

Figure 5-5: Collision-induced dissociation breakdown surface of a) the M^+ ion of *n*-butylbenzene showing the $91^+/92^+$ ratio. Both two-dimensional 5-point and spline smoothing of the data were performed. *n*-Butylbenzene at ≈ 2.0×10^{-6} torr; He buffer gas added to 1.0×10^{-4} torr.

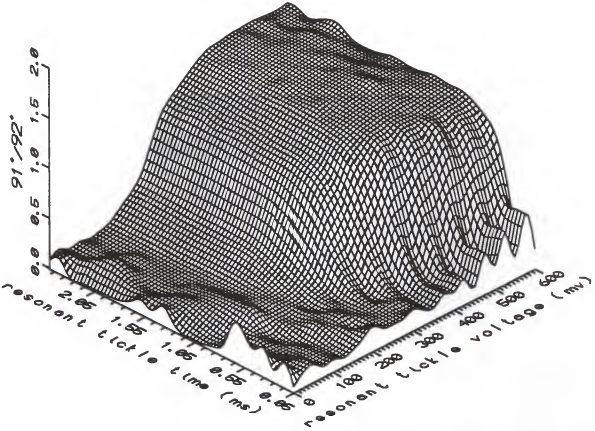

Figure 5-5: (continued) Collision-induced dissociation breakdown surface of b) the M^+ ion of *n*-pentylbenzene showing the $91^+/92^+$ ratio. Both two-dimensional 5-point and spline smoothing of the data were performed. *n*-Pentylbenzene at ≈ 2.0×10^{-6} torr; He buffer gas added to 1.0×10^{-4} torr.

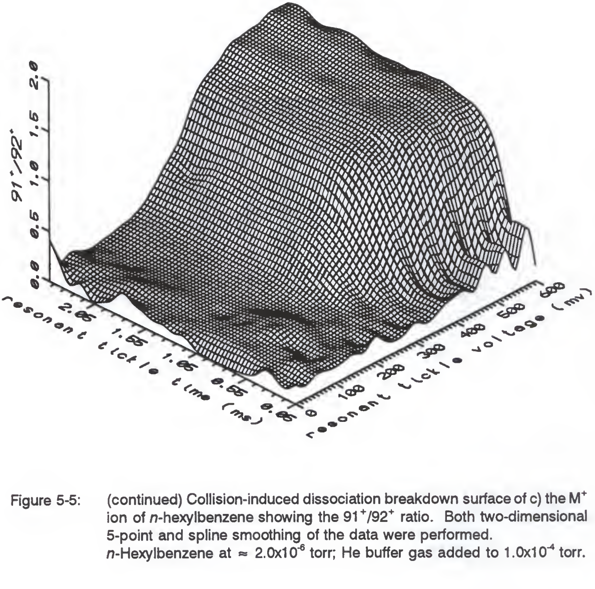

Figure 5-5: (continued) Collision-induced dissociation breakdown surface of c) the M^+ ion of *n*-hexylbenzene showing the $91^+/92^+$ ratio. Both two-dimensional 5-point and spline smoothing of the data were performed. *n*-Hexylbenzene at ≈ 2.0×10^{-6} torr; He buffer gas added to 1.0×10^{-4} torr.

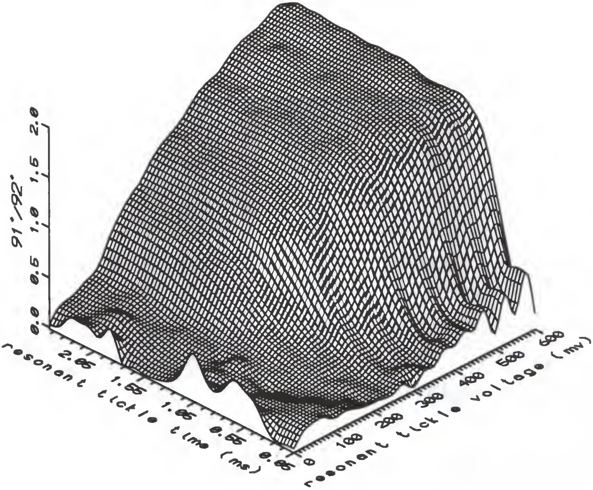

Figure 5-5: (continued) Collision-induced dissociation breakdown surface of d) the M^+ ion of *n*-octylbenzene showing the $91^+/92^+$ ratio. Both two-dimensional 5-point and spline smoothing of the data were performed. *n*-Octylbenzene at ≈ 2.0×10^{-6} torr; He buffer gas added to 1.0×10^{-4} torr.

The upper average internal energy limits are more clearly seen in the topographical representations of the *n*-alkylbenzene surfaces presented in Figures 5-6a through h. Note that each surface is shown on both a linear (top) and log-log scale (bottom). The $91^+/92^+$ ratio for the M^+ ion of *n*-butylbenzene varies from ≈ 0.1 to a maximum plateau value of 0.7, corresponding to a range of assigned internal energies from 1.5 eV (extrapolated from the CEMS breakdown graph in Figure 5-2) to an upper average internal energy of ≈ 2.9 eV. The $91^+/92^+$ ratios of *n*-pentylbenzene range from 0.4 to 1.4, indicating a range of internal energies between ≈ 3.0 eV and ≈ 4.4 eV The M^+ ion of *n*-hexylbenzene has a range of internal energies between ≈ 3.2 and ≈ 5.0 eV while the internal energy of the M^+ ion of *n*-octylbenzene ranges from ≈ 4.0 to ≈ 7.5 eV (extrapolated from Figure 5-2) over the range of excitation times and amplitudes employed. These average internal energy limits will be discussed in greater detail below.

It is interesting to compare the similar hyperbolic shapes of the topographical representations of the $91^+/92^+$ ratios of the *n*-alkylbenzenes in Figures 5-6a, c, e, and g with those observed in the plot of resonant excitation times versus voltages of the M^+ ion of propane at the *m/z* 44 and 28 crossover points in Figure 4-17a. The excitation voltage/time relation noted for the QET molecules thus appears to be a general relation for other M^+ ions undergoing CID in the QITMS. The slopes of selected $91^+/92^+$ contour lines in the topographical log-log plots of the *n*-alkylbenzenes and the corresponding average internal energies are presented in Table 5-1. An average slope of -1.4 ± 0.2 is obtained over the internal energy range 2.6 to 4.4 eV, in good agreement with that found for the QET molecules (Table 4-5). Moreover, the slope changes to -2.2 at an average internal energy of 7.0 eV for the M^+ ion of *n*-octylbenzene similar to the increase seen with the M^+ ion of benzene (QET crossover energy = 5.6 eV). Thus, the conclusion that

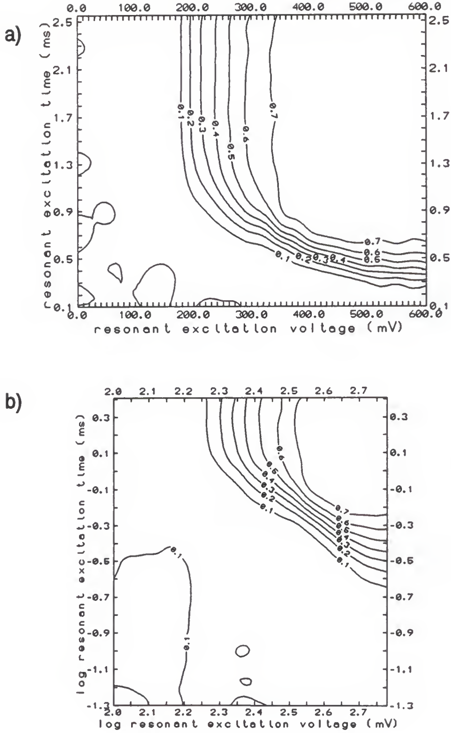

Figure 5-6: Topographical plot of a) the collision-induced dissociation breakdown surface of the M^+ ion of *n*-butylbenzene showing the $91^+/92^+$ ratio presented in Figure 5-5a. b) The same data on a log-log scale. *n*-Butylbenzene at ≈ 2.0×10^{-6} torr; He buffer gas added to 1.0×10^{-4} torr.

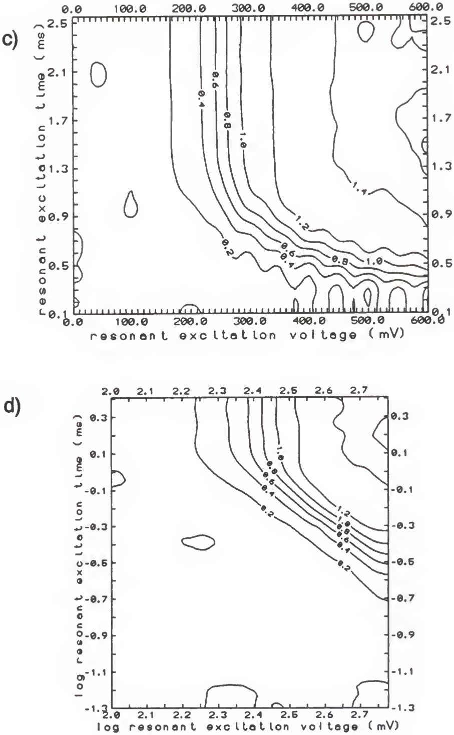

Figure 5-6: (continued) Topographical plot of c) the collision-induced dissociation breakdown surface of the M$^+$ ion of *n*-pentylbenzene showing the 91$^+$/92$^+$ ratio presented in Figure 5-5b. d) The same data on a log-log scale. *n*-Pentylbenzene at ≈ 2.0x10^{-6} torr; He buffer gas added to 1.0x10^{-4} torr.

e)

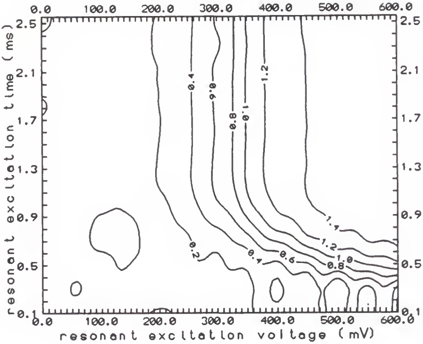

f)

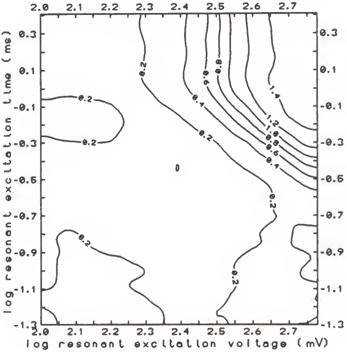

Figure 5-6: (continued) Topographical plot of e) the collision-induced dissociation breakdown surface of the M$^+$ ion of *n*-hexylbenzene showing the 91$^+$/92$^+$ ratio presented in Figure 5-5c. f) The same data on a log-log scale. *n*-Hexylbenzene at ≈ 2.0x10^{-6} torr; He buffer gas added to 1.0x10^{-4} torr.

g)

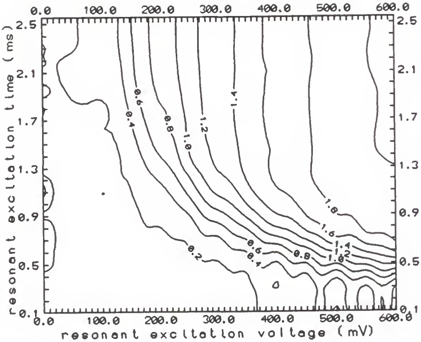

h)

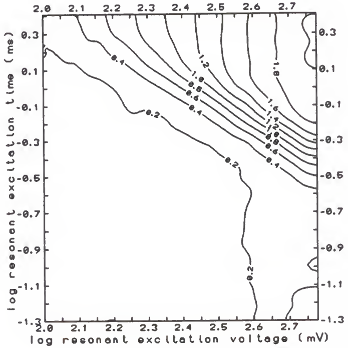

Figure 5-6: (continued) Topographical plot of g) the collision-induced dissociation breakdown surface of the M^+ ion of *n*-octylbenzene showing the $91^+/92^+$ ratio presented in Figure 5-5d. h) The same data on a log-log scale. *n*-Octylbenzene at ≈ 2.0×10^{-6} torr; He buffer gas added to 1.0×10^{-4} torr.

Table 5-1: Slopes of the resonant excitation voltage versus excitation time in the log-log CID topographical plots at selected $91^+/92^+$ ratios for the M^+ ions of the *n*-alkylbenzenes.

n-alkylbenzene	$91^+/92^+$ contour	average internal energy (eV)*	slope
butyl	0.6	2.6	-1.2
	0.7	2.7	-1.2
pentyl	0.6	3.4	-1.5
	1.2	4.0	-1.6
hexyl	0.6	3.7	-1.4
	1.0	4.4	-1.8
octyl	0.6	4.0	-1.4
	1.6	7.0	-2.2

* Average internal energies assigned from Figure 5-2 (Nacson and Harrison, 1985).

longer resonant excitation times are required for higher internal energy deposition appears to be a general feature of CID on the QITMS. Another feature common to the log-log topographical representations is that at lower resonant excitation voltages ($< \approx$ 200 mV), the contour lines show a dramatic change in slope. A similar break in the log-log plots of the resonant excitation voltage versus excitation time was found for the CID of the $(M+H)^+$ ion of diethyl ethylphosphonate (Johnson *et al.*, 1990b). These breaks indicate that cooling of the ions due to collisions with the He buffer successfully competes with collisional activation at lower resonant excitation amplitudes.

Two-dimensional CID Breakdown Graphs

Sample two-dimensional CID time-resolved breakdown graphs and voltage-resolved graphs for the M^+ ions of *n*-butylbenzene, *n*-pentylbenzene, *n*-hexylbenzene, and *n*-octylbenzene are presented in Figures 5-7a through g. Note that in the voltage-resolved breakdown graph for the M^+ ion of *n*-butylbenzene (Figure 5-7a) the M^+ ion is dissociated or ejected in 1.5 ms using a 600 mV excitation and that the voltage-resolved graph for the M^+ ion of *n*-octylbenzene clearly shows that the *m/z* 91 ion has not reached a plateau value. The fluences and CID efficiencies (E_f, E_c, and E_{CID}) calculated from the time-resolved breakdown graphs using 300 mV and 500 mV resonant excitation amplitudes are presented in Table 5-2. The time-resolved graphs were chosen for the calculation of the CID efficiencies since the voltage-resolved graphs were reconstructed from 30 time-resolved experiments acquired over a 60-minute as opposed to a 2-minute time period required for each of the time-resolved graphs. The fluence values indicate that larger amounts of resonant energy are required to reach the plateau values as the size of the *n*-alkyl group is increased. Lower fluences are required at higher excitation

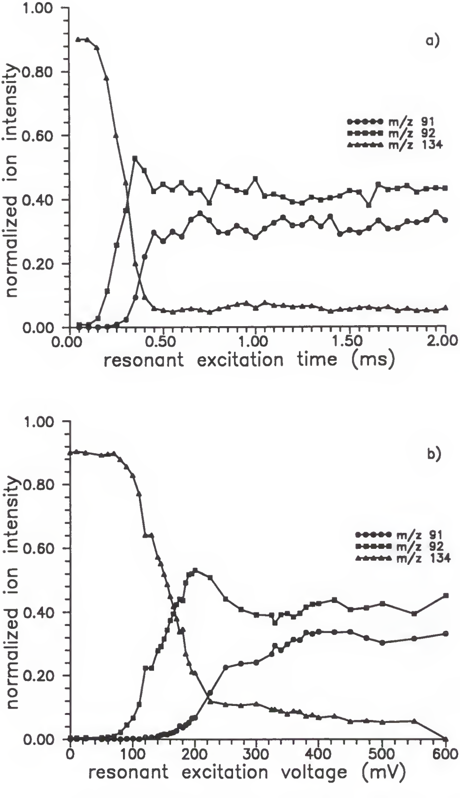

Figure 5-7: a) Time-resolved collision-induced dissociation breakdown graph of the M^+ ion of *n*-butylbenzene using a 500 mV excitation amplitude. b) Voltage-resolved breakdown graph at a 1.5 ms excitation time. *n*-Butylbenzene at ≈ 2.0×10^{-6} torr; He buffer gas added to 1.0×10^{-4} torr.

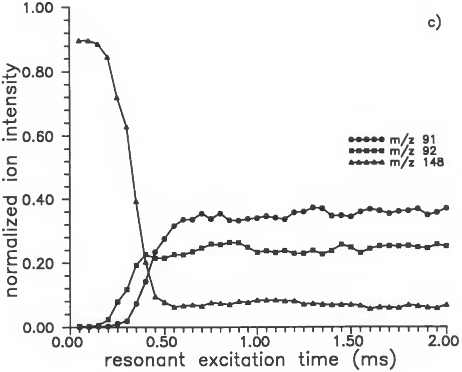

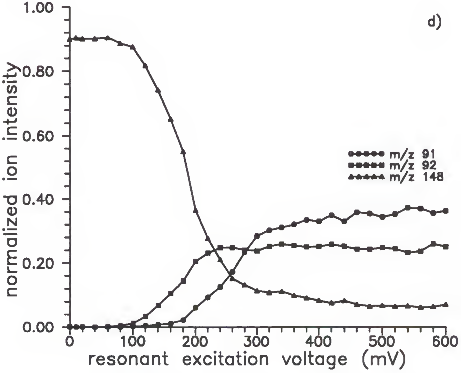

Figure 5-7: (continued) c) Time-resolved collision-induced dissociation breakdown graph of the M^+ ion of *n*-pentylbenzene using a 500 mV excitation amplitude. d) Voltage-resolved breakdown graph at a 1.5 ms excitation time. *n*-Pentylbenzene at ≈ 2.0×10^{-6} torr; He buffer gas 1.0×10^{-4} torr.

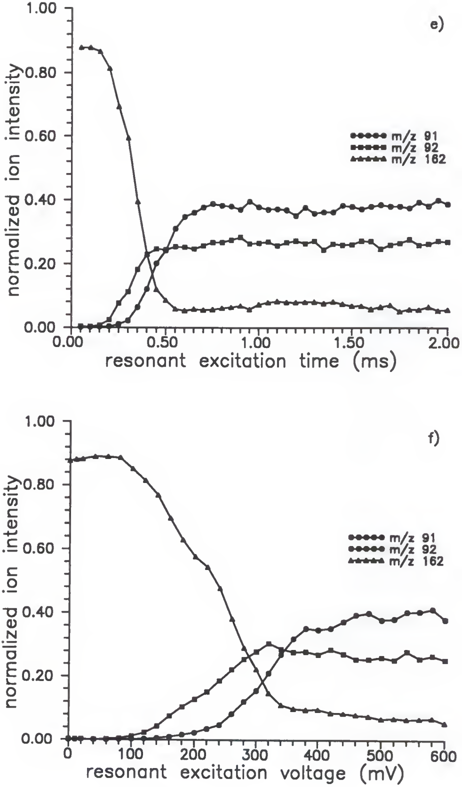

Figure 5-7: (continued) e) Time-resolved collision-induced dissociation breakdown graph of the M^+ ion of *n*-hexylbenzene using a 500 mV excitation amplitude. f) Voltage-resolved breakdown graph at a 1.5 ms excitation time. *n*-Hexylbenzene at ≈ 2.0×10^{-6} torr; He buffer gas to 1.0×10^{-4} torr.

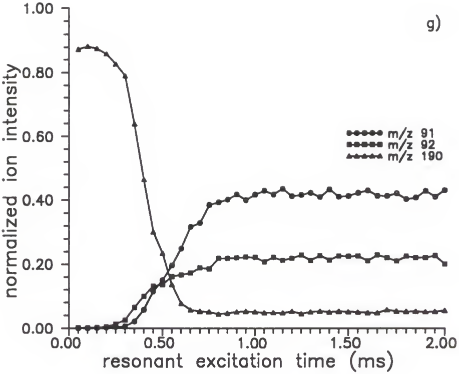

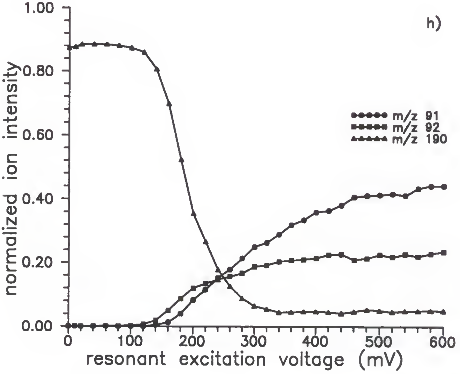

Figure 5-7: (continued) g) Time-resolved collision-induced dissociation breakdown graph of the M^+ ion of *n*-octylbenzene using a 500 mV excitation amplitude. h) Voltage-resolved breakdown graph at a 1.5 ms excitation time. *n*-Octylbenzene at ≈ 2.0×10^{-6} torr; He buffer gas 1.0×10^{-4} torr.

Table 5-2: Fluences and CID efficiencies for the M^+ ions of the *n*-alkylbenzenes calculated at the onset of the $91^+/92^+$ plateaus.

n-alkylbenzene[a]	excitation voltage ($V_{0\text{-}p}$)	plateau time (ms)	fluence (Vms)	normalized fluence	CID efficiencies[b] E_f (%)	E_c (%)	E_{CID} (%)
butyl	0.300	1.05	0.315	0.78	94	54	51
pentyl	0.300	1.15	0.345	0.85	93	62	58
hexyl	0.300	1.20	0.365	0.90	85	75	64
octyl	0.300	1.35	0.405	1.0	94	64	60
butyl	0.500	0.55	0.275	0.61	96	26	25
pentyl	0.500	0.65	0.325	0.72	95	31	30
hexyl	0.500	0.75	0.375	0.83	96	30	29
octyl	0.500	0.90	0.450	1.0	96	41	40

[a] *n*-Alkylbenzene pressures ≈ 2.0×10^{-6} torr (uncorrected ion gauge reading).

[b] E_f = fragmentation efficiency; E_c = collection efficiency; E_{CID} = CID efficiency.

amplitudes due to a decrease in the requisite excitation time. The resulting efficiency values indicate that while the E_f values remain ≈ 94%, the E_c values decrease as the amplitude is increased due to increased trapping losses. (This trend is not apparrent in the normalized CID breakdown graphs in Figures 5-7 a through h). This is in keeping with the trend in CID efficiencies reported by Louris *et al.* (1987) and Johnson *et al.* (1990a).

The $91^+/92^+$ ratios for the M^+ ions of the *n*-alkylbenzenes from the time-resolved breakdown graphs using a 500 mV amplitude and the voltage-resolved graphs using a 1.5 ms excitation time are presented in Figures 5-8a and b, respectively. In general, the $91^+/92^+$ ratio is found to increase as the size of the alkyl group is increased, although the *n*-pentylbenzene and *n*-hexylbenzene have approximately the same plateau value. Table 5-3 presents the $91^+/92^+$ ratios, fluences (from Table 5-2), assigned average internal energies (from the CEMS breakdown graphs in Figure 5-2), and the corresponding percent energy transfer, *%E*, calculated from the the time-resolved breakdown graphs using 300 mV and 500 mV excitation amplitudes. The *%E* values were calculated using the *maximum* kinetic energy of the ion prior to ejection. $K.E._{max}$, calculated from the Dehmelt pseudo-potential well depth for the M^+ ions at a $q_z = 0.300$. The E_{cm} values were calculated using equation 4-1 by setting $K.E._{cm} = E_{lab}$ and thus represent the *maximum* amount of energy that can be transferred to the M^+ ion upon a *single* collision with a He buffer gas atom. The assigned average internal energies transferred and the corresponding *%E* values are found to increase as the size of the *n*-alkyl group is increased. This agrees with the trend in average and percent energy transferred reported by Nacson and Harrison (1985) for the M^+ ions of the *n*-alkylbenzenes in the TQMS. The trend in energy transfer in the present study indicates

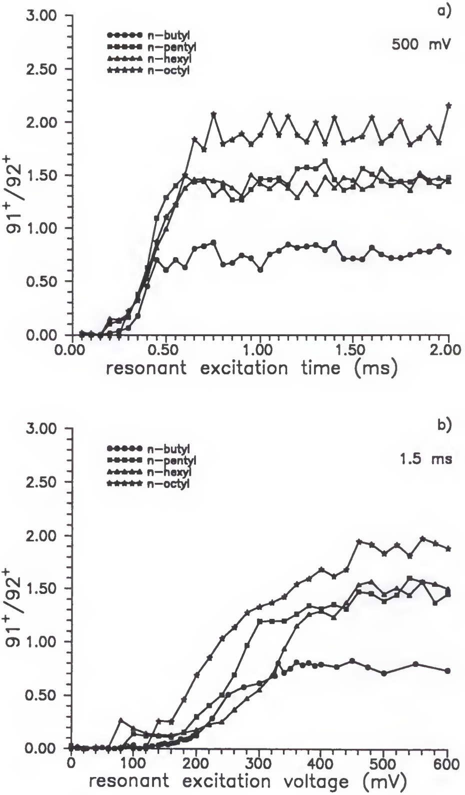

Figure 5-8: The $91^+/92^+$ ratios from a) time-resolved collision-induced dissociation of the M^+ ions of the *n*-alkylbenzenes, 500 mV excitation amplitude and b) voltage-resolved CID of the M^+ ions, 1.5 ms excitation time. *n*-Alkylbenzenes at $\approx 2.0\times10^{-6}$ torr; He buffer gas 1.0×10^{-4} torr.

Table 5-3: Internal energies and percent energy conversions from the *n*-alkylbenzene thermometers.

n-alkylbenzene[a]	MW (amu)	normalized fluence	$91^+/92^+$	internal energy[b] (eV)	$\overline{D}_z$[c] (V)	$K.E._{max,total}$[c] (eV)	E_{cm}[d] (eV)	%*E*[e]
				300 mV resonant excitation				
butyl	134	0.78	0.65	2.7 ± 0.1	19	38	1.1	250
pentyl	148	0.85	1.15	4.12 ± 0.09	21	42	1.1	375
hexyl	162	0.90	0.59	3.66 ± 0.09	23	46	1.1	330
octyl	190	1.0	1.30	6.2 ± 0.3	27	54	1.1	565
				500 mV resonant excitation				
butyl	134	0.61	0.75	2.9 ± 0.2	19	38	1.1	265
pentyl	148	0.72	1.43	4.4 ± 0.1	21	42	1.1	400
hexyl	162	0.83	1.45	5.0 ± 0.1	23	46	1.1	455
octyl	190	1.0	1.90	7.5 ± 0.4	27	54	1.1	680

[a] *n*-Alkylbenzene pressures ≈ 2.0×10^{-6} torr (uncorrected ion gauge reading).

[b] Internal energies assigned from Nacson and Harrison, 1985. Errors expressed as range of internal energies arising from the range of observed $91^+/92^+$ ratios.

[c] $\overline{D}_z$ and $K.E._{max,total}$ values calculated with Equations 1-16 and 1-18 using $V_{0\text{-}p}$ values for the drive rf potential.

[d] E_{cm} calculated with respect to He buffer gas.

[e] %*E* calculated from assigned internal energy divided by E_{cm}.

that the CID mechanism in the QITMS is similar to that thought to occur in a TQMS. Thus, the low-energy CID process likely occurs *via* the formation of a relatively long-lived M^+-N collision complex, (where N= the target gas species) in which the relative translational energy of the collision is converted into vibrational energy of the ion leading to the dissociatin of the ion (Douglas, 1982; Dawson and Douglas, 1983). Based on this model, there should be a more efficient translational to vibrational energy as the number of vibrational degrees of freedom of the M^+ ion increases. This is reflected in the effect of the *n*-alkyl group size on the average and %*E* transfer observed in both the low-energy TQMS and present QITMS results.

The percent energies transferred in Table 5-3 calculated from the E_{cm} energy available in a *single* collision with a He atom are greater than 100% for all of the *n*-alkylbenzenes, and increase to as high as 680% for the M^+ ion of *n*-octylbenzene using 500 mV excitation. This indicates that the CID process in the QITMS must be occurring *via* multiple collisions. The number of collisions per millisecond can be estimated from the Langevin approximation presented in chapter 2 (equation 2-21). Using the collision rates calculated for CH_4^+ in He, the M^+ ions of the *n*-alkylbenzenes will experience ≈ 8 collisions ms^{-1} in He buffer at 1.0×10^{-4} torr. (Note that in this calculation the He pressure was corrected with the ion gauge correction factor of 5.1 presented in Table 2-1). The $91^+/92^+$ ratio for the M^+ ion of *n*-butylbenzene reaches a plateau value in ≈ 0.45 ms (Figure 5-8a) which corresponds to ≈ 4 collisions with the He buffer. Thus, if each collision is ≈ 63% efficient, a %*E* = 250% can be obtained. The $91^+/92^+$ ratios of the M^+ ions of *n*-pentylbenzene, *n*-hexylbenzene, and *n*-octylbenzene reach plateau values in ≈ 0.65 ms, corresponding to ≈ 5 collisions with the He buffer. However, to acheive the 680% energy transfer to the M^+ ion of *n*-octylbenzene, each of the 5 collisions would have to result in an ≈ 140% energy transfer. This indicates that the Langevin approximation is likely underestimating the number of collisions per millisecond. Moreover, recall that the %*E* values were calculated assuming the that the ions were travelling with the *maximum* kinetic energy predicted by the pseudo-potential well model. For ions travelling with less than this maximum energy, an ever greater number of collisions would be required to deposit the internal energies presented in Table 5-3. A more complete calculation of the total number of collisions which lead to the dissociation of an M^+ ion in the QITMS would have to consider not only the number density of the He atoms, but also the path length travelled by the ion under a given set of resonant excitation conditions. This in turn would be a function of the initial internal energy distribution of the ions and the kinetic energy distribution of the ions upon resonant excitation (McLuckey *et al.*, 1991a).

Variable He Buffer and *n*-Butylbenzene Pressure Studies

Variable He buffer and *n*-butylbenzene pressure studies were undertaken to determine what, if any, role the pressures of these neutrals play in the mechanism and energetics of the CID process in the QITMS. *n*-Butylbenzene was chosen for these studies since it is the most well-studied of the *n*-alkylbenzenes of interest.

The time-resolved breakdown graphs for the M^+ ion of *n*-butylbenzene showing the *m/z* 134 and 92 ions at a variety of He buffer gas pressures using 500 mV excitation and $2.6\text{x}10^{-6}$ torr of *n*-butylbenzene are presented in Figure 5-9a. The corresponding relative intensities of the *m/z* 91 ions are shown in Figure 5-9b. As the He buffer is increased from $2.0\text{x}10^{-5}$ torr to $2.2\text{x}10^{-4}$ torr, the onset of dissociation of the M^+ ions (*m/z* 134) shifts towards longer excitation times. This indicates that at higher He pressures

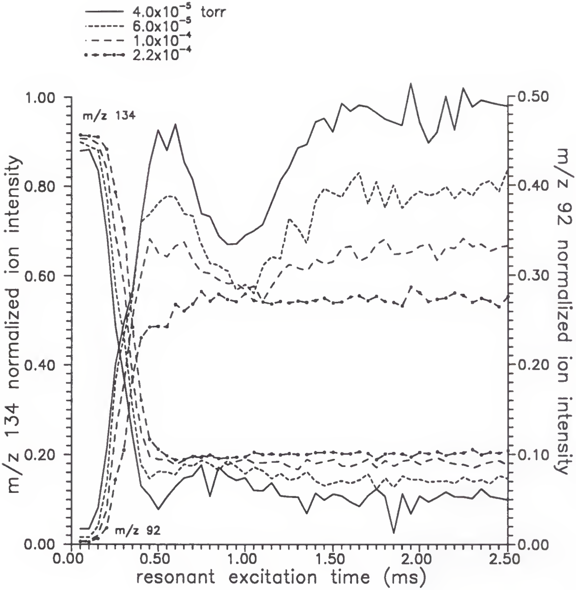

Figure 5-9: a) The time-resolved collision-induced dissociation breakdown graph of the M$^+$ ion of *n*-butylbenzene showing the relative intensities of the *m/z* 134 and *m/z* 92 ions at a variety of He buffer gas pressures. *n*-Butylbenzene at 2.6x10^{-6} torr; 500 mV resonant excitation amplitude.

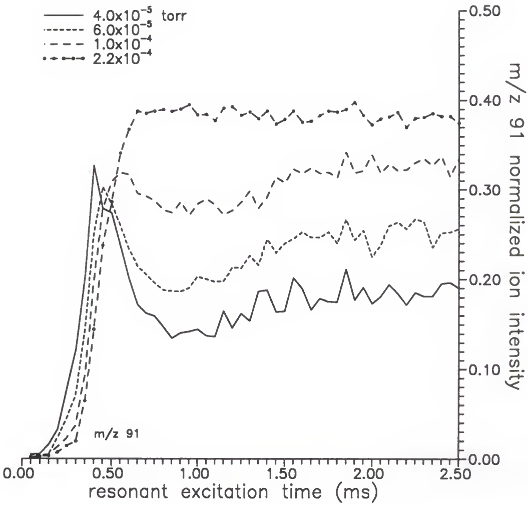

Figure 5-9: (continued) b) The *m/z* 91 ion intensities following collision-induced dissociation of the M^+ ion of *n*-butylbenzene at a variety of He buffer gas pressures. *n*-Butylbenzene at 2.6x10^{-6} torr; 500 mV resonant excitation amplitude.

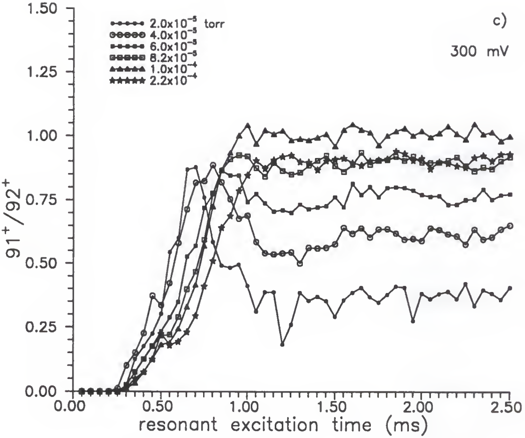

Figure 5-9: (continued) The $91^+/92^+$ ratios from the time-resolved collision-induced dissociation of the M^+ ions of *n*-butylbenzene at a variety of He buffer gas pressures using c) a 300 mV resonant excitation amplitude. *n*-Butylbenzene at ≈ 2.6×10^{-6} torr.

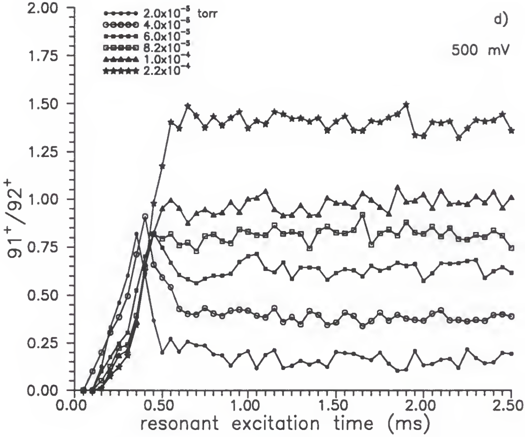

Figure 5-9: (continued) The $91^+/92^+$ ratios from the time-resolved collision-induced dissociation of the M^+ ions of *n*-butylbenzene at a variety of He buffer gas pressures using d) a 500 mV resonant excitation amplitude. *n*-Butylbenzene at ≈ 2.6×10^{-6} torr.

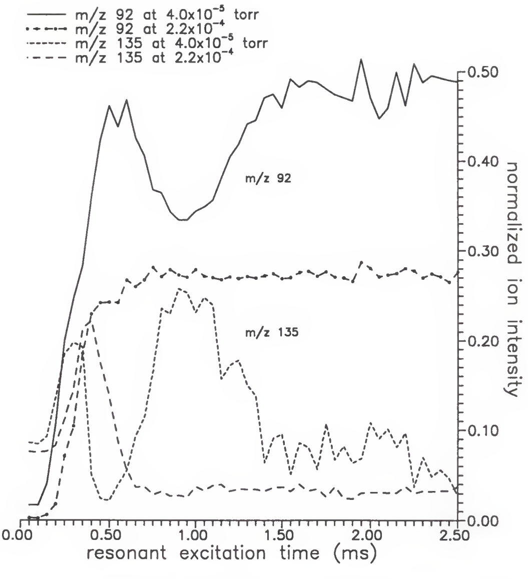

Figure 5-9: (continued) e) The *m/z* 92 and *m/z* 135 ion intensities from the time-resolved collision-induced dissociation breakdown graph of the M$^+$ ion of *n*-butylbenzene at He buffer pressures of 4.0x10^{-5} torr and 2.2x10^{-4} torr. *n*-Butylbenzene at 2.6x10^{-6} torr; 500 mV resonant excitation amplitude.

the initial M^+ ions are lower in internal energy due to increased collisional cooling prior to mass-selection and during resonant excitation; thus longer resonant excitation times are required to induce dissociation. Moreover, the relative intensity of the undissociated M^+ ions also increases as the He buffer pressure is increased. This is also likely due to the increase in momentum-loss versus activating collisions at the higher He buffer pressures resulting in fewer dissociated M^+ ions. The *m/z* 92 ion intensities (Figure 5-9a) are found to decrease as the He buffer pressure is increased, while the *m/z* 91 ion intensities show the opposite trend (Figure 5-9b). (The minima in the *m/z* 92 curve at $4.0x10^{-5}$ torr will be discussed in greater detail below).

The $91^+/92^+$ ratios over the range of He pressures employed using a 300 mV resonant excitation amplitude are presented in Figure 5-9c; the corresponding ratios using a 500 mV excitation are presented in Figure 5-9d. The onet of dissociation occurs at approximately twice the excitation time ($\approx$ 0.3 ms) using a 300 mV amplitude than it does using a 500 mV amplitude ($\approx$ 1.5 ms). Moreover, the $91^+/92^+$ ratios are found to rise at an initially greater rate at lower He pressures. In all cases, the $91^+/92^+$ ratios are found to reach plateau values; however, at lower He buffer pressures, the $91^+/92^+$ ratios reach a maxima, and then decrease to a plateau value. The initially higher rate of increase of the $91^+/92^+$ ratios and the formation of maxima followed by a plateau at lower He pressures may be attributed to different energy deposition mechanisms active at the lower versus the higher He pressures. According to the Langevin approximation, the M^+ ions of *n*-butylbenzene will experience at least 1.5 collisions ms^{-1} at $2.0x10^{-5}$ torr (based on the collision rate of CH_4^+ in He in Table 2-7); at a ten-fold greater pressure of $2.2x10^{-4}$ torr, the M^+ ions will experience at least 15 collisions ms^{-1}. Thus, the $91^+/92^+$ ratio found, for example, at 0.50 ms and $2.0x10^{-5}$ torr corresponds to the fragment ion ratio following ≈ 1 collision; that at 2.2×10^{-4} torr corresponds to the ratio following ≈ 10 collisions. The *m/z* 91 and 92 ions formed under the single-collision conditions likely have more internal energy than those formed under multiple collision conditions since the M^+ ion will have had higher kinetic energy upon collision due to the decreased number of momentum-loss collisions at lower He pressures. This increased internal energy of the *m/z* 91 and 92 ions would allow the opening of other reaction channels leading to a decrease in the *m/z* 91 or 92 ion intensities. One such channel is the proton transfer between the *m/z* 92 ion and the neutral *n*-butylbenzene presented in Figure 5-9e. Figure 5-9e clearly shows that there is a correlation between the decrease in intensity of the *m/z* 92 ion following the maimum of the $91^+/92^+$ ratio.

The reason for the minimum in the *m/z* 92 ion intensity and corresponding maximum in the *m/z* 135 ion intensity in Figure 5-9e is less clear. The fact that the depth of the *m/z* 92 minimum decreases as the He buffer pressure increases implies that the proton transfer reaction is related to the internal energy of the *m/z* 92 ion. One possible explanation is that the *m/z* 92 ion formed upon CID of the M^+ ion of *n*-butylbenzene may be isomerizing to a structure with a higher proton affinity than *n*-butylbenzene; as such the rate of proton transfer to *n*-butylbenzene would decrease as the isomerization proceeds. A second possible explanation is that upon formation of a sufficient population of *m/z* 135 ions at longer excitation times, the proton transfer reaction with the *m/z* 92 ions reaches an equilibrium. Futher studies into the reactivity of the mass-selected *m/z* 92 ion formed upon CID of the M^+ ion of *n*-butylbenzene would be required to determine which, if either, of the mechanisms is active.

The internal energies assigned from the PEPICO breakdown graph (Figure 5-1) based on the $91^+/92^+$ ratios in Figures 5-9c and d are presented in Table 5-4. It should

Table 5-4: Internal energies and CID efficiencies for the M$^+$ ion of *n*-butylbenzene at various He buffer pressures.

300 mV resonant excitation

He pressure[a] (/10^{-5} torr)	time (ms)	$91^+/92^+$	internal energy[b] (eV)
2.0	0.70[*]	0.86	3.8_0
4.0	0.78[*]	0.89	3.8_4
6.0	0.93[*]	0.85	3.8_0
8.2	0.95	0.92	3.8_7
10	1.05	1.00	3.9_4
22	1.08	0.92	3.8_7
	500 mV resonant excitation		
2.0	0.35[*]	0.82	3.7_5
4.0	0.45[*]	0.90	3.8_5
6.0	0.50	0.82	3.7_5
8.2	0.53	0.82	3.7_5
10	0.51	1.00	3.9_4
22	0.74	1.43	4.3_0

[a] He buffer pressures are uncorrected ion gauge readings. All studies performed with 2.6×10^{-6} torr of *n*-butylbenzene (uncorrected ion gauge reading).

[b] All ion energies were assigned from the $91^+/92^+$ plateau values except [*] which were read from the $91^+/92^+$ maxima. Internal energies assigned from PEPICO breakdown graph (Baer *et al.*, 1988) and corrected for thermal energy of the neutrals. Estimated 95% confidence limits of ± 0.3 eV.

be noted that the ion energies at the lower He pressures (2.0×10^{-5}, 4.0×10^{-5}, and 6.0×10^{-5} torr) were assigned based on the maximum $91^+/92^+$ ratios as opposed to the plateau values, since the maxima reflect the *m/z* 91 and 92 ion intensities prior to any subsequent reaction. The average internal energy of the M^+ ions is 3.83 ± 0.05 eV over the range of He buffer pressures studied, with somewhat of an increase to 4.30 eV at 2.2×10^{-4} torr using a 500 mV excitation. Based on these assignments, the pressure of the He buffer gas appears to play a relatively small role in the average energy transferred on collision over the range of He buffer pressures employed until higher excitation amplitudes are employed. It is interesting to compare the ion internal energies assigned from the $91^+/92^+$ plateau values in Figures 5-9 c and d versus those assigned from the maxima. Assignments from the plateau values result in an increase in the internal energy from $\approx$ 3.2 eV to $\approx$ 4.1 eV at a 300 mV amplitude and in an increase from 2.2 eV to 4.4 eV at 500 mV. It is therefore important to consider the time at which the $91^+/92^+$ ratios are read prior to assigning internal energies with this thermometer.

Time-resolved breakdown graphs for the M^+ ion of *n*-butylbenzene showing the *m/z* 134 and 92 ions at a variety of *n*-butylbenzene pressures using 500 mV excitation and 1.0×10^{-4} torr of He are presented in Figure 5-10a. The corresponding relative intensities of the *m/z* 91 ions are shown in Figure 5-10b. Note that in comparison to the ion intensities in Figure 5-9a, as the *n*-butylbenzene pressure is increased from 9.8×10^{-7} to 5.6×10^{-6} torr, the dissociation onset remains relatively constant at $\approx$ 0.15 ms. This indicates that *n*-butylbenzene pressure is not playing a role in determining the initial internal energy distribution of the M^+ ions. The relative intensities of the *m/z* 134 parent ions are again found to increase as the *n*-butylbenzene pressure is increased. Since the M^+ ions will have experienced the same number of collisions with the He buffer over the

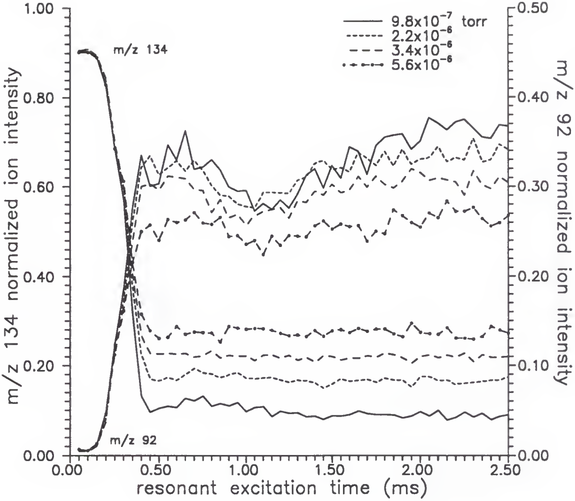

Figure 5-10: a) The time-resolved collision-induced dissociation breakdown graph of the M$^+$ ion of *n*-butylbenzene showing the relative intensities of the *m/z* 134 and *m/z* 92 ions at a variety of *n*-butylbenzene pressures. He buffer at 1.0x10^{-4} torr; 500 mV resonant excitation amplitude.

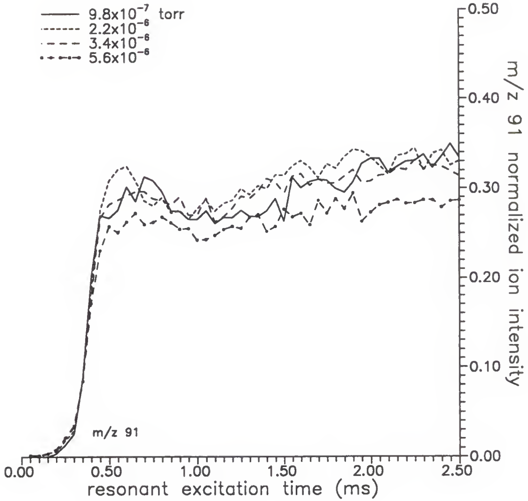

Figure 5-10: (continued) b) The *m/z* 91 ion intensities following collision-induced dissociation of the M^+ ion of *n*-butylbenzene at a variety of *n*-butylbenzene pressures. He buffer at 1.0×10^{-4} torr; 500 mV resonant excitation amplitude.

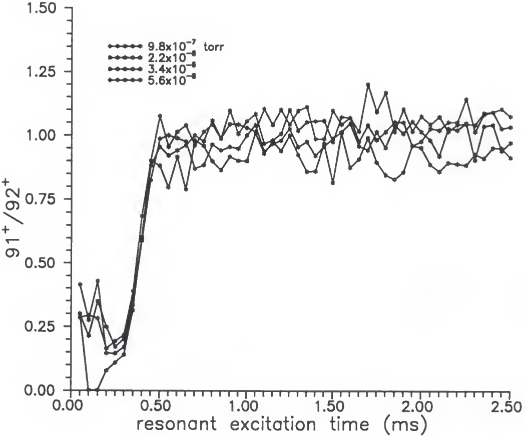

Figure 5-10: (continued) c) The $91^+/92^+$ ratios from the time-resolved collision-induced dissociation of the M^+ ions of *n*-butylbenzene at a variety of *n*-butylbenzene pressures. He buffer at 1.0×10^{-4} torr; 500 mV excitation amplitude.

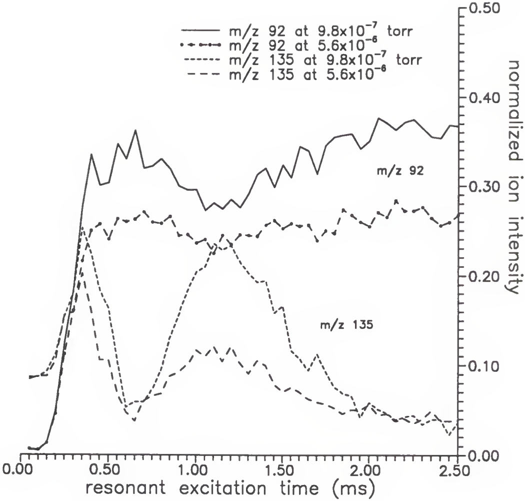

Figure 5-10: (continued) d) The *m/z* 92 and *m/z* 135 ion intensities from the time-resolved collision-induced dissociation breakdown graph of the M$^+$ ion of *n*-butylbenzene at *n*-butylbenzene pressures of 9.8x10^{-7} torr and 5.6x10^{-6} torr. He buffer at 1.0x10^{-4} torr; 500 mV resonant excitation amplitude.

range of *n*-butylbenzene pressures employed, this increase in *m/z* 134 ion intensity may be arising from reactions which regenerate the *m/z* 134 ions. These reactions include symmetric charge transfer between the M^+ ion and neutral *n*-butylbenzene, or charge transfer from either of the *m/z* 91 or 92 fragment ions to *n*-butylbenzene. The *m/z* 92 ion intensities in Figure 5-9a are found to decrease as the *n*-butylbenzene pressure is increased, similar to the trend noted in in Figure 5-9a with increasing He buffer pressure. However, in contrast to Figure 5-9b, the *m/z* 91 intensities in Figure 5-10b remain relatively constant over the range of *n*-butylbenzene pressures employed. The $91^+/92^+$ ratio presented in Figure 5-10c are found to remain constant at ≈ 1.0 (corresponding to ≈ 3.9 eV) over the range of *n*-butylbenzene pressures employed. This again suggests that the *n*-butylbenzene pressure is playing no role in the average internal energy of the M^+ ions even upon resonant excitation.

A minimum is again noted in the *m/z* 92 ion curves in Figure 5-10a which is of approximately the same order of magnitude as that found for the *m/z* 92 curve in Figure 5-9a corresponding to 1.0×10^{-4} torr of He. This indicates that collisions with the He buffer are playing the principal role in the processes which give rise to the minima. Reaction between the *m/z* 92 ions and the neutral *n*-butylbenzene is again evident in the plots of the *m/z* 92 and 135 ion intensities in Figure 5-10d, indicating that the $91^+/92^+$ ratios can be affected by subsequent reactions as the *n*-butylbenzene pressure is varied.

The variable He buffer and *n*-butylbenzene pressure studies indicate that the CID breakdown graphs may reflect a number of competeing dissociation, proton transfer, and charge exchange reactions. CID of a resonantly excited M^+ ion can be considered to involve the following possible reactions:

$$M^{+} + He \rightarrow M^{+}(cooled) + He \quad (5\text{-}10)$$

$$\rightarrow F_i^{+} + N_i + He \quad (5\text{-}11)$$

$$M^{+} + M \rightarrow M + M^{+}(cooled) \quad (5\text{-}12)$$

$$\rightarrow F_i^{+} + N_i + M \quad (5\text{-}13)$$

$$F_i^{+} + M \rightarrow F_i + M^{+} \quad (5\text{-}14)$$

$$\rightarrow (F_i\text{-}H) + (M{+}H)^{+} \quad (5\text{-}15)$$

$$F_i^{+} + F_i \rightarrow F_i + F_i^{+} \quad (5\text{-}16)$$

$$\rightarrow (F_i\text{-}H) + (F_i{+}H)^{+} \quad (5\text{-}17)$$

where F_i^{+} and N_i are the fragment and neutral species, respectively.

Collision of the M^{+} ion with a He buffer gas atom (reaction 5-10) can involve either momentum transfer from the M^{+} ion to He resulting in a "cooling" of the M^{+} ion, or it can result in internal excitation of the M^{+} ion and possible subsequent fragmentation (reaction 5-11). The momentum-loss process plays a central role since, in the absence of He buffer, application of a resonant excitation potential results in trapping losses by resonant ejection of the M^{+} ion with little or no dissociation. Internal excitation of the M^{+} ion *via* a single collision with He can transfer up to an estimated 1.1 eV of internal energy, based on the maximum E_{cm} for an ion of *m/z* 134 and He at a $q_z(M^{+}) = 0.300$ (Table 5-3). Since the activation energy, ϵ_0, for the formation of *m/z* 92 from the M^{+} ion of *n*-butylbenzene is 1 eV (Baer *et al.*, 1988), a single collision of M^{+} ion with a He atom with 90% energy transfer can lead to the formation of the *m/z* 92 fragment ion. However, formation of the *m/z* 91 ion requires ≈ 1.7 eV of energy (Baer *et al.*, 1988), and as such, multiple activating collision of M^+ ion with the He buffer would be required if the calculated maximum E_{cm} values are correct.

Direct evidence of the symmetric charge exchange reaction between M^+ ion and M (reaction 5-12) is difficult to elucidate from the present studies, although the increase in the *m/z* 134 ion intensities with increasing *n*-butylbenzene pressure (Figure 5-10a) suggests that this reaction may be playing a significant role. However, the increasing *m/z* 134 ion intensities may also be attributed to charge exchange between the *m/z* 91 and 92 fragment ions and *n*-butylbenzene (reaction 5-14). Collision of an M^+ ion with neutral *n*-butylbenzene may also lead to CID of the M^+ ion (reaction 5-13) since the E_{cm} is ≈ 17x greater for a collision of an *m/z* 134 ion with a neutral *n*-butylbenzene molecule than with a neutral He atom. However, the variable *n*-butylbenzene pressure study indicates that the $91^+/92^+$ ratio is unaffected by the *n*-butylbenzene pressure and as such reaction 5-13 likely is playing a minor role. Direct evidence of the symmetric charge exchange reactions 5-14 and 5-16 is also difficult to elucidate, although these reaction should have no effect on the final $91^+/92^+$ ratio. However, the proton transfer reaction 5-15 witnessed for the *m/z* 92 ions in Figures 5-9e and 5-10d does ultimately affect the measured $91^+/92^+$ ratio. Further studies are necessary to elucidate the relative rates of these competing reactions and what role they may be playing in the resulting $91^+/92^+$ ratios and thus the assigned average ion internal energies.

Conclusions

This chapter presents the breakdown surfaces of the $91^+/92^+$ ratios arising from the collision-induced dissociation of the M^+ ions of *n*-butylbenzene, *n*-pentylbenzene, *n*-hexylbenzene, and *n*-octylbenzene. The $91^+/92^+$ ratios of the M^+ ions of *n*-butylbenzene and *n*-pentylbenzene are found to reach characteristic plateau values over the range of resonant excitation times (0 to 2.5 ms) and voltages employed (0 to 600 mV). The $91^+/92^+$ ratios for the M^+ ions of *n*-hexylbenzene and *n*-octylbenzene are found to reach plateau values over the range of excitation times employed, and are approaching plateau values over the range of excitation voltages employed. These plateau values indicated that there is a limit to amount of internal energy which can be depositied under a given set of resonant excitation conditions. These limiting values are attributed to the successful competition of momentun-loss versus activating collisions with the He buffer gas atoms as the resonant excitation times are increased. The avaerage internal energy transferred upon resonant excitation were assigned from the observed $91^+/92^+$ ratios based on the previously reported charge exchange breakdown graphs for the M^+ ions of the *n*-alkylbenzenes (Nacson and Harrison, 1988). The average ion internal energy at a $q_z(M^+) = 0.300$ varies from ≈ 1.5 eV for the M^+ ion of *n*-butylbenzene using 100 mV excitation, to ≈ 7.5 eV for the M^+ ion of *n*-octylbenzene using 500 mV excitation. This range of internal energies is in good agreement with previously reported values (Louris *et al.*, 1987; Brodbelt *et al.*, 1988a; Johnson *et al.*, 1990a). The average internal energy transferred is found to increase as the size of the *n*-alkyl group of the M^+ ion is increased. This suggests that the CID process likely proceeds *via* a two-step activation/dissociation mechanism similar to that proposed for the low-energy CID process in a TQMS (Douglas, 1982; Nacson and Harrision, 1988).

In the variable He buffer pressure studies, the $91^+/92^+$ ratios in the time-resolved CID breakdown graphs are found to first reach a maxima and then decrease to a plateau value at low He pressures. The maxima are not seen at higher He pressures. If the ion internal energies are assigned from the maximum $91^+/92^+$ ratios, ion energies of ≈3.8eV are found for the M^+ ions upon resonant excitation, with little change in energy over the range of He buffer pressures employed ($2.0x10^{-5}$ torr to $2.2x10^{-4}$ torr), except, perhaps, at high pressures ($2.2x10^{-4}$ torr) and high excitation amplitudes (500 mV), where the maximum $91^+/92^+$ ratio results in an ion internal energy of ≈ 4.3 eV. The internal energy deposited at low He buffer pressures is attributed to the higher ion kinetic energies attained under the near single-collision conditions, whereas the internal energy deposited at the higher He pressures is due to multiple activating collisions with the He buffer. The variable *n*-butylbenzene pressure studies reveal that the *n*-butylbenzene pressure plays no role in the average ion internal energy over the range of *n*-butylbenzene pressures employed. In both the varaible He buffer and *n*-butylbenzene pressure studies there is evidence of the proton transfer reaction from the *m/z* 92 fragment ion to neutral *n*-butylbenzene resulting in the formation of the $(M+H)^+$ at *m/z* 135 at excitation times > 0.50 ms. This indicates that the time-resolved CID breakdown graphs may reflect a number of competeing dissociation, proton transfer, and charge exchange reactions. Further studies are necessary to elucidate the relative rates of these competing reactions to determine what role they may be playing in the measure $91^+/92^+$ ratios and the resulting assigned ion internal energies.

Utility of *n*-Alkylbenzene Internal Energy Thermometers

The *n*-alkylbenzene thermometers employed in this study provide average ion internal energy measurements over the range of ≈ 2 to ≈ 8 eV available from the previously published PEPICO (Baer *et al.*, 1988) and CEMS breakdown graphs (Nacson and Harrison, 1988) of the $91^+/92^+$ ratios. This range of internal energies should span the range of anticipated energies of the resonantly excited M^+ ions under a variety of experimental conditions. The PEPICO breakdown graph provides a more accurate means of assigning ion energies given the more accurate control and measurement of the internal energy deposited into the M^+ ion of *n*-butylbenzene in the PEPICO method. However, internal energies assigned from the PEPICO must be corrected for the difference in the thermal energy of the *n*-butylbenzene neutrals ($\approx$ 0.21 eV at 298 K versus $\approx$ 0.33 eV at 373 K). The *n*-alkylbenzene thermometer do, however, require accurate determinations of the $91^+/92^+$ ratios arising from collision-induced dissociation of the M^+ ions in the QITMS. As such, should any secondary reactions be occurring which either deplete or enhance the relative intensities of the *m/z* 91 or *m/z* 92 ions, assigned ion internal energies will be in error.

CHAPTER 6
CONCLUSIONS AND FUTURE WORK

Conclusions

This dissertation presents a series of studies which elucidate the energies of the ions stored in a quadrupole ion trap mass spectrometer, QITMS. The studies make use of a number of chemical "thermometer" reactions to probe the ion energies under a variety of experimental conditions. Two "kinetic" and three "thermodynamic" thermometer reactions are used to assign ion energies when no supplemental resonant excitation potentials are employed. The collision-induced dissociation, CID, breakdown graphs for a series of small molecules are then used to determine average ion internal energies upon the application of a resonant excitation potential to effect CID. The CID breakdown graphs also provide some insight into the mechanism of CID in the QITMS.

The two kinetic thermometers employed are the charge exchange reaction of Ar^+ with N_2 and the reaction of O_2^+ with CH_4. Previous flow-drift experiments have shown that the rate constants for these reactions change in a well-defined manner as a function of the center-of-mass kinetic energies, $K.E._{cm}$. As such, the rate constants obtained under a given set of experimental conditions can be used to assigned $K.E._{cm}$ energies to the Ar^+ and O_2^+ ions. The $K.E._{cm}$ of the Ar^+ ions were determined as a function of the Ar and N_2 pressures, the q_z value of the Ar^+ ion, and the pressure of the He buffer gas. The values are found to reflect anticipated trends in ion energy, *i.e.*, there is a consistent decrease in the $K.E._{cm}$ values upon addition of the He buffer, and there is an increase in the $K.E._{cm}$ with increasing q_z of the Ar^+ ion both with and without He buffer gas. The $K.E._{cm}$ values are found to lie within the range 0.11 to 0.34 eV. These values correspond to "effective" ion temperatures of ≈ 1700 K to 3300 K for the He-buffered Ar^+ ions. The O_2^+ ions were found to have $K.E._{cm}$ values of 0.23 eV with no He buffer in the trap and 0.17 eV with He buffer in the trap at a $q_z(O_2^+) = 0.400$. These values agree within experimental error to those measured by the Ar^+ reaction with N_2 and verify the cooling effect of the He buffer.

The three thermodynamic thermometers employed were the proton transfer equilibrium of protonated toluene with ethylbenzene, the proton transfer equilibrium of protonated diethylamine with di-*n*-propylamine, and the charge exchange equilibrium of ionized fluorobenzene with *m*-dichlorobenzene. These thermometers were used to calculate temperatures for the ions stored for between 2 s and 10 s (versus the 100 ms to 250 ms employed in the kinetic thermometer experiments). The ion-molecule equilibrium constants, K_{eq}, for these equilibria were determined and effective ion temperatures were calculated from known changes in the free energies of these reactions *via* the relation $\Delta G = -RT\ln K_{eq}$. Average temperatures of 280 ± 170 K with no He buffer and 220 ± 153 K with He buffer were obtained resulting in an effective cooling of 60 ± 10 K when He buffer is present in the trap at the standard operating pressure of 1.0×10^{-4} torr (uncorrected ion gauge reading). The subthermal temperatures are attributed principally to errors in the literature values for the relative free energies used in the calculation of the ion temperatures.

The time-resolved CID breakdown graphs for the molecular ions, M^+, of acetone, 2-propanone, propane, toluene, and benzene were compared to the corresponding graphs calculated from quasi-equilibrium theory, QET. The experimentally determined

CID curves are generally characterized by sharp dissociation onsets, similar to those seen in the QET breakdown graphs. However, the ion intensities reach plateau values as opposed to the maxima predicted by QET. These plateau values indicate that there is a limit to the amount of internal energy which can be deposited under a given set of excitation conditions. This limitation is likely due to the successful competition of cooling versus activating collisions with the He buffer at longer resonant excitation times. Anomalies in the shapes of the *m/z* 91 and 92 curves in the breakdown graph of the M^+ ion of toluene were noted. These anomalies are attributed to the possible isomerization of the toluene cation to the cycloheptatriene cation over the course of the resonant excitation time. Correlations between the energies for selected crossover points on the QET graphs and the requisite experimental fluences indicate that there is a 1.4:1 relation between the resonant excitation time and the excitation amplitude for fragmentation processes requiring less than 3 eV of internal energy. This increases to ≈ 3:1 for processes requiring greater than 6 eV. These relations indicate that excitation times longer than those predicted from a 1:1 excitation time/voltage relationship are required to deposit a given amount of internal energy due to the collisional cooling effects of the He buffer.

Complete time-resolved and voltage-resolved CID breakdown surfaces of the M^+ ions of *n*-butylbenzene, *n*-pentylbenzene, *n*-hexylbenzene, and *n*-octylbenzene were generated for the first time in an effort to assign average internal energies to the ions upon resonant excitation. The ratio of the *m/z* 91 and 92 fragment ions, $91^+/92^+$, arising from CID of the M^+ ions of the *n*-alkylbenzenes are known to increase in a well-characterized manner with increasing internal energy of the M^+ ions. The maximum $91^+/92^+$ ratios were used to assign ion energies as a function of the duration and amplitude of the resonant excitation potential and, for the M^+ ion of *n*-butylbenzene, as a function of the He buffer and *n*-butylbenzene pressures. The average internal energies at a $q_z(M^+) = 0.300$ ranged from ≈ 1.5 eV for the M^+ ion of *n*-butylbenzene using a 100 mV excitation amplitudes to ≈ 7.5 eV for the M^+ ion of *n*-octylbenzene using a 500 mV excitation. The percent energy transferred under a given set of experimental conditions was found to increase with increasing size of the *n*-alkyl group. This indicates that the CID process likely arises from a two-step activation/dissociation mechanism in which a translational to vibrational energy transfer occurs *via* a relatively long-lived M^+-He complex. The pressures of the He buffer and *n*-butylbenzene were found to have little effect on the average internal energy of the M^+ ion of *n*-butylbenzene over the range of He (4.0×10^{-5} to 2.2×10^{-4} torr, uncorrected ion gauge readings) and *n*-butylbenzene (9.8×10^{-7} to 5.6×10^{-6} torr, uncorrected ion gauge readings) pressures employed. However, at low He buffer pressures the *m/z* 92 ions were found to undergo proton transfer to the neutral *n*-butylbenzene to form protonated *n*-butylbenzene. This indicates that the CID breakdown graphs may reflect a number of competing dissociation, proton transfer and possibly charge exchange reactions.

Overview of the Chemical "Thermometer" Results

The chemical thermometers used in this work provide a detailed profile of the energies of the ions stored in a QITMS. The kinetic thermometers reveal that the ions have average center-of-mass kinetic energies on the order of 0.2 eV prior to the application of any supplemental excitation potential. This energy is about 4 times above the thermal energy imparted to the ions from the ion trap manifold at 373 K. This average kinetic energy can be lowered by ≈ 0.1 eV by decreasing the q_z of the ion or by increasing the pressure of the He buffer gas. However, even at a $q_z = 0.300$ and a He buffer pressure of 1.0×10^{-4} torr (uncorrected ion gauge reading) these energies are still above thermal indicating that the rf field is adding a significant amount of energy to the trapped ions. The ions can be "cooled" to near thermal energies by employing storage times on the order of seconds. However, the thermodynamic thermometers reveal that even at these long storage times, the addition of He buffer does result in a cooling of the ions by ≈ 60 K. Thus, the rf field is still contributing to the overall energy of the ions even after 1 to 10 s storage.

No direct measures of the kinetic energies of resonantly excited ions were possible with the chemical thermometers employed in this study. However, calculations using the pseudo-potential well model using zero-to-peak values for the amplitude of the rf drive potential indicate that ions of *m/z* 150 can have a maximum kinetic energy before ejection on the order of 45 eV at a $q_z = 0.300$. This corresponds to a center-of-mass collision energy, E_{cm}, with a He atom of ≈ 1.1eV, *i.e.*, 1.1eV of energy is available for transfer to the M^+ ion upon a single collision with a He atom. This energy is about 5 times greater than the 0.2 eV average center-of-mass kinetic energy without resonant excitation measured by the kinetic thermometers. Average ion internal energy measurements of resonantly excited ions using the *n*-alkylbenzenes range from ≈ 2 eV to ≈ 8 eV based on the amplitude and time of the resonant excitation potential and the size of M^+ ion. These energies are a fraction of the estimated maximum kinetic energy calculated from the pseudo-potential well model. However, these internal energies are greater than the 1.1 eV available upon a single collision with He. Thus, CID in the ion trap must proceed *via* multiple activating collisions with He to deposit the 2 eV to 8 eV of internal energy measured by the *n*-alkylbenzene thermometers.

Future Work

Future studies related to this work could involve a more detailed study of the reaction of O_2^+ with CH_4 to determine if the $K.E._{cm}$ values vary as a function of the O_2 and CH_4 pressure, the q_z of the O_2^+ ion, and the He buffer pressure in the same manner as those found with the reaction of Ar^+ with N_2. It would also be interesting to study a third kinetic thermometer to explore the general utility of kinetic thermometer reactions. Suggested thermometers include the reaction of CH_3^+ with NH_3 since the relative intensities of the product ions of this reaction have been shown to vary as a function of the $K.E._{cm}$ (Thomas *et al.*, 1980). The branching ratios of the O_2^+, NO^+, and O^+ product ions of the reaction of N^+ with O_2 also show a dependence on $K.E._{cm}$ (McFarland *et al.*, 1973b; Howorka *et al.*, 1980; Anicich *et al.*, 1977; Smith *et al.*, 1978).

Should the QITMS see extensive use in the determination of gas-phase ion-molecule thermodynamic quantities, it would be important to further study the role of the He buffer gas in the shifting of the K_{eq} witnessed in thermodynamic thermometer studies presented here. Thus, a detailed study of changes in the K_{eq} as a function of He buffer pressure to determine the possible range of ΔK_{eq} values would be important. It would also be interesting to determine the K_{eq} as a function of the temperature of the ion trap manifold to see whether or not a quantitative heating or cooling of the ions would be measured with these thermometers.

Further studies comparing the experimentally determined breakdown curves with those calculated from QET could involve obtaining the breakdown curve of molecules with crossover energies on the order of 5 eV. For example the *m/z* 26 and 25 fragment ions from the M^+ ion of acetylene have a QET crossover energy of ≈ 5.8 eV. This would strengthen (or weaken) the conclusion that the excitation time/voltage relation increases from 1.4:1 to ≈3:1 at higher internal energies. It would also be interesting to explore further the proposed isomerization between the toluene and cycloheptatriene cation in the time-resolved breakdown curve of the M^+ ion of toluene. This could be accomplished by obtaining the CID breakdown graphs of the M^+ ion of toluene and cycloheptatriene under the same excitation conditions.

Further studies involving the *n*-alkylbenzene thermometers might include obtaining the CID breakdown surface for *n*-heptylbenzene to complete the homologous series. It would also be interesting to measure the percent energy transferred to the M^+ ions of the *n*-alkylbenzenes at a variety of q_z values. Further insight into the reactions of the *m/z* 91 and 92 ions at CID times greater than 0.50 ms could be obtained by mass-selecting the *m/z* 91 or 92 ions formed from CID and then allowing the ions to react with the background neutrals. The nature and relative intensities of the product ions would provide insight into any possible reactions which could deplete or enhance the *m/z* 91 and 92 ion intensities and in so doing distort the assigned ion energies. It would also be interesting to compare the $91^+/92^+$ ratios and assigned ion energies obtained in the present studies with those obtained in an experiment paralleling the method for performing CID on an ICR mass spectrometer. This would involve resonantly exciting the ion with a short 80 to 100 μs pulse of ≈ 1 to 5 V amplitude and then monitoring the ion intensities as a function of time. This approach would determine what role continued excitation of the ions between collisions with the He plays in the average internal energy transferred upon resonant excitation.

Another future direction of these studies could involve an examination of the use of other "thermometers" for assigning average internal energy of the ions upon CID. Other M^+ ion for which the charge exchange mass spectrometric and breakdown graphs have been obtained include benzyl methyl ether, nitrobenzene, cyclohexene, *n*-propanol, and nitromethane (Zwinselman *et al.*, 1985 and references therein). Further, a detailed profile of the activated or inactivated ion internal energy distributions in the QITMS could be obtained from the branching ratios of the successive loss of CO groups from ionized tungsten hexacarbonyl, $W(CO)_6$. The M^+ ion has been shown to be an effective probe of ion internal energy distributions following activation by various methods (Wysocki *et al.*, 1987; Cooks *et al.*, 1990).

Practical Suggestions for Chemical Thermometer Studies

The following general suggestions/comments collected over the course of this work may be of help in performing future chemical thermometer studies. The list is by no means exhaustive.

Experimental Considerations

1) Accurate rate constant and equilibrium constant determinations require high purity gases to reduce the likelihood of side reactions due to trace contaminants. This is particularly important for ion-molecule reactions with rate constants which are less than 10^{-11} cm^3 s^{-1} since these reaction will require reaction times on the order of 500 ms and for all equilibria studies since they involve storage times on the order of seconds.

2) Trace water in the ion trap chamber, the sample lines, and particularly the He buffer gas line is a particular problem in charge exchange studies. This can be reduced by baking both the ion trap and by cryocooling the sample and He lines with liquid N_2. It is important to monitor the level of the liquid N_2 to keep the trapped water frozen throughout a run. Other trace contaminants in the sample lines can be reduced by

washing the sample lines with a series of solvents (methanol, acetone, *etc.*) and flame drying the lines while purging them with N_2. Trace contaminants are not as severe a problem in the CID thermometer studies.

3) For the kinetic thermometer reactions, the effect of possible back reactions on the measured rate constant should also be examined by ejecting the product ion as it is formed.

4) Accurate rate constant and equilibrium constant measurements involve accurate neutral pressure measurements and as such ion gauge calibrations are required. The best approach is to calibrate the ion gauge reading against that of a capacitance manometer. However, it should be noted that the lowest pressure measured by a capacitance manometer is on the order of 10^{-6} torr. The capacitance manometer readings will likely not stabilize until $\approx 10^{-5}$ torr, based on the nature of the neutral species. Because of these factors, accurate calibrations of the ion gauge against the capacitance manometer are only obtained at sample pressure a factor of 10 to 100 times higher than those used experimentally. An alternative to obtaining ion gauge sensitivity factors is to apply the correction method of Bartmess and Georgiadis (1983). In this approach the chemical sensitivity, R_x, relative to N_2 ($R_x = 1.00$) is given by the relation $R_x = 0.36\alpha + 0.30$, where α = the polarizability of the neutral in $Å^3$. The polarizabilities of the neutrals can be found in McClellan (1963, 1972). Note, however, that Bartmess and Georgiadis (1983) define the ion gauge chemical sensitivity factor as the ratio of the observed pressure (ion gauge reading) to the true pressure (capacitance manometer reading) whereas in the present the study the sensitivity factors are taken as the slope of the plot of the capacitance manometer reading versus that of the ion gauge. As such, the factors of Bartmess and Georgiadis are the inverse of those presented here.

Relatively good agreement was found between the ion gauge correction factors obtained for toluene and ethylbenzene from calibration with a capacitance manometer (0.205 ± 0.003 for toluene and 0.176 ± 0.010 for ethylbenzene) with those calculated by Bartmess and Georgiadis (0.211 for toluene and 0.185 for ethylbenzene).

5) Ion gauge calibration can be avoided by preparing sample bulbs containing known pressure ratios of the neutrals of interest employing a capacitance manometer and high pressures. This approach to sample introduction also avoids having to monitor the pressures metered by two inlet valves. Nevertheless, fractional diffusion of the mixture components due to differences in boiling point, or differences due to losses by adsorption on the bulb walls or seals, add new opportunities for error.

6) Because of the range of ionizing electron energies in the ITMS^{TM}, it is recommended that a cooling time allowing at least 10 collisions of the ions with the background neutrals be added to all scan functions following ionization but before mass-selection. At 1.0×10^{-4} torr of He (uncorrected ion gauge reading), this would amount to a cooling time of 1 to 1.5 ms. This will help cool any excited states ionic states formed on electron impact. Cooling times added after mass-selection can result in unwanted ion-molecule reactions.

Calculation Considerations

1) For the thermodynamic thermometers, tabulated absolute ΔG values, must be used with caution as these values are based on equilibrium measurements relative to a given standard compound. Thus, tabulated ΔG values may change from publication to publication and from year to year. Relative ΔG values obtained from the same experimental method - and if possible the same publication - are preferred.

2) The calculated pseudo-potential well depths presented in this study are based on zero-to-peak values of the rf drive voltage. Other publications may make use of peak-to-peak values; thus, all well depth calculations should be checked for the voltage measurement employed.

3) All collision rates of the ions with the neutrals based on the Langevin approximation make use of absolute pressure values. All ion gauge readings must therefore be corrected with the ion gauge sensitivity factors prior to calculating the collision rates.

4) All ion energy assignments must consider the thermal energy imparted to the neutral species M and thus to the M^+ ion from the ion trap manifold. For species as large as *n*-butylbenzene this can contribute as much as 0.33 eV of energy to the M^+ ion.

APPENDIX A
FORTH PROGRAM FOR VARYING REACTION TIME

The following FORTH program (RXNTIME) was written by Nathan A. Yates and used in the variable reaction time studies in chapter 2 and in the CID studies in chapters 4 and 5.

RXNTIME:

```
Screen: 1 choose scan function and data file
        R EXP <CR>                          \ load Experiment Editor
[[                                          \ go to FORTH
        LOAD-SCAN-FUNCTION:  CEARISOA       \ load scan function of interest
        1 INIT-DATAFILE                     \ open data file; call it #1
        DATA-FILE-COMMENT                   \ add data file comment
]]                                          \ exit FORTH

Screen: 2 turn on ITMS components
[[                                          \ go to FORTH
        MULTIPLIER-ON                       \ turn on multiplier
        FILAMENT-ON                         \ turn on filament
        RF-ON                               \ turn on rf
        TICKLE-ON                           \ turn on tickle
        10 SET-MICRO-SCANS                  \ microscans for first normalized scan
        DC-ON                               \ turn dc on
        TAKE-ONE-SCAN                       \ first normalized scan
        NORMALIZE-Y-AXIS                    \ normalize y-axis
        0 SET-THRESHOLD                     \ set threshold = 0
        20 SET-MICRO-SCANS                  \ set microscans for data acquisition
        ACQUIRE-MODE-ON                     \ turn acquire on
]]                                          \ exit FORTH

Screen: 3 reaction time loop page
[[                                          \ go to FORTH
        1 CHOOSE-FILE                       \ choose data file
        13 SET-TABLE                        \ choose table in scan function
        3 SET-PARAMETER                     \ vary table time (= parameter 3)
]]
```

```
        [[ -50. ]]                              \ set negative of increment (μsec/scan)
        [[ 51 0 ]] <DO>                         \ loop from 0 to 51; rxntime = 250μsec
        [[ 50. D+ DDUP                          \ add increment to stack and duplicate
        SET-TABLE-TIME                          \ read top of stack to table time
        1 SCAN-ACQUIRE                          \ acquire scan to data file
        ]] <LOOP>                               \ end of loop
        [[ EMIT EMIT                            \ clear stack
]]                                              \ exit FORTH

Screen: 4 shut down ITMS components
[[                                              \ go to FORTH
        1 TINI-DATAFILE                         \ close datafile
        ACQUIRE-MODE-OFF                        \ turn acquire off
        MULTIPLIER-OFF                          \ turn multiplier off
        FILAMENT-OFF                            \ turn filament off
        RF-OFF                                  \ turn rf off
]] <ESC>                                        \ exit FORTH
```

The equilibrium studies in chapter 3 required reaction times greater than 1 ms. To accomplish this the requisite number of reaction time tables were added to the scan function, and the following Screen 3 was substituted into the RXNTIME program.

```
LRXNTIME:

Screen: 3 reaction time loop page
[[                                              \ go to FORTH
        1 CHOOSE-FILE                           \ choose data file
]]
        [[ -10000. ]]                           \ set negative of increment (μsec/scan)
        [[ 51 0 ]] <DO>                         \ loop from 0 to 51; rxntime = 250μsec
        [[ 10000. D+                            \ add increment to stack
        DDUP DDUP DDUP DDUP DDUP                \ duplicate 5 times
        13 SET-TABLE-TIME 3 SET-TABLE-PARAMETER SET-TABLE-TIME
        14 SET-TABLE-TIME 3 SET-TABLE-PARAMETER SET-TABLE-TIME
        15 SET-TABLE-TIME 3 SET-TABLE-PARAMETER SET-TABLE-TIME
        16 SET-TABLE-TIME 3 SET-TABLE-PARAMETER SET-TABLE-TIME
        17 SET-TABLE-TIME 3 SET-TABLE-PARAMETER SET-TABLE-TIME
        ]] <LOOP>
        [[ EMIT EMIT
]]                                              \ exit FORTH
```

APPENDIX B
FORTH PROGRAM FOR OPTIMIZING RESONANT EXCITATION FREQUENCIES

The following FORTH program (JQFRCEC) was written by Jodie V. Johnson and used for all resonant frequency optimizations.

JQFRCEC:

```
Screen: 1 choose scan function and data file
      R EXP <CR>                           \ load Experiment Editor
[[                                         \ go to FORTH
      LOAD-SCAN-FUNCTION: CECNBB           \ load scan function of interest
      1 INIT-DATAFILE                      \ open data file; call it #1
      DATA-FILE-COMMENT                    \ add data file comment
]]                                         \ exit FORTH

Screen: 2 turn on ITMS components
[[                                         \ go to FORTH
      MULTIPLIER-ON                        \ turn on multiplier
      FILAMENT-ON                          \ turn on filament
      RF-ON                                \ turn on rf
      TICKLE-ON                            \ turn on tickle
      10 SET-MICRO-SCANS                   \ microscans for first normalized scan
      DC-ON                                \ turn dc on
      TAKE-ONE-SCAN                        \ first normalized scan
      NORMALIZE-Y-AXIS                     \ normalize y-axis
      0 SET-THRESHOLD                      \ set threshold = 0
      20 SET-MICRO-SCANS                   \ set microscans for data acquisition
      ACQUIRE-MODE-ON                      \ turn acquire on
]]                                         \ exit FORTH

Screen: 3 frequency delta loop page
[[                                         \ go to FORTH
      1 CHOOSE-FILE                        \ choose data file
      13 SET-TABLE                         \ choose table in scan function
      5 SET-PARAMETER                      \ vary frequency delta (=parameter 5)
      200 0                                \ loop counter from 0 to 200
]]
```

```
        <DO>                                \ start of loop
        <I>                                 \ counter (= UM)
        [[ 100 UM* 10000. DNEGATE D+        \ multiply counter by 100 then subtract
                                             \ 10000; where 100 = frequency
                                             \ shift/scan and 10000 = starting
                                             \ frequency delta; thus frequency
                                             \ delta = (UM)*100-10000
        SET-FREQUENCY-DELTA                 \ read top of stack to table time
        1 SCAN-ACQUIRE                      \ acquire scan to data file
        ]] <LOOP>                           \ end of loop
]]                                          \ exit FORTH

Screen: 4 shut down ITMS components
[[                                          \ go to FORTH
        1 TINI-DATAFILE                     \ close datafile
        ACQUIRE-MODE-OFF                    \ turn acquire off
        MULTIPLIER-OFF                      \ turn multiplier off
        FILAMENT-OFF                        \ turn filament off
        RF-OFF                              \ turn rf off
]] <ESC>                                    \ exit FORTH
```

APPENDIX C
BASIC PROGRAM FOR TWO-DIMENSIONAL DATA SMOOTHING

This BASIC program was written by Micheal S. Freund and used to smooth the three-dimensional CID surface data presented in chapter 5.

```
'***************************************************************
'This program is designed to smooth 3-D data in both x and y directions
'Input data has 6 columns: potential,time,91,92,91/92,134.
'The last four columns are smoothed (5 point smoothing routine)
'with respect to time and potential.
'****************************************************************


DECLARE SUB segout (fl$,segn!,tot!)
DECLARE SUB inseg (fl$,segn!,tot!)
DECLARE SUB nxydat (fl$,segn!,tot!)
DECLARE SUB xtoy (fl$,segn,tot)
DECLARE SUB smooth (segn,tot)

'****************************************************************
'setup
'****************************************************************
SCREEN 9,0
COLOR 11,0

'array continuing file names of files to be smoothed(1) (or input) and output
'names(2) without extensions
DIM flnm$(2,100)

'array containing data for current file in segments
COMMON SHARED segm()

' make sure all input and output files are closed
CLOSE


'****************************************************************
'determine directory and files to operate on
```

```
'*****************************************************************
'locate path
LOCATE 12,20
1 CLS
INPUT "File Path"; p$
CLS

'direct files into temporary file and list them
SHELL "dir "+p$+"\*.dat>temp.fls"

'input filenames from temporary file
OPEN "temp.fls" FOR INPUT AS #1
FOR i = 1 TO 4
        INPUT #1,junk$
NEXT i

'isolate filename prefixes
j = 1
CLS
WHILE NOT EOF(1)
        INPUT #1,flnm$(1,j)
        flnm$(1,j) = RTRIM$(LEFT$(flnm$(1,j),8))
        j = j+1
WEND

PRINT : PRINT : PRINT "PATH:   ";
PRINT UCASE$(p$): PRINT

'list prefixes
p$ = p$+"\"
FOR i = 2 TO j - 3
        IF i = 20 OR i = 40 OR i = 60 THEN
          INPUT "press enter to continue",yn$
          CLS
          PRINT : PRINT : PRINT : PRINT : PRINT
        END IF
  PRINT SPACE$(10);
  PRINT UCASE$(flnm$(1,i))
NEXT

'get rid of temporary file
CLOSE #1
KILL "temp.fls"

'determine if these files are to be operated on
PRINT
PRINT "These are the files which can be smoothed."
INPUT "Is this the correct directory [Y.N.Q]"; yn$
```

```
IF yn$ = "n" OR yn$ = "N" THEN GOTO 1
IF yn$ = "q" OR yn$ = "Q" THEN END

'Give user a choice of files to be smoothed
'if enter is the only response then do not smooth!
CLS
PRINT : PRINT : PRINT
PRINT "Give file name for output (without path and extension)"
PRINT "  Press enter alone if file is not to be smoothed": PRINT : PRINT
z = 1
newpage = 0
FOR i = 2 TO j - 3
   IF i - newpage * 20 = 20 THEN
     CLS
     newpage = newpage+1
   END IF
   LOCATE 4+i - newpage * 20,4: PRINT UCASE$(flnm$(1,i));
   LOCATE 4+i - newpage * 20,12: PRINT "   --->   ";
  INPUT flnm$(2,z)
  IF flnm$(2,z) = "" THEN GOTO 111
    flnm$(1,z) = flnm$(1,i)
    z = z+1
111 NEXT
z = z - 1

CLS
FOR i = 1 TO z
  LOCATE 4+i,4: PRINT UCASE$(flnm$(1,i))
NEXT

'**********************************************************************
' operate on each file
'**********************************************************************
newpage = 0
  FOR i = 1 TO z
    ERASE segm
    IF i - newpage * 20 = 20 THEN
      CLS
      newpage = newpage+1
    END IF
    fl1$ = p$+flnm$(1,i)
    fl2$ = p$+flnm$(2,i)
    LOCATE 4+i - newpage * 20,12: PRINT "   --->   ";
    PRINT UCASE$(flnm$(2,i))

   ' determine the number of segments and the number of data rows per segment
    CALL nxydat(fl1$,segn,tot)
   ' input data into segment arrays
    CALL inseg(fl1$,segn,tot)

   'smooth segment
    CALL smooth(segn,tot)

   'output segment
    CALL segout(fl2$,segn,tot)

8  NEXT i
SHELL "cd\"
SHELL "c:"
END
'**************************************************************
'**************************************************************


'**************************************************************
' Subroutines
'**************************************************************
'**************************************************************
SUB inseg (fl$,segn,tot)
DIM segm(segn,tot,6)
'segment number; data number; all data per line
'1=x
'2=y
'3=m/z 91
'4=m/z 92
'5=91/92
'6=m/z 134

' input data into arrays corresponding to segments of constant
' x values
OPEN fl$+".dat" FOR INPUT AS #1

FOR i = 1 TO segn
  FOR j = 1 TO tot
   INPUT #1,x,y,z,zz,zzz,zzzz
    segm(i,j,1) = x
    segm(i,j,2) = y
    segm(i,j,3) = z
    segm(i,j,4) = zz
    segm(i,j,5) = zzz
    segm(i,j,6) = zzzz
  NEXT
NEXT

CLOSE #1
```

```
END SUB
'******************************************************************

'******************************************************************
REM $STATIC
SUB nxydat (fl$,segn,tot)

' Determine the number of segments (or different x values)
CLOSE #1
OPEN fl$+".dat" FOR INPUT AS #1
segnum = 1
tot = 1
  INPUT #1,x,y,z,zz,zzz,zzzz
  xold = x
WHILE NOT EOF(1)
  INPUT #1,x,y,z,zz,zzz,zzzz
  tot = tot+1
  IF x <> xold THEN
    xold = x
    segnum = segnum+1
  END IF
WEND
CLOSE #1
tot = tot / segnum  'number of data points per segment
segn = segnum
END SUB
'******************************************************************

'******************************************************************
SUB segout (fl$,segn,tot)

' output data
OPEN fl$+".dat" FOR OUTPUT AS #1
FOR i = 1 TO segn
  FOR j = 1 TO tot
    PRINT #1,segm(i,j,1);
    PRINT #1,segm(i,j,2);
    PRINT #1,segm(i,j,3);
    PRINT #1,segm(i,j,4);
    PRINT #1,segm(i,j,5);
    PRINT #1,segm(i,j,6)
  NEXT
NEXT
CLOSE #1
END SUB
'******************************************************************

'******************************************************************
```

```
SUB smooth (segn,tot)
'Smooth in both x and y direction

'for smoothing in the time direction 0.05,0.10,0.15...2.55 ms
'q = 3 through 6 for m/z 91, m/z 92, 91/92, m/z 134
FOR i = 1 TO segn
 FOR q = 3 TO 6
  FOR j = 1 TO tot
  'if j is 1 or tot; or if j is 2 or tot-1; these are two special cases
    IF j=1 THEN segm(i,1,q)=(segm(i1,q)+segm(i,2,q)+segm(i,3,q))  / 3
     IF j=2 THEN
          segm(i,2,q)=(segm(i,1,q)+segm(i,2,q)+segm(i,3,q)+segm(i,4,q))/4
     END IF
     IF j=tot THEN segm(i,tot,q)=(segm(i,tot,q)+segm(i,tot-1,q)+segm(i,tot-2,q))/3
     IF j=tot - 1 THEN
          segm(i,tot-1,q)=(segm(i,tot-1,q)+segm(i,tot-2,q)+segm(i,tot-3,q))
          segm(i,tot-1,q)=(segm(i,tot-1,q)+segm(i,tot,q))/4
     END IF
  'else normal case
     IF j>2 AND j<tot-1 THEN
          segm(i,j,q)=(segm(i,j-2,q)+segm(i,j-1,q)+segm(i,j,q)+segm(i,j+1,q))
          segm(i,j,q)=(segm(i,j,q)+segm(i,j+2,q))  / 5
     END IF
  NEXT
 NEXT
NEXT

'for smoothing in potential direction 0,20,40...600 mV
FOR j=1 TO tot
 FOR q=3 TO 6
  FOR i=1 TO segn
  'if i is 1 or segn; or if i is 2 or segn-1; these are two special cases
   IF i=1 THEN segm(i,1,q)=(segm(i,j,q)+segm(i+1,j,q)+segm(i+2,j,q))/3
   IF i=2 THEN segm(i,j,q)=(segm(i-1,j,q)+segm(i,j,q)+segm(i+1,j,q)+segm(i+2,j,q))/4
   IF i=segn THEN segm(i,j,q)=(segm(i-2,j,q)+segm(i-1,j,q)+segm(i,j,q))  / 3
   IF i=segn-1 THEN
          segm(i,j,q)=(segm(i-2,j,q)+segm(i-1,j,q)+segm(i,j,q)+segm(i+1,j,q))/4
   END IF
  'else normal case
   IF i>2 AND i<segn-1 THEN
          segm(i,j,q)=(segm(i-2,j,q)+segm(i-1,j,q)+segm(i,j,q)+segm(i+1,j,q))
          segm(i,j,q)=segm(i,j,q)+segm(i+2,j,q))/5
   END IF
  NEXT
 NEXT
NEXT
END SUB
'**************************************************************
```

REFERENCES

Adams, N.G.; Smith, D.; Ferguson, E.E. "Comparative Effects of Temperature and Kinetic Energy Change on the Reaction of O_2^+ with CH_4 and CD_4," *Int. J. Mass Spectrom. Ion Processes*, **1985**, *67*, 67-74.

André, J. "Étude Théorique de L'influence des Collisions Élastiques sur un Gaz Dilué de Particules Chargées, Confinées par un Champ de Radio-Fréquence a Symétrie Quadrupolaire," *J. de Phys.*, **1976**, *37*, 719-730.

André, J.; Vedel, F. "Influence des Collisions Élastiques sur les Propriétés Élastiques d'Ions Confinés dans une Trappe Électrodynamique," *J. de Phys.*, **1977**, *38*, 1381-1398.

Anicich, V.G.; Huntress, W.T.; Futrell, J.H. "Ion Cyclotron Resonance Studies of Some Reactions of N^+ Ions," *Chem. Phys. Lett.*, **1977**, *47*, 488-489.

Ardanaz, C.E.; Traldi, P.; Vettori, U.; Kavka, J.; Guidugli, F. "The Ion Trap Mass Spectrometer in Ion Structure Studies - The Case of $[M-H]^+$ Ions from Chalcone," *Rap. Comm. Mass Spectrom.*, **1991**, *5*, 5-10.

Armitage, M.A. "Applications of Quadrupole Ion Storage Mass Spectrometry," Master of Science Thesis, Trent University, **1979**.

Armitage, M.A.; Fulford, J.E.; Duong-Nhu-Hoa; Hughes, R.J.; March, R.E. "The Application of Resonant Ion Ejection to Quadrupole Ion Storage Mass Spectrometry: a Study of Ion/Molecule Reactions in the QUISTOR," *Can. J. Chem.*, **1979**, *57*, 2108-2113.

Armitage, M.A.; Higgins, M.J.; Lewars, G.G.; March, R.E. "Methylketene Ion Chemistry and Proton Affinity," *J. Am. Chem. Soc.*, **1980**, *102*, 5064-5068.

Aue, D.H.; Webb, H.M.; Bowers, M.T. "Quantitative Relative Gas-Phase Basicities of Alkylamines. Correlation with Solution Basicity," *J. Am. Chem. Soc.*, **1972**, 4726-4728.

Ausloos, P. "Structure and Isomerization of $C_7H_7^+$ Ions Formed in the Charge-Transfer-Induced Fragmentation of Ethylbenzene, Toluene, and Norbornadiene," *J. Am. Chem. Soc.*, **1982**, *104*, 5259-5265.

Ausloos, P.; Jackson, J.-A.A.; Lias, S.G. "Reactions of Benzyl Ions with Alkanes, Alkenes, and Aromatic Compounds" *Int. J. Mass Spectrom. Ion Phys.*, **1980**, *33*, 269-283.

Baer, T.; Dutuit, O.; Mestdagh, H.; Rolando, C. "Dissociation Dynamics of *n*-Butylbenzene Ions: The Competitive Production of *m/z* 91 and 92 Fragment Ions," *J. Phys. Chem.*, **1988**, *92*, 5674-5679.

Baril, M. "Phase Space Concepts and Best Operating Point for the Three-Dimensional Quadrupole Ion Trap," *Dynamic Mass Spectrometry*, D. Price, Ed., Heyden and Sons, Ltd. London, **1981**, vol.6, 33-43.

Barlow, S.E.; Van Doren, J.M.; Dupuy, C.H.; Bierbaum, V.M.; Dotan, I.; Ferguson, E.E.; Adams, N.G.; Smith, D.; Rowe, B.R.; Marquette, J.B.; Dupeyrat, G.; Durup-Ferguson, M. "Studies of the Reaction of O_2^+ with Deuterated Methanes," *J. Chem. Phys.*, **1986**, *85*, 3851-3859.

Bartmess, J.E. "Gas-Phase Ion Chemistry of 5-Methylene-1,3-cyclohexadiene (o-Isotoluene) and 3-Methylene-1,4-cyclohexadiene (*p*-Isotoluene)," *J. Am. Chem. Soc.*, **1982**, *104*, 335-337.

Bartmess, J.E. "Ion Thermochemistry: Summary of the Panel Discussion," *Structure/ Reactivity, and Thermochemistry of Ions*," P. Ausloos and S.G. Lias, Eds., NATO ASI Series C. Mathematical and Physical Sciences, D. Reidel Pub. Co., Dordrecht, Holland, **1987**, vol. 193, 367-380.

Bartmess, J.E.; Georgiadis, R.M. "Empirical Methods for Determination of Ionization Gauge Relative Sensitivities for Different Gases," *Vacuum*, **1983**, *33*, 149-153.

Bartmess, J.E.; McIver, R.T. "The Gas-Phase Acidity Scale," *Gas Phase Ion Chemistry*, M.T. Bowers, Ed., Academic Press, New York, **1979**, vol. 2, 87-121.

Berberich, D.W.; Hail, M.E,; Johnson, J.V.; Yost, R.A. "Mass-Selection of Reactant Ions for Chemical Ionization in Quadrupole Ion Trap and Triple Quadrupole Mass Spectrometers," *Int. J. Mass Spectrom. Ion Proc.*, **1989**, *94*, 115-147.

Blatt, R.; Zoller, P.; Holzmuller, G.; Siemers, I. "Brownian Motion of a Parametric Oscillator: A Model for Ion Confinement in Radio Frequency Traps, *Z. Phys. D*, **1986**, *4*, 121-126.

Bohme, D.K.; Hemsworth, R.S.; Rundle, H.W.; Schiff, H.I. "Determination of Proton Affinity from the Kinetics of Proton transfer Reactions II. Kinetic Analysis of the Approach to the Attainment of Equilibrium," *J. Chem. Phys.*, **1973**, *58*, 3504-3518.

Bonner, R.F. "Derivation of the Field Equations and Stability Parameters for Three Operating Modes of the Three-Dimensional Quadrupole," *Int. J. Mass Spectrom. Ion Phys.*, **1977**, *23*, 249-257.

Bonner, R.F.; Lawson, G; Todd, J.F.J "A Low-pressure Chemical Ionisation Source: An Application of a Novel Type of Ion Storage Mass Spectrometer," *J.C.S. Chem. Comm.*, **1972**, 1179-1180.

Bonner, R.F.; Lawson, G.; Todd, J.F.J. "Ion-Molecule Reaction Studies with a Quadrupole Ion Storage Trap," *Int. J. Mass Spectrom. Ion Phys.*, **1972/73**, *10*, 197-203.

Bonner, R.F.; Lawson, G.; Todd, J.F.J; March, R.E. "Ion Storage Mass Spectrometry: Applications in the Study of Ionic Processes and Chemical Ionization" *Adv. Mass Spectrom.*, **1974**, *6*, 377-384.

Bonner, R.F.; March, R.E. "The Effects of Charge Exchange Collisions on the Motion of Ions in Three-Dimensional Quadrupole Electric Fields Part II. Program Improvements and Fundamental Results," *Int. J. Mass Spectrom. Ion Phys.*, **1977**, *25*, 411-431.

Bonner, R.F.; March, R.E.; Durup, J. "Effect of Charge Exchange Reactions on the Motion of Ions in Three-Dimensional Quadrupole Electric Fields," *Int. J. Mass Spectrom. Ion Phys.*, **1976**, *22*, 17-34.

Bowers, M.T.; Aue, D.H.; Webb, H.M.; McIver, R.T. "Equilibrium Constants for Gas-Phase Ionic Reactions. Accurate Determination of Relative Proton Affinities," *J. Am. Chem. Soc.*, **1971**, *93*, 4314-4315.

Boyd, R.K.; Harris, F.M.; Beynon, J.H. "Calibration of Energy Deposition in Collision-Induced Dissociations of the Butylbenzene Molecular Ion," *Int. J. Mass Spectrom. Ion Proc.*, **1985**, *66*, 185-194.

Brehm, B.; Puttkamar, E.V. "Koinzidenzmessung von Photoionen und Photoelektronen bei Methan" *Z. Naturforsch, Teil A*, **1967**, *22*, 8-10.

Brodbelt-Lustig, J.S.; Cooks, R.G. "Dissociation of Protonated 2,2,6-Trimethylcyclohexanone and Related Compounds upon High and Low Energy Collisional Activation," *Int. J. Mass Spectrom. Ion Proc.*, **1988**, *86*, 253-272.

Brodbelt-Lustig, J.S.; Cooks, R.G. "Determination of Relative Gas-Phase Basicities by the Proton-Transfer Equilibrium Technique and the Kinetic Method in a Quadrupole Ion-Trap," *Talanta*, **1989**, *36*, 255-260.

Brodbelt-Lustig, J.S.; Kenttämaa, H.I.; Cooks, R.G. "Energy-Resolved Collisional Activation of Dimethylphosphonate and DimethylPhosphite Ions in a Quadrupole Ion Trap and Triple Quadrupole Mass Spectrometer," *Org. Mass Spectrom.*, **1988**, *23*, 6-9.

Brown, P. "Kinetic Studies in Mass Spectrometry-VII: Competing Cleavage and Rearrangement Processes in Molecular Ion Decomposition Reactions," *Org. Mass Spectrom.*, **1970**, *3*, 1175-1186.

Bruce, J.E. "Kinetic Energies and Reactions of Trapped Ions in a Fourier Transform ion Cyclotron Resonance Mass Spectrometer," Ph.D. Dissertation, University of Florida, **1992**.

Bruce, J.E.; Eyler, J.R. "Probing Trapped Ion Energies *via* Ion-Molecule Reaction Kinetics: Fourier Transform Ion Cyclotron Resonance Mass Spectrometry," *J. Am. Soc. Mass Spectrom.*, **1992**, in press.

Chattopadhyaya, R.; Ghosh, P.K. "QUISTOR: Conical Injection of Ions Around the z-Axis," *Int. J. Mass Spectrom. Ion Proc.*, **1980**, *36*, 365-370.

Chattopadhyaya, R.; Ghosh, P.K. "QUISTOR: Injection of Two Concentric Rings of Ions in the X-Y Plane," *Int. J. Mass Spectrom. Ion Proc.*, **1981**, *41*, 1-6.

Chen, J.H.; Hayes, J.D.; Dunbar, R.C. "Competitive Two-Channel Photodissociation of *n*-Butylbenzene Ions in the Fourier-Transform Ion Cyclotron Resonance Mass Spectrometer," *J. Phys. Chem.*, **1984**, *88*, 4759-4764.

Church, D.A. "Stored-Ion Collisional Relaxation to Equilibrium," *Phys. Rev. A*, **1988**, *37*, 277-279.

Church, D.A.; Dehmelt, H.G. "Radiative Cooling of an Electrodynamically Contained Proton Gas," *J. Appl. Phys.*, **1969**, *40*, 3421-3424.

Clary, D.C.; Sonnenfroh, "D.M. Quantum Mechanical Calculations on the $Ar^+ + N_2$ Charge Transfer Reaction," *J. Chem. Phys.*, **1989**, *90*, 1686-1693.

Cody, R.B.; Burnier, R.C.; Freiser, B.S. "Collision-Induced Dissociation with Fourier Transform Mass Spectrometry," *Anal. Chem.*, **1982**, *54*, 96-101.

Cody, R.B.; Freiser, B.S. "Collision-Induced Dissociation in a Fourier Transform Mass Spectrometer," *Int. J. Mass Spectrom. Ion Proc.*, **1982**, *41*, 199-204.

Cone, C.; Dewar, M.J.S.; Landman, D. "Gaseous Ions. 1. MINDO/3 Study of the Rearrangement of Benzyl Cation to Tropylium" *J. Am. Chem. Soc.*, **1977**, *99*, 372-376.

Cooks, R.G., Ed. *Collisional Spectroscopy*, Plenum Press, New York, **1978**.

Cooks, R.G.; Ast, T.; Kralj, B.; Kramer, V.; Žigon, D. "Internal Energy Distributions Deposited in Doubly and Singly Charged Tungsten Hexacarbonyl Ions Generated by Charge Stripping, Electron Impact, and Charge Exchange," *J. Am. Soc. Mass Spectrom.*, **1990**, *1*, 18-27.

Cooks, R.G.; Glish, G.L; McLuckey, S.A.; Kaiser, R.E. "Ion Trap Mass Spectrometry," *C. and E. News*, **1991**, *March 25*, 26-41.

Cooks, R.G; Kaiser, R.E. "Quadrupole Ion Trap Mass Spectrometry," *Acc. Chem. Res.*, **1990**, *23*, 213-219.

Cunningham, A.J.; Payzant, J.P.; Kebarle, P. "A Kinetic Study of the Proton Hydrate $H^+(H_2O)_n$ Equilibria in the Gas Phase," *J. Am. Chem. Soc.*, **1972**, *94*, 7627-7632.

Cutler, L.S.; Flory, C.A.; Giffard, R.P.; McGuire, M.D. "Doppler Effects due to Thermal Macromotion of Ions in an RF Quadrupole Trap," *Appl. Phys. B*, **1986**, *39*, 251-259.

Cutler, L.S.; Giffard, R.P.; McGuire, M.D. "Thermalization of ^{199}Hg Ion Macromotion by a Light Background Gas in an RF Quadrupole Trap," *Appl. Phys. B*, **1985**, *36*, 137-142.

Davidson, W.R.; Bowers, M.T.; Su, T.; Aue, D.H. "On the Measurement of Gas-Phase Ion-Molecule Equilibrium Constants in an Ion Cyclotron Resonance Spectrometer," *Int. J. Mass Spectrom. Ion Phys.*, **1977**, *24*, 83-105.

Dawson, P.H. "Detailed Study of the Quadrupole Mass Filter," *Int. J. Mass Spectrom. Ion Phys.*, **1974**, *14*, 317-37.

Dawson, P.H., Ed. *Quadrupole Mass Spectrometry and Its Applications*, Elsevier Scientific, Amsterdam, **1976**.

Dawson, P.H. "The Collision-Induced Dissociation of Protonated Water Clusters Using a Triple Quadrupole," *Int. J. Mass Spectrom. Ion Phys.*, **1982**, *43*, 195-209.

Dawson, P.H. "A Study of the Collision-Induced Dissociation of $C_2H_5OH_2^+$ Using Various Target Gases," *Int. J. Mass Spectrom. Ion Phys.*, **1983**, *50*, 287-297.

Dawson, P.H. "Low-Energy Collision-Activated Dissociation of *n*-Butylbenzene. Effect of the Electron Energy Used During Parent Ion Formation," *Int. J. Mass Spectrom. Ion Proc.*, **1985**, *63*, 339-341.

Dawson, P.H.; Douglas, D.J. "Collisionally Activated Dissociation of Low Kinetic Energy Ions," *Tandem Mass Spectrometry*, McLafferty, F.W., Ed., John Wiley and Sons, **1983**, 125-148.

Dawson, P.H.; French, J.B.; Buckley, J.A.; Douglas, D.J.; Simmons, D. "Use of Triple Quadrupoles for Sequential Mass Spectrometry 1. Instrumental Parameters," *Org. Mass Spectrom.*, **1982a**, *17*, 205-211.

Dawson, P.H.; French, J.B.; Buckley, J.A.; Douglas, D.J.; Simmons, D. "Use of Triple Quadrupoles for Sequential Mass Spectrometry 2. A Detailed Case Study," *Org. Mass Spectrom.*, **1982b**, *17*, 212-219.

Dawson, P.H.; Lambert, C. "A Detailed Study of The Quadrupole Ion Trap," *Int. J. Mass Spectrom. Ion Phys.*, **1975**, *16*, 269-280.

Dawson, P.H.; Sun, W.-F. "Comparison of Low-Energy Collisionally Induced Dissociation of *n*-Butylbenzene Ions with Photodissociation," *Int. J. Mass Spectrom. Ion Phys.*, **1982**, *44*, 51-59.

Dawson, P.H.; Whetten, N.R. "Ion Storage in Three-Dimensional Rotationally Symmetric Quadrupole Fields. I," *J. Vac. Sci. Technol.*, **1968a**, *5*, 1-10.

Dawson, P.H.; Whetten, N.R. "Ion Storage in Three-Dimensional Rotationally Symmetric Quadrupole Fields. II," *J. Vac. Sci. Technol.*, **1968b**, *5*, 11-18.

Dawson, P.H.; Whetten, N.R. "The Three-Dimensional Quadrupole Ion Trap," *Naturwissenschaften*, **1969**, *56*, 109-112.

Dawson, P.H.; Whetten, N.R. "Quadrupole Mass Spectrometry," *Dynamic Mass Spectrometry*, D. Price, Ed., Heyden and Son, Ltd., London, **1971**, vol. 2, 1-60.

DeBrou, G.B.; Fulford, J.E.; Lewars, E.G.; March, R.E. "Ketene: Ion Chemistry and Proton Affinity," *Int. J. Mass Spectrom. Ion Phys.*, **1978**, *26*, 345-352.

Dehmelt, H.G. "Radiofrequency Spectroscopy of Stored Ions. I. Storage," *Adv. At. Mol. Phys.*, **1967**, *3*, 53-72.

Dehmelt, H.G. "Radiofrequency Spectroscopy of Stored Ions. II. Spectroscopy," *Adv. At. Mol. Phys.*, **1969**, *5*, 109-154.

Dewar, M.J.S.; Landman, D. "Gaseous Ions. 2. [1]MINDO/3 Study of the Rearrangements of Toluene and Cycloheptatriene Molecular Ions and the Formation of Tropylium" *J. Am. Chem. Soc.*, **1977**, *99*, 2446-2453.

Doran, M.C.; Fulford, F.E.; Hughes, R.J.; Morita, Y.; March, R.E.; Bonner, R.F. "Effects of Charge Exchange Reactions on the Motion of Ions in Three-Dimensional Quadrupole Electric Fields. Part III. A Two-Ion Model" *Int. J. Mass Spectrom. Ion Phys.*, **1980**, *33*, 139-159.

Dotan, I.; Fehsenfeld, F.C.; Albritton, D.L. "Energy Dependence of the Reaction of O_2^+ with CH_4," *J. Chem. Phys.*, **1978**, *68*, 5665.

Dotan, I.; Lindinger, W. "Energy Dependence of the Reactions of Ar^+ with H_2, N_2, CO, O_2, CO_2, N_2O and COS," *J. Chem. Phys.*, **1982**, *76*, 4972-4977.

Douglas, D.J. "Mechanism of the Collision-Induced Dissociation of Polyatomic Ions Studied by Triple Quadrupole Mass Spectrometry," *J. Phys. Chem.*, **1982**, *86*, 185-191.

Dunbar, R.C. "Photodissociation of Toluene Parent Cations" *J. Am. Chem. Soc.*, **1973**, *95*, 472-476.

Dunbar, R.C. "Nature of the $C_7H_7^+$ Ions from Toluene Parent Ion Photodissociation" *J. Am. Chem. Soc.*, **1975**, *97*, 1382-1384.

Durup-Ferguson, M.; Bohringer, H.; Fahey, D.W.; Fehsenfeld, F.C.; Ferguson, E.E. "Competitive Reaction and Quenching of Vibrationally Excited O_2^+ Ions with SO_2, CH_4 and H_2O," *J. Chem. Phys.*, **1984**, *81*, 2657-2666.

Evans, C.; Catinella, S.; Traldi, P.; Vettori, U.; Allegri, G. "Ion-Trap Mass Spectrometry in Ion Structure Studies. 1. Characterization of Isomeric Hydroxyindoles by Electron Ionization and Energy-Resolved Collision-Activated Mass Spectrometry," *Rap. Comm. Mass Spectrom.*, **1990**, *4*, 335-340.

Evans, C.; Traldi, P.; Mele, A.; Sottani, S. "A Comparison Between Ion Trap and Triple Quadrupole Collision Results," *Org. Mass Spectrom.*, **1991**, *26*, 347-349.

Fehsenfeld, F.C.; Ferguson, E.E.; "Thermal Energy Positive Ion Reactions in a Wet Atmosphere Containing Ammonia," *J. Chem. Phys.*, **1973**, *59*, 6272-6276.

Ferguson, E.E. "Vibrational Quenching of Small Molecular Ions in Neutral Collisions," *J. Phys. Chem.*, **1986**, *90*, 731-738.

Fetterolf, D.D.; Yost, R.A. "Energy-Resolved Collision-Induced Dissociation in Tandem Mass Spectrometry," **1982**, *44*, 37-50.

Fischer, E. "Three-dimensional Stabilization of Charged Carriers in a Quadrupolar Field," *Z. Phys.*, **1959**, *156*, 1-26.

Fulford, J.E.; Dupuis, J.W.; March, R.E. "Gas-Phase Ion-Molecule Reactions of Dimethylsulphoxide," *Can. J. Chem.*, **1978**, *56*, 2324-2330.

Fulford, J.E.; Hoa, D-N.; Hughes, R.J.; March, R.E.; Bonner, R.F.; Wong, G.J. "Radio-Frequency Mass Selective Excitation and Resonant Ejection of Ions in a Three-Dimensional Quadrupole Ion Trap," *J. Vac. Sci. Technol.*, **1980**, *17*, 829-835.

Fulford, J.E.; March, R.E. "A New Mode of Operation for the Three-Dimensional Quadrupole Ion Store (QUISTOR): The Selective Ion Reactor," *Int. J. Mass Spectrom. Ion Phys.*, **1978**, *26*, 155-162.

Fulford, J.E.; March, R.E. "Ion Withdrawal Studies of the Quadrupole Ion Storage Trap (QUISTOR). Part I. Characterization of the Ion Trapping Potential Well and the Location of Extractable Ions," *Int. J. Mass Spectrom. Ion Phys.*, **1979a**, *30*, 39-55.

Fulford, J.E.; March, R.E. "Ion Withdrawal Studies of the Quadrupole Ion Storage Trap (QUISTOR). Part II. The Effects of R.F. Grating on Ion Withdrawal Efficiency," *Int. J. Mass Spectrom. Ion Phys.*, **1979b**, *30*, 373-378.

Futrell, J.H.; Tiernan, T.O. "Dissociative Charge-Exchange Reactions of Rare-Gas Ions with Propane," *J. Chem. Phys.*, **1963**, *39*, 2539-2545.

Gioumousis, G.; Stevenson, D.P. "Reactions of Gaseous Molecule Ions with Gaseous Molecules. V. Theory," *J. Chem. Phys.*, **1958**, *29*, 294-299.

Glasstone, S.; Laidler, K.J.; Eyring, H. *The Theory of Rate Processes*, McGraw-Hill, New York, **1941**.

Glish, G.L.; McLuckey, S.A.; Goeringer, D.E.; Van Berkel, G.J.; Hart, K.J. "Ion Activation in a Quadrupole Ion Trap," *Proceedings of the 39th ASMS Conference on Mass Spectrometry and Allied Topics*, Nashville, TN, **1991**, 536-537.

Good, M.L. Univ. California Rad. Lab. Report UCRL-4146, Berkeley, CA, **1953**.

Griffiths, I.W.; Harris, F.M.; Mukhtar, E.S.; Beynon, J.H. "Calculation of the Abundance Ratio [$91^+/92^+$] from *n*-Butylbenzene Molecular Ion as a Function of Internal Energy," *Int. J. Mass Spectrom. Ion Phys.*, **1981**a, *41*, 83-88.

Griffiths, I.W.; Mukhtar, E.S.; Harris, F.M.; Beynon, J.H. "Effect of Source Temperature on the Average Internal Energy of Positive Ions," *Int. J. Mass Spectrom. Ion Phys.*, **1982**, *43*, 283-292.

Griffiths, I.W.; Mukhtar, E.S.; March, R.E.; Harris, F.M.; Beynon, J.H. "Comparison of Photo-Excitation of Ions and Collisional Excitation Using Gases," *Int. J. Mass Spectrom. Ion Phys.*, **1981**b, *39*, 125-132.

Gronowska, J.; Paradisi, C.; Traldi, P.; Vettori, U. "A Study of the Relevant Parameters in Collisional-activation of Ions in the Ion-Trap Mass Spectrometer," *Rap. Comm. Mass Spectrom.*, **1990**, *4*, 306-313.

Haddon, W.F.; McLafferty, F.W. "Metastable Ion Characteristics VII. Collision-Induced Metastables," *J. Am. Chem. Soc.*, **1968**, *90*, 4745-4746.

Hamdan, M.; Birkinshaw, K.; Twiddy, N.D. "Energy Dependence of the Reactions of $Ar^{+\cdot}(^2P_{1/2})$ and $Ar^{+\cdot}(^2P_{3/2})$ with N_2," *Int. J. Mass Spectrom. Ion Proc.*, **1984**, *57*, 225-231.

Harrison, A.G. *Chemical Ionization Mass Spectrometry*, CRC Press, Boca Raton, Florida, **1983**.

Harrison, A.G. "Charge-Exchange Mass Spectrometry," *Ionic Processes in the Gas Phase*, M.A.A. Ferreira, Ed., D. Reidel Publishing Co., New York, **1984**, 23-40.

Harrison, A.G.; Lin, M.S. "Energy Dependence of the Fragmentation of the *n*-Butylbenzene Molecular Ion," *Int. J. Mass Spectrom. Ion Phys.*, **1983**, *51*, 353-356.

Harrison, A.G.; Mercer, R.S.; Reiner, E.J.; Young, A.B.; Boyd, R.K.; March, R.E.; Porter, C.J. "A Hybrid BEQQ Mass Spectrometer for Studies in Gaseous Ion Chemistry," *Int. J. Mass Spectrom. Ion Proc.*, **1986**, *74*, 13-31.

Harrison, A.G.; Tsang, C.W. "Origin of Mass Spectra," *Biochemical Applications of Mass Spectrometry*, G.R. Waller, Ed., Wiley-Interscience, Toronto, **1972**, 135-156.

Hehre, W.J.; McIver, R.T.; Pople, J.A.; Scheyer, P.v.R.; "Alkyl Substituent Effects on the Stability of Protonated Benzene," *J. Am. Chem. Soc.*, **1974**, *96*, 7162-7163.

Herman, J.A.; Li, Y.-H.; Harrison, A.G. "Energy Dependence of the Fragmentation of Some Isomeric $[C_6H_{12}]^+$ Ions," *Org. Mass Spectrom.*, **1982**, *17*, 143-150.

Howorka, F.; Dotan, I.; Fehsenfeld, F.C.; Albritton, D.L. "Kinetic Energy Dependence of the Branching Ratios of the Reaction of N^+ Ions with O_2," *J. Chem. Phys.*, **1980**, 73, 758-764.

Hughes, R.J.; March, R.E.; Young, A.B. "Multiphoton Dissociation of Ions Derived from 2-Propanol in a QUISTOR with Low-Power CW Infrared Laser Radiation," *Int. J. Mass Spectrom. Ion Phys.*, **1982**, *42*, 255-263.

Hughes, R.J.; March, R.E.; Young, A.B. "Multiphoton Dissociation of Gaseous Ions in a Quadrupole Ion Store (QUISTOR)," *Int. J. Mass Spectrom. Ion Phys.*, **1983a**, *47*, 85-88.

Hughes, R.J.; March, R.E.; Young, A.B "Optimization of Ion Trapping Characteristics for Studies of Ion Photodissociation," *Can. J. Chem.*, **1983b**, *61*, 824-833.

Hughes, R.J.; March, R.E.; Young, A.B. "Multiphoton Dissociation of Ions Derived from Isopropanol and Deuterated Analogues in a QUISTOR with Low-Power CW Infrared Laser Radiation," *Can. J. Chem.*, **1983c**, *61*, 834-845.

Hüwel, L.; Guyer, D.R.; Lin, G-H.; Leone, S.R. "Laser-induced Fluorescence Measurement of Nascent Vibrational and Rotational Product State Distributions in the Charge Transfer of $Ar^+ + N_2 \rightarrow Ar + N_2^+$ (v=0,1) at 0.2eV," *J. Chem. Phys.*, **1984**, *81*, 3520-3535.

Iffländer, R.; Werth, G. "Optical Detection of Ions Confined in a RF Quadrupole Trap," *Metrologia*, **1977**, *13*, 167-170.

Ikezoe, Y.; Matsuoka, S.; Takebe, M.; Viggiano, A. *Gas Phase Ion-Molecule Reaction Rate Constants Through 1986*, Maruzen Company, Tokyo, **1987**.

Jackson, J.-A.; Lias, S.G.; Ausloos, P. "An Ion Cyclotron Resonance Study of the Structures of $C_7H_7^+$ Ions," *J. Am. Chem. Soc.*, **1977**, *99*, 7515-7521.

Jennings, K.R. "Collision-Induced Decompositions of Aromatic Molecular Ions," *Int. J. Mass Spectrom. Ion Phys.*, **1968**, *1*, 227-235.

Johnson. J.V.; Pedder, R.E.; Kleintop B.; Yost, R.A. "Resonant Excitation for the CID in the Quadrupole Ion Trap: Energetics and Efficiencies," *Proceedings of the 38th*

ASMS Conference on Mass Spectrometry and Allied Topics, Tucson, AZ, **1990a**, 1130-1131.

Johnson, J.V.; Yates, N.A.; Yost, R.A., unpublished results, **1992**.

Johnson, J.V.; Yost, R.A.; Kelley, P.E.; Bradford, D.C. "Tandem-in-Space and Tandem-in-Time Mass Spectrometry: Triple Quadrupoles and Quadrupole Ion Traps," *Anal. Chem.*, **1990b**, *62*, 2162-2172.

Julian, R.K.; Reiser, H.P.; Cooks, R.G. "Large Scale Simulation of Mass Spectra Recorded with a Quadrupole Ion Trap Mass Spectrometer," **1991**, submitted.

Kamar, A.; Young, A.B.; March, R.E. "A Comparative Ion Chemistry Study of Acetone, Diacetone Alcohol, and Mesityl Oxide," *Can. J. Chem.*, **1986a**, *64*, 1979-1988.

Kamar, A.; Young, A.B.; March, R.E. "Experimentally Determined Proton Affinities of 4-methyl-3-penten-2-one, 2-propyl ethanoate and 4-hydroxy-4-methyl-2-pentanone in the Gas Phase," *Can. J. Chem.*, **1986b**, *64*, 2368-2370.

Kebarle, P. "Ion Thermochemistry and Solvation from Gas Phase Ion Equilibria," *Annual Review of Physical Chemistry*, Annual Reviews, Inc., Palo Alto, California, **1977**, vol. 28, 445-476.

Kebarle, P.; Godbole, E.W. "Mass Spectrometry Study of Ions from the α-Particle Irradiation of Gases at Near Atmospheric Pressures" *J. Chem. Phys.*, **1963**, *39*, 1131-1132.

Kelley, P.E.; Stafford, G.C.; Stephens, P.R. Method of Mass Analyzing a Sample by Use of a Quadrupole Ion Trap, U.S. Patent 4,540,884, 10 September **1985a**.

Kelley, P.E.; Stafford, G.C.; Syka, J.E.P.; Reynolds, W.E.; Louris, J.N.; Amy, J.W.; Todd, J.F.J. "New Advances in the Operation of the Ion Trap Mass Spectrometer," *Proceedings of the 33rd ASMS Conference on Mass Spectrometry and Allied Topics*, San Diego, CA, **1985b**, 707-708.

Kenttämaa, H.I.; Cooks, R.G. "Tautomer Characterization by Energy Resolved Mass Spectrometry. Dimethyl Phosphite and Dimethyl Phosphonate Ions" *J. Am. Chem. Soc.*, **1985**, *107*, 1881-1886.

Kennard, E.H. *Kinetic Theory of Gases with an Introduction to Statistical Mechanics*, McGraw-Hill, New York, **1938**.

Kim, M.S.; McLafferty, F.W. "Efficiency of Collisional Activation of Gaseous Ions," *J. Am. Chem. Soc.*, **1978**, *100*, 3279-3282.

Kirchner, N.J.; Van Doren, J.M.; Bowers, M.T. "On the Structure of $CH_3O_2^+$ Product Ions in $Ar/O_2/CH_4$ Mixtures: the First Example of a Kinetic Surface," *Int. J. Mass Spectrom Ion Proc.*, **1989**, *92*, 37-51.

Kishore, M.N.; Ghosh, P.K. "Trapping of Ions Injected from an External Source into a Three-Dimensional R.F. Quadrupole Field," *Int. J. Mass Spectrom. Ion Phys.*, **1979**, *29*, 345-350.

Knight, R.D. "The General Form of the Quadrupole Ion Trap Potential," *Int. J. Mass Spectrom. Ion Proc.*, **1983**, *51*, 127-131.

Knight, R.D.; Prior, M.H. "Laser Scanning Measurement of the Density Distribution of Confined $^6Li_+$ Ions," *J. Appl. Phys.*, **1979**, *50*, 3044-3049.

Kondrat, R.W.; Cooks, R.G. "Direct Analysis of Mixtures by Mass Spectrometry," *Anal. Chem.*, **1978**, *50*, 81A-92A.

Langevin, P. "Une Formule Fondamentale de Théorie Cinetique," *Annales de Chimie et de Physique*. Series 8, **1905**, *5*, 245-288.

Laramée, J.A.; Cameron, D.; Cooks, R.G. "Collision-Induced Dissociation Mass Spectrometry: Target Gas Effects upon Scattering and Charge Exchange," *J. Am. Chem. Soc.*, **1981**, *103*, 12-17.

Lau, Y.K.; Kebarle, P. "Substituent Effects on the Intrinsic Basicity of Benzene: Proton Affinities of Substituted Benzenes," *J. Am. Chem. Soc.*, **1976**, 7452-7453.

Lawson, G.; Bonner, R.F.; Mathers, R.E.; Todd, J.F.J; March, R.E. "Quadrupole Ion Storage (QUISTOR) Part I. Ion-molecule Reactions in Methane, Water and Ammonia," *J. Chem. Soc., Faraday Trans. I*, **1976a**, *72*, 545-557.

Lawson, G.; Bonner, R.F.; Todd, J.F.J "The Quadrupole Ion Store (QUISTOR) as a Novel Source for a Mass Spectrometer," *J. of Physics E: Sci. Instrum.*, **1973**, *6*, 357-362.

Lawson, G.; Todd, J.F.J "Weak Peak Enhancement by Selective Ion Trapping in a Quadrupole Ion Storage Source," *Anal. Chem.*, **1977**, *49*, 1619-1622.

Lawson, G.; Todd, J.F.J; Bonner, R.F. "Theoretical and Experimental Studies with the Quadrupole Ion Storage Trap (QUISTOR)," *Dynamic Mass Spectrometry*, D. Price and J.F.J. Todd, Eds., Heyden and Sons, Ltd., London, **1976b**, vol. 4, 39-81.

Levsen, K.; Schwarz, H. "Gas-phase Chemistry of Collisionally Activated Ions," *Mass Spectrom. Rev.*, **1983**, *2*, 77-148.

Li, Y.-H.; Herman, J.A.; Harrison, A.G. "Charge Exchange Mass Spectra of Some C_5H_{10} Isomers," *Can. J. Chem.*, **1981**, *59*, 1753-1759.

Liao, C.-L.; Xu, R.; Ng, C.Y. "Fine Structure Effect on the Charge Transfer Reaction of $Ar^+(^2P_{3/2,1/2}) + N_2\ (X^1\Sigma_g^+, v=0)$," *J. Chem. Phys.*, **1986a**, *84*, 1948-1950.

Liao, C.-L.; Shao, J.-D.; Xu, R.; Flesch, G.D.; Li, Y.-G.; Ng, C.Y. "A State-to-State Study of the Electron Transfer Reactions $Ar^+(^2P_{3/2,1/2})$ + N_2 (X,v=0) → $Ar(^1S_o)$ + $N_2^+(X,v')$," *J. Chem. Phys.*, **1986**b, *85*, 3874-3890.

Lias, S.G.; Ausloos, P. "Ionization Energies of Organic Compounds by Equilibrium Measurements," *J. Am. Chem. Soc.*, **1978**, *100*, 6027-6034.

Lias, S.G.; Jackson, J.H.; Argentar, H.; Liebman, J.F. "Substituted N,N-Dialkylanilines: Relative Ionization Energies and Proton Affinities through Determination of Ion-Molecule Reaction Rate Equilibrium Constants," *J. Org. Chem.*, **1985**, *50*, 333-338.

Lias, S.G.; Liebman, J.F.; Levin, R.D. "Evaluated Gas Phase Basicities and Proton Affinities of Molecules; Heats of Formation of Protonated Molecules," *J. Phys. Chem. Ref. Data*, **1984**, *13*, 695-808.

Lin, G.-H.; Maier, J.; Leone, S.R. "Nascent Rotational Distribution of the Minor v=0 Channel in the N_2^+ Product of the Ar^+ + N_2 Charge Transfer Reaction at Near Thermal Energies," *J. Chem. Phys.*, **1986**, *125*, 557-560.

Lindinger, W.; Albritton, D.L.; Fehsenfeld, F.C. "Rate Constant for the Reaction of $O_2^+(a^4\pi_u)$ Ions with CH_4 at Relative Kinetic Energies 0.04 - 1.2 eV" *J.Chem. Phys.*, **1979**, *70*, 2038-2039.

Lindinger, W.; Howorka, F.; Lukac, P.; Kuhn, S.; Villinger, H.; Alge, E.; Ramler, H. "Charge Transfer of $Ar^+ + N_2 \rightarrow N_2^+ + Ar$ at Near Thermal Energies," *Phys. Rev. A*, **1981**, *23*, 2319-2326.

Lindsay, B.G.; Irvine, A.D.; Latimer, C.J.; "Charge Exchange of O_2^+ Ions with O_2 and CH_4: The Effect of Internal Energy Studied Using a New Fixed Wavelength PEPICO Technique," *Int. J. Mass Spectrom. Ion Proc.*, **1989**, *91*, 113-122.

Louris, J.N.; Brodbelt-Lustig, J.S.; Cooks, R.G.; Glish, G.L; Van Berkel, G.J.; McLuckey, S.A. "Ion Isolation and Sequential Stages of Mass Spectrometry in a Quadrupole Ion Trap Mass Spectrometer," *Int. J. Mass Spectrom. Ion Proc.*, **1990**, *96*, 117-137.

Louris, J.N.; Cooks, R.G.; Syka, J.E.P.; Kelley, P.E.; Stafford, G.C.; Todd, J.F.J. "Instrumentation, Applications, and Energy Deposition in Quadrupole Ion Trap Mass Spectrometry," *Anal. Chem.*, **1987**, *59*, 1677-1685.

Lunney, M.D.N.; Buchinger, F.; Moore, R.B. "The Temperature of Buffer-Gas Cooled Ions in a Paul Trap," *J. Mod. Optics*, accepted August **1991**.

Major, F.G.; Dehmelt, H.G. "Exchange-Collision Techniques for Radiofrequency Spectroscopy," *Phys. Rev.*, **1968**, *170*, 91-107.

March, R.E. "A Musing on the Present State of the Ion Trap and Prospects for Future Applications," *Org. Mass Spectrom.*, **1991**, *26*, 627-632.

March, R.E.; Hughes, R.J. *Quadrupole Storage Mass Spectrometry and Its Applications*, John Wiley and Sons, New York, **1989**.

March, R.E.; Londry, F.A.; Alfred, R.L.; Todd, J.F.J.; Penman, A.D.; Vedel, F.; Vedel, M. "Resonance Excitation of Ions Stored in a Quadrupole Ion Trap Part III. Introduction to the Field Interpolation Simulation Method," *Int. J. Mass Spectrom. Ion Proc.*, **1991**, *110*, 159-178.

March, R.E.; McMahon, A.W.; Allison, E.T.; Londry, F.A.; Alfred, R.L.; Todd, J.F.J.; Vedel, F. "Resonance Excitation of Ions Stored in a Quadrupole Ion Trap Part II. Further Simulation Studies, *Int. J. Mass Spectrom. Ion Proc.*, **1990**, *99*, 109-124.

March, R.E.; McMahon, A.W.; Londry, F.A.; Alfred, R.L.; Todd, J.F.J; Vedel, F. "Resonance Excitation of Ions Stored in A Quadrupole Ion Trap. Part 1. A Simulation Study," *Int. J. Mass Spectrom. Ion Proc.*, **1989**, *95*, 119-156.

Marshall, A.G.; Grosshams, P.B. "Fourier Transform Ion Cyclotron Resonance Mass Spectrometry: The Teenage Years," *Anal. Chem.*, **1991**, *63*, 215A-229A.

Mather, R.E.; Todd, J.F.J. "The Quadrupole Ion Store (QUISTOR). Part V. A Simple Model for the Ion Ejection Process," *Int. J. Mass Spectrom. Ion Phys.*, **1979**, *31*, 1-13.

Mather, R.E.; Todd, J.F.J "The Quadrupole Ion Store (QUISTOR). Part VII. Simultaneous Positive/Negative Ion Mass Spectrometry," *Int. J. Mass Spectrom. Ion Proc.*, **1980**, *33*, 159-165.

Mathieu, É., "Mémoire sur le Mouvement Vibratoire d'une Membrane de Forme Elliptique," *J. Math. Pures Appl. (J. Liouville)*, **1868**, *13*, 137.

McClellan, A.L. *Tables of Experimental Dipole Moments*, H. Freeman and Co., San Francisco, **1963** and **1972**.

McDaniel, A.M. "Langevin's Calculation of the Diffusion and Mobility Coefficients," *Collision Phenomena in Ionized Gases*, E.W. McDaniel, Ed., John Wiley, New York, **1964**, pp. 701-726.

McFarland, M.; Albritton, D.L.; Fehsenfeld, F.C.; Ferguson, E.E.; Schmeltekopf, A.L. "Flow-DRIFT Technique for Ion Mobility and Ion-Molecule Reaction Rate Constant Measurements. I. Apparatus and Mobility Measurements," *J. Chem. Phys.*, **1973a**, *59*, 6610-6619.

McFarland, M.; Albritton, D.L.; Fehsenfeld, F.C.; Ferguson, E.E.; Schmeltekopf, A.L. "Flow-DRIFT Technique for Ion Mobility and Ion-Molecule Reaction Rate Constant

Measurements. II. Positive Ion Reactions of N^+, O^+, and N_2^+ with O_2 and O^+ with N_2 from Thermal to 2eV," *J. Chem. Phys.*, **1973b**, *59*, 6620-6628.

McLafferty, F.W., Ed. *Tandem Mass Spectrometry*, John Wiley and Sons, New York, **1983**.

McLafferty, F.W.; Bente, III, P.F.; Kornfeld, R. "Collisional Activation Spectra of Organic Ions," *J. Am. Chem. Soc.*, **1973**, *95*, 2120-2129.

McLafferty, F.W.; Bockhoff, F.M. "Formation of Benzyl and Tropylium Ions from Gaseous Toluene and Cycloheptatriene Cations," *J. Am. Chem. Soc.*, **1979**, *101*, 1783-1786.

McLafferty, F.W.; Winkler, J. "Gaseous Tropylium, Benzyl, Tolyl, and Norbornadienyl Cations," *J. Am. Chem. Soc.*, **1974**, *96*, 5182-5189.

McLuckey, S.A.; Cameron, D.; Cooks, R.G. *J. Am. Chem. Soc.*, "Proton Affinities from Dissociation of Proton-Bound Dimers," **1981**, *103*, 1313-1317.

McLuckey, S.A.; Cooks R.G.; Fulford, J.E. "Gas-Phase Thermochemical Information from Triple Quadrupole Mass Spectrometers: Relative Proton Affinities of Amines," *Int. J. Mass Spectrom. Ion Phys.*, **1983**, *52*, 165-174.

McLuckey, S.A.; Glish, G.L.; Asano, K.G.; Van Berkel, G.J. "Self-Chemical Ionization in an Ion Trap Mass Spectrometer," *Anal. Chem.*, **1988**, *60*, 2312-2314.

McLuckey, S.A.; Glish, G.L.; Van Berkel, G.J. "Multiple Stages of Mass Spectrometry in a Quadrupole Ion Trap Mass Spectrometer-Prerequisites," *Int. J. Mass Spectrom. Ion Proc.*, **1991a**, *106*, 213-235.

McLuckey, S.A.; Goeringer, D.E.; Glish, G.L. "Selective Ion Isolation/Rejection Over a Broad Mass Range in the Quadrupole Ion Trap," *J. Am. Soc. Mass Spectrom.*, **1991b**, *2*, 11-21.

McLuckey, S.A.; Ouwerkerk, C.E.D.; Boerboom, A.J.H.; Kistemaker, P.G. "The Effect of Collision Energy in Polyatomic Ion-Neutral Target Collisions over a Range of 10-6000 eV," *Int. J. Mass Spectrom. Ion Proc.*, **1984**, *59*, 85-101.

McLuckey, S.A.; Sallans, L.; Cody, R.B.; Burnier, R.C.; Verma, S.; Freiser, B.S.; Cooks, R.G. "Energy-Resolved Tandem and Fourier-Transform Mass Spectrometry," *Int. J. Mass Spectrom. Ion Proc.*, **1982**, *44*, 215-229.

Moylan, C.R.; Brauman, J.I. "Gas Phase Acid-Base Chemistry," *Annual Review of Physical Chemistry*, B.S. Rabinovitch, J.M. Schurr, H.L. Strauss, Eds., Annual Reviews, Inc., Palo Alto, California, **1983**, vol. 34, 187-215.

Mukhtar, E.S.; Griffiths, I.W.; Harris, F.M.; Beynon, J.H. "Photodissociation of Mass-Selected Ions Investigated Using a Modified ZAB-2F Spectrometer," **1981**, *37*, 159-166.

Murad, E.; Inghram, M.G. "Photoionization of Aliphatic Ketones," *J. Chem. Phys.*, **1964**, *40*, 3263-3275.

Münch, A.; Berkler, M.; Gerz, Ch.; Wilsdorf, D. Werth, G. "Precise Ground-State Hyperfine Splitting in ^{173}Yb II," *Phys. Rev. A*, **1987**, *35*, 4147-4150.

Nacson, S.; Harrison, A.G. "Energy Transfer in Collisional Activation. Energy Dependence of the Fragmentation of *n*-Alkylbenzene Molecular Ions," *Int. J. Mass Spectrom. Ion Proc.*, **1985**, *63*, 325-337.

Nourse, B.D.; Cooks, R.G. "Aspects of Recent Developments in Ion-Trap Mass Spectrometry," *Anal. Chim. Acta*, **1990**, *228*, 1-21.

Nourse, B.D.; Cooks, R.G. "Proton Affinity Determinations Using the Kinetic Method in an Ion Trap Mass Spectrometer," *Int. J. Mass Spectrom. Ion Proc.*, **1991**, *106*, 249-272.

Nourse, B.D.; Cox, K.A.; Morand, K.L.; Cooks, R.G. "Collisional Activation of Pyrene and Anthracene in an Ion-Trap Mass Spectrometer," *J. Am. Chem. Soc.*, **1992**, *114*, 2010-2016.

Nourse, B.D.; Kenttämaa, H.I. "Effective Ion Temperature in a Quadrupole Ion Trap," *J. Phys. Chem.*, **1990**, *94*, 5809-5812.

Paul, W.; Steinwedel. H. "A New Mass Spectrometer without a Magnetic Field," *Z. Naturforsch.*, **1953**, *8a*, 448-450.

Paul, W.; Steinwedel. H. Apparatus for separating charged particles of different specific charges. German Patent 944,900, **1956**, U.S. Patent 2,939,952 7 June **1960**.

Pedder, R.E; Yost, R.A. "Computer Simulation of Ion Trajectories in a Quadrupole Ion Trap Mass Spectrometer," *Proceedings of the 36th ASMS Conference on Mass Spectrometry and Allied Topics*, San Francisco, CA, **1988**, 632-633.

Post, R.F.; Henrich, L. Univ. California Rad. Lab Report (S. Shewchuck) UCRL-2209, Berkeley, CA, **1953**.

Reiser, H.P.; Julian, R.K.; Cooks, R.G. "A Versatile Method of Simulation of the Operation of Ion Trap Mass Spectrometers," **1991**a, submitted.

Reiser, H.P.; Kaiser, K.E.; Savickas, P.J.; Cooks, R.G. "Measurement of Kinetic Energies of Ions Ejected from a Quadrupole Ion Trap," *Int. J. Mass Spectrom. Ion Proc.*, **1991**b, *106*, 237-247.

Rosenstock, H.M.; Draxl, K.; Steine, B.W.; Herman, J.T. *J. Phys. Chem. Ref. Data*, **1977**, *6*, suppl. 1.

Rosenstock, H.M.; Krauss, M. *Mass Spectrometry of Organic Ions*, McLafferty, F.W., Ed., Academic Press, New York, **1963**.

Rosenstock, H.M.; Wallenstein, M.B.; Wahrhaftig, A.L.; Eyring, H. "Absolute Rate Theory for Isolated Systems and the Mass Spectra of Polyatomic Molecules," *Proc. Nat. Acad. Sci.*, **1952**, *38*, 667-678.

Rowe, B.R.; Dupeyrat, G.; Marquette, J.B.; Smith, D.; Adams, N.; Ferguson, E.E. "The Reaction $O_2^+ + CH_4 \rightarrow CH_3O_2^+ + H$ Studied from 20 to 560 K in a Supersonic Jet and in a SIFT," *J. Chem. Phys.* **1984**, *80*, 241.

Schaaf, H.; Schmeling, U.; Werth, G. "Trapped Ion Density Distribution in the Presence of He Buffer Gas," *Appl. Phys.*, **1981**, *25*, 249-251.

Shoemaker, D.P.; Garland, C.W.; Steinfeld, J.I.; Nibler, J.W. *Experiments in Physical Chemistry*, 4th ed., McGraw-Hill Book Co., New York, **1981**, 25-55.

Siemers, I,; Blatt, R.; Sauter, Th.; Neuhauser, W. "Dynamics of Ion Clouds in Paul Traps," *Phys. Rev. A*, **1988**, *38*, 5121-5128.

Smith, D.; Adams, N.G. "Recent Advances in Flow Tubes: Measurement of Ion-Molecule Rate Coefficients and Product Distribution," *Gas Phase Ion Chemistry*, M.T. Bowers, Ed., Academic Press, New York, **1979**, vol. 1, 2-40.

Smith, D.; Adams, N.G. "Charge Transfer of $Ar^+ + N_2 \rightarrow N_2^+ + Ar$ at Thermal Energies," *Phys. Rev. A*, **1981**, *23*, 2327-2330.

Smith, D.; Adams, N.G.; Miller, J.M. "A Laboratory Study of the Reactions of N^+,N_2^+,, N_3^+, N_4^+, O^+, O_2^+, and NO^+ Ions with Several Molecules at 300 K," *J. Chem. Phys.*, **1978**, *69*, 308-318.

Sonnenfroh, D.M.; Leone, S.R. "A Laser-induced Fluorescence Study of Product Rotational State Distributions in the Charge Transfer Reaction: $Ar^+(^2P_{3/2}) + N_2 \rightarrow Ar + N_2^+(X)$ at 0.28 and 0.40eV," *J. Chem. Phys.*, **1989**, *90*, 1677-1685.

Stafford, G.C.; Kelley, P.E.; Syka, J.E.P.; Reynolds, W.E.; Todd, J.F.J. "Recent Improvements in and Analytical Applications of Advanced Ion Trap Technology," *Int. J. Mass Spectrom. Ion Phys.*, **1984**, *60*, 85-98.

Su, T; Bowers, M.T. "Classical Ion-Molecule Collision Theory" *Gas Phase Ion Chemistry*, M.T. Bowers, Ed., Academic Press, New York, **1979**, vol. 1, 83-118.

Taft, R.W. "Gas-Phase Proton-Transfer Equilibria," *Proton-Transfer Reactions*, E. Caldin, V. Gold, Eds., Chapman and Hall, London, **1975**, 31-77.

Thomas, R.; Barassin, J.; Barassin, A. Etude Cinétique du Système Réactionnel CH_3^+-NH_3 Dans le Domaine D'Énergie Compris Entre 0,04 eV et 1 eV," *Int. J. Mass Spectrom. Ion Phys.*, **1980**, *33*, 383-391.

Todd, J.F.J. "Recent Developments in the Theory and Application of the Quadrupole Ion Storage Trap (QUISTOR)," *Dynamic Mass Spectrometry*, D. Price, Ed., Heyden and Sons, Ltd., London, **1981**, vol.6, 44-70.

Todd, J.F.J. "Ion Trap Mass Spectrometer-Past, Present, and Future(?)," *Mass Spectrom. Rev.*, **1991**, *10*, 3-52.

Todd, J.F.J.; Freer, D.A.; Waldren, R.M. "The Quadrupole Ion Store (QUISTOR) Part XI. The Model of Ion Motion in a Pseudo-Potential Well: An Appraisal in Terms of Phase-Space Dynamics," *Int. J. Mass Spectrom. Ion Phys.*, **1980a**, *36*, 185-203.

Todd, J.F.J.; Freer, D.A.; Waldren, R.M. "The Quadrupole Ion Store (QUISTOR) Part XII. The Trapping of Ions Injected from an External Source: A Description in Terms of Phase-Space Dynamics," *Int. J. Mass Spectrom. Ion Phys.*, **1980b**, *36*, 371-386.

Todd, J.F.J.; Lawson, G.; Bonner R.G. "Quadrupole Ion Traps," *Quadrupole Mass Spectrometry*, P.H. Dawson, Ed., Elsevier Scientific, New York, **1976**, 181-224.

Todd, J.F.J.; Penman, A.D. "The Recent Evolution of the Quadrupole Ion Trap Mass Spectrometer - An Overview," *Int. J. Mass Spectrom. Ion Proc.*, **1991**, *106*, 1-20.

Todd, J.F.J.; Waldren, R.M. "The Quadrupole Ion Store (QUISTOR). Part II. Phase-Synchronised Ion Ejection from a Quadrupole Ion Storage Mass Spectrometer, *Int. J. Mass Spectrom. Ion Phys.*, **1979**, *29*, 301-314.

Todd, J.F.J.; Waldren, R.M.; Bonner, R.F. "The Quadrupole Ion Store (QUISTOR) Part VIII. The Theoretical Estimation of Ion Kinetic Energies: a Comparative Survey of the Field," *Int. J. Mass Spectrom. Ion Phys.*, **1980c**, *34*, 17-36.

Todd, J.F.J.; Waldren, R.M.; Freer, D.A.; Turner, R.B. "The Quadrupole Ion Store (QUISTOR) Part X. Space-Charge and Ion Stability. B. On the Theoretical Distribution and Density of Stored Charge in RF Quadrupolar Fields," *Int. J. Mass Spectrom. Ion Phys.*, **1980d**, *35*, 107-150.

Todd, J.F.J.; Waldren, R.M.; Mather, R.E. "The Quadrupole Ion Store (QUISTOR) Part IX. Space-Charge and Ion Stability. A Theoretical Background and Experimental Results," *Int. J. Mass Spectrom. Ion Phys.*, **1980e**, *34*, 325-349.

Todd, J.F.J.; Waldren, R.M.; Mather, R.E.; Lawson, G. "On the Relative Efficiencies of Confinement of Ar^+ and Ar^{2+} Ions in a Quadrupole Ion Storage Trap (QUISTOR)," *Int. J. Mass Spectrom Ion Phys.*, **1978**, *28*, 141-151.

Turner, R.B.; Lawson, G.; Todd, J.F.J. "Appendix: An Ultra-Simple Method for the Calculation of Ion Trajectories and Stability Zones for 'Real' Radio Frequency

Quadrupole-Type Devices," *Dynamic Mass Spectrometry*, D. Price and J.F.J. Todd, Eds., Heyden and Sons, Ltd., London, **1976**, vol. 4, 79-81.

Van Doren, J.M.; Barlow, S.E.; DePuy, C.H.; Bierbaum, V.M.; Dotan, I.; Ferguson, E.E. "Chemistry and Structure of the $CH_3O_2^+$ Product of the O_2^+ + CH_4 Reaction," *J. Phys. Chem.*, **1986**, *90*, 2772-2777.

Vedel, F. "On the Dynamics of Ion Clouds Stored in an R.F. Quadrupole Trap," *Int. J. Mass Spectrom. Ion Proc.*, **1991**, *106*, 3-61.

Vedel, F.; André, J. "Influence of Space Charge on the Computed Statistical Properties of Stored Ions Cooled by a Buffer Gas in a Quadrupole RF Trap," *Phys. Rev. A*, **1984**, *29*, 2098-2101.

Vedel, F.; André, J. "Computation for Ions Stored in a Quadrupole R.F. Trap Cooled by a Buffer Gas: Influence of Working Parameters on Space-Charge Effects," *Int. J. Mass Spectrom. Ion Proc.*, **1985**, *65*, 1-22.

Vedel, F.; André, J.; Vedel, M. "Invariance Temporelle et Propriétés Statistique Énergétiques et Spatiales d'Ions Confinés dans une Trappe Quadrupolaire R.F. II. Introduction à l'Étude de la Charge d'Espace," *J. de Phys.*, **1981**a, *42*, 391-398.

Vedel, F.; André, J.; Vedel, M. "Invariance Temporelle et Propriétés Statistique Énergétiques et Spatiales d'Ions Confinés dans une Trappe Quadrupolaire R.F. III. Fréquences Séculaires du Mouvement en Présence de Charge d'Espace," *J. de Phys.*, **1981**b, *42*, 1611-1622.

Vedel, F.; André, J.; Vedel, M.; Brincourt, G. "Computed Energy and Spacial Statistical Properties of Stored Ions Cooled by a Buffer Gas," *Phys. Rev. A*, **1983**, *27*, 2321-2330.

Vedel, F.; Vedel, M. "Nonlinear Effects in the Detection of Stored Ions," *Phys. Rev. A*, **1990**, *41*, 2348-2351.

Vedel, F.; Vedel, M.; March, R.E. "New Schemes for Resonant Ejection in R.F. Quadrupole Ion Traps," *Int. J. Mass Spectrom. Ion Proc.*, **1990**, *99*, 125-138.

Vestal, M.L. "Theoretical Studies on the Unimolecular Reactions of Polyatomic Molecule Ions. I. Propane," *J. Chem. Phys.*, **1965**, *43*, 1356-1369.

Vestal, M.L. "Ionic Fragmentation Processes," *Fundamental Processes in Radiation Chemistry*, Ausloos, P., Ed., Wiley-Interscience, New York, **1968**, 59-118.

Vestal, M.; Lerner, G. "Fundamental Studies Relating to the Radiation Chemistry of Small Organic Molecules," Office of Aerospace Research USAF, ARC, 67-01114, **1967**.

Vestal, M.L.; Wahrhaftig, A.L.; Johnson, W.H. "Improved Rate Expression in the Quasi-Equilibrium Theory of Mass Spectra," *J. Chem. Phys.*, **1962**, *37*, 1276-1283.

Viggiano, A.A.; Morris, R.A.; Van Doren, J.M.; Paulson, J.F. "The Effect of Low Frequency CH_4 Vibrations on the Rate Constant for the Reaction of O_2^+ ($X^2\Pi_g$, v=0) with CH_4," *J. Chem. Phys.*, **1992**, *96*, 275-284.

Viggiano, A.A.; Van Doren, J.M.; Morris, R.A.; Paulson, J.F. "Evidence for an Influence of Rotational Energy on the Rate Constants for the Reaction of Ar^+ ($^2P_{3/2}$) with N_2," *J. Chem. Phys.*, **1990**, *93*, 4761-4765.

Villinger, H.; Richter, R.; Lindinger, W. "On the Structure of $CH_3O_2^+$," *Int. J. Mass Spectrom. Ion Phys.*, **1983**, *51*, 25-30.

Wahrhaftig, A.L. *Mass Spectrometry*, Reed, R.I., Ed., Academic Press, New York, **1965**.

Walder, R.; Franklin, J.L. "Proton Affinities of Neutral Molecules" *Int. J. Mass Spectrom. Ion Phys.*, **1980**, *36*, 85-112.

Waldren, R.M.; Todd, J.F.J. "The Quadrupole Ion Store (QUISTOR). Part III. Studies on Phase-Synchronised Ion Ejection: the Effects of Ejection Pulse Width and Detection Pulse Delay," *Int. J. Mass Spectrom. Ion Phys.*, **1979a**, *29*, 315-335.

Waldren, R.M.; Todd, J.F.J. "The Quadrupole Ion Store (QUISTOR). Part IV. "Total Pressure" Mode Operation with Phase-Synchronised Ion Ejection," *Int. J. Mass Spectrom. Ion Phys.*, **1979b**, *29*, 337-344.

Waldren, R.M.; Todd, J.F.J. "The Quadrupole Ion Store (QUISTOR). Part VI. Studies on Phase-Synchronised Ion Ejection: The Effects of Ejection Pulse Amplitude," *Int. J. Mass Spectrom. Ion Phys.*, **1979c**, *31*, 15-29.

Walls, F.L.; Dunn, G.H. "Storing Ions for Collision Studies," *Physics Today*, **1974**, Aug., 30-35.

Weber-Grabau, M.; Kelley, P.E.; Bradshaw, S.C.; Hoekman, D.J.; "Advances in MS/MS Analysis with the Ion Trap Mass Spectrometer," *Proceedings of the 36th ASMS Conference on Mass Spectrometry and Allied Topics*, San Francisco, CA, **1988**, 1106-1107.

Weber-Grabau, M.; Kelley, P.E.; Syka, J.E.P.; Bradshaw, S.C.; Brodbelt, J.S. "Improved Ion Trap Performance MS/MS Scan Functions," *Proceedings of the 35th Conference on Mass Spectrometry and Allied Topics*, **1987**, 1114-1115.

Williams, K.R. *Error Analysis in Physical and Analytical Chemistry*, University Copy Center, Gainesville, **1990**.

Winkler, J.; McLafferty, F.W. "Long-Lived Benzyl and Tolyl Cations in the Gas Phase," *J. Am. Chem. Soc.*, **1973**, *95*, 7533-7535.

Wolf, J.F.; Staley, R.H.; Koppel, I.; Tagepera, M.; McIver, R.T.; Beauchamp, J.L.; Taft, R.W. "Gas-Phase Basicities and Proton Affinities of Compounds between Water and Ammonia from Pulsed Ion Cyclotron Resonance Thermal Equilibria Measurements," *J. Am. Chem. Soc.*, **1977**, *99*, 5417-5429.

Wu, Hui-Fen; Brodbelt, J.S. "Effects of Collisional Cooling on Ion Detection in a Quadrupole Ion Trap Mass Spectrometer," **1991**, submitted.

Wuerker, R.F.; Shelton, H.; Langmuir, R.V. "Electrodynamic Containment of Charged Particles," *J. Appl. Phys.*, **1959**, *30*, 342-349.

Wysocki, V.H.; Kenttämaa, H.I.; Cooks, R.G. "Internal Energy Distributions of Isolated Ions After Activation by Various Methods," *Int. J. Mass Spectrom. Ion Proc.*, **1987**, *75*, 181-208.

Yamdagni, R.; Kebarle, P. "Gas-Phase Basicities and Proton Affinities of Compounds Between Water and Ammonia and Substituted Benzenes from a Continuous Ladder of Proton Transfer Equilibria Measurements," *J. Am. Chem. Soc.*, **1976**, *98*, 1320-1324.

Yates, N.A.; Yost, R.A. "A Comparative Study of Selective Mass Storage and Two-Step Isolation in the Quadrupole Ion Trap," *Proceedings of the 39th ASMS Conference on Mass Spectrometry and Allied Topics*, Nashville, TN, **1991**, 1489-1490.

Yost, R.A.; Enke, C.G. "Selected Ion Fragmentation with a Tandem Quadrupole Mass Spectrometer," *J. Am. Chem. Soc.*, **1978**, *100*, 2274-2275.

Yost, R.A.; Enke, C.G. "Triple Quadrupole Mass Spectrometers for Direct Mixture Analysis and Structure Elucidation," *Anal. Chem.*, **1979**, *51*, 1251A-1264A.

Yost, R.A.; Enke, C.G.; McGilvery, D.C.; Smith, D.; Morrison, J.D. "High Efficiency Collision-Induced Dissociation in an RF-Only Quadrupole," *Int. J. Mass Spectrom. Ion Proc.*, **1979**, *30*, 127-136.

Young, A.B.; March, R.E.; Hughes, R.J. "Studies of Infrared Multiphoton Dissociation: Roles of Protonated Aliphatic Alcohol Dimers," *Can. J. Chem.*, **1985**, *63*, 2324-2331.

Zwillinger, D. *Handbook of Differential Equations*, Academic Press, Boston, **1989**, 575-579.

Zwinselman, J.J.; Nacson, S.; Harrison, A.G. "A Comparison of Charge-Exchange, Energy-Resolved and Angle-Resolved Mass Spectrometric Methods for Studying the Energy Dependence of Ionic Fragmentation Reactions," *Int. J. Mass Spectrom. Ion Proc.*, **1985**, *67*, 93-108.

BIOGRAPHICAL SKETCH

Cecilia Basic was born in Winnipeg, Manitoba, Canada, on April 13, 1962. After graduating from Kelvin High School in 1980, she went on to the University of Winnipeg where she completed her Bachelor of Science degree (Four-Year) in May 1985. During the following year, she worked as a research assistant in the Faculty of Human Ecology at the University of Manitoba, after which she spent four months travelling throughout Europe.

Upon returning from Europe in the summer of 1986, she entered the Department of Chemistry at the University of Toronto, where, under the supervision of Dr. Alex G. Harrison, she completed her Master of Science degree in mass spectrometry (conferred October 1988). During her studies at the University of Toronto, she received the Susan C. and William G. Gollop Scholarship (1986-87), the F.E. Beamish Analytical Chemistry Award (1986-87), and a University of Toronto Open Master's Fellowship (1987). In August 1988, she moved to Gainesville, Florida, to pursue her doctoral studies in analytical mass spectrometry at the University of Florida under the supervision of Drs. Richard A. Yost and John R. Eyler. Upon completion of her graduate work, she will begin postdoctoral studies as a Research Fellow at the Beckman Research Institute at the City of Hope in Duarte, California.

I certify that I have read this study and that in my opinion it conforms to acceptable standards of scholarly presentation and is fully adequate, in scope and quality, as a dissertation for the degree of Doctor of Philosophy.

Richard A. Yost, Chairman
Professor of Chemistry

I certify that I have read this study and that in my opinion it conforms to acceptable standards of scholarly presentation and is fully adequate, in scope and quality, as a dissertation for the degree of Doctor of Philosophy.

John R. Eyler
John R. Eyler, Cochairman
Professor of Chemistry

I certify that I have read this study and that in my opinion it conforms to acceptable standards of scholarly presentation and is fully adequate, in scope and quality, as a dissertation for the degree of Doctor of Philosophy.

Anna Brajter-Toth
Associate Professor of Chemistry

I certify that I have read this study and that in my opinion it conforms to acceptable standards of scholarly presentation and is fully adequate, in scope and quality, as a dissertation for the degree of Doctor of Philosophy.

W. W. Harrison
Willard W. Harrison
Professor of Chemistry

I certify that I have read this study and that in my opinion it conforms to acceptable standards of scholarly presentation and is fully adequate, in scope and quality, as a dissertation for the degree of Doctor of Philosophy.

Stephen T. Gottesman
Professor of Astronomy

This dissertation was submitted to the Graduate Faculty of the Department of Chemistry in the College of Liberal Arts and Sciences and to the Graduate School and was accepted as partial fulfillment of the requirements for the degree of Doctor of Philosophy.

August 1992

Dean, Graduate School